**UvA-DARE (Digital Academic Repository)**

**Water interacting with interfaces, ions and itself**

Piatkowski, L.

Water Interacting
with Interfaces,
Ions and
Itself

Łukasz Piątkowski

Water Interacting with Interfaces, Ions and Itself.

Ł. Piątkowski
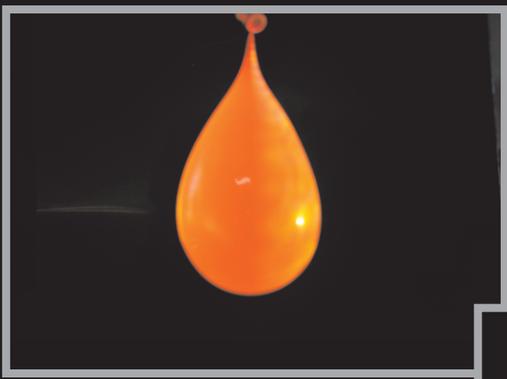
# Water Interacting with Interfaces, Ions and Itself

Cover design: Łukasz Piątkowski and Yves Rezus.

# Water Interacting with Interfaces, Ions and Itself

ACADEMISCH PROEFSCHRIFT

ter verkrijging van de graad van doctor
aan de Universiteit van Amsterdam
op gezag van de Rector Magnificus
prof. dr. D. C. van den Boom
ten overstaan van een door het college voor promoties
ingestelde commissie,
in het openbaar te verdedigen in de Agnietenkapel
op vrijdag 27 januari 2011, te 12:00 uur

door

Łukasz Piątkowski

geboren te Sieraków, Polen

*Dla Mamy*

Publications covered in this thesis

L. Piatkowski, K. B. Eisenthal and H. J. Bakker. Ultrafast intermolecular energy transfer in heavy water. *Phys. Chem. Chem. Phys. 11*, 9033-9038 (2009).

L. Piatkowski and H. J. Bakker. Vibrational relaxation pathways of AI and AII modes in N-methylacetamide clusters. *J. Phys. Chem. A 114*, 11462-11470 (2010).

Z. Zhang, L. Piatkowski, H. J. Bakker and M. Bonn. Communication: Interfacial water structure revealed by ultrafast two-dimensional surface vibrational spectroscopy. *J. Chem. Phys. 135*, 021101 (2011).

Z. Zhang, L. Piatkowski, H. J. Bakker and M. Bonn. Ultrafast vibrational energy transfer at the water/air interface revealed by two-dimensional surface vibrational spectroscopy. *Nature Chem. 3*, 888-893 (2011).

L. Piatkowski and H. J. Bakker. Vibrational dynamics of the bending mode of water interacting with ions. *J. Chem. Phys. 135*, 214509 (2011).

L. Piatkowski, J. de Heij and H. J. Bakker. Distribution of water molecules in lipid membranes. Manuscript in preparation.

L. Piatkowski and H. J. Bakker. Vibrational relaxation pathways of AI and AII modes in N-methylacetamide. Manuscript in preparation.


Other publications

A. Jarosz, D. Stefanska, M. Elantkowska, J. Ruczkowski, A. Buczek, B. Furmann, P. Glowacki, A. Krzykowski, L. Piatkowski, E. Stachowska and J. Dembczynski. High precision investigations of the hyperfine structure of metastable levels in a chromium atom. *J. Phys. B: At. Mol. Opt. Phys. 40*, 2785 (2007).

K. J. Tielrooij, D. Paparo, L. Piatkowski, H. J. Bakker and M. Bonn. Dielectric Relaxation Dynamics of Water in Model Membranes Probed by Terahertz Spectroscopy. *Biophys. J. 97*, 2484 (2009).

L. Piatkowski, A. D. Wexler, E. C. Fuchs, H. Schoenmaker and H. J. Bakker. Ultrafast vibrational energy relaxation of the water bridge. *Phys. Chem. Chem. Phys.*, DOI:10.1039/C1CP22358E.

# CONTENTS

# 1 INTRODUCTION

## 1.1 WATER AND HYDROGEN BONDS

One does not have to be a scientist to realize that without water the world would have looked much different. In fact, we would not be here to see it! All life relies on the presence of water. Water is an important and most of the time major component of cells, with its content ranging from 20% in plant seeds, $\sim$80% in human cells, up to as much as 96% in jellyfish. Moreover water covers about 2/3 of the Earths surface and forms the habitat of many organisms. Water is barely ever encountered in a "pure" state, especially in biological systems where it acts as a transporter or medium in which biochemical reactions take place. Out of many, few major functions of water are:

- solvent - water often acts passively as the medium in which other molecules and/or ions are dissolved. As an example, mineral salts can only be obtained by plants in the form of solutes in water. Many crucial reactions of the metabolism take place in aqueous solution.

- transporter - many substances (blood cells, food, waste products) in our bodies are transported by water.

- reactant - water actively participates in chemical reactions like photosynthesis, e.g. by taking up or releasing photons.

- lubricant - water is a major constituent of joint membranes in between different bones. Another example is the pleural cavity that contains the lungs. A water film lubricates the two pleural walls, thus minimizing the friction of the lungs during respiration.

- temperature controller - water possesses high specific heat and can thus take up a lot of energy at a moderate increase in temperature. The vaporization of water at the surface of the organism (sweat) helps to maintain a constant temperature.

The above rather macroscopic functions of water can be traced back to its molecular scale interactions. With respect to biological systems we would like to underline a few examples of fundamental, molecular interactions of water and biomolecules. Many of these interactions, crucial for the proper functioning of cells, are still not well understood:

- structure, stability and folding of proteins - hydrophobic hydration and hydrogen-bond formation are crucial for protein structure and stability [93]. Moreover, water is thought to diminish repulsive phosphate-phosphate interactions (thanks to its high dielectric constant), and thus contributes significantly to the stability of nucleic acids [62, 103].
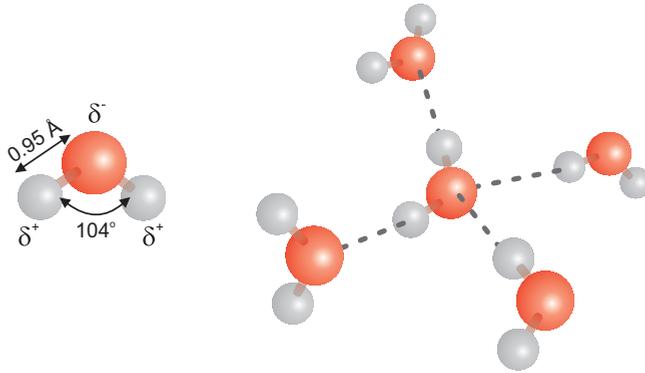
FIGURE 1.1. Left: A water molecule with its dimensions and partial charge distribution. Right: The tetrahedral arrangement of the hydrogen-bonded water network. Hydrogen bonds are indicated with the dashed lines.

- molecular recognition involving bio-molecules - water can function as an extension of the protein structure, allowing various ligands to be accommodated at a given binding site [151].

- local energy dump - the interactions among water molecules and between water and biomolecules lead to a large number of vibrational modes that can be excited. As a result, the solvating water can accept a lot of energy.

It is intriguing that in spite of its simple chemical composition, water has such an impact on many biochemical processes. A water molecule consists of three atoms: two hydrogens and one oxygen. Out of the four pairs of valence electrons two are shared between the oxygen atom and the hydrogen atoms forming covalent O-H bonds and the other two are lone pairs. Due to its bend structure and an uneven distribution of partial charges water possesses a dipole moment. Water can act as both: as hydrogen-bond donor (the two hydroxyl groups) or hydrogen-bond acceptor (the two lone pairs on oxygen atom), and thus can form up to four hydrogen-bonds with its neighbors.

The high propensity of water molecules to form extensive hydrogen-bonded networks (see figure 1.1) is what makes water so special. Even though the whole hydrogen-bond network is a transient state (hydrogen bonds are ∼20 times weaker than covalent bonds and are constantly broken and reformed), most water molecules are at all times at least 3 fold coordinated [2]. The polarity of water molecules makes water an excellent solvent for charged or polar particles. Inversely, uncharged particles dissolve in water rather poorly. The drive of water molecules to form hydrogen-bonded network has a strong biological impact. For instance, certain parts of a protein molecule can interact such to prevent water to access a specific binding site, in order to allow a ligand to bind there. The reason why such a small molecule like water would be expelled while other bigger ligand molecules are not [2] is due the drive of water molecules to stick together and to form hydrogen-bonded clusters. In other words, it is energetically highly
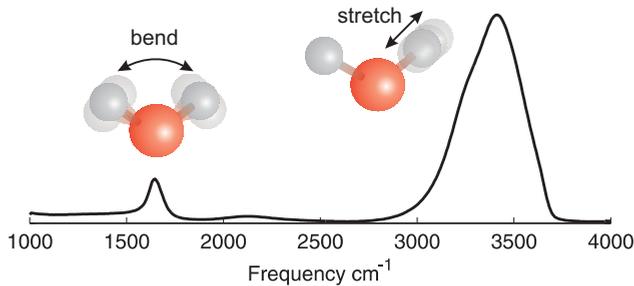
FIGURE 1.2. Linear absorption spectrum of water in the mid-infrared region. The two water molecules depict the three intramolecular vibrational modes: the bend and the stretch vibrations, of which one is shown.

unfavorable for water molecules to break the hydrogen bonds to other water molecules.

We investigate the properties of water using its interactions with light. Water molecules absorb light at specific frequencies. As most substances, it strongly absorbs ultraviolet light as a result of electronic excitations. Water molecules do not absorb the visible spectrum, except for a very weak absorption in the red part of the spectrum (which make water look slightly bluish). Strong water-light interactions show up again in the mid-infrared region, due to the vibrational resonances of water (see figure 1.2).

## 1.2 VIBRATIONAL SPECTROSCOPY

The investigation of the vibrational properties of water molecules allows us to elucidate the local structure of the measured molecules, their dynamics and the role they play in energy redistribution pathways. The high sensitivity of the O-H stretch and bend modes to the strength of the hydrogen bonds allows us to probe the local environment via the frequencies of these modes. One can thus say that the intramolecular vibrations act as a window through which we can look outside, at the surroundings of the water molecule we probe.

For about a decade spectroscopists have addressed the structural and functional implications of the interactions between water and biomolecules [123, 124, 125]. One of the complications in understanding the role of water and its interactions with other molecules is the extreme diversity of systems in which it plays a role. Due to a strong interplay of interactions and the huge variety in structure and dynamics, the properties of water molecules in one system cannot be simply extrapolated to understand its behavior in another system.

In this thesis we use two spectroscopic techniques, one of them suitable for studying bulk systems, the other for investigating molecules at an interface. The first one is mid-infrared pump-probe spectroscopy [9, 47, 32, 49, 50, 86, 82, 171, 69, 96, 10], the second is surface sum frequency generation spectroscopy [23, 51, 52, 20, 24, 66, 145, 147, 148, 42, 142, 40, 41]. Both of these techniques probe
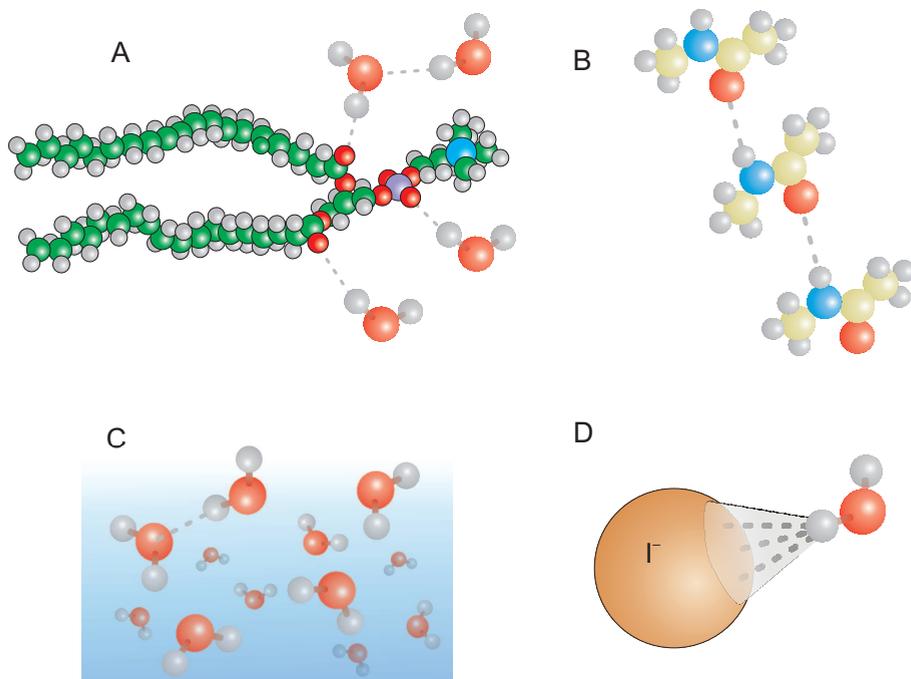
FIGURE 1.3. A cartoon showing different molecular systems studied in this thesis. A - Water interacting with lipids and lipid membranes; B - NMA and NMA clusters in apolar environment; C - Bulk and interfacial water and D - Water molecules interacting with ions.

the vibrational properties of molecules. Using the dependence of the vibrational resonant frequency on the strength of the hydrogen-bonds, we can map the local structure of the probed molecules [10] and the distribution of vibrationally distinct molecular species. The time-resolved experiments provide information on the vibrational relaxation rates and, via polarization-resolved measurements, on the orientational mobility of molecules. In addition, both techniques can be extended to a two-dimensional scheme, in which one excites a specific molecular vibration and probes the response of a different vibration, either within the same molecule or in a neighboring molecule. The two-dimensional approach thus provides access to vibrational couplings, which contain information about the relative distances and orientations between molecular moieties.

## 1.3   OUTLINE

In this thesis we study the vibrational relaxation, the molecular-scale structure, and the vibrational energy transfer and reorientation of molecules in various bio-relevant systems. We study the properties of bulk water molecules, water molecules hydrating ions and lipids, and amide molecules. In the following chapter we describe the theoretical basis for understanding the molecular processes studied in this thesis. In Chapter 3 we describe the experimental setups used in the experiments. In Chapter 4 we study vibrational resonant energy transfer in bulk liquid water. Chapter 5 describes the vibrational dynamics and structure of water molecules interacting with ions. In Chapter 6 we discuss the effect of clustering on the vibrational energy relaxation of the N-methylacetamide (NMA) molecules. In chapter 7 we study the vibrational energy relaxation pathways of the amide vibrations of NMA molecules. The distribution of water molecules embedded in cell model membranes is discussed in Chapter 8. Chapters 9 and 10 describe the structure and energy transfer of interfacial water molecules.

# 2  SPECTROSCOPY

Until about 1800, visible light was considered to be the only form of radiation. It took nearly the whole 19th century for scientists to realize the existence of different forms of radiation, the near infrared to be discovered first (William Herschel experiment), followed by the ultraviolet (Johann Ritter experiment). Soon after, Maxwell formulated his description of the properties of electromagnetic (EM) radiation. With the discovery of different forms of radiation a world of applications opened up. The electromagnetic spectrum we know now, forms a continuum of radiation, of which the wavelength spreads over many orders of magnitude (see figure 2.1).

In the early 19th century people realized that it is possible to match radiation of a certain frequency to obtain or enhance certain effects in matter. This realization gave birth to quantum mechanics and spectroscopy, the field that investigates the properties of matter with the use of EM radiation.

We now realize that life exists thanks to light-matter interactions. The light emitted by the sun is absorbed by plants and used in chemical reactions that are crucial for their existence. Not all of the EM radiation, however is beneficial. A big part of the high energy radiation (X-rays and gamma-rays) is highly destructive for live tissues. Interestingly, the same type of interactions with the molecules present in the Earths atmosphere protects us against this radiation.

Different parts of the electromagnetic spectrum are named differently, partially because they were discovered over the course of many years and were believed to be separate types of radiation, and partially because they interact
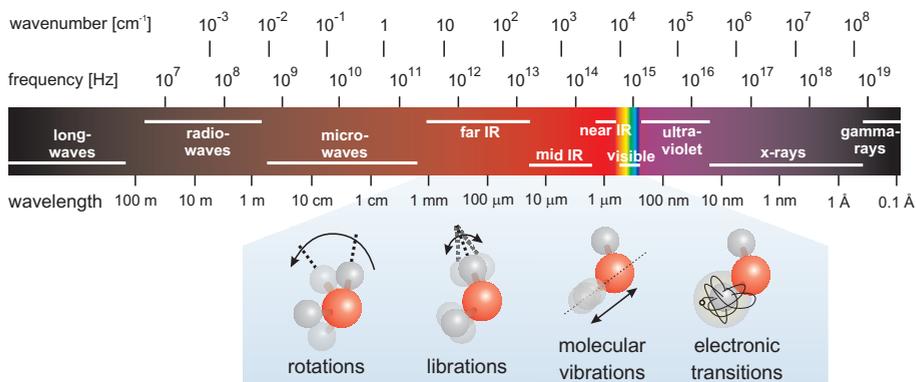


FIGURE 2.1. Electromagnetic spectrum and molecular processes associated with the mid-infrared region.
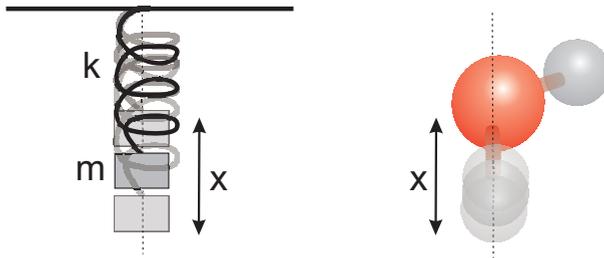
FIGURE 2.2. Examples of a harmonic oscillator: classical example of a mass $m$ connected to a spring with a force constant $k$. An analogous molecular example of the O-H stretch vibration (an oscillating hydrogen atom with respect to an oxygen atom).

with different degrees of freedom. The part of the spectrum characterized with the longest wavelengths ($\lambda = \sim$m), called 'radio waves' is used for instance in radio astronomy or in medicine in magnetic resonance imaging (MRI). The most energetic waves with the shortest wavelengths ($\lambda < 10^{-8}$ m) are x-rays and gamma rays and are used in medicine and sensing applications.

In this thesis we have used only a small fraction of the EM spectrum in the near- and mid-infrared (mid-IR) region (see figure 2.1). We have used wavelengths ranging from 800 nm to about 6000 nm. The near infrared part ($\sim$800 nm - 2100 nm) has been used in frequency mixing processes (see section 2.6) in order to generate light in the mid-IR region ($\sim$2800 nm - 6000 nm). The mid-IR part of the spectrum is associated mainly with intramolecular vibrations (motions of atoms forming molecules) and librations (hindered rotations of the molecular moieties).

## 2.1   HARMONIC OSCILLATOR

*"Physics is that subset of human experience which can be reduced to coupled harmonic oscillators"*

Michael Peskin

Following classical mechanics the periodic harmonic motion of an object is described by Newton's second law of motion:

$$F(t) = m\frac{d^2x}{dt^2} = -kx\,, \tag{2.1}$$

where $F$ is the force acting on an object with mass $m$ that is displaced from its equilibrium by a distance $x$. The constant $k$ is called the force constant. A solution of the above equation is:

$$x = \sin(\omega t)\,, \tag{2.2}$$

where $\omega$ is the frequency of the oscillation defined as:

$$\omega = \sqrt{k/m}\,. \tag{2.3}$$

The motion of an object is periodic, repeating itself in a sinusoidal manner with a constant amplitude. The frequency of the oscillation is dependent only on the objects mass $m$ and the force constant $k$. In the classical picture, the energy of a system is defined in terms of its position and momentum, which implies that the time evolution of the system can be predicted with any given accuracy:

$$E = \frac{1}{2}mv^2 + \frac{1}{2}kx^2\,. \tag{2.4}$$

The above description of an oscillator is in many ways simplified. The largest simplification lies in the linear dependence between the displacement ($x$) and the force ($F$). In reality no motion is truly harmonic and the forces acting on the system contain higher order terms. In spite of its simplicity, however, the harmonic oscillator can be successfully applied to many complex systems exhibiting small amplitude periodic motions. In figure 2.2 we show the harmonic oscillator in the form of a spring/mass system and in analogy an OH stretch vibration of the water molecule.

## 2.2 QUANTUM HARMONIC OSCILLATOR

The quantum world is known to us for about a century now, since Bohr's postulate that the electrons have quantized energy levels and their first experimental observation by Stern and Gerlach. Once the size of an object becomes comparable to the atomic scale we enter the so-called quantum realm. Quantum particles possess quantized energy states and can behave both as classical particles as well as waves (wave-particle duality). In analogy to classical mechanics we describe the motion of a particle as a quantum mechanical harmonic oscillator [22]. Let us consider the same example of a mass $m$ connected by a spring with force constant $k$ to an infinitely massive object. The energy of the system is given by the Hamiltonian:

$$\hat{H}_0 = \frac{\hat{p}^2}{2m} + \frac{1}{2}k\hat{x}^2\,, \tag{2.5}$$

where $\hat{p}$ and $\hat{x}$ are the momentum and position operators. The first term describes the kinetic energy of the system (with $\hat{p}=-i\hbar\frac{\partial}{\partial x}$), whereas the second term represents the potential energy.

The set of energies and corresponding eigenstates are obtained by solving the time-independent Schrödinger equation:

$$\hat{H}\,|\,\phi(x)\,\rangle = E\,|\,\phi(x)\,\rangle\,. \tag{2.6}$$

The solution of this equation yields a set of eigenstates of the form:

$$|\,\phi_n(r)\,\rangle = \sqrt{\frac{1}{2^n n!}} \left(\frac{m\omega_0}{\pi\hbar}\right)^{1/4} \exp\left(\frac{-m\omega_0 r^2}{2\hbar}\right) H_n\left(\sqrt{\frac{m\omega_0}{\hbar}}r\right)\,, \tag{2.7}$$
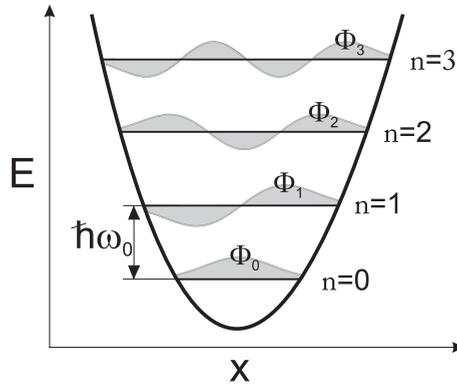
FIGURE 2.3. Energy level scheme for quantum harmonic oscillator. $\phi_n$ are the eigenstates of the corresponding energy states $E_n$. The energy levels are spaced equally with the spacing equal to $\hbar\omega_0$.

where n=0,1,2,... and the functions $H_n(r)$ represent the so-called Hermite polynomials. When squared ($|\phi(x)|^2$), this function describes the probability of a particle to be at a distance $x$. The energy of each state is given by:

$$E_n = \hbar\omega_0\left(n + \frac{1}{2}\right),\tag{2.8}$$

where $\omega_0$ is the resonance frequency of the oscillating particle. In figure 2.3 we show the eigenstates $\phi_n(r)$ at corresponding eigenvalues $E_n$ for n = 0, 1, 2 and 3.

So far we have considered the isolated case of a system in equilibrium, showing no interactions with its surroundings. The experimental determination of the state of the system and its properties, however, often involves the interaction with an electromagnetic field. The presence of the electromagnetic field will perturb the energetic state of the system and may promote it to an energetically higher state (i.e. $E_{n\rightarrow n+1}$). Such inter-state transitions can be described by adding a time-dependent perturbation to the Hamiltonian [21, 141]:

$$\hat{H}\,|\,\Phi(r,t)\,\rangle = i\hbar\frac{\partial}{\partial t}\,|\,\Phi(r,t)\,\rangle,\tag{2.9}$$

where $\hat{H}(t)$ is now the time dependent total energy of the system including the energy of the unperturbed system $\hat{H}_0$ and the time-dependent perturbing term $\hat{V}(t)$:

$$\hat{H}(t) = \hat{H}_0 + \hat{V}(t).\tag{2.10}$$

In case the perturbing force originates from electromagnetic radiation $\hat{V}(t)$ is defined as:

$$\hat{V}(t) = \frac{1}{2}\vec{\hat{\mu}}\cdot\vec{E}_0(e^{i\omega t} + e^{-i\omega t}),\tag{2.11}$$

where $\vec{\hat{\mu}}$ is the transition dipole moment operator, $\vec{E}_0$ is the amplitude of the electric field oscillating with frequency $\omega$. Solving the time-dependent

Schrödinger equation to first order in the perturbation yields the probability of the particle going from its initial state $a$ to state $b$:

$$P_{a \to b} = \frac{2\pi t}{\hbar^2} \int |\langle \Phi_b | \hat{V} | \Phi_a \rangle|^2 \, \delta(\omega \pm \omega_{ab}) d\omega \,, \tag{2.12}$$

where $\delta(\omega \pm \omega_{ab})$ is a delta function that ensures that the resonant condition is fulfilled. The transition between two states can only occur if the driving field has a frequency $\omega$ that is equal to the energy difference between the two states expressed in $\omega_{ab}$. Equation 2.12 is known as Fermi's golden rule.

According to equation 2.12 the transition probability $P_{a \to b}$ is proportional to the time $t$ over which the interaction takes place. Differentiating the formula over time $\left(\frac{\partial P_{a \to b}}{\partial t}\right)$ we obtain the transition rate $\Gamma_{a \to b}$. We further substitute the perturbing term $\hat{V}$ according to equation 2.11 and obtain:

$$\Gamma_{a \to b} = \frac{\pi}{2\hbar^2} \int E_0^2 \cos^2 \theta \, |\langle \Phi_b | \hat{\mu} | \Phi_a \rangle|^2 \, \delta(\omega \pm \omega_{ab}) d\omega \,. \tag{2.13}$$

The dipole operator $\hat{\mu}$ depends on the electronic structure of the molecule and may refer to any type of transition (vibrational, translational, etc..). In this thesis we are interested in the molecular vibrations, thus it is more appropriate to express $\hat{\mu}$ in terms of a vibrational coordinate $x$ (particles displacement axis):

$$\vec{\hat{\mu}} = \vec{\mu_0} + \hat{x} \frac{\partial \vec{\mu}}{\partial x} \,. \tag{2.14}$$

We substitute expression 2.14 into equation 2.13 and arrive at:

$$\Gamma_{a \to b} = \frac{\pi}{2\hbar^2} \int E_0^2 \cos^2 \theta \left(\frac{\partial \vec{\mu}}{\partial x}\right)^2 |\langle \Phi_b | \hat{x} | \Phi_a \rangle|^2 \, \delta(\omega \pm \omega_{ab}) d\omega \,. \tag{2.15}$$

The above formula carries important consequences for vibrational spectroscopy:

- The delta function involves both the sum and the difference of the molecules resonant frequency and the driving frequency. Since the states $a$ and $b$ can be situated differently with respect to each other (either $E_a > E_b$ or $E_b > E_a$) the transition represents either absorption or stimulated emission. As the transition dipole moment is the same, the probability of the two processes to occur is the same.

- The term $\left(\frac{\partial \vec{\mu}}{\partial x}\right)$ indicates that the vibrational transition can only be observed (= is infrared active) if the vibration changes the dipole moment of the oscillator.

- It follows from equation 2.15 that the transition dipole moment $\vec{\mu}_{ab}$ is:

$$\vec{\mu}_{ab} = \left(\frac{\partial \vec{\mu_{el.}}}{\partial x}\right) \langle \Phi_b | \hat{x} | \Phi_a \rangle \,, \tag{2.16}$$

where $\partial \vec{\mu_{el.}}$ (Born-Oppenheimer approximation) reflects the dependence of the electronic dipole moment on the vibrational coordinate. It can be
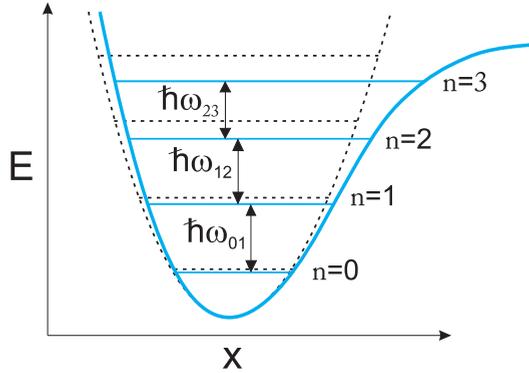
FIGURE 2.4. Anharmonic oscillator with associated states (blue solid). Black line indicates harmonic oscillator with associated energy states (dashed)

shown that for the harmonic oscillator $\langle \Phi_b | \hat{x} | \Phi_a \rangle$ has the following properties [141, 22]:

$$\langle \Phi_b | \hat{x} | \Phi_a \rangle = \begin{cases} 0 & \text{if b} \neq \text{a} \pm 1 \\ \frac{1}{\alpha}\sqrt{\frac{a+1}{2}} & \text{if b=a+1} \\ \frac{1}{\alpha}\sqrt{\frac{a}{2}} & \text{if b=a}-1 \end{cases} \tag{2.17}$$

where $\alpha$ is a constant for a harmonic oscillator and equals $(\alpha = \sqrt{\hbar/m\omega})$.

○ The first property tells us that the transition can only occur between consecutive levels.

○ It further follows that for a transition from the ground state ($a$=0) to the first excited state ($b$=1), $\langle \Phi_b | \hat{x} | \Phi_a \rangle = \sqrt{\hbar/2m\omega}$, whereas for a transition from the first excited state ($a$=1) to the second excited state ($b$=2) $\langle \Phi_b | \hat{x} | \Phi_a \rangle = \sqrt{\hbar/m\omega}$. This means that for a harmonic oscillator the transition dipole moment of the 1→2 transition is $\sqrt{2}$ times larger than the transition dipole moment of the 0→1 transition.

$$\frac{\vec{\mu}_{12}}{\vec{\mu}_{01}} = \sqrt{2}. \tag{2.18}$$

## 2.3   QUANTUM ANHARMONIC OSCILLATOR

If we assume that the resonance condition is fulfilled, meaning that $\delta(\omega \pm \omega_{ab})$=1, the transition rate becomes:

$$\Gamma_{a \to b} = \frac{\pi}{2\hbar^2} E_0^2 \cos^2\theta \left(\frac{\partial \vec{\mu}}{\partial x}\right)^2 |\langle \Phi_b | \hat{x} | \Phi_a \rangle|^2. \tag{2.19}$$

We can express the transition rate in terms of the intensity of light using the following relation:

$$E_0^2 = \frac{2I(\omega_{ab})}{nc\epsilon_0}\,, \tag{2.20}$$

where $n$ is the refractive index, $c$ is the speed of light and $\epsilon_0$ is the vacuum electric permittivity. Replacing the position operator $\hat{x}$ with the dipole moment operator $\hat{\mu}$ and using the property that the average value of $\cos^2\theta = 1/3$ we obtain:

$$\Gamma_{a\rightarrow b} = \frac{\pi\mu^2}{3\hbar^2 nc\epsilon_0}I(\omega_{ab}). \tag{2.21}$$

The proportionality term between the transition rate and the intensity of light is called the absorption cross section:

$$\sigma_{ab} = \frac{\pi\mu^2}{nc\hbar^2\epsilon_0}\,. \tag{2.22}$$

We will see later that the absorption of the sample (or the absorption change measured in pump-probe experiment) is directly proportional to the absorption cross section $\sigma_{ab}$.

As mentioned before a harmonic oscillator is a great simplification of reality. The motion of a particle does not depend linearly on the forces acting on it. When the restoring force is nonlinear, the energy levels can be written as:

$$E_n = \hbar\omega_0\left(n + \frac{1}{2}\right)\left[1 - A_1(n + \frac{1}{2}) + A_2(n + \frac{1}{2})^2 + ...\right], \tag{2.23}$$

where $A_n$ are $n$-th order anharmonicity constants. In figure 2.4 we show a comparison of a harmonic (black) and an anharmonic (blue) potential for a particle moving along coordinate $x$. In the anharmonic potential the energy levels are not spaced equally anymore and the selection rules of the harmonic oscillator (equation 2.17) no longer apply.

## 2.4  LINEAR LIGHT-MATTER INTERACTION

Light-matter interactions can be measured in various ways. One of these is by measuring the attenuation of light that passes through the sample. The frequency dependent intensity of the outcoming light defines the absorption spectrum of the sample. The linear absorption spectrum carries information on the spectral position of various resonances and their line shape. Let us consider a sample with thickness L (see figure 2.5) and a concentration of absorbers C. The intensity of the incident beam is denoted as $I_0(\omega)$ and the intensity of the transmitted light is denoted as $I(\omega)$. The light intensity change induced by the sample is proportional to the concentration of absorbers $C$, the absorption cross section of the absorbing molecules $\sigma(\omega)$, and the intensity of the incoming beam:

$$dI(\omega) = -\sigma(\omega)CI_0(\omega)dL\,. \tag{2.24}$$
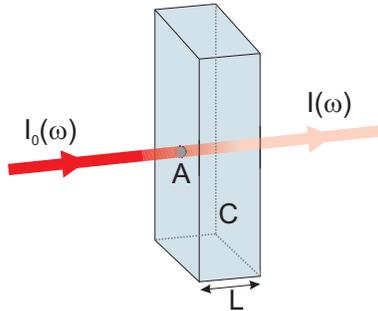
FIGURE 2.5. Schematic representation of the Lambert-Beer's law.

The solution of this differential equation is:

$$\ln(I(\omega)) = -\sigma(\omega)CL + \ln(I_0(\omega)) \,. \tag{2.25}$$

Now we can calculate the difference between the light intensity before the sample and the transmitted intensity:

$$\ln(I(\omega)) - \ln(I_0(\omega)) = -\sigma(\omega)CL \,, \tag{2.26}$$

and arrive at the expression for the transmission of the sample:

$$T(\omega) = \frac{I(\omega)}{I_0(\omega)} = \exp\left(-\sigma(\omega)CL\right) \,. \tag{2.27}$$

The absorbance is defined as:

$$\alpha(\omega) = \sigma(\omega)CL \,. \tag{2.28}$$

Equation 2.27 is known as Lambert-Beer's law and relates a macroscopic, measurable property - the absorption of light with the microscopic properties of the absorbing molecules.

## 2.5 NONLINEAR LIGHT-MATTER INTERACTION

### 2.5.1 PUMP-PROBE EXPERIMENT

Linear absorption spectroscopy as described in section 2.4 provides information about a system in equilibrium, meaning that the interactions between the molecules and light do not lead to a (significant) change in the population distribution. In order to access the vibrational (population) relaxation properties of the system it is necessary to first bring the system to a non-equilibrium state and then probe its recovery (see figure 2.6). We can achieve this by using a high intensity laser beam that perturbs the population distribution. We first induce vibrational population changes (excite some of the molecules to their first
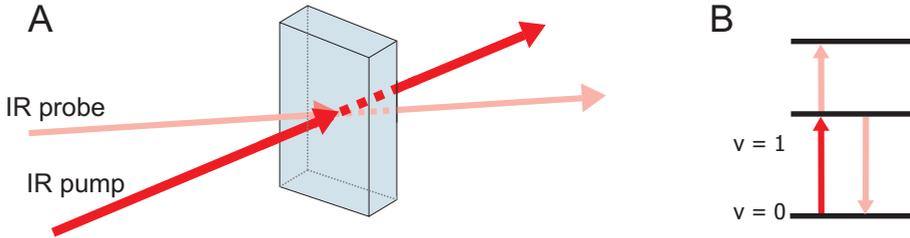
FIGURE 2.6. Schematic representation of the pump-probe experiment (A). IR pump and probe beams are overlapped in time and space in the sample. Pump beam excites a subset of molecules to their excited state (B). Pump induced absorption changes are monitored with the weaker probe pulse.

excited state) and then we probe the population dynamics with a weak probe beam (which is too weak to significantly change the population distribution by itself). The absorbance of the probe light is given by:

$$\alpha_0(\omega) = \sigma_{01}(\omega)n \,, \tag{2.29}$$

where $n$ is the amount of absorbers per unit surface ($n = CL$). The pump induced absorption changes in the sample comprise of:
- ground state bleach - molecules promoted to the first vibrationally excited state will no longer absorb at the fundamental $\omega_{01}$ frequency,
- stimulated emission - molecules in the excited state are stimulated back to the ground state emitting photons at the fundamental frequency,
- induced absorption - molecules in the excited state will absorb light at the frequency matching the transition to the second excited state $\omega_{12}$. We can thus describe the modified absorption as:

$$\alpha(\omega) = \sigma_{01}(\omega)(n - 2N_1) + \sigma_{12}(\omega)N_1 \,, \tag{2.30}$$

where $N_1$ denotes concentration of the excited molecules. We can represent the absorption changes as:

$$\Delta\alpha(\omega) = (-2\sigma_{01}(\omega) + \sigma_{12}(\omega))N_1 \,. \tag{2.31}$$

The measured pump induced transient absorption spectrum consists of a negative contribution called the bleach signal and a positive contribution called the induced absorption (figure 2.7 B).

Combining equations 2.18 and 2.22 we see that the cross section for the transition $1\rightarrow2$ is two times bigger that for $0\rightarrow1$. Since for the harmonic oscillator $0\rightarrow1$ and $1\rightarrow2$ transitions have the same frequency and the absorption change for the two transition is the same we would not be able to perform any pump-probe experiments. However for the anharmonic oscillator the $0\rightarrow1$ and $1\rightarrow2$ transition frequencies are different, and thus we observe a bleaching and an induced absorption at different frequencies.
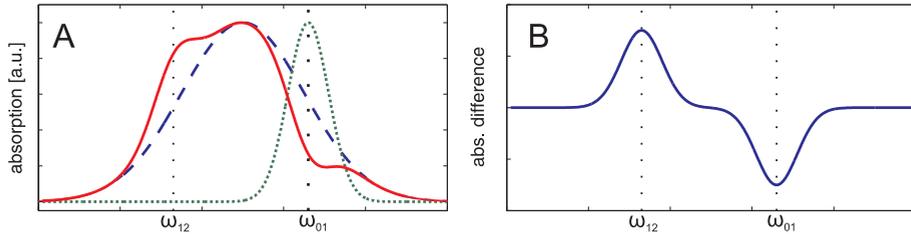
FIGURE 2.7. Schematic representation of the pump probe signal. Panel A: The dashed line represents the absorption band of the sample. Dotted line indicates the pump beam spectrum. Solid line shows pump-induced changes in the absorption spectrum. Panel B shows differential pump-probe spectrum characterized with the negative contribution at $\omega_{01}$ and positive contribution at $\omega_{12}$.

The pump induced changes in the population distribution are transient. After a certain time the excited molecules will relax back to the ground state. The transient absorption changes in the presence of the relaxation is given by:

$$\Delta\alpha(\omega) = (-2\sigma_{01}(\omega) + \sigma_{12}(\omega))N_1(t{=}0)\exp(-kt)\,, \tag{2.32}$$

where $k$ is the relaxation rate. Rather than the relaxation rate we often use a vibrational lifetime (defined as $T_1 = 1/k$) as a measure of how long a molecule stays in the excited state.

### MOLECULAR REORIENTATION

We have shown in section 2.2 that if the pump beam is polarized linearly the excitation probability is a $\cos^2(\theta)$ distribution (equation 2.13), where $\theta$ is the angle between the pump beam polarization and the vibrational coordinate. After the excitation we thus have an anisotropic distribution of vibrationally excited molecules (see figure 2.8 A). If we use a linearly polarized probe beam we can separately detect the induced absorption changes that are parallel $\Delta\alpha_{||}$ and perpendicular $\Delta\alpha_{\perp}$ to the pump light polarization (figure 2.8 B).

It is immediately obvious that the rate with which the amplitudes of $\Delta\alpha_{||}$ and $\Delta\alpha_{\perp}$ change is related to the orientational motion of the probed molecules. Initially excited molecule will contribute at early delays predominantly to the parallel component of the pump-probe signal $\Delta\alpha_{||}$. In time the molecule will reorient and contribute more and more to the perpendicular signal. The ratio between the two signals changes continuously in time and eventually the two signals will become the same and the excited molecules will acquire an orientationally isotropic distribution. The normalized difference between the two signals, $\Delta\alpha_{||}$ and $\Delta\alpha_{\perp}$ is called the anisotropy parameter $R(t)$:

$$R(t) = \frac{\Delta\alpha_{||} - \Delta\alpha_{\perp}}{\Delta\alpha_{||} + 2\Delta\alpha_{\perp}}\,, \tag{2.33}$$

where $\Delta\alpha_{||} + 2\Delta\alpha_{\perp}$ represents the isotropic signal. The orientational motion of the oscillator is expressed by the rate at which the relative magnitudes of
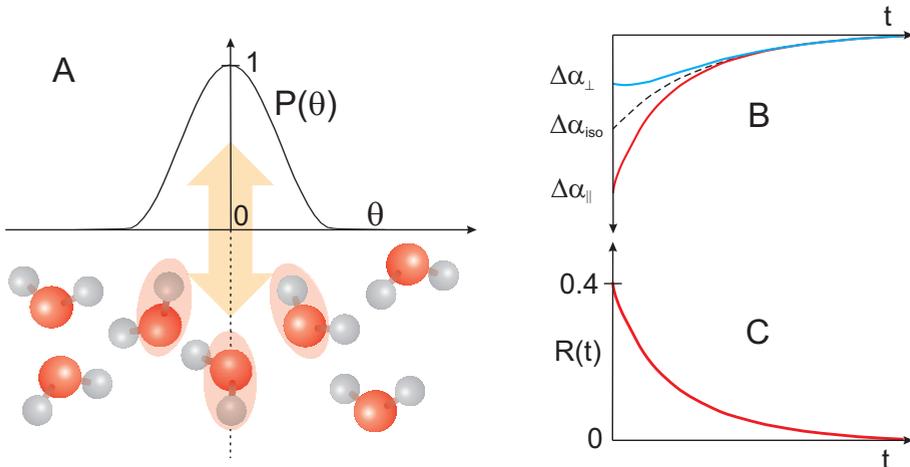
FIGURE 2.8. The concept of anisotropy measurements. A: A linearly polarized pump beam (indicated with an arrow) excites a sub-ensemble of molecules (indicated with red ovals) within a $\cos^2(\theta)$ distribution around the pump polarization orientation. B: The transient absorption changes measured at a polarization parallel and perpendicular to the pump polarization orientation. C: The reconstructed anisotropy parameter $R(t)$, using equation 2.33.

the parallel $\Delta\alpha_{||}$ and perpendicular $\Delta\alpha_{\perp}$ absorption components change. The temporal window over which we can determine the anisotropy parameter is thus limited by the vibrational lifetime of the oscillator.

Depending on the system and the local environment of the probed oscillator its orientational motion can be a complicated function. In the simplest case the anisotropy decay due to orientational diffusion is described with a monoexponential function:

$$R(t) = \exp\left(-t/\tau_{\mathrm{or}}\right), \tag{2.34}$$

where $\tau_{\mathrm{or}}$ is the reorientation time.

VIBRATIONAL RESONANT ENERGY TRANSFER
The ratio between the measured parallel $\Delta\alpha_{||}$ and perpendicular $\Delta\alpha_{\perp}$ absorption changes may change not only due to orientational diffusion of the molecules, but also due to resonant vibrational energy transfer between oscillators oriented in different directions. Vibrational resonant energy transfer (VRET) results from the dipole-dipole interactions between the excited donor molecule and an unexcited acceptor molecule. The formulation of this molecular dipole-dipole coupling was developed by Förster and originally used to describe the transfer of an electronic excitation between fluorescent dye molecules.

In general the rate of energy transfer - $k_F$ (Förster rate) is [48, 112, 132]:

$$k_{F,ab} \propto \frac{|\vec{\mu}_a|^2 |\vec{\mu}_b|^2 \kappa_{ab}^2}{|\vec{R}_{ab}|^6} \int d\nu \; \sigma_a(\nu) \, \sigma_b(\nu), \tag{2.35}$$
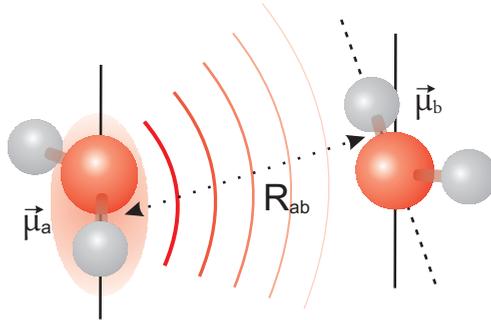
FIGURE 2.9. Schematic representation of dipole-dipole interaction between two water molecules.

where $\vec{\mu}_a$ and $\vec{\mu}_b$ are the vibrational transition dipole moments of the emitting and receiving molecules, $\kappa_{ab}$ is a geometrical factor taking into account the mutual orientation of the coupled oscillators and $R_{ab}$ is the distance between the two molecules. The integral reflects the spectral overlap between the emission and absorption spectra of the donor and acceptor, respectively.

For the energy transfer between the same type of oscillators the emission and absorption spectra are similar. If we further assume that the orientation between the dipoles is independent on the distance $R_{ab}$ between them, for a given donor/acceptor pair, we can express the Förster transfer rate as:

$$k_j = \frac{1}{T_1} \left( \frac{r_0}{r_j} \right)^6 , \qquad (2.36)$$

where $T_1$ is the intrinsic lifetime of the excitation in the absence of the energy transfer and $r_0$ is the so-called Förster radius, which defines the distance at which the rates of relaxation and resonant energy transfer are equal (i.e. the distance for which there is a probability of 50% that energy transfer occurs within the lifetime).

The probability that the excited molecules remain excited at time $t = \tau$ is:

$$\rho(\tau) = \sum_{j=1}^{N_{\mathrm{OD}}} \exp \left( -k_j \tau \right) , \qquad (2.37)$$

where $N_{\mathrm{OD}}$ ($N_{\mathrm{OD}}=2N_{\mathrm{D_2O}}$) is the number of accepting oscillators and $k_j$ is the rate constant for energy transfer. The probability to find an accepting molecule at a distance $r_j$ and $r_j + dr_j$ is equal to the contents of the spherical shell normalized to the total volume of the sample $V$:

$$\eta(r) = \frac{4\pi r_j^2 dr_j}{V} , \qquad \text{where } V = \frac{4\pi R^3}{3} , \qquad (2.38)$$

and $R$ is the radius of the sphere. Substituting equation 2.36 in equation 2.37

and integrating over all possible acceptors we arrive at:

$$\rho(t) = \left\{ \frac{4\pi}{V} \int_0^R exp\left(-\frac{tr_0^6}{T_1 r^6}\right) r^2 dr \right\}^{N_{OD}} .$$  (2.39)

Performing the integration, we obtain:

$$\rho(\tau) = \left\{ \exp\left(-\frac{tr_0^6}{T_1 r^6}\right) + \sqrt{\frac{\pi tr_0^6}{T_1 R}}\, \mathrm{Erf}\left(\sqrt{\frac{\pi tr_0^6}{T_1 R}}\right) \right\}^{N_{OD}} .$$

We can express the concentration of the sample as the number of molecules in the volume $C_{OD} = \frac{3N_{OD}}{4\pi R^3 N_A}$ (expressed in [mol/Å$^3$]), where $N_A$ is Avogadro's number. Using this expression we can eliminate $R$. Performing the power expansion in terms of $1/N_{OD}$ we arrive at:

$$\rho(\tau) = \left\{ 1 - \frac{4\pi^{3/2} C_{OD} N_A}{3} \sqrt{\frac{r_0^6 \tau}{T_1}} \left(\frac{1}{N_{OD}}\right) + \alpha \left(\frac{1}{N_{OD}}\right)^2 \right\}^{N_{OD}} .$$  (2.40)

The number of accepting molecules is in most cases very large so the term containing $(1/N_{OD})^2$ becomes small and can be neglected. We then obtain:

$$\rho(t) = exp\left(-\frac{4\pi^{3/2} C_{OD} N_A \sqrt{tr_0^6}}{3\sqrt{T_1}}\right) .$$  (2.41)

The above expression describes resonant vibrational energy transfer for molecules in the bulk. If we assume that after transfer the excitation becomes isotropic the anisotropy will be proportional to the excitation survival probability (equation 2.41):

$$R(t) = \rho(t) \propto exp\left(-\frac{4\pi^{3/2} C_{OD} N_A \sqrt{tr_0^6}}{3\sqrt{T_1}}\right) .$$  (2.42)

The two processes - orientational diffusion (equation 2.34) and vibrational energy transfer (equation 2.41) occur at the same time. The anisotropy decay in the presence of both effects is expressed as:

$$R(t) = exp\left(-\frac{t}{\tau_{or}} - \frac{4\pi^{3/2} C_{OD} N_A \sqrt{tr_0^6}}{3\sqrt{T_1}}\right) .$$  (2.43)

## 2.6    FREQUENCY MIXING

A common way of describing nonlinear light-matter interactions is by writing the light induced polarization as a sum of different contributions $P^{(n)}(t)$:

$$P(t) = P^{(1)}(t) + P^{(2)}(t) + P^{(3)}(t) + ... ,$$  (2.44)

that differ in their order dependence $n$ on the light electric field:

$$P(t) = \epsilon_0 \left( \chi^{(1)} E(t) + \chi^{(2)} E^2(t) + \chi^{(3)} E^3(t) + ... \right), \tag{2.45}$$

where $\chi^{(n)}$ represents the $n$-th order susceptibility. We assume here that the polarization at time $t$ depends only on the instantaneous value of the electric field strength. This implies that the medium is lossless and dispersionless. This description becomes handy when describing mixing of fields oscillating with different frequencies.

Second-order nonlinear processes
Let us consider the case where two electromagnetic field overlap in space and time in a material with a non-zero $\chi^{(2)}$. The two electromagnetic fields are characterized with their frequencies $\omega_1$ and $\omega_2$:

$$E(t) = E_1 e^{-i\omega_1 t} + E_2 e^{-i\omega_2 t} + \text{c.c.}. \tag{2.46}$$

In this case the second-order non-linear polarization ($P^{(2)}$) of the material is given by:

$$
\begin{aligned}
P^{(2)} &= \chi^{(2)} E^2 \\
&= \chi^{(2)} \left( E_1 e^{-i\omega_1 t} + E_1^* e^{i\omega_1 t} + E_2 e^{-i\omega_2 t} + E_2^* e^{i\omega_2 t} \right)^2 \\
&= \chi^{(2)} \Big\{ 2(|E_1|^2 + |E_2|^2) + && \text{(OR)} \\
&\qquad E_1^2 e^{-i\,2\omega_1 t} + E_2^2 e^{-i\,2\omega_2 t} \; + \text{c.c.} + && \text{(SHG)} \\
&\qquad 2E_1 E_2 e^{-i(\omega_1+\omega_2)t} \qquad\quad + \text{c.c.} + && \text{(SFG)} \\
&\qquad 2E_1 E_2^* e^{-i(\omega_1-\omega_2)t} \qquad\quad + \text{c.c.} \;\Big\} && \text{(DFG)},
\end{aligned}
\tag{2.47}
$$

where the asterisk symbol indicates a complex conjugate.

The interaction of the two electromagnetic waves leads to polarizations at frequencies that are different from the two driving light fields. These polarizations will generate light beams at the corresponding frequencies. We thus distinguish difference frequency generation (DFG) that leads to a new frequency component at $\omega_3 = \omega_1 - \omega_2$, sum frequency generation (SFG) at a frequency that is the sum of the two original frequencies, $\omega_3 = \omega_1 + \omega_2$, and second harmonic generation (SHG), a process that generates fields at frequencies $\omega_3 = 2\omega_1$ and $\omega_3 = 2\omega_2$.

One of the most commonly used frequency conversion processes is difference frequency generation (DFG). It is commonly used in two steps: first - to generate intense near-infrared photons (1.1 - 2.2 $\mu$m) and second - to use the two near infrared photons to generate photons in the mid-infrared range 3 - 8 $\mu$m. This light can be used to study the properties of molecular vibrations.

phase matching
The second-order nonlinear susceptibility of a material is usually very small. Nevertheless the generated new field may still have a significant intensity if

the two input electric fields are very strong, as often is the case for ultrashort laser pulses. Another frequency conversion efficiency limiting factor is the phase mismatch between the fields generated at different positions in the material. The time and position varying electric field is expressed by:

$$E(x,t) = \exp\left(i(kx - \omega t)\right) , \tag{2.48}$$

where the wave vector $k$ is defined as $k(\omega) = \frac{n(\omega)\omega}{c}$, where $c$ is the speed of light. The polarization induced by two incident fields at position $x$ and time $t$ is given by:

$$P^{(2)}(x,t) = E_1 E_2^* \exp\left(i((k_1 - k_2)x - \omega_3 t)\right) . \tag{2.49}$$

In a material with normal dispersion, in which the refractive index increases with frequency, the new $\omega_3$ field generated at position $x$ will travel through the material at a different speed than the two original fields ($\omega_1$ and $\omega_2$). After the input fields travelled a distance $\Delta x$, the newly generated $\omega_3$ field (at $x + \Delta x$) will have a different phase than the $\omega_3$ field generated at position $x$. After a certain length (the so-called coherence length) this phase mismatch leads to a destructive interference which significantly lowers the intensity of the $\omega_3$ light exiting from the nonlinear material.

To take full advantage of a nonlinear frequency conversion process we need to match the $k_3$ phase with $(k_1 - k_2)$.

$$k_3 = k_1 - k_2 , \tag{2.50}$$

or using the relation $k(\omega) = \frac{n(\omega)\omega}{c}$:

$$n_3 \omega_3 = n_1 \omega_1 - n_2 \omega_2 . \tag{2.51}$$

A commonly used method to ensure phase matching is by using a birefringent material. A birefringent material possesses two axes that exhibit different refractive indices for light of different (orthogonal) polarizations: $n_e$ along the optical axis and $n_o$ in the other two directions. By rotating the crystal over an axis perpendicular to the optical axis we can change the refractive index (between $n_e$ and $n_o$) for the light polarized in the plane perpendicular to the rotation axis. By using different polarizations for the light fields at $\omega_1$, $\omega_2$ and $\omega_3$ we can thus vary their specific refractive indices. This method allows us to significantly extend the coherence length in the material and enhance the frequency conversion.

## 2.6.1    TIME-RESOLVED SUM-FREQUENCY GENERATION

One of the frequency mixing processes described in section 2.5 forms a base for an important spectroscopic technique called surface sum frequency generation (SFG). This technique relies on an important property which is that the second order nonlinear susceptibility is zero in centrosymmetric media. The second order polarization is given by:

$$P^{(2)} = \chi^{(2)} E^2 . \tag{2.52}$$

In a centrosymmetric medium both the polarization and the electric field have the same magnitude when their direction is inverted. In other words $E^2=(-E)^2$ and $P^{(2)}(E) = -P^{(2)}(-E)$, which can only be fulfilled if $\chi^{(2)}=0$. This means that molecules with a center of inversion do not have a non-zero second-order nonlinear susceptibility and thus do not generate an SFG signal. Even for media consisting of molecules that are non-centrosymmetric the second-order nonlinear susceptibility is zero if their arrangement is fully isotropic like in liquids or glasses.

The zero second order nonlinear susceptibility of the isotropic, bulk phase can be advantageous, as it makes the SFG process extremely selective and specific for only a few molecular layers at the surface at which the symmetry is broken.

The only conditions for obtaining an SFG signal from the surface is that the two beams can access the surface of the sample and that the generated SFG beam can escape the surface. Once the beams are overlapped in space and time SFG signal is generated. The intensity of the SFG signal is given by:

$$I_{SFG}(\omega_3) \propto |\chi^{(2)}|^2 I_1(\omega_1) I_2(\omega_2)\,. \qquad (2.53)$$

To relate the macroscopic quantity which is the nonlinear susceptibility to the molecular scale properties of the system an approximation of weakly interacting absorbers is made:

$$\chi^{(2)} = N_S \langle \alpha^{(2)} \rangle_{or.}, \qquad (2.54)$$

where $N_S$ is the number of molecules per centimeter square (surface density of molecules) and $\langle \alpha^{(2)} \rangle$ is the averaged (over all possible orientations) second order nonlinear polarizability of the interfacial molecules.

The direction of propagation of the SFG signal (see figure 2.10) is determined by the phase-matching relation:

$$\omega_1 \sin\theta_1 + \omega_2 \sin\theta_2 = \omega_3 \sin\theta_3\,. \qquad (2.55)$$

The intensity of the SFG signal depends on the square of the surface density of the molecules $N_S$. One of the consequences of this dependence is that the measured SFG signal gives direct information on the propensity of molecules to reside at the interface. The nonlinear susceptibility, $\chi^{(2)}$ is frequency dependent. $\chi^{(2)}$ becomes large when one of the frequencies involved is close to a (vibrational) resonance. Hence, by scanning the infrared beam one can obtain a vibrational spectrum of the interfacial molecules, in analogy to obtaining vibrational spectra from a linear absorption experiment. SFG can thus be used to investigate the local structure and other properties that are encoded in the vibrational spectrum of interfacial molecules.

Similarly to infrared pump-probe experiments, SFG spectroscopy can be extended to access the vibrational dynamics of interfacial molecules. Analogously we can perturb the system by exciting a vibrational transition of the molecule and monitor its relaxation with the SFG process. Figure 2.10 B shows the concept of an IR pump - SFG probe experiment. IR-pump SFG-probe spectroscopy allows us to resolve vibrational relaxation rates of interfacial molecules, vibrational couplings between interfacial molecules as well as between the interfacial
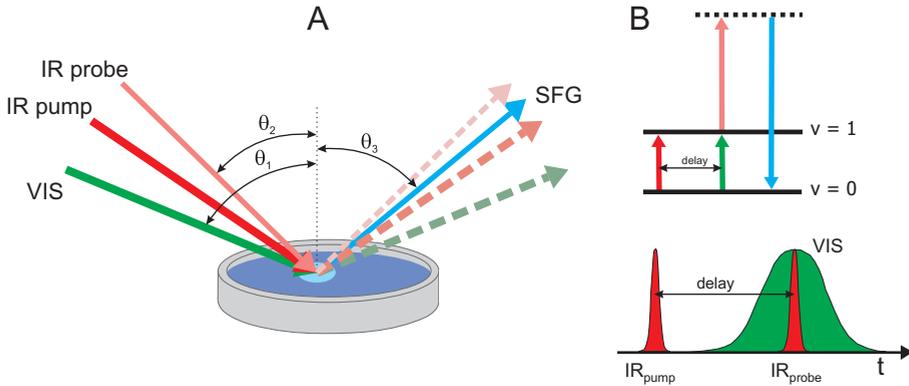
Figure 2.10. Schematic representation of the time-resolved SFG experiment. Panel A shows experimental TR-SFG realisation. In panel B we show the TR-SFG concept in terms of the energy level scheme and timing between different pulses.

and bulk phases (as discussed in chapter 10), or the orientational mobility of for instance water molecules at the water-air interface [66].

It should be noted here that in contrast to IR pump-probe spectroscopy described in the previous chapter, the $1{\rightarrow}2$ induced SFG component is very small in the IR-pump SFG-probe signal. The magnitude of the induced SFG signal is proportional to $\Delta N^2$ (where $N$ is the ground state population), whereas the SFG bleach signal is proportional to $2N\Delta N$. Taking into account that the $1{\rightarrow}2$ transition cross section is two times the cross section of the $0{\rightarrow}1$ transition, the ratio between the bleach and the induced absorption signals is thus $N/\Delta N$. With a typical population change $\Delta N$ of a few percent, the induced SFG signal is not observed.

## 2.6.2   Two-dimensional TR-SFG

To get more insight into molecular interactions at interfaces one can extend the time-resolved SFG experiments to a two-dimensional scheme. 2D spectroscopy generally refers to the fact that the measured signals can be presented in the form of contour plots as a function of two frequencies - a pump frequency and a probe frequency. This technique reveals the couplings between molecules absorbing at different frequencies. In the TR-SFG experiment described in the previous section the pump pulse and the infrared probe pulse of the SFG process have the same spectral width and central frequency. These pulses thus excite and probe the same molecular vibration.

In the 2D case we scan a spectrally narrow pump across the vibrational resonance thus exciting only specific sub-ensembles of molecules, whereas with a broadband infrared probe pulse we probe all molecules. This approach is sometimes called a spectral hole burning experiment. That means that we generate a hole in the spectrum by exciting only a very narrow distribution (with respect to the whole absorption band) of molecules. In time these molecules, due
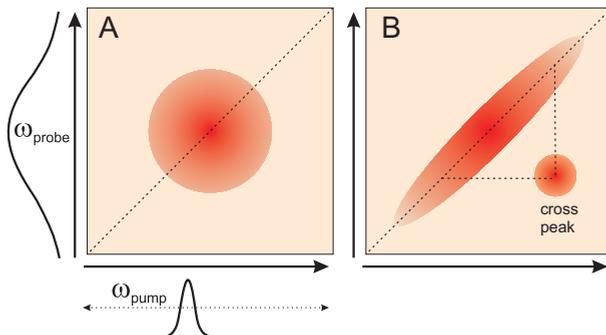
FIGURE 2.11. Representation of the 2D spectra in A - homogeneous limit and B - inhomogeneous limit.

to intra- and intermolecular interactions, may change their resonant frequency and induce a reduction of the SFG signal in a spectral region different from the excitation spectral window. Using the 2D approach we can follow these spectral fluctuations in time. At time delay $\tau=0$ ps only molecules that are directly excited will give a response and thus the detected signal will lie along the diagonal on the 2D plot as shown in figure 2.11, panel B. On the other hand if the system is fully homogeneous, the same SFG response is measured across the whole resonance (figure 2.11 A) irrespectively of the excitation frequency. In most cases a molecular system exhibits mixed behavior and is neither fully homogeneous nor fully inhomogeneous. For dynamic systems like the water-air interface (studied in chapter 10) the occurrence of spectral diffusion leads to a complete loss of the frequency-frequency correlation between the excitation and detection. The rate of spectral randomization can be quantified by measuring the time-dependent slope of the 2D SFG response.

The two-dimensional approach to vibrational spectroscopy may provide additional molecular scale information about the coupling between molecules or parts of molecules absorbing at different frequencies. If two vibrational modes are coupled, the excitation of one of the modes will cause an appearance of signal at frequencies corresponding to the other mode. Such couplings manifest themselves in a 2D spectrum in the form of cross-peaks (see figure 2.11 B).

# 3    Experimental methods

In the experiments presented in this thesis we use ultrashort, femtosecond pulses in the mid-infrared spectral region. The complete experimental setup consists of three main blocks (figure 3.1): the laser system that provides high intensity, ultrashort pulses; a frequency conversion part where we generate mid-IR pulses of desired wavelength, energy and bandwidth, and finally the part where the actual experiment takes place. In the following we briefly describe each of these stages.
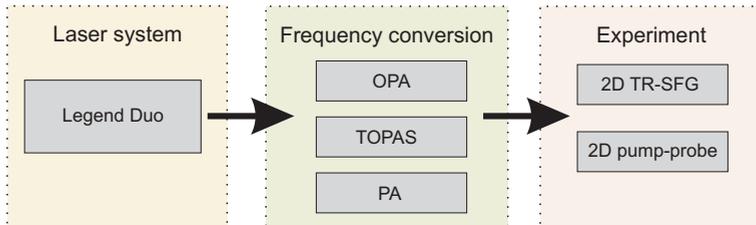


FIGURE 3.1. Three main blocks constituting the experimental setup used for the experiments presented in this thesis.

## 3.1   Laser system

In the time-resolved, pump-probe experiments presented in this thesis we use ultrashort laser pulses in the mid-infrared frequency region between 2.8 and 7 $\mu$m (1450-3500 cm$^{-1}$). These pulses are generated by multiple frequency conversion and amplification processes that are pumped with the near-infrared 800 nm pulses derived from a high energy Ti:Sapphire amplifier system (Coherent - "Legend Duo"). The amplifier is seeded by an oscillator (Coherent - "Mantis") which delivers 800 nm pulses with a bandwidth of ∼80 nm at FWHM (corresponding to a pulse duration of ∼35 fs), at a repetition rate of 80 MHz. The seed pulses are subsequently stretched and amplified at a repetition rate of 1 kHz. The pulses are first amplified in a regenerative Ti:sapphire amplifier. This amplifier is pumped with the pulses from a diode pumped frequency-doubled 527 nm Nd:YLF laser (high energy "Evolution"). The resulting pulses are amplified further in a single-pass amplification stage in a Ti:sapphire crystal. After compression we obtain 40 fs pulses, centered at 800 nm, with a pulse energy of 7.5 mJ at a repetition rate of 1 kHz.

## 3.2 Frequency conversion

The resulting 800 nm beam is split into four branches. Two of these are used to generate mid-infrared pulses, one is used to characterize the pulses in a $\beta$-barium borate crystal (BBO) based autocorrelator, and the last one is used as an upconversion beam in the sum-frequency generation experiments. A schematic representation of the different frequency conversion stages is shown in figure 3.2.
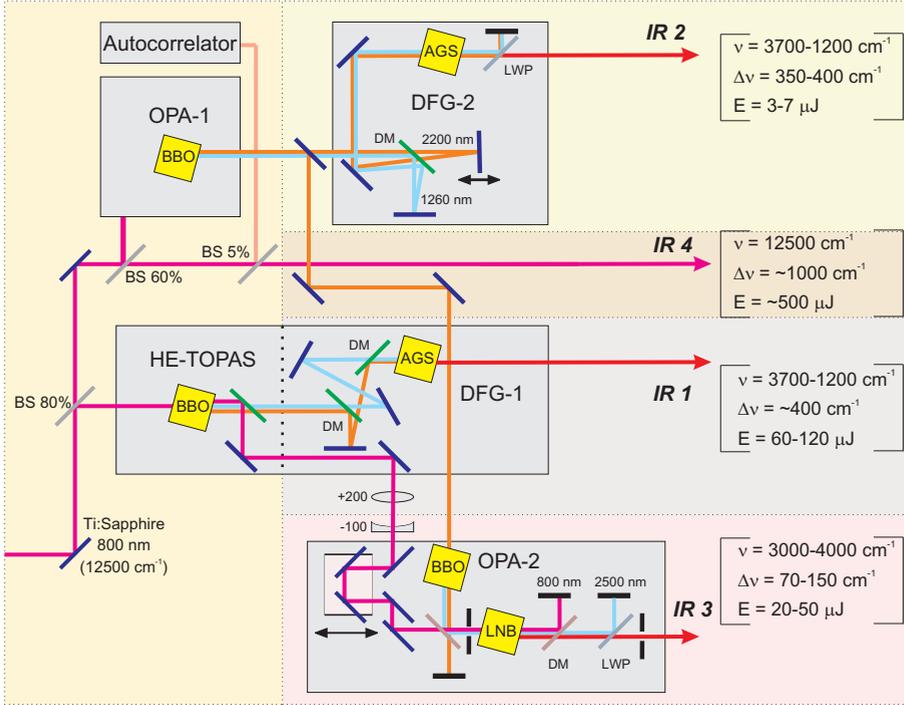


Figure 3.2. Schematic representation of the generation of the pulses used in the experiments. The 800 nm light from the Ti:Sapphire amplifier is split in four parts using beam splitters (BS). We sample a few $\mu$J of the 800 nm beam and send it to an autocorrelator to monitor the pulse duration during the experiments. We use about $\sim$80% to pump a high energy OPA (HE-TOPAS), which generates (DFG-1) high intensity ($\sim$60-120 $\mu$J), broadband ($\sim$400 cm$^{-1}$) mid-infrared pulses (IR 1). The third part ($\sim$12%) is used to pump the home-built OPA which yields (DFG-2) low energy ($\sim$7 $\mu$J), broadband ($\sim$350 cm$^{-1}$) mid-infrared pulses (IR 2). The remaining part of the 800 nm light is used in the SFG experiments as an up-conversion pulses (IR 4). For the 2-dimensional time-resolved SFG experiments we use high intensity, narrowband mid-infrared pulses (IR 3) that are generated via parametric amplification of the frequency doubled idler from the OPA and pumped with the residual 800 nm pulses from the HE-TOPAS.

The mid-infared pulses are generated in two separate optical parametric amplifiers (OPA). We use about $\sim$6 mJ to pump a high-energy OPA (Light

Conversion - "HE-TOPAS"). A small fraction of the 800 nm light is focused in a sapphire plate to generate a white light continuum that is used as a seed in three subsequent amplification process in BBO crystals. These processes are pumped with the remaining 800 nm light. The produced signal and idler pulses are used in a difference frequency mixing process (DFG) in a silver gallium disulphide (AgGaS$_2$) crystal, resulting in 60-120 $\mu$J pulses in a frequency range of 1450-3500 cm$^{-1}$, with a pulse duration of $\sim$60 fs, and with a spectral bandwidth of $\sim$400 cm$^{-1}$ (DFG-1).

About 1 mJ of the original 800 nm beam is used to pump the home-built OPA (OPA-1). Similarly to the high energy TOPAS, this OPA uses white light as a seed. This OPA has two BBO based amplification stages. The resulting signal and idler pulses have energies of 60 $\mu$J an 110 $\mu$J, respectively, and are used either in a DFG process generating mid-infrared pulses (DFG-2), or in other frequency conversion processes.

The 2-dimensional time-resolved SFG experiments require spectrally narrow and intense mid-infrared excitations pulses. We generate these pulses by means of another optical parametric amplification process (OPA-2) seeded with the idler beam from OPA-1 and pumped with the residual 800 nm beam from the HE-TOPAS. We frequency double the idler in a 3 mm BBO crystal. Due to phase-matching limitations, the resulting $\sim$1000 nm pulses have a bandwidth of only $\sim$ 10 nm. We then parametrically amplify these pulses with 800 nm light in a 10 mm long lithium niobate (LiNbO$_3$) crystal. We thus obtain mid-infrared pulses in the range of 2200-2800 cm$^{-1}$, with a bandwith of 70-150 cm$^{-1}$ (pulse duration of $\sim$150-200 fs) and a pulse energy of 20-50 $\mu$J.

## 3.3 IR PUMP-PROBE SETUP

The infrared two-color pump-probe setup used in the experiments is shown in figure 3.3. The probe and reference infrared beams are split ($\sim$4% reflection) from the main beam (IR 1) using wedged barium fluoride windows. The reference beam is used to correct the detected signal for pulse to pulse fluctuations in the infrared intensity. The remaining transmitted beam is used as a pump. We can use the pump beam directly thus performing the experiment in a one-color configuration (the pump and probe beams have the same central frequency and spectral bandwidth). In the two-color experiment we propagate the pump beam through a home-built Fabry-Pérot interferometer thus spectrally shaping the pump beam in terms of its central frequency (within the original bandwidth) and its bandwidth. This spectral filter consists of an air spaced cavity that is created by two closely spaced parallel semi-transparent windows (reflectivity R = 90%). The Fabry-Pérot filter transmits only the wavelengths that constructively interfere in the cavity. By changing the distance between the two windows we can tune the wavelength of the transmitted beam and its bandwidth. The spectral bandwidth of the pump pulses used in the experiments is 40 - 50 cm$^{-1}$. If the experiment requires beams with very different frequencies (separation larger than the bandwidth of IR 1) we use a separately generated IR 2 beam as the pump (dotted red line in figure 3.3). Thereby we can per-
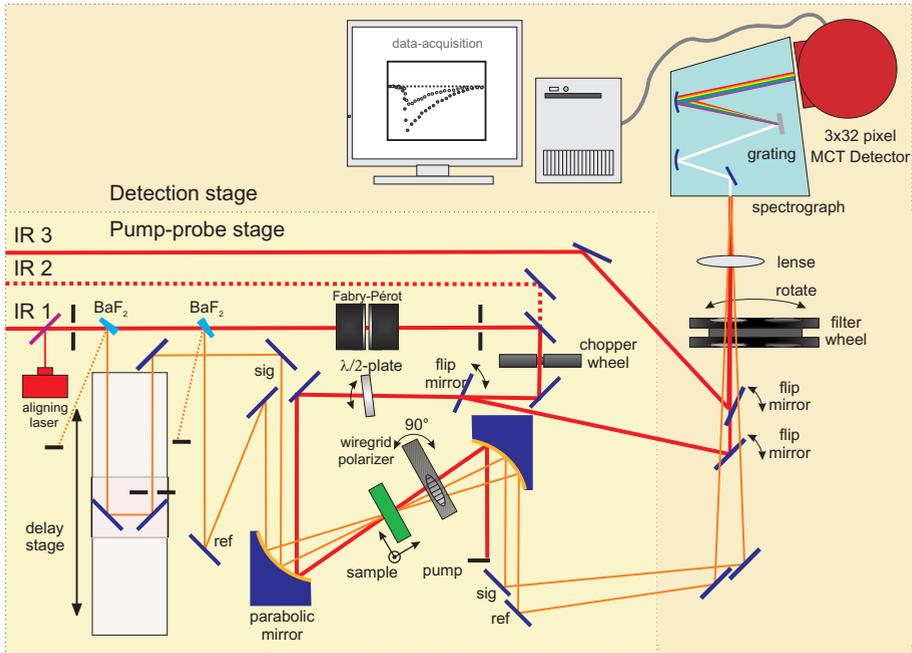
FIGURE 3.3. Schematic representation of the two color, time and polarization resolved pump-probe setup.

form two-color experiments with the pump and probe pulses covering a broad $\sim$2.8-8 $\mu$m spectral range.

The probe beam is sent onto a delay stage (resolution of $\sim$0.66 fs) that allows us to control the time delay between the pump and probe pulses. Both the probe and the reference beams are focused onto the sample with a gold-coated parabolic mirror ($\sim$110 mm effective focal length). Every second pulse in the pump beam is blocked by a chopper wheel rotating with a frequency of 500 Hz. The polarization of the pump pulses is adjusted with a $\lambda/2$ plate and set to 45° with respect to the original IR1 beam polarization. The pump beam is focused on the sample with the same parabolic mirror and spatially overlapped with the probe beam. After traveling through the sample, both the reference and the probe beam travel through a wire grid polarizer mounted on a motorized rotation stage. By rotating the polarizer between +45° and -45° with respect to the original polarization we select the polarization component that is parallel or perpendicular with respect to pump beam polarization. The beams are recollimated with a second parabolic mirror. The pump beam is blocked, and the probe and reference beams are propagated to the detection part of the setup. The probe and reference beams are dispersed with a spectrograph and detected with a 2x32 pixel mercury-cadmium-telluride (MCT) detector array (InfraRed Associates). Optionally the spectrum of the pump beam or any other infrared beam (2D TR-SFG pump beam) can be analyzed/recorded in the detection
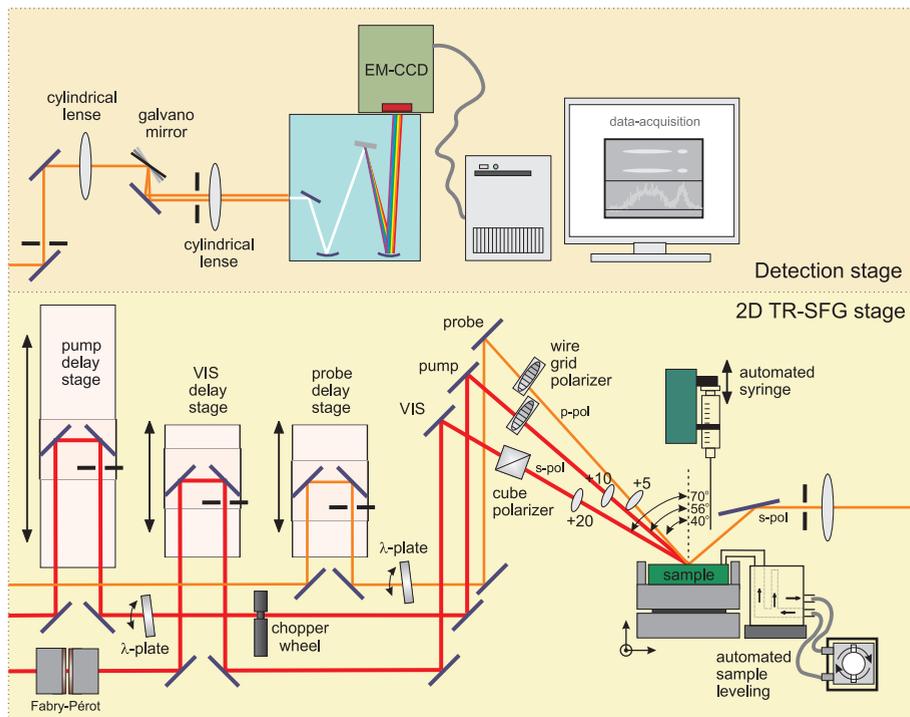
Figure 3.4. Schematic representation of the 2D TR-SFG setup.

stage.

## 3.4  Two-color IR-pump SFG-probe setup

The 2D TR-SFG setup, shown in figure 3.4, uses an IR-pump and an SFG-probe scheme. The three beams used in the experiment: IR probe, IR pump and 800 nm (VIS) are sent onto motorized delay stages that ensure the temporal overlap of the probe and VIS pulses and allow the adjustment of the time delay between the excitation pulse and the detection IR-VIS pulse pair. A combination of a $\lambda/2$ plate and wire grid polarizer in the IR beam paths allow us to control the polarization of the pulses and their intensity. Every other pump pulse is blocked with a chopper wheel rotating at a frequency of 500 Hz. We use a Fabry-Pérot interferometer (SLS Optics) that spectrally narrows the VIS pulses to $\sim$15 cm$^{-1}$, a value that determines the spectral resolution of the recorded SFG signal. The instrumental resolution is $\sim$0.7 cm$^{-1}$. The polarization of the VIS beam is controlled with a cube polarizer. The three beams are focused using calcium fluoride ($CaF_2$) lenses and overlapped at the samples interface. Spatial and temporal overlap of the beams is achieved and optimized by measuring the third-order cross correlation signal of the two infrared and visible beams

(IIV). The SFG signal generated at the interface by the infrared detection pulse and the visible pulse is collected with a mirror, collimated with a lense, and directed to the detection stage. The pumped and unpumped SFG signals travel collinearly. We separate the two signals using a mirror mounted on a galvano scanner motor which is synchronized with the chopper wheel. The pumped and unpumped SFG signals are dispersed using a spectrograph and detected with an electron multiplaying CCD (EM-CCD) camera (Newton DU971P-BV, Andor Technology).

# 4 ULTRAFAST INTERMOLECULAR ENERGY TRANSFER IN HEAVY WATER

We studied the vibrational energy relaxation and resonant vibrational (Förster) energy transfer of the OD vibrations of $D_2O$ and mixtures of $D_2O$ and $H_2O$ using polarization-resolved, femtosecond mid-infrared spectroscopy. We observed the lifetime of the OD vibrations of bulk $D_2O$ to be $400 \pm 30$ fs. The rate of Förster energy transfer is measured via the dynamics of the anisotropy of the OD vibrational excitation. For a solution of 0.5% $D_2O$ in $H_2O$ resonant energy transfer is negligible, and the anisotropy shows a single exponential decay with a time constant of $2.7 \pm 0.05$ ps, representing the time scale of the molecular reorientation. With increasing concentration, the anisotropy decay becomes faster and non-exponential, showing the increased contribution of resonant energy transfer between the OD oscillators. We determined the Förster radius of the OD vibration of HDO in $H_2O$ to be $r_0 = 2.3 \pm 0.2$ Å.

## 4.1 INTRODUCTION

Resonant intermolecular energy transfer is an important process in nature that leads to delocalized excitations (excitons) and the equilibration of energy. This process is often denoted as Förster energy transfer after Theodor Förster. Förster energy transfer has been observed both for electronic excitations [13, 39, 132] and vibrational excitations [27, 32, 45, 79, 171]. Well-known examples of systems showing resonant (Förster) vibrational energy transfer are the amide vibrations of polypeptides [45] and the OH stretch vibrations of liquid water [32, 171]. The energy transfer is the result of the coupling between an excited oscillator and an oscillator in the ground state. In most cases, this coupling is formed by a dipole-dipole interaction which implies that the coupling is inversely proportional to the sixth power of the distance between the coupled oscillators.

For water the resonant coupling between the OH stretch vibrations has been studied by measuring the decay of the anisotropy of the excitation of the OH vibration for different isotopic mixtures of water and heavy water [171]. At a low concentration of water in heavy water (<1%) the OH groups are too far apart

to show energy transfer within the vibrational lifetime of the OH stretch vibrations. In this dilute limit the anisotropy only decays as a result of the molecular reorientation of the water molecules. However, with increasing concentration of OH groups, the anisotropy decay is accelerated showing the presence of resonant energy transfer between OH groups that are differently oriented [32, 79, 171]. Up to high OH concentrations this resonant energy transfer could be well described with a dipole-dipole interaction mechanism, meaning that the rate scales inversely proportional to the sixth power of the distance between the OH groups. However, for pure liquid $H_2O$ the observed rate of resonant energy transfer was significantly faster than expected from the dipole-dipole interaction mechanism, indicating that higher-order multipole interactions also contribute to the energy transfer [171].

Here we study the rate and mechanism of resonant vibrational energy transfer between OD vibrations in water. We measure the anisotropy dynamics of the OD vibration of pure $D_2O$ and of solutions of HDO dissolved in $H_2O$ for a large range of concentrations. We observe resonant energy transfer of the OD vibrations for all solutions for which the concentration of OD oscillators is larger than 2%.

## 4.2   Experiment

We study the vibrational relaxation and resonant energy transfer of the OD stretch vibrations in water using polarization-resolved, femtosecond mid-IR pump-probe spectroscopy. The laser system and the set of frequency conversion processes used to generate the pump and probe pulses are described in detail in sections 3.1 and 3.2, respectively. In the experiment we used 10 $\mu$J pulses, centered at 4000 nm, with a pulse duration of about 70 fs, and a spectral bandwidth of $\sim$450 cm$^{-1}$. The pulses are used in a one-color, polarization-resolved pump-probe experiment using the setup described in section 3.3.

We studied the vibrational relaxation and anisotropy dynamics for pure $D_2O$ and four mixtures of $D_2O$ and $H_2O$. The samples were positioned between two 2 mm thick $CaF_2$ windows separated by teflon spacers with thicknesses ranging from 3.8 $\mu$m to 100 $\mu$m. To check a possible contribution of coherent artifacts to the signals at early delay times we also performed the experiment on pure $D_2O$ with 500 nm $Si_3N_4$ membrane windows instead of 2 mm $CaF_2$ windows. From the comparison of the data sets we concluded that the coherent signal that originates from the $CaF_2$ windows is small and does not influence the fitted values for the lifetime and the anisotropy decay. During the experiment the samples were rotated to avoid accumulation of heat in the focus.

## 4.3   Results and discussion

### 4.3.1   Vibrational relaxation

Figure 4.1 shows the linear spectra for pure $D_2O$ and mixtures of $D_2O$ and $H_2O$. It is seen that an increase of the amount of $H_2O$ causes a narrowing of
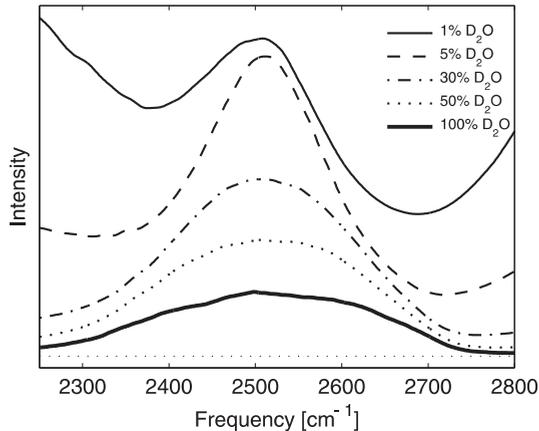
FIGURE 4.1. Linear spectra of pure $D_2O$ and mixtures of $D_2O$ and $H_2O$. Spectra for higher $D_2O$ concentrations have been scaled for clarity.

the $D_2O$ band. In addition, for the two lowest concentrations, we observe a background absorption. This background is caused by the low frequency part of the OH stretch vibrations of $H_2O$ and the high frequency part of the combination band [105] centered around 2150 cm$^{-1}$.

The OD vibration has a short lifetime and after a few picoseconds the vibrational energy becomes thermal which corresponds to a temperature increase of the sample in the focus. An increase in temperature leads to a decrease of the cross-section and a blueshift of the absorption spectrum of the OD stretch vibration. In the transient spectrum these effects correspond to a persistent bleaching in the red wing and center of the absorption band, and a small induced absorption in the blue wing of the absorption band. As this heating signal is isotropic, this signal should be subtracted from the measured transient spectra for a proper determination of the anisotropy dynamics of the vibrational excitation.

The subtraction of the heating signal is especially important for $D_2O$ concentrations higher than 50%, since for these samples the heating signal is of comparable magnitude or bigger than the absorption changes originating from the population dynamics of the $v = 1$ state. To determine the dynamics of the heating signal, we fit the isotropic signals to a two-step relaxation model. In this model the vibrational energy of the excited $v = 1$ state is first transferred to a non-thermal intermediate state. In the second step the intermediate state relaxes leading to a full thermalization of the energy. The rate of the first step is characterized by a vibrational lifetime $T_1$, the second step by an equilibration time constant $T^*$. As has been shown before [134] the fit of the data to this model thus yields the contribution of the heating signal to the measured absorption changes at all delay times. The transient absorption spectrum for pure $D_2O$ corrected for the heating effect is shown in figure 4.2 for two delay times. From the fit we obtain a vibrational lifetime $T_1$ of 400 $\pm$ 30 fs for pure
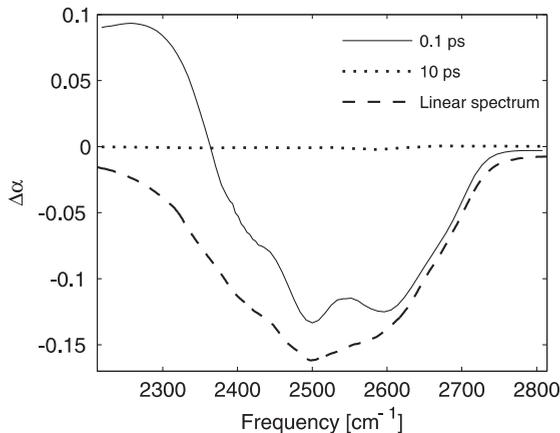
FIGURE 4.2. Transient spectra of pure $D_2O$ recorded at 0.1 ps and 10 ps. Linear spectrum of pure $D_2O$ is shown with the dashed line.

$D_2O$ and a heat ingrowth time $T^*$ of $630 \pm 50$ fs. The lifetime of $400 \pm 30$ fs agrees well with the value of $350 \pm 50$ fs reported by Volkov $et$ $al.$ [164].

We used the same fitting procedure for all $D_2O/H_2O$ mixtures. For the two lowest concentrations (1% and 5% of $D_2O$ in $H_2O$) the fit resulted in a vibrational lifetime $T_1$ for the isolated OD vibration of $1.7 \pm 0.1$ ps and a heat ingrowth time $T^*$ of $850 \pm 50$ fs. Both excited and intermediate state lifetimes depend nearly linearly on the isotopic composition.

The intermediate state represents a state of the system in which the energy is no longer residing in the excited $v = 1$ state, but in which the energy has also not yet become thermally distributed. The intermediate state likely represents specific combined excitations of low-frequency modes. The occupation of these modes can induce an anharmonic frequency shift of the absorption spectrum of the studied vibration. In this case the transient spectrum associated with the intermediate state will consist of a bleaching and an induced absorption signal of which the magnitude are determined by the amount of the anharmonic frequency shift. From the spectral decomposition we find however that the intermediate state in the relaxation of the OD vibration does not have such an associated spectrum. In fact, the intermediate state has the same absorption spectrum as the ground state of the OD vibration. This means that the transient occupation of the intermediate state only functions to describe a delay in the rise of the spectral responses that are characteristic for heating of the sample. The spectral changes associated with heating of the sample are largely due to the weakening of the hydrogen bonds between the water molecules. Hence, the time constant $T^*$ likely represents the time scale at which the hydrogen bonds adapt to an ultrafast local dissipation of energy. This adaptation is relatively slow as the frequencies of the hydrogen-bond vibrations are low. This type of behavior can be expected to occur in all systems in which the intermolecular dynamics is
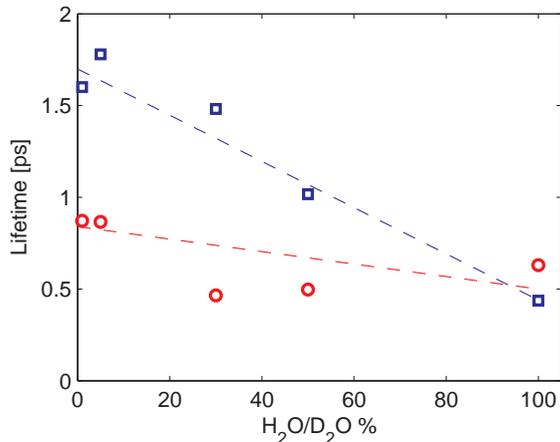
FIGURE 4.3. The excited and intermediate state lifetimes (squares and circles, respectively) as a function of isotopic composition of water. The dashed lines are guides to the eyes.

not much faster than the relaxation of the excited state of a high-energy degree of freedom and in which the intermolecular dynamics have a strong effect on the absorption spectrum of the high-energy degree of freedom. Water is a clear example showing this type of behavior.

### 4.3.2   FÖRSTER ENERGY TRANSFER

Figure 4.4 shows the anisotropy decays as a function of delay for pure $D_2O$ and for four mixtures of $D_2O/H_2O$. The anisotropy is constructed after subtracting the heat signal at all delay times. The decay of the anisotropy reflects both the effects of molecular reorientation and resonant energy transfer between differently oriented OD groups. The two effects can be distinguished by varying the concentration of OD oscillators. For the lowest concentration (0.5% of $D_2O$ in $H_2O$) the contribution of the energy transfer to the decay of the anisotropy is very small and the anisotropy decays mainly because of the molecular reorientation of the HDO molecules. The observed decay can be fitted well with a single exponential with a time constant $\tau_{or}$ of $2.7 \pm 0.05$ ps. This reorientation time constant agrees well with previous reports [9, 108, 134]. With increasing concentration of $D_2O$, we observe the depolarization of the OD excitation to become faster, showing the contribution of Förster energy transfer to the anisotropy decay.

In the presence of intermolecular energy transfer, the anisotropy dynamics can be described with the following equation:

$$R(t) = \exp(-\frac{t}{\tau_{or}} - \frac{4\pi^{3/2}}{3}[OD]\sqrt{\frac{r_0^6 t}{T_1}}),$$
(4.1)
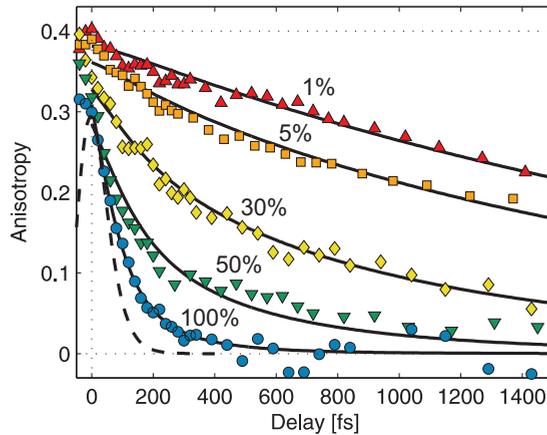
FIGURE 4.4. Orientational anisotropy decay curves for different concentrations of $D_2O$ in $H_2O$. The result of the fits to equation 4.6 are represented by the solid curves. The dashed line represents a gaussian profile fitted to the cross-correlated signal of pump and probe pulses.

where $\tau_{or}$ is the reorientation time and [OD] is the concentration of OD moieties in the system. The rate of energy transfer is governed by $r_0$, the so called Förster radius. This parameter denotes the distance between donor and acceptor at which the energy transfer efficiency is 50% within the vibrational lifetime.

Equation 4.1 provides a good description of the experimentally determined $R(t)$ in case the reorientation and the characteristic time scale of the Förster energy transfer are short compared to the instrument response function, i. e. the cross-correlation of the pump and probe pulses. For dynamics that are comparable with the time duration of the cross-correlate, the measured response includes the instrument response function. Unfortunately, the effect of the limited time resolution of the experiment cannot be accounted for by comparing the experimentally determined $R(t)$ with a convolution of equation 8.7 and the cross-correlate of pump and probe, as the experimental $R(t)$ anisotropy is not measured directly but constructed from the measured $\Delta\alpha_{\parallel}(t)$ and $\Delta\alpha_{\perp}(t)$. Hence the instrument response has to be accounted for in the separately measured $\Delta\alpha_{\parallel}(t)$ and $\Delta\alpha_{\perp}(t)$. The isotropic absorption change is given by:

$$\Delta\alpha_{\text{iso}}(t) = \int P(\tau)G(t-\tau)d\tau \,, \tag{4.2}$$

with $G(t-\tau)$ being the instrument response function and $P(\tau)$ the population relaxation function. The function $P(\tau)$ can be a single exponential, i.e. $e^{-\tau/T_1}$, but it can also be more complicated if the relaxation process involves more than two states. We can construct model parallel and perpendicular responses from:

$$\Delta\alpha_{\parallel}(t) = \Delta\alpha_{\text{iso}}(t) + \frac{2}{3}\int R(\tau)P(\tau)G(t-\tau)d\tau \,, \tag{4.3}$$
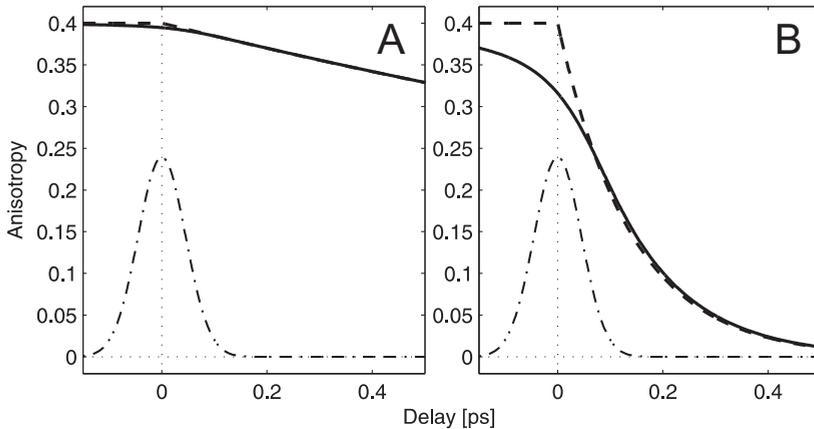
FIGURE 4.5. Effect of the system response function on the observed anisotropy decay. The dash-dotted line represents the system response function, i.e. the cross correlation function of the pump and probe pulses. The dashed line represents the experimental anisotropy decay in case of infinitely good time resolution. The solid line represents the anisotropy decay constructed from the parallel and perpendicular signals that are convoluted with the system response function. Panel A shows a case in which the anisotropy decay is relatively slow ($\tau_{or} = 2.55$ ps), panel B shows the case for a fast decaying anisotropy ($\tau_{or} = 140$ fs).

and

$$\Delta\alpha_\perp(t) = \Delta\alpha_{\mathrm{iso}}(t) - \frac{1}{3}\int R(\tau)P(\tau)G(t-\tau)d\tau \,. \qquad (4.4)$$

Both signals are affected by the function $R(\tau)$ which reflects the anisotropy decay. This function corresponds to equation 4.1. The difference between the two signals is then given by:

$$\Delta\alpha_\|(t) - \Delta\alpha_\perp(t) = \int R(\tau)P(\tau)G(t-\tau)d\tau \,. \qquad (4.5)$$

The expression for the model anisotropy $R_{\mathrm{mod}}(t)$ is thus

$$R_{\mathrm{mod}}(t) = \frac{\int R(\tau)P(\tau)G(t-\tau)d\tau}{\Delta\alpha_{\mathrm{iso}}(t)} \,. \qquad (4.6)$$

Clearly, the expression for $R_{\mathrm{mod}}(t)$ is not the same as $\int R(\tau)G(t-\tau)d\tau$. The difference is negligible for a slowly decaying anisotropy, however, it becomes significant when $R(\tau)$ shows dynamics on the same scale as the cross-correlation (see figure 4.5).

To determine the Förster radius $r_0$, expression 4.6 is fitted to the experimentally determined $R_{\mathrm{exp}}(t)$. The function $G(t-\tau)$ represents a gaussian fit to the experimental cross-correlation and $P(\tau)$ is a monoexponential population decay with a $T_1$ value that follows from the isotropic data. All curves can be
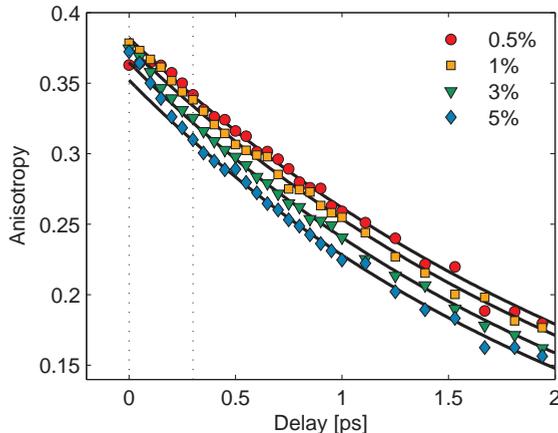
FIGURE 4.6. Anisotropy decay curves for low concentrations of $D_2O$ in $H_2O$. The result of the fits to monoexponential function are represented by the solid curves.

described well by equation 4.6. Fitting the data to equation 4.6 using a least-squares fitting method yields a value for the Förster radius $r_0$ of $2.3 \pm 0.2$ Å, which is very similar to the value of 2.1 Å found previously for the OH stretch vibration in water [171].

Figure 4.4 shows that the anisotropy decay observed for a solution of 5% $D_2O$ in $H_2O$ significantly differs from that observed for a solution of 1% $D_2O$ in $H_2O$. For the solution containing 5% $D_2O$ the anisotropy is observed to decay to a much lower level in the first 400 fs after the excitation. This findings shows that Förster energy transfer already plays a role at this concentration at which the average distance between the OD oscillators is approximately 6 Å.

To study the contribution of Förster energy transfer to the anisotropy dynamics for low concentrations at early delays, we have performed additional experiments on four samples of 0.5%, 1%, 3% and 5% of $D_2O$ in $H_2O$. The results are shown in figure 4.6. We have fitted the data with a single exponential function between 0.3 ps and 8 ps and found that at all concentrations the decay can be fitted well with a time constant of $2.6 \pm 0.1$ ps. However, there is a significant effect in the extrapolated starting value of the single exponential fit at delay zero. Decreasing the amount of $D_2O$ resulted in an increase of the starting value for the anisotropy from 0.35 for a 5% mixture up to 0.39 for a 0.5% mixture.

Using equation 4.1 we can determine the contribution of Förster energy transfer to the decay of the anisotropy. We rewrite formula 4.1 in a form $R(t) = \exp(-O - F)$, where $O$ and $F$ represent the orientational relaxation and the energy transfer contributions. In figure 4.7 we plot the function $1 - \exp(-F)$ as a function of the concentration of $D_2O$ at a delay of 400 fs. This function represents the decay of the anisotropy in case there would only be Förster energy transfer. The inset shows the amount of energy transfer at very low $D_2O$
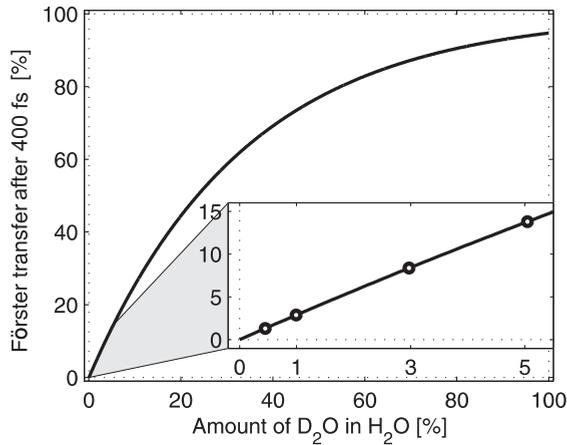
FIGURE 4.7. Anisotropy decay due to Föerster energy transfer after 400 fs. The contribution is calculated using equation 8.7 with parameters derived from the experimental results.

concentrations. The open circles correspond to the concentrations used in the experiment. It follows that energy transfer contributes to the anisotropy decay even for a solution of 0.5% $D_2O$ in $H_2O$.

From the results of figure 4.6 it follows that for solutions containing 3% and 5% $D_2O$ Förster energy transfer leads to a decay of the anisotropy up to ∼20% in the first 400 fs after the excitation. Fast initial anisotropy decays have been observed before for mixtures of $D_2O$ and $H_2O$ [9, 108, 134], but these initial decays were assigned to librational motions that keep the O–H···O hydrogen bond intact. However, the present comparison of the results obtained for 5% $D_2O$ in $H_2O$ and 0.5% $D_2O$ in $H_2O$ shows that a significant part of this initial decay is in fact due to Förster energy transfer. Librational motions are certainly expected to be present in liquid water and to contribute to a fast initial decay of the anisotropy [85], but their amplitude is smaller than has been reported [9, 108, 134].

For pure $D_2O$, a significant part of the energy transfer will take place between the two OD vibrations within the $D_2O$ molecule. In a recent experimental and theoretical study of the intra- and intermolecular couplings of $H_2O$ it was found that the spectral dynamics of the OH stretch vibrations of $H_2O$ mainly result from this intramolecular coupling [121]. However, with respect to the anisotropy, the intramolecular coupling can only account for a partial decay, as intramolecular energy transfer only leads to the equilibration of the energy in the plane of the molecule. Hence, the observed complete rapid decay of the anisotropy shows that for $D_2O$ fast intermolecular energy transfer processes must be present.

The process of Förster energy transfer in water has been studied before for the OH stretch vibrations of solutions of HDO in $D_2O$ [171] and for pure

$H_2O$ [32, 79, 171]. From the measurements on HDO in $D_2O$, the Förster radius was determined to be 2.1 Å, which is very comparable to the Förster radius of $2.3 \pm 0.2$ Å we find here for the OD vibration in water. To compare the Förster energy transfer rates of the OD and the OH vibrations in water we use:

$$k_F(r) = \frac{1}{T_1} \left(\frac{r_0}{r}\right)^6 . \tag{4.7}$$

The values of $T_1$ of the OH vibration of HDO in $D_2O$ is 740 fs [172] and of the OD vibration of HDO in $H_2O$ is 1.7 ps. Assuming that the values of $r_0$ are the same for OD and OH (within their error margins), we thus find that $k_{F,\text{OH}}(r) \approx 2.3 k_{F,\text{OD}}(r)$.

The ratio of the Förster energy transfer rates of the OD and OH vibrations in water can be compared to the ratio that follows from the linear absorption spectra of these vibrations assuming that the energy transfer results from a dipole-dipole interaction mechanism. In this case the Förster energy transfer rate between the same type of oscillators is given by [112, 172]:

$$k_F(r) \sim \frac{\sigma^2}{r^6} \int g^2(\nu) d\nu , \tag{4.8}$$

where $\sigma$ denotes the cross-section and $g(\nu)$ the absorption line profile. The cross-section of the OD vibration of HDO in $H_2O$ is approximately 1.9 times smaller than that of the OH vibration of HDO in $D_2O$. Another difference between the linear absorption spectra is that the frequency axis of the OD vibration is contracted by a factor of $\sim \sqrt{2}$. If we assume the line shapes of the OH and the OD vibrations to be Gaussian, it follows from equation 4.8 that $k_{F,\text{OH}}(r) \approx (1.9^2/\sqrt{2}) k_{F,\text{OD}}(r) \approx 2.6 k_{F,\text{OD}}(r)$. This ratio compares very well with the experimentally observed ratio of $\sim 2.3$, which corroborates that the energy transfer among the OD vibrations of HDO in $H_2O$ indeed relies on a dipole-dipole interaction mechanism.

For pure $H_2O$ the resonant energy transfer among the OH vibrations was observed to be significantly faster than expected from an extrapolation of the dipole-dipole interaction of the OH vibrations of solutions of HDO in $D_2O$ [171]. Possible explanations for this deviation are a break-down of the dipole-dipole description, i. e. the presence of additional multi-pole electric field interactions and the contribution of (intramolecular) anharmonic couplings to the energy transfer. Interestingly, this behavior is not observed for pure $D_2O$. The observed anisotropy decay of pure $D_2O$ can be quite well accounted for by using the same dipole-dipole coupling that accounts for the anisotropy decay of the solutions of HDO in $H_2O$ (figure 4.4). This finding indicates that intramolecular anharmonic couplings of the OD vibrations do not contribute to the energy transfer within the $D_2O$ molecule. Recent molecular dynamics simulations by the Skinner group have discussed the validity of the Förster model (equation 4.8) in describing the anisotropy decay in liquid water [175]. The theory behind the Förster formula contains a number of assumptions:

- the energy transfer between donor and acceptor is irreversible,
- the spatial and orientational distribution of acceptors is statistical,

- energy hopping leads to a complete decay of the anisotropy.

Skinner found that the orientation of the nearest acceptors is such that energy transfer leads to a negative anisotropy, therefore the anisotropy decay is not proportional to the survival probability, but in fact decays faster. The survival probability itself, however, becomes slower if reversible energy transfer is taken into account, and becomes faster again if the intramolecular energy transfer is included. With respect to the latter we would like to point out that this is included in the present chapter and in the previous work on $H_2O$ of Woutersen and Bakker, by considering the concentration of OD/OH oscillators. This concentration has a maximum value of 110 M and this also includes the transfer between two OD/OH groups located in the same molecule. Of course it is still assumed that the distance between the OH/OD groups is statistical. Skinner found that the effects of reversible energy transfer (slowing down) more or less compensates the effects of the non-random orientation of the acceptors and the intramolecular energy transfer (speeding up), which explains why the simple model works so well in describing the data.

## 4.4   CONCLUSIONS

We study the vibrational energy relaxation and resonant Förster energy transfer dynamics of the OD stretch vibrations in pure $D_2O$ and solutions of HDO in $H_2O$ with polarization-resolved femtosecond mid-infrared pump-probe spectroscopy. The vibrational relaxation of the OD vibration of pure $D_2O$ is observed to occur with a time constant of $400 \pm 30$ fs.

We monitor the occurrence of Förster resonant energy transfer of the OD vibrations by measuring the dynamics of the anisotropy of the vibrational excitation of the OD vibration for different concentrations of HDO in $D_2O$. With increasing HDO concentration the anisotropy decay accelerates and becomes increasingly non-exponential. These observations can be modeled well with a resonant energy transfer model in which the OD vibrations interact via a dipole-dipole coupling mechanism. From a fit to the data obtained at different concentrations we determine the Förster radius $r_0$ to be $2.3 \pm 0.2$ Å. The rate constant of the Förster energy transfer is observed to be $\sim$2.3 times smaller than for the OH vibrations of HDO dissolved in $D_2O$. This ratio is fully consistent with a dipole-dipole interaction mechanism and can be well explained from the difference in cross-section and spectral distribution of the OD and the OH stretch vibrations.

We observe that the Förster energy transfer already significantly contributes to the decay of the anisotropy of the OD vibration for $D_2O$ concentrations $\leqslant 5\%$. At these concentrations, the resonant energy transfer is observed to induce a fast partial decay of the anisotropy in the first 400 fs after the vibrational excitation. For a $D_2O$ concentrations of 5% this fast initial decay amounts to $\sim$15% of the anisotropy decay. This result implies that previous observations of a fast initial anisotropy decay for the same system are only partly the result of librational motions.

# 5   VIBRATIONAL DYNAMICS OF THE BENDING MODE OF WATER INTERACTING WITH IONS

We studied the vibrational relaxation dynamics of bending mode ($\nu_2$) of $H_2O$ water molecules in the presence of different salts (LiCl, LiBr, LiI, NaI, CsI, NaClO$_4$ and NaBF$_4$). The linear and nonlinear spectra of the bending mode show distinct responses of water molecules hydrating the anions. We observe that the bending mode of water molecules that are hydrogen-bonded to an anion exhibit much slower relaxation rates ($T_1 \sim 1$ ps) than water molecules that are hydrogen-bonded to other water molecules ($T_1 = 400$ fs). We find that the effect of the anion on the absorption spectrum and relaxation time constant of the water bending mode is not only determined by the strength of the hydrogen-bond interaction but also by the shape and structure of the anion.

## 5.1   INTRODUCTION

Water is rarely encountered as a pure liquid, and usually contains dissolved (bio)molecules and ions [101, 125]. The interactions between water and the dissolved ions and molecules can lead to completely different molecular motions and energy dynamics of the solvating water molecules compared to water in the pure liquid [80, 110, 154]. In turn, these different water dynamics will have an effect on the conformations and the (bio)chemical reactivity of the dissolved molecules and ions [125].

The dynamics of the OH stretch vibrations of water molecules solvating ions have been studied extensively with femtosecond mid-infrared spectroscopic techniques [8, 110, 126, 154]. For water molecules hydrating halogenic anions like Cl$^-$, Br$^-$ and I$^-$ it was found that the vibrational lifetime of the OH stretch vibration is significantly longer than for water molecules in bulk liquid water. It was also observed that water in the hydration shells of ions often show a much slower reorientation, depending on the strength of the interaction of the ion with the water [110, 154].

In most of the experimental and theoretical studies of the properties of water hydrating ions, the dynamics are probed via the response of the OH stretch vibrations ($\nu_1$, $\nu_3$) of the water molecules. Here we probe the wa-

ter dynamics via the bending mode ($\nu_2$) of the $H_2O$ water molecules. Previous mid-infrared femtosecond studies of the bending mode of water focused on the vibrational relaxation mechanism of the bending mode of bulk water and its role in the vibrational relaxation pathway of the OD/OH stretch vibration [5, 19, 68, 87, 94, 122, 139]. It was found that the relaxation of the bending mode of bulk water (both of $H_2O$ and HDO molecules in HDO:$D_2O$ isotopic mixture) is a two-step process consisting of the depopulation of the excited state $\nu=1$ of the bending mode and excitation of the lower frequency modes (librations), followed by the thermal equilibration of the vibrational energy. The vibrational lifetime of the bending mode of $H_2O$ in HDO:$D_2O$ was found to be $T_1 = 380 \pm 50$ fs. The thermal equilibration had a time constant of $\sim$1.2 ps [19, 87]. The same relaxation pathway was found for pure $H_2O$. However, due to more efficient intermolecular coupling in comparison to the isotopically diluted mixture, both the vibrational lifetime and the thermalization are faster and show time constants $T_1 = 170 \pm 30$ fs and $T_{eq} = \sim$0.8-1 ps, respectively [5, 68]. Up to now no studies have been reported on the vibrational dynamics of the bending mode of water in salt solutions. Since the vibrational coordinate of the bending mode is very different from that of the stretch vibrations, this mode presents an interesting, complementary probe of the interaction between water and ions.

## 5.2    EXPERIMENT

We measure the vibrational dynamics of the bending mode of water molecules using polarization-resolved mid-infrared pump-probe spectroscopy. The femtosecond mid-infrared pulses needed for this experiment are generated using the laser system and the frequency conversion processes described in detail in sections 3.1 and 3.2. The generated pulses (IR 1) have a central wavelength of $\sim$6000 nm ($\sim$1650 cm$^{-1}$), a pulse duration of $\sim$65 fs, a pulse energy of 40 $\mu$J, and a spectral bandwidth of $\sim$350 cm$^{-1}$. The pump-probe setup is described in section 3.3.

The samples are solutions of LiCl, LiBr, LiI, NaI, CsI, NaClO$_4$ and NaBF$_4$ in water. We use a mixture of 1:2 $H_2O$ in $D_2O$ ($\sim$11:44:44% $H_2O$:HDO:$D_2O$) in order to minimize the intermolecular resonant energy transfer between water molecules while at the same time maintaining sufficient optical density for the $H_2O$ bending mode. The bending mode has a different resonant frequency for different isotopologues of water: $\sim$1250 cm$^{-1}$ for $D_2O$, $\sim$1450 cm$^{-1}$ for HDO and $\sim$1650 cm$^{-1}$ for $H_2O$ [43]. This allows us to selectively excite the bending mode of the $H_2O$ molecules. We study salt solutions at the following concentrations: 10 m for solutions of LiCl, LiBr, LiI, CsI, and NaBF$_4$, a series of 3, 6, 9 and 12 m for LiI, and a series of 3, 6, 10 and 14 m for NaClO$_4$. The samples are placed between two 2 mm thick CaF$_2$ windows separated by a teflon spacer with a thickness of 50 $\mu$m. During the experiments the experimental setup is constantly flushed with N$_2$ gas to prevent any influence of the absorption lines of ambient water vapor on the measured spectra and dynamics.

## 5.3   Results and Discussion

### 5.3.1   Linear spectra

In figure 5.1, we present linear absorption spectra of the OD-stretch vibration and the bending mode for solutions of 10 m of different salts in a $D_2O/H_2O$ mixture. The top panel presents the linear spectra of the OD-stretch vibration of salt solutions in a 1:7 $D_2O/H_2O$ mixture, and the bottom panel shows the linear spectra of the $H_2O$ bending mode for salt solutions in a 1:2 $H_2O/D_2O$ mixture. For comparison also the spectra of the pure $D_2O/H_2O$ mixtures are shown (without salt). For clarity all linear spectra are corrected (by subtraction) for the background signal of the broadband librational band. The addition of salts leads to a blueshift of the absorption spectrum of the OD stretch vibration. This blueshift can be explained from the fact that the hydrogen bonds between water molecules and halide anions ($Cl^-$, $Br^-$, $I^-$) are weaker than between water molecules [80]. The hydrogen bond to the anion becomes weaker within the halogenic series $Cl^- \rightarrow Br^- \rightarrow I^-$, and thus the blueshift increases, as illustrated in the top panel of figure 5.1. In the cases of the very weak hydrogen bonds between water molecules and hydrated $ClO_4^-$ and $BF_4^-$, the absorption band of the OD stretch mode even splits into two, with a high frequency subband (rather than a shift) at $\sim 2650$ cm$^{-1}$ [25, 61]. This subband corresponds to water molecules hydrating $ClO_4^-$.

The lower panel of figure 5.1 shows that the addition of salts leads to a red shift of the vibrational frequency of the bending mode of $H_2O$. This redshift demonstrates the opposite effect of hydrogen-bond formation on the frequencies of the stretch vibrations and the bend vibration of water. For the bending mode, hydrogen-bond formation leads to a blueshift of the absorption band, therefore weakening of the hydrogen-bond leads to a redshift of the absorption band [43]. The redshift of the bending mode increases in the halogenic series $Cl^- \rightarrow Br^- \rightarrow I^-$, in line with the weakening of the $O-H \cdots X^-$ hydrogen bond in this series. For the multiatomic $ClO_4^-$ and $BF_4^-$ anions, the bending mode frequency is similarly affected as for the other salts and shifts towards lower frequency. However, in contrast to the observations for the OD-stretch vibration, the $H_2O$ bending mode spectrum remains a single band. In fact the absorption spectra of the $H_2O$ bending mode in $ClO_4^-$ and $BF_4^-$ solutions resembles very much that of a $Br^-$ solution, and is less redshifted in comparison to that of an $I^-$ solution.

In figure 5.2 we show absorption spectra for pure water, LiI and NaClO$_4$ solutions as a function of salt concentration. With increasing salt concentration, the bending mode spectra show a progressive redshift with respect to the pure $H_2O$ bending mode spectrum. The bending mode spectrum of pure $H_2O$ possesses a slight asymmetry that in previous studies has been described with two gaussians [166, 167]. This asymmetry is however small compared to the asymmetry resulting from the addition of salts. Here we neglect the asymmetry of the pure $H_2O$ bending mode spectrum and we fit the linear spectra of the salt solutions to a sum of two gaussian spectral profiles. In this fit the position of the two bands and their spectral widths are kept constant for spectra
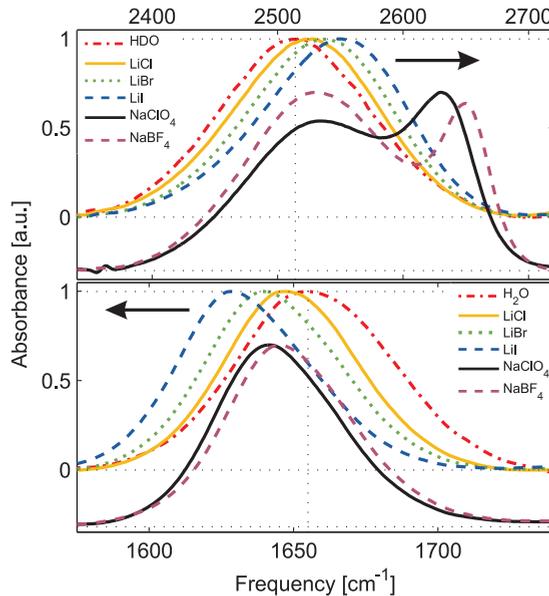
Figure 5.1. Normalized linear absorption spectra of the OD stretch vibration of HDO molecules in 10 m salt solutions of LiCl, LiBr, LiI, NaClO$_4$, NaBF$_4$ in a H$_2$O/D$_2$O (1:7) mixture (top panel), and of the H$_2$O bending mode in 10 m salt solutions of LiCl, LiBr, LiI, NaClO$_4$, NaBF$_4$ in a H$_2$O/D$_2$O (1:2) mixture (bottom panel).

at different concentrations and only the amplitudes are varied. This approach provides an excellent fit of the spectra at all salt concentrations. This implies that the redshift of the overall absorption spectrum can be fully described in terms of two inter-converting water species that we tentatively assign to bulk and anion-bound water molecules.

The two gaussian bands used to describe the linear spectra at all concentrations are shown in figure 5.2 as solid black lines. For iodide associated water molecules we find a redshift of 28 cm$^{-1}$, and for water molecules interacting with perchlorate the redshift is 21 cm$^{-1}$. This observation is surprising, in view of the effect these two anions have on the frequency of the stretch vibrations of water (the blueshift for the perchlorate solution is larger than for the iodide solution). The bending mode frequency of H$_2$O appears to be less affected by the formation of a very weak hydrogen bond to ClO$_4^-$ than by the formation of a less weak hydrogen bond to I$^-$.

By integrating the bands resulting from the global fit we obtain the populations of the bulk-like and anion-bound waters. In figure 5.3 we show the fraction of bulk-like water as a function of concentration for LiI and NaClO$_4$. The population of the bulk-like water decreases with increasing salt concentration, whereas the anion-bound population increases with increasing salt concentration. To translate the spectral amplitudes to relative fractions of bulk-like and anion-
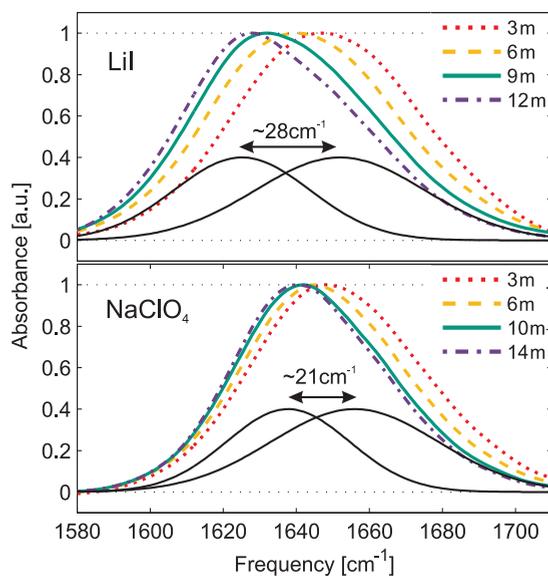
FIGURE 5.2. Absorption spectra of the $H_2O$ bending mode for different concentrations of LiI and $NaClO_4$ in a $H_2O/D_2O$ ($\sim$1:2) mixture.
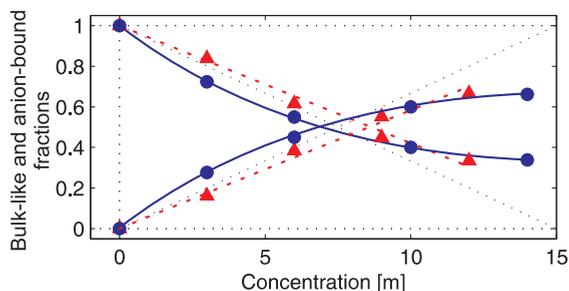


FIGURE 5.3. Fractions of bulk and anion-bound water molecules for LiI (triangles, red) and $NaClO_4$ (dots, blue), extracted from a global fit of the linear absorption spectra at different concentrations. The lines are guide to the eyes.

bound water molecules, we need to know the ion concentration dependence of the bending-mode spectra of these species. We found that the cross-section of both species is larger by $\sim$95% for a solution of 12 m LiI and by $\sim$110% for a solution of 14 m NaClO$_4$. As the cross-section increase is similar for both species, the ratio of the spectral amplitudes directly represents the ratio of the bulk-like and anion-bound water at all salt concentrations.

For the highest concentrations measured (12 m for LiI and 14 m for NaClO$_4$) we find that approximately 35% of the water molecules behave bulk like and do not form hydrogen bonds with the anions. This means that for $\sim$35% of the water molecules both OH groups are bonded to other water molecules (O$\cdots$H–O–H$\cdots$O), even at these very high concentrations. Assuming a statistical distribution of hydrogen bonds, this implies that $\sim$60% of the hydroxyl groups form O–H$\cdots$O hydrogen bonds to a water molecule and $\sim$40% of the hydroxyl groups form O–H$\cdots$X$^-$ hydrogen bonds to an X$^-$ anion. From this distribution it follows that for $\sim$48% of the water molecules one O–H group is hydrogen bonded to an anion and the other O–H group is hydrogen bonded to a water molecule (O$\cdots$H–O–H$\cdots$X$^-$). For $\sim$16% of the water molecules both O–H groups are hydrogen bonded to anions (X$^-\cdots$H–O–H$\cdots$X$^-$). Hence, even at the highest salt concentrations, the bulk-like waters (O$\cdots$H–O–H$\cdots$O) and the water molecules that are only singly hydrogen bonded to an anion (O$\cdots$H–O–H$\cdots$X$^-$) dominate. The water molecules that are doubly hydrogen bonded to anions form a minority at all studied salt concentrations. This explains why at all concentrations the absorption spectrum of the water bending vibrations can be well described with only two inter-converting bands. If the water molecules with two hydrogen bonds to anions had become important at high salt concentrations, a third, even more redshifted absorption component would have been expected to show up in the absorption spectrum.

Based on this estimation and the salt concentration we find that at high salt concentrations there are $\sim$3 - 3.5 H-bonds per anion. For the lowest concentration of 3 m approximately 85% (LiI) and 75% (NaClO$_4$) of water molecules behave bulk like implying that $\sim$8% and $\sim$13% of the hydroxyl groups are bonded to the anion for LiI and NaClO$_4$, respectively. The hydration numbers for the low salt concentration are higher and amount to $\sim$4 and $\sim$5 H-bonds for I$^-$ and ClO$_4^-$, respectively.

## 5.3.2    Vibrational energy relaxation dynamics

Figure 5.4 shows transient spectra at different delays after the excitation. The excitation is observed to result in a transient absorption decrease of the fundamental $v = 0 \rightarrow 1$ transition between 1620 and 1680 cm$^{-1}$, due to the depopulation of the $v = 0$ state of the bending mode and $v = 1 \rightarrow 0$ stimulated emission out of the excited $v = 1$ state. At lower frequencies the signal changes sign and we observe the induced $v = 1 \rightarrow 2$ absorption. The shape of the bleaching signal of the transient spectra follows the lineshape of the linear absorption spectrum. The nonlinear spectra of LiI clearly show the two subbands that were extracted from the linear spectra. In the case of NaClO$_4$, the overlap between the two subbands is larger, making the transient spectra appear as a broad single band.
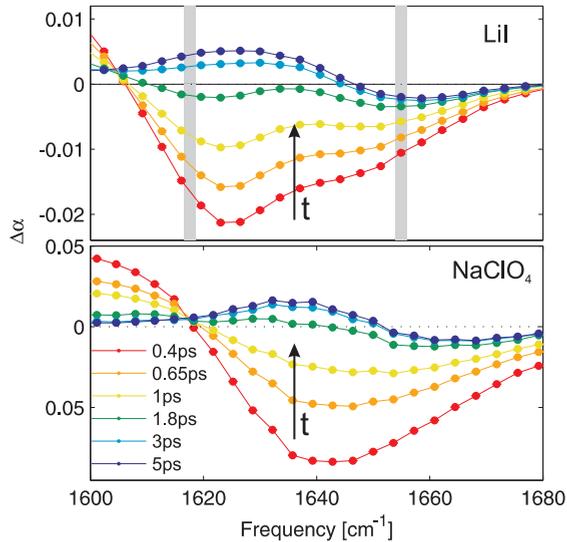
FIGURE 5.4. Transient spectra of solutions of 12 m LiI and 14 m NaClO$_4$ as a function of delay time between the pump and probe pulses. The arrows indicate the time evolution of the amplitude of the spectra. The solid lines represent fits to the model described in the text. The two gray bars in the top panel indicate the frequencies for which the two delay traces in figure 8.6 are shown.

With increasing delay time the signals decay and the shape of the transient spectra invert. After ∼5 ps the spectrum does not change anymore and the observed spectral shape is a signature of an increase in sample temperature. An increase in sample temperature leads to a redshift of the fundamental absorption spectrum [43, 102]. As a result we observe a negative signal at the blue side of the spectrum (>1650 cm$^{-1}$) and a positive signal at the red side of the spectrum (<1650 cm$^{-1}$). The increase in temperature reflects the equilibration of the bending mode excitation energy over the low-frequency librational and translational modes.

In figure 8.6 we show the transient absorption changes as a function of delay time for the frequencies indicated by the gray bars in the transient spectra of the LiI solution shown in figure 5.4. The dynamics at these frequencies are representative for the dynamics of the two subbands for LiI. Clearly the excitation at the red side of the spectrum (red) decays more slowly than the transient signal at the high-frequency edge of the spectrum (black). The vibrational relaxation of the anion-bound water molecules is thus approximately twice as slow as the vibrational relaxation of the bulk water species. The inset in figure 8.6 shows the same time traces on a logarithmic scale. For delays >300 fs the data can be fit well with a straight line, which implies that from this delay on the decays are single exponential.

Based on these observations we model the data with a model containing three
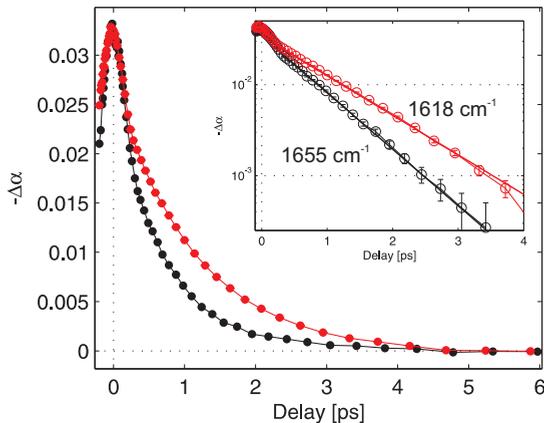
FIGURE 5.5. Transient absorption change as a function of delay time between pump and probe for a solution of 12 m LiI at frequencies of 1618 cm$^{-1}$ and 1655 cm$^{-1}$ (indicated by the gray bars in figure 5.4). The inset shows the same delay traces on a logarithmic scale - the lines are single-exponential functions that serve as a guide to the eye.

transient spectral components: two spectra reflect the bulk-like and anion-bound water and one spectrum represents the change in the spectral response due to the thermal equilibration. Each of the spectral components is described as a product of its population dynamics $N(t)$ and its associated spectral signature $\sigma(\nu)$. The isotropic data ($\Delta\alpha_{iso}$) at all times and frequencies are thus described with the following equation:

$$\Delta\alpha_{iso}(t,\nu) = N_b(t) \cdot \sigma_b(\nu) + N_a(t) \cdot \sigma_a(\nu) + N_{0*}(t) \cdot \sigma_{0*}(\nu), \qquad (5.1)$$

where the symbols in the subscript refer to bulk-like water ($b$), anion-bound ($a$) water band, and the heated final state ($0^*$). We assume that the bulk and anion-bound water molecules relax independently with a single rate constant to the common final heated state. We find that this model describes the experimental data very well for LiI and NaClO$_4$ solutions at all concentrations. The results of the fits are represented in figure 5.4 by the solid lines.

From the fit we can extract the transient spectra associated with each state. In figure 5.6 we show these spectra for a 12 m solution of LiI (top panel) and a 14 m solution of NaClO$_4$. The blueshifted (solid line) and redshifted (dashed line) spectra reflect the bulk-like and anion-bound water molecules respectively. The dashed-dotted line represents the transient spectrum of the final heated state. The frequency difference between the maxima of the bulk-like and anion-bound water bands is consistent with the frequency differences extracted from the analysis of the linear spectra ($\sim$30 cm$^{-1}$ for LiI and $\sim$20 cm$^{-1}$ for NaClO$_4$).

In figure 5.7 we show the initial populations $N_a(t=0)$ and $N_b(t=0)$ as a function of concentration (triangles). Here we use that the bulk-like and anion-bound water molecules have equal absorption cross sections (defined as
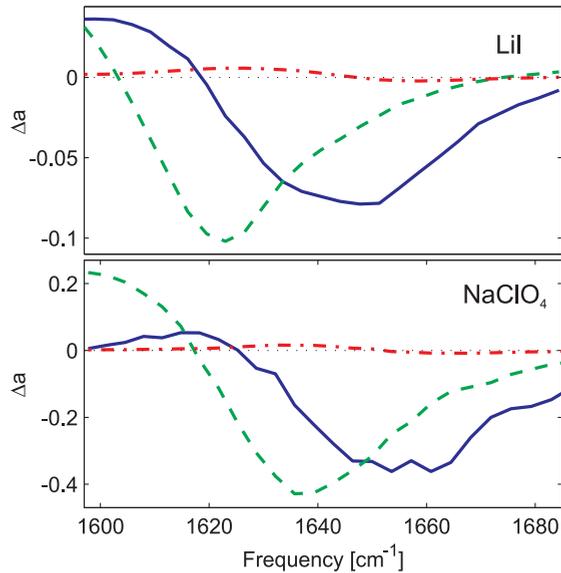
FIGURE 5.6. Spectra extracted from the fit of the isotropic data to the three-level kinetic model. The solid line (blue) represents bulk-like water, the dashed line (green) represents anion-bound water, and the dash-dotted line (red) represents the final heated spectrum.

the integral of the bleaching component of the corresponding spectra) at all concentrations. For comparison we also show the populations obtained from the fits of the linear absorption spectra at different concentrations (dots). The populations $N_a(t = 0)$ and $N_b(t = 0)$ are observed to correlate very well with the amplitudes of the subbands determined from the linear absorption spectra.

The decay rates of the bulk-like and anion-bound bands directly reflect the vibrational lifetimes of the two species. For all salt solutions, the bending mode of the anion-bound water molecules is observed to relax slower than the bending mode of the bulk-like water molecules. Water molecules bonded to $Cl^-$, $Br^-$ and $I^-$ anions relax on a $\sim 1 \pm 0.1$ ps timescale, whereas bulk-like water molecules have a lifetime of $\sim 400 \pm 80$ fs. The water molecules bound to $ClO_4^-$ and $BF_4^-$ anions relax slower ($\sim 750 \pm 80$ fs) than bulk-like water molecules, but not as slow as water molecules bound to monoatomic anions. We also compared the vibrational relaxation dynamics of the bending mode for NaI and CsI salt solutions and we found no effect of the cation on the vibrational relaxation rates. As a reference we have also analyzed a pure $H_2O/D_2O$ mixture (1:2), for which we find a vibrational lifetime of $380 \pm 50$ fs, in excellent agreement with previous experimental results [87, 94] and theoretical predictions [88]. Table I summarizes the vibrational lifetimes of both bulk ($T_{1\ HOH\cdot\cdot O}$) and anion-bound ($T_{1\ HOH\cdot\cdot X^-}$) water for all the studied salt solutions.
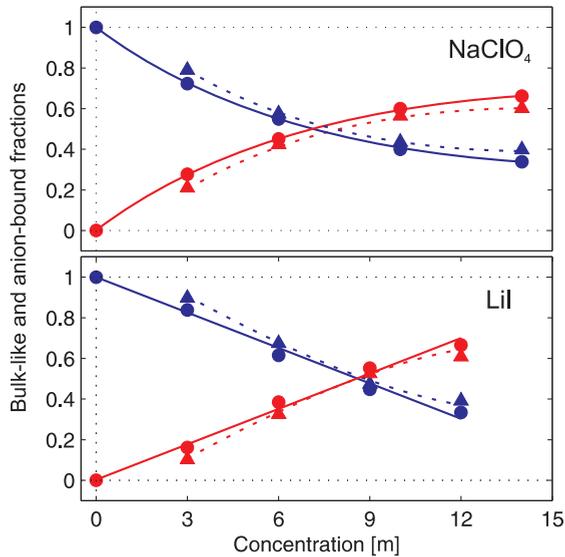
FIGURE 5.7. Concentration dependent populations of the bulk-like (blue) and anion-bound (red) water for LiI and NaClO$_4$ solutions. The points (dots) connected by the solid lines represent the spectrally integrated absorption bands of each of the species that followed from the decomposition of the linear absorption spectra. The dashed lines connect the points (triangles) that are obtained from fitting the transient spectra with the kinetic model described in the text.

TABLE I. Vibrational lifetimes of the bending mode of H$_2$O in different salt solutions.

| Sample | C [m] | T$_{1\ HOH\cdot\cdot O}$ [ps] | T$_{1\ HOH\cdot\cdot X^-}$ [ps] |
|---|---|---|---|
| H$_2$O | - | T$_1$=0.38 $\pm$ 0.05 | - |
|  | - | T$_{eq}$=1.3 $\pm$ 0.1 | - |
| LiCl | 10 | 0.40 $\pm$ 0.08 | 0.94 $\pm$ 0.12 |
| LiBr | 10 | 0.39 $\pm$ 0.09 | 0.86 $\pm$ 0.08 |
| LiI | 3 | 0.45 $\pm$ 0.08 | 1.0 $\pm$ 0.13 |
|  | 6 | 0.42 $\pm$ 0.06 | 1.03 $\pm$ 0.1 |
|  | 9 | 0.45 $\pm$ 0.1 | 1.06 $\pm$ 0.12 |
|  | 12 | 0.47 $\pm$ 0.08 | 1.10 $\pm$ 0.09 |
| NaI | 10 | 0.35 $\pm$ 0.07 | 1.03 $\pm$ 0.08 |
| CsI | 10 | 0.43 $\pm$ 0.05 | 0.97 $\pm$ 0.1 |
| NaClO$_4$ | 3 | 0.35 $\pm$ 0.08 | 0.81 $\pm$ 0.1 |
|  | 6 | 0.36 $\pm$ 0.11 | 0.75 $\pm$ 0.08 |
|  | 10 | 0.41 $\pm$ 0.08 | 0.72 $\pm$ 0.07 |
|  | 14 | 0.40 $\pm$ 0.05 | 0.75 $\pm$ 0.1 |
| NaBF$_4$ | 10 | 0.48 $\pm$ 0.08 | 0.83 $\pm$ 0.08 |

### 5.3.3    DISCUSSION

Both the linear and the transient spectra show that the addition of the multiatomic $ClO_4^-$ and $BF_4^-$ anions has less effect on the bending mode frequency than the addition of $I^-$. For $H_2O$ hydrating $ClO_4^-$, the bending mode shows a redshift of 20 cm$^{-1}$ with respect to bulk liquid water, whereas for $H_2O$ hydrating $I^-$ this redshift is 30 cm$^{-1}$. This observation is surprising as $ClO_4^-$ and $BF_4^-$ are observed to have a much stronger effect on the OD stretch vibrational frequency than $I^-$. To understand this difference we need to look in more detail at the effect of the hydrogen-bond interaction on the frequencies of the OD/OH stretch vibrations and the bending mode of water.

For the stretch vibration, hydrogen-bond formation leads to a lowering of the vibrational frequency because the hydrogen bond weakens the O–H chemical bond within the water molecule. As a result of this weakening, the restoring force associated with stretching or compressing the O–H bond coordinate decreases, and thus the frequency of the stretch vibration decreases. For the bending mode, hydrogen-bond formation introduces an additional restoring force because the hydrogen bond will resist a rotation of the O–H group out of the linear O–H$\cdots$O hydrogen-bonded system. An increase of the angle of the O–H group with respect to the O$\cdots$O hydrogen-bond coordinate will weaken the hydrogen bond and thus has an associated energy cost that adds up to the potential energy curve of the bending mode of the unbonded $H_2O$ molecule. The presence of the hydrogen bond thus leads to a blueshift of the vibrational frequency of this mode. Due to this effect the frequency of the bending mode of $H_2O$ shifts from ~1600 cm$^{-1}$ in the gas phase to ~1650 cm$^{-1}$ in the liquid phase.

When the hydrogen bond between $H_2O$ molecules is replaced by the weaker hydrogen bonds between $H_2O$ and an anion, the redshift of the OD/OH stretch vibrations will be smaller. Hence, the addition of halogenic anions that form weak hydrogen bonds to $H_2O$ will lead to a blueshift of the vibrational frequency of OD stretch vibration, as is observed in the upper panel of figure 5.1. The hydrogen bonds to $ClO_4^-$ and $BF_4^-$ are even weaker leading to an even larger blueshift. For the bending mode, the replacement of a hydrogen bond to $H_2O$ by a weaker hydrogen bond to an anion will lead to a redshift of the vibrational frequency. The reason that the redshift of the bending mode is smaller for $ClO_4^-$ and $BF_4^-$ than for $I^-$ is most likely related to the geometry of the ions. The overall charge density of these anions will be rather similar, they are similar in size and the only parameter in which they differ is their shape: $I^-$ is a sphere, whereas $ClO_4^-$ has a tetrahedral shape.

The large spherical shape of $I^-$ implies that the strength of the hydrogen bond is not very sensitive to the angle between the O–H group and the O$\cdots$I$^-$ hydrogen-bond coordinate. When the O–H group bends out of the O–H$\cdots$I$^-$ system, it will still interact favorably with another part of the large negatively charged sphere of the $I^-$ ion [64]. This means that the energy penalty for bending the O–H group out of the O–H$\cdots$I$^-$ coordinate is low. Hence, this hydrogen bond will provide very little additional restoring force to the bending mode vibration. The replacement of the strong, highly directional O–H$\cdots$O hydrogen bond between two water molecules by the O–H$\cdots$I$^-$ hydrogen bond will thus
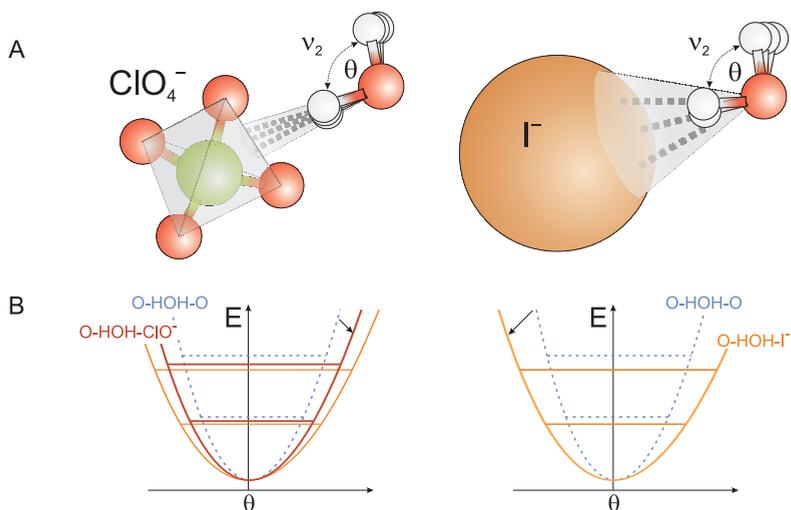
FIGURE 5.8. A: Schematic representation of a water molecule binding to $I^-$ and to $ClO_4^-$. The spherical shape of the $I^-$ ion allows for a much larger angular freedom of the hydrogen bond than the tetrahedral shape of the $ClO_4^-$ ion. B: Potential energy changes of the bending mode of water molecule associated with the molecule binding to $I^-$ and $ClO_4^-$ anions.

lead to a strong decrease of the restoring force of the bending mode vibration, and thus to a relatively large redshift of the frequency of this vibration (see figure 5.8 B).

For $ClO_4^-$ it has been shown that the solvating water molecules preferentially form hydrogen bonds towards the oxygen-oxygen "ridges" of the tetrahedron (see figure 5.8) with the hydrogen bond being mostly parallel to the O–Cl–O angle bisector [127, 165]. Due to the much more structured charge density of the $ClO_4^-$ ion, the strength of the O–H$\cdots ClO_4^-$ hydrogen bond will be quite sensitive to the angle between the O–H group and the O–Cl–O angle bisector. Hence, the energy penalty for creating a non-zero angle between the O–H group and the O–Cl–O angle bisector will be high, which means that the O–H$\cdots ClO_4^-$ hydrogen bond provides a relatively large restoring force to the bending mode vibration of the water molecule (see figure 5.8 B). Hence, in spite of the fact that the O–H$\cdots ClO_4^-$ hydrogen bond is weaker than the O–H$\cdots I^-$, its contribution to the restoring force of the bending mode is higher, as this contribution to the restoring force is not determined by the strength of the hydrogen bond interaction, but rather by the change in this strength when bending the O–H group with respect to the hydrogen-bond coordinate. This difference between $ClO_4^-$ and $I^-$ is illustrated in figure 5.8.

The vibrational lifetime of the bending mode is longer for $H_2O$ molecules hydrating an anion than for $H_2O$ molecule in the pure liquid. This observation is in line with the results of previous studies on the lifetime of the OD/OH stretch vibrations of HDO molecules in isotopically diluted salt solutions. The lifetime

of the OD/OH stretch vibrations was observed to increase by a factor of 3 for
$Cl^-$ to 5 for $I^-$ [81]. This increase has been explained from the relatively low
frequency of the $O-H\cdots X^-$ hydrogen bond stretch vibration. The frequency
of this vibration is lower than that of the $O-H\cdots O$ hydrogen-bond stretch vi-
bration in liquid water, because the hydrogen bond is weaker and because of
the relatively large mass of the halogenic anion. The hydrogen-bond stretch
vibration plays an important role in the relaxation of the OD/OH stretch vi-
bration and likely takes up part of the vibrational energy. The lower frequency
of the vibration implies that the same amount of energy corresponds to more
vibrational quanta which decreases the anharmonic coupling. A similar effect
may be responsible for the longer vibrational lifetime of the bending mode of
$H_2O$ molecules hydrating an anion. It is interesting to note that the increase
in lifetime is smaller than observed for the OD/OH stretch vibration. This can
be explained from the fact that the bending mode involves both OH groups of
the $H_2O$ molecule, and one of these OH groups will remain hydrogen bonded
to another water molecule.

Recent theoretical reports by the Hynes group showed that the vibrational
energy relaxation pathways of the bending mode of water involve the transfer
of the vibrational energy to the librational modes of the excited water molecule,
followed by energy transfer to the neighboring water molecules [70, 133]. The
water molecules that are hydrogen bonded to an anion will have less water
molecules as direct neighbors. Hence, the density of water librational modes in
the first hydration shell of the excited water molecule will be lower which may
explain the lengthening of the vibrational lifetime.

It is interesting to note that the vibrational lifetime is less lengthened for
$H_2O$ hydrating $ClO_4^-$ than for $H_2O$ hydrating a halogenic anion. This can be
due to the stronger dependence of the hydrogen bond on the angle between
O–H and the hydrogen-bond coordinate. This stronger dependence may also
lead to a stronger anharmonic coupling of the bending mode with the libra-
tions, thus also leading to a faster vibrational relaxation. Another explanation
is that the vibrational energy of the bending mode can be partially transferred
to the intramolecular vibrations of the $ClO_4^-$ anion. The $ClO_4^-$ anion possesses
9 intramolecular vibrations that can take up part of the vibrational energy of
the bending mode and thereby provide additional pathways of vibrational en-
ergy relaxation in comparison to the mono-atomic halogenic anions [71, 73]. The
latter explanation agrees with the observation that the vibrational relaxation
of the OH stretch vibration of HDO is also somewhat faster in case the OH is
hydrogen bonded to $ClO_4^-$ ($\sim$2.2 ps [8]) than in case the OH is bonded to $I^-$
($\sim$4 ps [81]), in spite of the fact that the hydrogen bond to $I^-$ is stronger. Prob-
ably, the internal vibrations of the $ClO_4^-$ assist in the vibrational relaxation of
the OH stretch vibration.

The relaxation of the bending mode appears to be negligibly affected by the
cations. We have tested the effect of the cation on the dynamics of the bulk-like
and anion-bound water. Changing the cation for the iodide salt from Li to Na
and Cs did not have any affect on the lifetimes of the two water species. This
notion likely follows from the fact that the cation and the hydrogen atoms of
the water molecule are located at opposite sides of the oxygen atom of the water

molecule, even at very high salt concentrations. Hence, there will be very little interaction between the cations and the hydrogen atoms, and as the bending mode primarily involves the motion of the hydrogen atoms, it can be understood that the cation has very little effect on its relaxation.

## 5.4  CONCLUSIONS

We studied the vibrational absorption spectra and the vibrational energy relaxation dynamics of the bending mode of $H_2O$ interacting with different ions. With increasing salt concentration, the overall absorption spectrum of the bending mode shows a redshift, and this redshift can be fully accounted for by the interconversion of two gaussian-shaped bands with concentration-independent central frequencies and spectral widths. One of these bands is associated with bulk-like $H_2O$ molecules that form hydrogen bonds with other $H_2O$ molecules, the other band is associated with the anion-bound $H_2O$ molecules of which one O–H group is hydrogen bonded to an anion. The latter band is redshifted with respect to the bulk-like band, and this redshift increases in the halogenic series $Cl^- \rightarrow Br^- \rightarrow I^-$.

For $H_2O$ hydrogen bonded to the multiatomic, tetrahedral anions $ClO_4^-$ and $BF_4^-$ the redshift of the bending mode is smaller than for $H_2O$ hydrogen bonded to $I^-$, even though the hydrogen bonds to $ClO_4^-$ and $BF_4^-$ are weaker than to $I^-$. This observation can be explained from the difference in structure of the ions. For $ClO_4^-$ and $BF_4^-$ the hydrogen bond is formed towards the narrow O–O and F–F ridges of the ions, which makes this bond more directional than the hydrogen bond to the large spherical $I^-$ anion. Due to the stronger directional character, the energy penalty of bending the hydrogen-bonded O–H group is larger and thus this bond contributes a stronger restoring force to the bending mode vibration. Hence, the bending mode frequency of $H_2O$ hydrogen bonded to $ClO_4^-$ or $BF_4^-$ is higher than for $H_2O$ hydrogen bonded to $I^-$.

We find that the bending mode vibrational lifetime $T_1$ of the bending mode is longer for water bound to halogenic anions ($\sim 1 \pm 0.1$ ps) than for bulk liquid water ($\sim 380 \pm 0.05$ fs). For $ClO_4^-$ the $T_1$ lifetime is not as long ($\sim 750 \pm 0.08$ fs) as for $H_2O$ hydrogen bonded to the halogenic anions. This somewhat shorter $T_1$ lifetime likely results from the participation of the internal vibrations of the $ClO_4^-$ anion in the vibrational relaxation of the $H_2O$ bending mode.

# 6    VIBRATIONAL RELAXATION PATHWAYS OF AI AND AII MODES IN N-METHYLACETAMIDE CLUSTERS

We studied the pathways of vibrational energy relaxation of the amide I ($\sim$1660 cm$^{-1}$) and amide II ($\sim$1560 cm$^{-1}$) vibrational modes of N-methylacetamide (NMA) in CCl$_4$ solution using two-color femtosecond vibrational spectroscopy. We measured the transient spectral dynamics upon excitation of each of these amide modes. The results show that there is no energy transfer between the amide I (AI) and amide II (AII) modes. Instead we find that the vibrational energy is transferred on a picosecond time scale to a combination tone of lower-frequency modes. Using polarization-resolved femtosecond pump-probe measurements we also study the reorientation dynamics of the NMA molecules and the relative angle between the transition dipole moments of the AI and AII vibrations. The spectral dynamics at later times after the excitation (>40 ps) reveal the presence of a dissociation process of the NMA aggregates, trimers and higher order structures, into dimers and monomers. By measuring the dissociation kinetics at different temperatures, we determined the activation energy $E_a$ of this dissociation to be 35 $\pm$ 3 kJmol$^{-1}$.

## 6.1   INTRODUCTION

The function of proteins is intimately related to their spatial structure and conformational dynamics. Any deviations of the functional structure, e.g. as a result of errors occurring during the folding process, can lead to disastrous consequences. For instance it has been shown that errors in the structure of particular proteins can cause diseases like Alzheimer and Parkinson [140]. The structure and conformational dynamics of proteins and polypeptides are closely connected to the dynamics of their intra- and intermolecular hydrogen bonds. The hydrogen bonds act to stabilize the conformation and also play an essential role in the energy dynamics of the protein [125].

To obtain molecular-scale insight into the hydrogen-bond dynamics of complex systems like proteins, it is often advantageous to study simpler molecular systems that form good model systems for these dynamics. An essential element of the structure of proteins is their backbone that consists of linked amide (-CO-NH-) groups. N-methylacetamide (NMA) is the simplest molecule containing the amide motif and a study of the hydrogen-bond interactions of NMA can thus give insight in the hydrogen-bond interactions of protein backbones.

The properties of NMA and NMA aggregates have been extensively studied with different experimental and theoretical methods like infrared spectroscopy [29, 36, 63, 67, 95, 119, 137], dielectric spectroscopy [120, 131] and molecular simulations [1, 18, 75, 100, 106, 158, 176]. These studies addressed different properties of NMA like its thermodynamical properties [63, 75, 95, 158] and its vibrational energy dynamics and couplings [18, 36, 137, 176]. In spite of its apparent chemical simplicity, NMA is quite complex in terms of its vibrational spectrum that contains no less than seven different amide vibrational bands [29, 63, 114, 176]. The fundamentals (residing between $\sim$400 cm$^{-1}$ and $\sim$1720 cm$^{-1}$) and combination tones of these amide vibrations form a dense manifold of states. In case the NMA molecules are hydrogen bonded, the vibrational spectrum becomes even more complex, as each intramolecular state becomes dressed with excitations and de-excitations of the coupled intermolecular hydrogen-bond modes.

The reported vibrational studies addressed the properties of NMA-water systems. So far no results have been reported on the vibrational properties of NMA$\cdots$NMA aggregate structures, although NMA aggregates constitute a nice model system for proteins that fold as a result of hydrogen-bond formation between the different amide groups of the protein backbone. Here we report on a polarization-resolved two-color femtosecond spectroscopic study of the vibrational dynamics of hydrogen-bonded NMA aggregates. We study the probability of energy transfer between the different amide modes of the NMA molecules and the vibrational energy relaxation pathways. We also study the kinetics of the formation and breaking of hydrogen bonds of NMA aggregates.

## 6.2    Experiment

The polarization-resolved two-dimensional experiment employs femtosecond mid-infrared pulses that are generated with the femtosecond laser system and frequency conversion processes described in detail in sections 3.1 and 3.2, respectively. In the experiments we used 60 $\mu$J pulses with a central wavelength of $\sim$6000 nm ($\sim$1650 cm$^{-1}$), a pulse duration of $\sim$55 fs and a spectral bandwidth of $\sim$400 cm$^{-1}$.

In the experiment the AI or AII mode is excited with a relatively narrow band pump pulse and the transient changes in absorption resulting from this excitation are monitored with a second broadband IR pulse. The narrow-band pump pulses are obtained by spectrally filtering the generated broadband infrared pump spectrum (see figure 6.1) with a home-built Fabry-Pérot filter (see section 3.3). The spectral bandwidth of the pump pulses used in the experiments
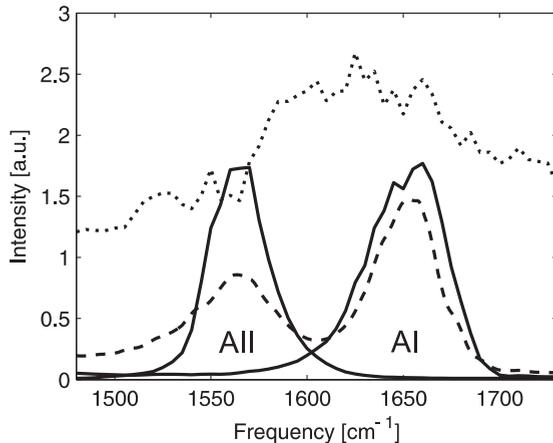
FIGURE 6.1. Experimental spectra of the probe pulse (dotted) and two pump spectra when pumping either the amide I or amide II vibration of NMA in CCl$_4$ solution (solid lines). The dashed line represents the absorption spectrum of a solution of 5 M.

is $\sim$40 - 50 cm$^{-1}$ and the pulse energy is $\sim$6 $\mu$J.

The pump pulse excites the NMA molecules from the equilibrium ground state $v = 0$ to the first excited state, $v = 1$ of the AI or AII mode. This excitation is observed as a bleach and stimulated emission at frequencies matching the $v = 0 \rightarrow 1$ transition, and an induced absorption at frequencies matching the $v = 1 \rightarrow 2$ transition. A detailed description of the pump-probe setup used in the experiment is provided in section 3.3.

The samples are formed by solutions of NMA in CCl$_4$. We study these solutions at 7 different concentrations: 10 mM (molecular ratio NMA-CCl$_4$ 1:1000), 30 mM (1:330), 50 mM (1:200), 0.1 M (1:100), 0.2 M (1:50), 0.5 M (1:20) and 5 M. In the study of the vibrational dynamics of the NMA aggregates we used a highly concentrated sample of 5 M of NMA in CCl$_4$ (see figure 6.2). The samples were placed between two 2 mm thick CaF$_2$ windows separated by teflon spacers with thicknesses ranging from 5 $\mu$m to 1.2 mm.

For the experiments at elevated temperatures we have used a home-built sample cell in which the heat source is formed by resistors surrounding the sample. The two resistive elements are attached to the bottom plate of the sample holder along the two CaF$_2$ windows. We have sent current through these elements, thereby heating the elements and the sample. The temperature of the sample was monitored with a temperature probe attached directly to the surface of one of the CaF$_2$ windows. During the experiments the experimental setup was constantly flushed with N$_2$ gas to prevent any influence of the absorption lines of ambient water vapor on the measured spectra and dynamics.
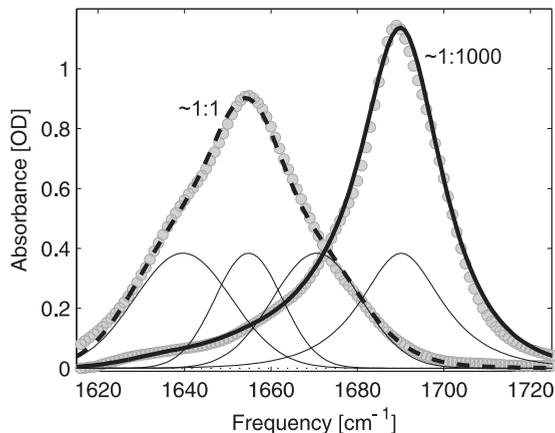
FIGURE 6.2. Linear spectra of a 10 mM and a 5 M solution of NMA in $CCl_4$. The grey circles represent the data points and the thick solid (10 mM) and dashed (5 M) lines are the result of a global fit. The thin lines represent the four subbands used to describe the linear spectra at all concentrations.

## 6.3   Results and discussion

### 6.3.1   Linear spectra

NMA is dominantly present in a trans conformation [1, 78, 106, 131] meaning that the C=O and N-H groups reside on the opposite sides of the C-N bond of the NMA molecule. As a result, NMA aggregates can form chain-like structures in which the C=O group of each NMA molecule is hydrogen-bonded to the N-H group of the next NMA molecule in the chain. A solution of NMA in $CCl_4$ thus consists of chain-wise arranged oligomers of different sizes. Information on the size distribution of these NMA oligomers can be obtained from the linear vibrational absorption spectra of solutions of NMA of different concentrations in $CCl_4$. Figure 6.2 shows two linear spectra of the two studied extreme concentrations of 10 mM (solid black line) and 5 M (dashed black line) of NMA in $CCl_4$.

The spectra are clearly asymmetric suggesting that they contain at least two subbands. The highest concentration spectrum consists of three gaussian subbands that closely coincide with the three subbands that have been observed before for pure NMA [67]. At the lowest concentration the spectrum consists primarily of a single asymmetric band centered at 1690 $cm^{-1}$ with a tail towards lower frequencies. We fitted this spectrum with a function which is a product of two profiles: a gaussian and a lorentzian (centered at different frequencies) with an 80% contribution of the lorentzian function [33]. This function allows for a description of the asymmetry of the observed line shape. We used this latter band in combination with the three gaussian subbands observed at the highest concentration in a global fit of all seven spectra. In this fit the po-

Table I. Summary of the spectral positions of oligomers.

| Species | Position [cm$^{-1}$] | FWHM $\Delta\nu$ [cm$^{-1}$] |
|---------|---------------------|------------------------------|
| Monomers | 1690 | $\sim$26 |
| Dimers | 1670 | $\sim$24 |
| Trimers | 1655 | $\sim$19 |
| Tetramers | 1640 | $\sim$26 |

sition and spectral widths of the subbands are kept constant throughout the concentrations and only the amplitudes have been varied. A separate fit at each concentration showed that the frequency shifts of the four subbands for all concentrations are small ($<$3 cm$^{-1}$) with respect to the separation between the subbands ($\sim$15 cm$^{-1}$) and thus can be neglected. Similarly, the widths of the fitted subbands at each concentration are very similar and differ only by $\sim$4 cm$^{-1}$ with respect to the average width of $\sim$24 cm$^{-1}$. Therefore, the spectra at all concentrations can be desribed with the same 4 subbands. The fitted central frequencies of the subbands and their spectral widths are summarized in table I. The fitted bands used to reconstruct the linear spectra are shown in figure 6.2 (thin lines).

In agreement with previous experimental and theoretical studies we assign the four subbands to monomers, dimers, trimers and tetramers [63, 67, 158]. The absolute positions of the bands differ somewhat between the different studies because different solvents and molecular dynamics algorithms have been used. The fitted central frequencies of the bands correspond well to those found in QCE (Quantum Cluster Equilibrium) simulations [100] and a 2D spectroscopy study on pure NMA [119].

The precise assignment of the 1640 cm$^{-1}$ and 1655 cm$^{-1}$ subbands is a topic of debate. Krimm at al., based on the polarization resolved Raman spectroscopy, showed that for neat NMA the presence of the two subbands may be the result of a frequency splitting (so called noncoincidence effect - NCE) within one subband due to transition dipole coupling between the NMA molecules involved in an oligomer [29]. For the present study it is important that both bands represent trimers and larger oligomers.

The fit yields the amplitudes of the sub-bands at each concentration. Assuming that the cross-section per NMA molecule is the same for each sub-band, we can thus estimate the relative amount of each species at all concentrations. As shown in figure 6.3, the monomers are most abundant at the lowest concentration (1:1000), accounting for almost 90% of all NMA present. This distribution however changes quickly with increasing concentration and at a concentration of 50 mM all species are almost equally present. At the highest concentration of 5 M (1:1), the monomers are no longer observable. The resemblance between our spectrum at the highest concentration and the spectrum reported by Huang for pure NMA [67], shows that for a 1:1 solution of NMA in CCl$_4$ the oligomer distribution is similar to that of pure NMA. However, here it should be noted
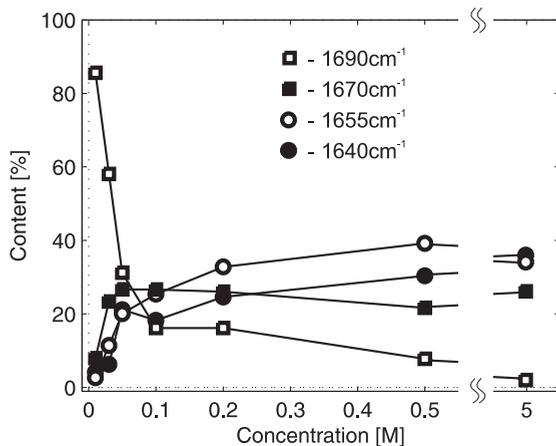
FIGURE 6.3. Contribution of different NMA aggregate sizes to the absorption spectra measured at different concentrations of NMA in $CCl_4$. Closed circles - 1640 cm$^{-1}$ ($\geqslant$tetramers); open circles - 1655 cm$^{-1}$ (trimers); closed squares - 1670 cm$^{-1}$ (dimers); open squares - 1690 cm$^{-1}$ (monomers).

that the most red shifted band not only contains the NMA tetramers but all oligomers consisting of four and more NMA molecules.

The distribution of NMA oligomers is very sensitive to the temperature. Figure 6.4 shows a linear spectrum of 50 mM NMA solution at three different temperatures. Upon increasing the temperature, the hydrogen bonds between the NMA molecules become weaker and break, causing almost all of the oligomers to dissociate into monomers at about 56° C. This sensitivity of the NMA oligomer size on temperature should be accounted for in the interpretation of the pump-probe data, as we will discuss in the following.

## 6.3.2   Vibrational energy relaxation

### Exciting the amide I mode
Figure 6.5 shows the transient spectral response in the frequency region of the AI and AII modes at different delays after excitation of the AI mode. The most prominent changes are observed at the mode that is being pumped, i.e. the AI mode. At early delays the AI spectrum shows the characteristic transient spectral shape of an excited anharmonic vibration with a negative signal at frequencies around 1660 cm$^{-1}$ originating from the bleaching of the $v = 0 \to 1$ transition, and a positive signal around 1625 cm$^{-1}$ due to the induced $v = 1 \to 2$ transition absorption from the $v = 1$ excited state. With increasing delay time these signals decay and the shape of the transient spectrum invert. After a few tens of picoseconds we observe a positive signal on the blue side of the AI absorption band and a negative signal on the red side of this band. This shape of the transient spectrum implies a blue shift of the absorption band of the AI mode and forms a characteristic signature of an increase in sample temperature. The
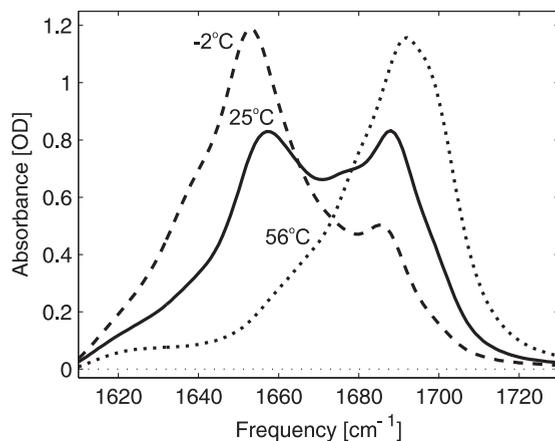
FIGURE 6.4. Linear absorption spectra of a solution of 50 mM NMA in CCl$_4$ (1:200) at three different temperatures.

blue shift of the absorption band reflects the weakening of the hydrogen bonds, caused by the eventual relaxation and dissipation of the vibrational excitation of the AI mode into heat. At late delays ($>40$ ps) we observe an additional small change of the transient spectrum: both the negative signal around 1650 cm$^{-1}$ and the positive signal between 1670 - 1680 cm$^{-1}$ increase somewhat further. In the frequency region between 1640 and 1650 cm$^{-1}$ the transient spectra show a quite irregular structure. This structure is closely connected to the asymmetric shape of the linear absorption spectrum of the AI mode. This spectrum shows a significant shoulder at 1640 cm$^{-1}$ corresponding to the absorption of the tetrameric (and higher order) aggregates (see figure 6.2, left spectrum). At early delays, the bleaching of the fundamental transition of the tetramers overlaps with the induced 1→2 absorption of the smaller oligomers and monomers, leading to an irregular structure. At later delay times, the heating of the sample results in a decrease of the concentration of tetramers and an increase of the concentrations of smaller oligomers and monomers. Again the signals of these two contributions overlap and produce an irregular structure of the transient spectrum.

The frequency region near the AII mode shows a very different response after excitation of the AI mode. At early delays, we observe a negative signal at the blue side of the spectrum and a positive signal at the red side. Since the pump spectrum has been tuned to excite only the AI mode, this signal cannot be due to direct excitation of the AII mode. With increasing delay we observe a slight increase of both the negative and positive signals. The signal at late delay times again corresponds to the effect of an increase in temperature, now on the absorption spectrum of the AII mode. For this mode, a temperature increase results in a red-shift of the absorption spectrum, which in the transient spectrum corresponds to a negative absorption change in the blue wing and a positive absorption change in the red wing of the absorption spectrum.
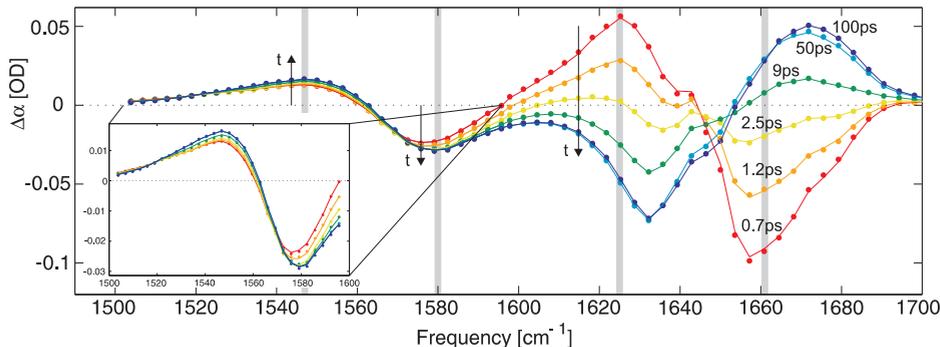
Figure 6.5. Transient spectra at different delay times following excitation of the amide I mode of NMA for a solution of 5 M NMA in CCl$_4$.

In figure 6.6 we present delay traces (dots representing the data points) taken at four frequencies marked on figure 6.5 with vertical grey bars. These frequencies correspond to the centers of the negative and positive parts of the signal for the AI and AII modes. For clarity the two traces of the AII mode were scaled and an offset was added. It is clear from the data that the dynamics of the two modes are different. The traces corresponding to the AII mode show slow dynamics (∼10 ps), whereas the data for AI show fast dynamics at early delays (∼1 ps) and much slower dynamics at later delays (∼10 ps).

Exciting the amide II mode
In figure 6.7 we show the transient spectral response of both the AI and AII modes after excitation of the AII mode. At frequencies corresponding to the excited AII mode, we observe a bleaching signal of the fundamental 0→1 transition and an induced absorption of the 1→2 transition at early delays. This signal appears to shift towards higher frequencies with increasing delay time. After about 10 ps, the AII spectrum does not change anymore, meaning that the AII mode has reached an equilibrated thermal state. At the AI mode frequencies, we observe a small signal at early delays (<1 ps) with a shape similar to the spectral shape observed at 2.5 ps in case the AI mode was excited (see figure 6.5). The latter signal is followed by the ingrowth of the thermalization signal. Similarly to the case when we pumped the AI mode, we again observe minor spectral changes at later delays in the center and blue side of the AI mode spectrum. No spectral changes at late delays are visible for AII mode.

Figure 6.8 presents delay traces at four frequencies marked with thin, grey vertical bars in figure 6.7. The two traces corresponding to the AI mode show a steady ingrowth in time and are very much alike. The traces corresponding to the AII mode show much faster dynamics at early delays. At later delays (>4 ps) the dynamics become much slower.

Interpretation
After excitation of the $v = 1$ state of the AI mode, the bleaching of the 0→1
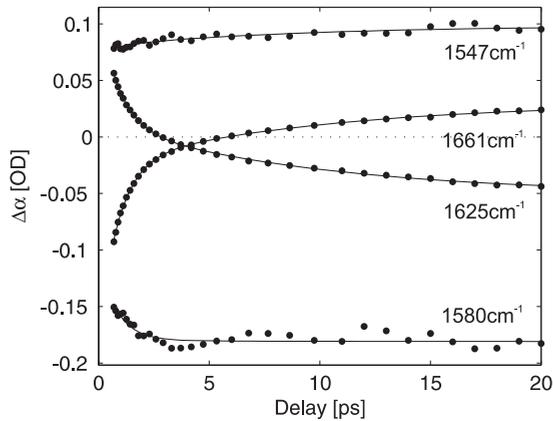
FIGURE 6.6. Time traces at four different frequencies corresponding to four grey vertical bars shown in figure 6.5. The time traces at 1547 and 1580 cm$^{-1}$ have been multiplied by 6 and offset was added for clarity.

transition and the induced absorption of the 1→2 transition of the AI mode rapidly decay with a time constant of ∼1 ps (figure 6.6). This rapid decay is followed by a much slower rise of a spectral signature that corresponds to a thermal difference spectrum. Hence, the vibrational relaxation of the $v = 1$ state of the AI mode does not directly lead to a heating effect. This heating effect is delayed, indicating that the excitation energy resides in a non-thermal intermediate state before thermalization occurs. The thermal difference spectrum shows a slow further evolution at time scales >40 ps.

After excitation of the AI mode, the AII mode directly shows a response that has the signature of an anharmonic shift. Due to the excitation of the AI mode, the frequency of the (unexcited) AII mode decreases, leading directly to an increased absorption in the red wing and a bleaching in the blue wing of the AII mode. There is no response of the AII mode rising with the vibrational lifetime of the AI mode, indicating that the vibrational relaxation of the AI mode does not involve energy transfer to the AII mode. At later times, the transient spectrum of the AII mode shows a small increase with the same time constant that is observed for the rise of the thermal difference spectrum in the frequency region of the AI mode.

Based on these observations we model the data using a four state consecutive model. Each state has an associated spectrum and the time evolution of these spectra is described with rates $k_1$, $k_2$ and $k_3$. The occupation of each of the states in time is described by a set of rate equations:

$$
\frac{d}{dt}
\begin{pmatrix}
N_1(t) \\
N_2(t) \\
N_3(t) \\
N_4(t)
\end{pmatrix}
=
\begin{bmatrix}
-k_1 & 0 & 0 & 0 \\
k_1 & -k_2 & 0 & 0 \\
0 & k_2 & -k_3 & 0 \\
0 & 0 & k_3 & 0
\end{bmatrix}
\begin{pmatrix}
N_1(t) \\
N_2(t) \\
N_3(t) \\
N_4(t)
\end{pmatrix}.
\tag{6.1}
$$
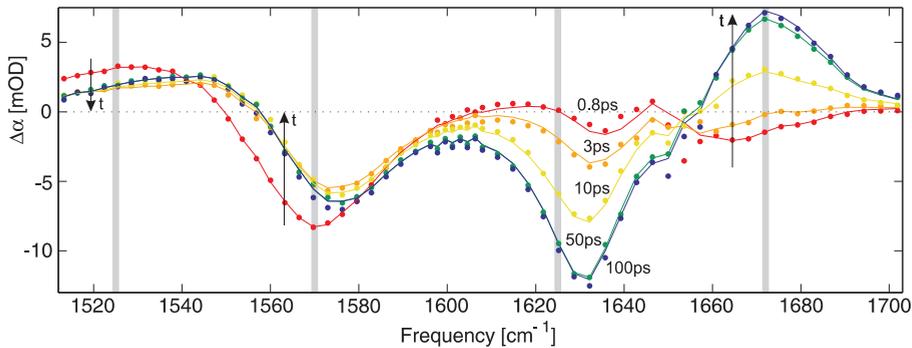
FIGURE 6.7. Transient spectra at different delay times following excitation of the amide II mode of NMA for a solution of 5 M NMA in CCl$_4$.

These rate equations are solved using a method described elsewhere [156]. The transient spectra at all delay times are the sum of the time-dependent populations times the associated spectra:

$$\Delta\alpha(t,\nu) = \sum_n N_n(t)\sigma_n(\nu)\,. \tag{6.2}$$

The fitted lifetimes for the consecutive states are shown in table II.

The results of the fits are represented as lines in figures 6.5 and 6.6. From the fits we extracted the spectra associated with the different states, as shown in figure 6.9.

The black line in figure 6.9 is the transient spectrum associated with the first level, i.e. the excited $v = 1$ state of AI. This spectrum shows a bleaching of the 0→1 transition and an induced absorption of the 1→2 transition. In the frequency region of the AII mode this spectrum shows an increased absorption in the red wing and a bleaching in the blue wing. These spectral changes show that the excitation of the AI mode leads to a direct anharmonic red shift of the frequency of the AII mode. The red side of the induced 1→2 transition of the AI mode overlaps with the blue wing of the AII mode. As a result, the dynamics at frequencies around 1580 cm$^{-1}$ (figure 6.6) are quite complicated.

The $v = 1$ state of the AI mode relaxes with T$_1$ = 0.85 ± 0.1 ps to a non-thermal intermediate state which has the spectrum represented by the red

TABLE II. Summary of the dynamic parameters of 5 M NMA in CCl$_4$

| Excited | Probed | T$_1$ [ps] | T$_2$ [ps] | T$_3$ [ps] | $\tau_r$ [ps] |
|---------|--------|-----------|-----------|-----------|---------------|
| AI | AI/AII | 0.85±0.1 | 10±1 | ∼85 | ∼6 |
| AII | AI/AII | 0.6±0.1 | 9±1 | ∼40 | ∼7 |
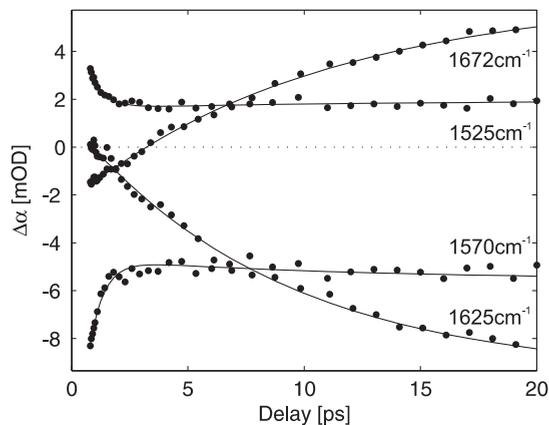
FIGURE 6.8. Time traces at four different frequencies corresponding to four vertical grey bars shown in figure 6.7.

line. This spectrum shows very little response in the frequency region of the AI mode, meaning that the absorption spectrum of the AI mode starting from the non-thermal intermediate state is very similar to the absorption spectrum of the AI mode before the excitation. In the frequency region of the AII mode, the transient spectrum of the non-thermal intermediate state is quite similar to that associated with the excited $v = 1$ state of AI.

The non-thermal intermediate state relaxes with $T_2 = 10 \pm 1$ ps to the third level that corresponds to a local hot state. In the frequency region of the AI mode, an increase in temperature leads to a blue shift of the absorption spectrum, corresponding to an absorption decrease in the red wing of the AI absorption spectrum and an increase in the blue wing of this spectrum. For the AII mode an increase in temperature results in a red shift, and the associated transient spectrum thus shows an increased absorption in the red wing and a decreased absorption in the blue wing of the AII absorption band. The transition from the non-thermal intermediate state to the local hot state leads to a small increase of the induced absorption in the red wing of the AII mode. This increase shows that the heating effect induces a somewhat larger redshift of the AII mode than the anharmonic coupling with the AI mode and the non-thermal intermediate state. The local hot level relaxes with $T_3 = 85 \pm 10$ ps to the final fully equilibrated state of which the transient spectrum is represented by the green line. This complete equilibration only leads to observable spectral changes in the frequency region of the AI mode.

The data are very well modeled with a frequency independent $T_1$ of the AI mode. This shows that there is no significant variation of the excited state lifetime over the different subbands that correspond to different oligomers.

Excitation of the $v = 1$ state of the AII mode leads to a similar relaxation scheme as is observed after excitation of the AI mode. The extracted lifetimes are
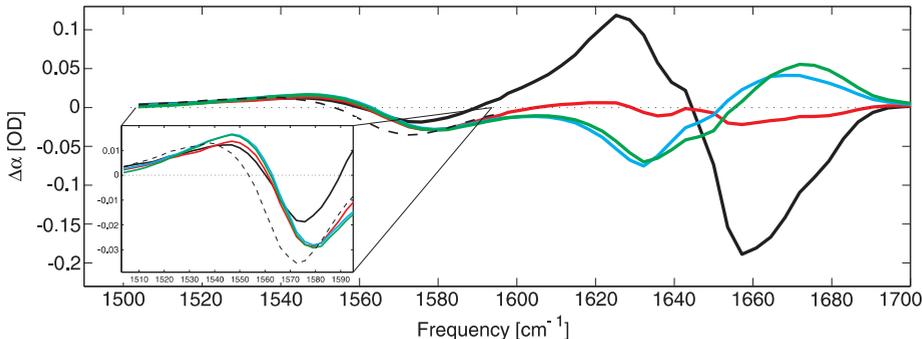
FIGURE 6.9. Extracted transient spectra corresponding to the four different states reached in the excitation and vibrational relaxation of the amide I vibration of NMA. For comparison the transient spectrum directly following excitation of the amide II mode is shown (dashed black line).

shown in table II. The result of the fit is shown with the solid lines in figures 6.7 and 6.8. The transient spectra that describe the spectral dynamics are illustrated in figure 6.10. The black line represents the transient spectrum associated with the excitation of the $v = 1$ mode of AII. This spectrum shows a bleaching of the 0→1 transition and an induced absorption of the 1→2 transition. It is noteworthy that the frequency difference between these two transitions is substantially larger (by $\sim 10$ cm$^{-1}$) than the difference between the positive and negative signals originating from the anharmonic shift of the AII absorption frequency induced by the excitation of the AI mode (see inset in figure 6.9). This notion confirms that the transient spectral shapes observed in figure 6.9 in the frequency region of the AII mode are not due to ultrafast energy transfer from the excited $v = 1$ state of the AI mode to the $v = 1$ state of the AII mode.

The transient spectrum associated with the $v = 1$ state of the AII mode does not show a strong response in the frequency region of the AI mode. The transient spectrum (black line) indicates the presence of a small anharmonic red shift of the AI absorption frequency upon excitation of the AII mode.

The $v = 1$ state of the AII mode relaxes with $T_1 = 0.65 \pm 0.1$ ps to a non-thermal intermediate state. The spectrum associated with this state (red line in figure 6.10) is similar to the transient spectrum observed for the non-thermal intermediate state in the relaxation of the AI mode. This suggests that the non-thermal intermediate state is composed of the same vibrational excitations in both cases. The non-thermal intermediate state relaxes to the local hot state with $T_2 = 9.5 \pm 1$ ps. This time constant is quite similar to the relaxation time constant of the non-thermal intermediate state in the relaxation of the AI mode, supporting the idea that the non-thermal intermediate state is the same in both cases. The local hot state relaxes to a fully equilibrated state with $T_3 = \sim 40$ ps. The transient spectrum of the local hot state and fully equilibrated state are also quite similar to what was observed after excitation of the AI mode. The transition to the fully equilibrated state again only leads to changes in the
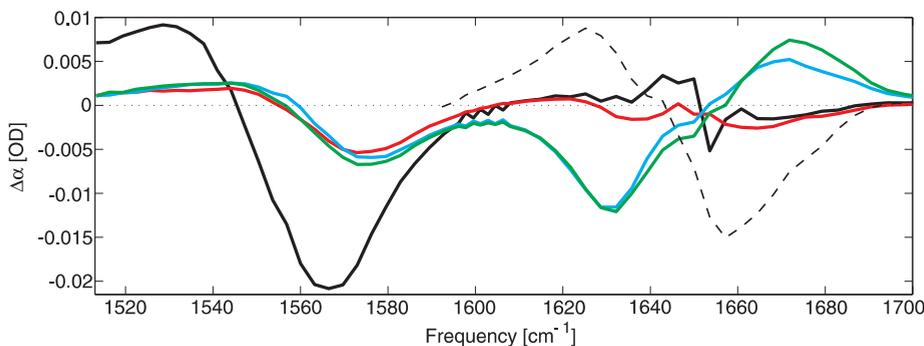
FIGURE 6.10. Extracted transient spectra corresponding to the four different states reached in the excitation and vibrational relaxation of the amide II vibration of NMA. For comparison the transient spectrum directly following excitation of the amide I mode is shown (dashed black line).

spectrum in the frequency region of the AI mode.

Figure 6.11 summarizes the observed relaxation pathways upon selective excitation of either AI or AII mode.

DISCUSSION

The AI mode shows much stronger changes in its transient spectral response during the vibrational relaxation than the AII mode. This stronger response can be explained from the fact that the frequency shifts of the AI mode at different stages of the relaxation have opposite signs. The excitation of the $v = 1$ state leads to a red shifted 1→2 induced absorption of the AI mode, whereas the relaxation to the local hot state and the final equilibrated state lead to a blue shift of the absorption of this mode. For the AII mode, heating and thus the final thermalization process of the relaxation results in a red shift of the absorption spectrum [67, 100, 119]. Hence, for this mode, both the transient spectral response directly after excitation of its $v = 1$ state, and the final response resulting from the thermalization are formed by red shifts. In addition, the non-thermal intermediate state also induces an anharmonic red shift of the absorption spectrum of the AII mode. Hence, at all stages the transient response of the AII mode is similar, making the changes in the transient spectral response during the relaxation relatively small. Nevertheless, there are changes in the spectral response during the relaxation as the transient spectral response of the 1→2 induced absorption of the AII mode is not the same as the change in spectral response resulting from the heating of the sample.

We observe quite similar relaxation mechanisms following excitation of the AI and the AII mode. In neither case we observe direct energy transfer between the AI and AII modes. The observed spectral signatures at early delays indicate the presence of an anharmonic coupling between the excited and the unexcited mode, in both cases leading to a red shift of the absorption spectrum of the unexcited mode. One possible reason for the lack of energy transfer between
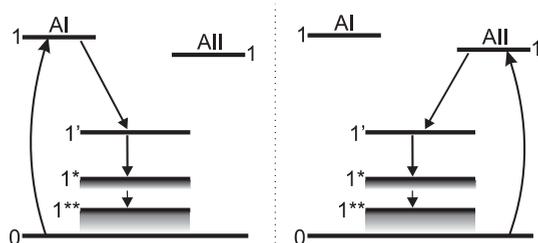
FIGURE 6.11. Energy level diagram and vibrational energy relaxation pathways of NMA upon excitation of the amide I mode (left panel) and excitation of the amide II mode (right panel).

AI and AII modes could be the formation of NMA clusters. The presence of hydrogen bonds in these clusters strongly increases the density of potentially accepting vibrational states. Hence, the relaxation of the excited $v = 1$ states to combination tones of lower-energy intra- and intermolecular vibration can be very efficient, thus preventing the energy transfer between the $v = 1$ states of the AI and AII modes.

There have been a few earlier experimental [36, 137] and theoretical [18, 57, 176] studies of the energy dynamics of the amide modes of NMA. DeFlores *et al.* [36] reported the occurrence of rapid vibrational equilibration between the AI and AII modes for hydrogen bonded NMA (NMA in $D_2O$ and in DMSO). These results were confirmed by results of molecular dynamics (MD) simulations [18], which found the population exchange time between the modes to be $\sim$0.5 ps. Interestingly, in two other MD simulation studies no energy transfer between the $v = 1$ states of the AI and AII modes was found. Instead, independently of which mode is excited (AI or AII), the vibrational energy is found to be directly transferred to lower frequency modes and then to the solvating bath [57, 176]. Clearly, these latter results are very much in line with the present experimental data.

The transient spectra shown in figures 6.9 and 6.10 contain some clues as to the nature of the non-thermal intermediate state. The fact that the occupation of this state leads to significant spectral changes in the frequency region of the AII mode, suggests that this state must comprise excitations of vibrational modes that are quite strongly anharmonically coupled to the AII mode. Similarly, the fact that the intermediate state has less effect on the AI mode suggests that the latter mode is of quite different character. The contributions of the different local modes of NMA to the amide normal modes have recently been determined with potential energy distribution calculations (PED),both for isolated NMA and hydrogen bonded NMA [29, 63, 114, 176]. Since the AI mode is dominated by the C=O stretch vibration ($\sim$80%) [106, 107, 114, 176], the non-thermal intermediate state likely does not contain much of this vibrational character. We can thus exclude the amide IV ($\sim$615 - 630 cm$^{-1}$) mode containing about 40% of C=O rocking mode character and the amide VI ($\sim$605 - 630 cm$^{-1}$) mode containing about 80% of C=O out-of-plane bending mode

character. The AII mode is of strongly mixed character and thus there are quite a few low-frequency modes (AIII, AV-AVII) that can efficiently couple to it. It is therefore likely that the non-thermal intermediate state represents excitations in modes other than the AIV and the AVI modes. The most feasible is the AIII mode, which, as shown in the MD simulations can act as a vibrational energy acceptor for either excited AI or AII modes [176].

The second time scale $T_2$ of ~10 ps found in the relaxation processes is assigned to the equilibration time between the non-thermal intermediate state (particular low-frequency modes excited) and the thermal excitation of the directly surrounding solvent molecules. A similar value of ~9 ps was found for the equilibration time between an excited dye molecule and tetrachloroethylene [34] which is similar to the carbon-tetrachloride which is used as a solvent in our experiments. In the present study we observe that the thermalization is not complete after the relaxation process with $T_2$ of ~10 ps. We observe an additional equilibration step with time constant $T_3$ representing the transition from a local hot state to the truly thermally equilibrated state of the solution (dashed line in figure 6.12). In this state the distribution of NMA clusters has completely adapted to the increased temperature in the focus.

The final equilibration process is observed to have a much stronger influence on the absorption spectrum of the AI mode than on the AII mode. This observation can be explained from the influence of the hydrogen-bond interaction on the spectrum of the two amide modes. The NMA molecules are hydrogen bonded via their N-H (hydrogen-bond donor) and C=O (hydrogen-bond acceptor) groups. A change in the strength of the hydrogen-bond interaction will thus most strongly influence the spectral response of the amide vibrations that possess strong N-H stretch or C=O stretch vibrational character. The AI mode possesses very strong C=O stretch vibrational character, and thus the weakening of the hydrogen-bond, as will occur in both the second and third relaxation process, will have a strong influence on the absorption spectrum of this mode. In contrast, the AII modes possesses neither strong N-H stretch nor C=O stretch vibrational character, thereby making this mode much less susceptible to changes in the hydrogen-bond interaction.

### 6.3.3   Thermalization dynamics

To investigate the thermalization processes following vibrational relaxation in more detail we performed a few additional experiments. In one experiment, we excited both the AI and AII modes with an intense broadband, high-energy pump pulse. We probe the AI mode, as this mode shows the strongest effects of the thermalization dynamics. As shown in figure 6.5, we observe a slow signal ingrowth in the center and blue wing of the AI absorption band in the delay time range between 30 ps and 100 ps. We fit the data with the same 4 level consecutive relaxation model that we used in the modeling of the 2D experiments. The two final extracted spectra are shown in figure 6.12. For comparison we also include a differential linear spectrum (solid thick line in figure 6.12) of the sample measured at two different temperatures. The differential linear spectrum shows a very good correspondence with the final thermal spectrum, thereby
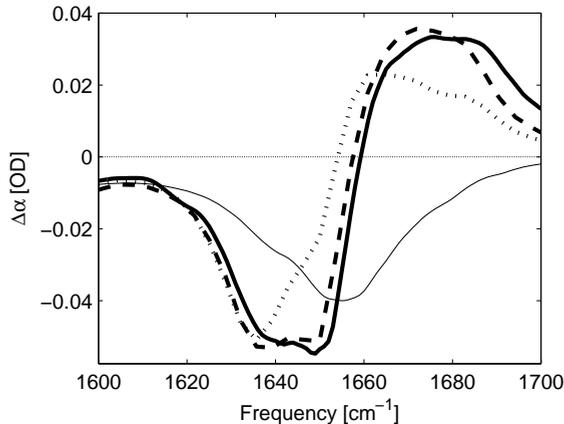
FIGURE 6.12. Spectra of the local hot state (dotted line) and final equilibrated state (dashed line) of NMA measured after broad-band infrared excitation of the amide I and amide II vibrations of NMA for a solution of 5 M NMA in $CCl_4$. The thick solid line represents the differential linear absorption spectrum obtained by subtracting linear absorption spectra at different temperatures. The thin solid line represents the linear absorption spectrum at 300 K.

confirming that the fourth state in the relaxation model indeed corresponds to a fully thermally equilibrated state. It is known from linear infrared spectroscopic studies that NMA clusters dissociate into smaller sizes upon an increase in temperature. We therefore attribute the change in the spectral response to the dissociation of NMA aggregates into smaller forms. The positive absorption signal at 1670 - 1680 $cm^{-1}$ is thus caused by the production of non-hydrogen bonded NMA and the bleach at $\sim$1650 $cm^{-1}$ reflects the disappearance of NMA dimers, trimers and larger oligomers.

In a second experiment, we studied the dependence of the thermalization dynamics on the nature of the excited NMA oligomer. In this experiment, we have selectively excited either dimers or tetramers and higher-order clusters with a spectrally narrow pump ($\Delta\nu = \sim$10 $cm^{-1}$) centered at 1675 $cm^{-1}$ or 1630 $cm^{-1}$, respectively. We found the time evolution and the spectral changes to be exactly the same. This observation shows that at the stage of the local hot state the energy is already quite delocalized over different NMA clusters. Hence, the last relaxation process with time constant $T_3$ does not represent an energy redistribution process but rather a repositioning of the NMA molecules, i.e. the partial dissociation of the NMA aggregates.

In a final experiment, we measured the relaxation dynamics at different initial sample temperatures, again using an intense broadband infrared excitation pulse. We observe that the lifetimes of the excited $v = 1$ and non-thermal intermediate states do not change with temperature. At all temperatures we obtain $T_1 = 1.1 \pm 0.1$ ps and $T_2 = 12 \pm 1$ ps. However, the time constant $T_3$ of the transition from the local hot state to the final fully equilibrated state is
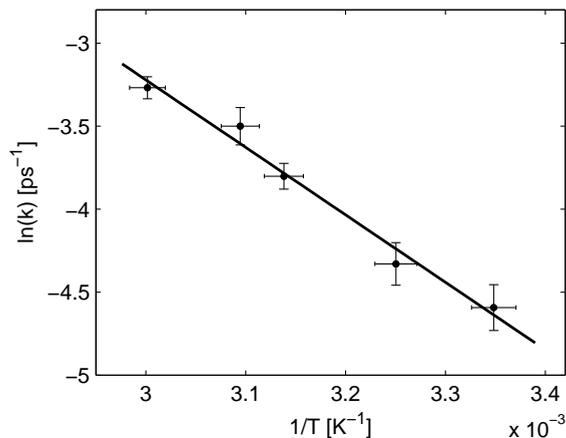
FIGURE 6.13. Arrhenius plot of the time scale $T_3$ of the final relaxation process after broad-band infrared excitation of the amide I and amide II vibrations of NMA for a solution of 5 M NMA in $CCl_4$.

observed to be strongly temperature dependent. These time constants are used to determine the activation energy of the dissociation process, using Arrhenius law:

$$\ln(k) = \ln(A) - \frac{E_a}{R} \cdot \left(\frac{1}{T}\right), \tag{6.3}$$

where $k$ is measured dissociation rate, $A$ is a pre-exponential factor, $R$ is the gas constant and $E_a$ is the activation energy. Figure 6.13 shows the dependence of the dissociation rate on the temperature. The slope of the fitted linear function gives the activation energy for the dissociation process $E_a = 35 \pm 3$ kJmol$^{-1}$.

The activation energy for the dissociation process represents the energy barrier to move two hydrogen-bonded NMA molecules apart and will be similar to the binding energy of the hydrogen bond with which the two NMA molecules are connected. In a strongly interacting solvent the activation energy could be somewhat lower than the binding energy of the hydrogen bond if the dissociation of the hydrogen bond would directly allow new favorable interactions between the NMA molecules and the solvent. However, in a weakly interacting solvent like $CCl_4$ this effect will be negligible, and thus $E_a$ will be close to the hydrogen bond binding energy. The value of $E_a$ of $35 \pm 3$ kJmol$^{-1}$ is in excellent agreement with previously reported values that are obtained from infrared measurements [129] ($\sim$33 - 38 kJmol$^{-1}$) and dielectric measurements [120] (31.5 kJmol$^{-1}$). In view of the cooperativity of the hydrogen-bond interaction, the hydrogen-bond binding energy $E_H$ will depend on the size of the oligomer and the position within the NMA oligomer. Using infrared spectroscopy Herrebout *et al.* finds average hydrogen-bond binding energies of 31.8 kJmol$^{-1}$, 35.3 kJmol$^{-1}$ and 37.3 kJmol$^{-1}$ for dimers, trimers and tetramers, respectively [63]. Very similar values are reported in molecular orbital simulations [158] and molecular dynamics simulations [75] (dimer: 29 kJmol$^{-1}$, trimer:
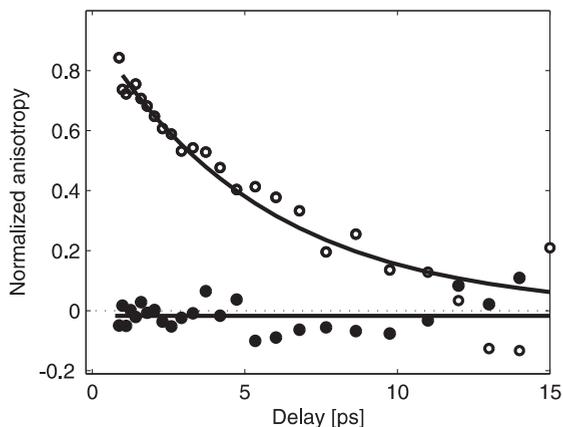
FIGURE 6.14. Anisotropy decays for the amide I mode (open circles) and amide II mode (black circles) following excitation of the amide I mode of NMA for a solution of 5 M NMA in CCl4.

36 kJmol$^{-1}$ and tetramer: 39 kJmol$^{-1}$).

## 6.3.4   Anisotropy dynamics

The polarization resolved pump-probe experiments were used to construct the anisotropy parameter $R(t, \nu)$. Figure 6.14 presents time traces of the anisotropy at the central frequency of the AI mode (open circles) and the central frequency of the AII mode (closed circles), both after excitation of the AI mode. The anisotropy of the AI mode thus reflects the reorientation of the AI transition dipole moment. The anisotropy of the AII mode reflects the relative angle between the transition dipole moment orientations of the two modes. In case the AII mode is excited we observe the same anisotropy dynamics for the excited and unexcited mode (not shown).

The anisotropy of the excited AI mode decays with a time constant of $\tau_{or} = {\sim}6$ ps. This time constant represents the reorientation time of this mode, averaged over all oligomers. This reorientation time is relatively long for a weakly interacting solute-solvent system like NMA-CCl4. However, the NMA molecules are hydrogen-bonded to each other which will strongly slow down their reorientation. A similar value of ${\sim}6$ ps has been reported previously for NMAD (deuterated NMA) in $D_2O$ [60].

The anisotropy of the AII mode is close to zero at all delay times. The anisotropy shows the following dependence on the relative angle $\theta$ between the transition dipole moments of the excited and probed mode:

$$R = \frac{1}{5}(3\cos(\theta)^2 - 1).$$  (6.4)

From equation 6.4 it follows that the observed AII anisotropy can be zero

only at all delay times for $\theta$ very close to the 'magic angle' (54.7°). The observed anisotropy traces thus imply that the average angle between the transition dipole moment orientations of AI and AII amounts to $55° \pm 3°$. This angle agrees with the angle found previously for both bonded and non-bonded NMA [36]. Hence, upon clustering/hydrogen bonding of the NMA molecules the angle between the transition dipole moment orientations of the AI and AII modes does not change, which indicates that the contributions of the different local modes to these amide modes is not strongly affected by the hydrogen bonds between the NMA molecules.

## 6.4    CONCLUSIONS

We studied the vibrational absorption spectra and energy relaxation dynamics of N-methylacetamide (NMA) aggregates in carbon-tetrachloride ($CCl_4$) using linear and two-color femtosecond infrared spectroscopy. We measured infrared spectra over a large concentration range ranging from 10 mM to 5 M. With increasing concentration, the absorption spectrum of the amide I mode of NMA is observed to shift towards lower frequencies, indicating the formation of hydrogen-bond clusters. The spectra at all concentrations can be decomposed into four subbands that correspond to NMA clusters of different sizes: monomers (1690 cm$^{-1}$), dimers (1670 cm$^{-1}$), trimers (1655 cm$^{-1}$) and tetramers + higher-order oligomers (1640 cm$^{-1}$).

We observe similar vibrational relaxation pathways following excitation of the amide I and amide II vibrations. In a first relaxation step, the energy is transferred from the excited $v = 1$ state of either vibrational mode to a non-thermal intermediate state. For the amide I mode this process has a time constant $T_1$ of $0.85 \pm 0.1$ ps, for the amide II mode $T_1 = 0.65 \pm 0.1$ ps. We do not observe energy transfer between the amide I and amide II modes. The intermediate state is formed by a combination tone of excited lower-energy vibrational states, and appears to be quite similar in character for amide I and amide II excitation, as evidenced by the similarity in the effects of the occupation of this state on the absorption spectra of the amide I and amide II modes. In both excitation schemes, the occupation of the intermediate state has a much stronger (anharmonic) effect on the absorption spectrum of the amide II mode than on the absorption spectrum of the amide I mode, which shows that this state comprises local vibrational modes that are much more strongly coupled to the amide II mode than to the amide I mode. The intermediate state relaxes in a second process with a time constant $T_2 = {\sim}10 \pm 1$ ps to a local hot state. In this state the energy has been equilibrated over the NMA aggregates and the neighboring solvent molecules. In a third and final relaxation process with time constant $T_3 = 40\text{-}100$ ps, a full equilibration of the sample in the focus takes place. In this latter process the NMA clusters partly dissociate, thus forming the equilibrium aggregate size distribution that corresponds to the new, higher temperature. The measurement of the rate of this final process at different temperatures yields the activation energy of the dissociation of the NMA clusters $E_a = 35 \pm 3$ kJmol$^{-1}$. This energy corresponds to the average binding energy

of a hydrogen bond between two NMA molecules.

We also studied the reorientation time of the NMA molecules and the relative orientation of the transition dipole moments of the amide I and amide II modes using polarization-resolved femtosecond pump-probe measurements. We found that the average reorientation time of the NMA molecules equals 6 ps. The relative angle between the transition dipole moment orientations of the amide I and amide II modes $\theta$(AI,AII) is $56° \pm 3°$.

# 7 VIBRATIONAL RELAXATION PATHWAYS OF AI AND AII MODES IN N-METHYLACETAMIDE

We studied the vibrational energy relaxation mechanisms of the amide I and amide II modes of N-methylacetamide (NMA) monomers dissolved in bromoform using polarization-resolved femtosecond two-color vibrational spectroscopy. The results show that the excited amide I vibration transfers its excitation energy to the amide II vibration with a time constant of 8.3±1 ps. The transfer from the excited amide II to the amide I mode has a time constant of 16.6±2 ps. In addition to this energy exchange process, we observe that the excited amide I and amide II vibrations both relax to a final thermal state. For the amide I mode this latter process has a time constant of ∼1.5 ps and dominates the vibrational relaxation of this mode. We further find that the vibrational relaxation of the amide I mode depends on frequency which can be well explained from the presence of two sub-bands with different vibrational lifetimes in the amide I absorption spectrum.

## 7.1 INTRODUCTION

The amide motif (O=C–N–H) is extremely important in living systems as it forms the building block of the backbone of proteins. The structural dynamics of this backbone play a crucial role in the folding and functional conformational dynamics of proteins. These dynamics are very much dependent on the hydrogen-bond interactions among the amide moieties and their interactions with surrounding and solvating molecules like water.

An excellent system for studying the properties of the amide motif is N-methylacetamide (NMA). This molecule forms hydrogen bonds with other NMA molecules which mimic well the intra- and interchain hydrogen-bonding interactions of the backbones of proteins [170]. NMA has thus been widely used to investigate the properties of the amide motif in various molecular environments.

The vibrational relaxation dynamics of the amide modes of NMA have been studied before with infrared vibrational spectroscopy [35, 36, 60, 173] and with

molecular dynamics simulations [18, 83, 157, 176]. All previous studies of the vibrational dynamics of NMA showed that the amide vibrations relax via intramolecular energy transfer, irrespective of the solvent used. The highest frequency amide vibration, amide I, with a frequency of $\sim 1650$ cm$^{-1}$, is always found to relax in two subsequent steps. The first step involves intramolecular energy transfer from the amide I mode to lower frequency amide modes, and the second step involves the further redistribution of the vibrational energy among low frequency intra- and intermolecular modes, leading to a complete thermalization of the vibrational energy.

DeFlores *et al.* studied the vibrational relaxation mechanism of NMA in D$_2$O and DMSO with two-dimensional vibrational spectroscopy. In both solvents they observe a rapid energy exchange and equilibration between the amide I and the amide II modes. This rapid energy redistribution is followed by a much slower relaxation process that leads to thermalization of the vibrational energy. Interestingly, we did not find any evidence of energy transfer between the amide I and amide II vibrations for hydrogen-bonded NMA clusters dissolved in carbontetrachloride (see previous chapter). We observed that both the amide I and the amide II mode directly relax on a time scale <1 picosecond to lower frequency intramolecular modes.

The hydrogen-bonded NMA clusters of the previous chapter formed a good model for the helical parts of proteins for which the amide motifs of the aminoacids are connected via hydrogen bonds. So far no experimental work has been reported on the relaxation pathways of isolated non-bonded NMA molecules. Here we study the relaxation mechanisms of the amide I and amide II vibrations of isolated NMA molecules using polarization-resolved femtosecond two-color pump-probe spectroscopy.

## 7.2   Experiment

The polarization-resolved two-color pump-probe experiment employs femtosecond mid-infrared pulses that are generated with the laser system and frequency conversion processes described in sections 3.1 and 3.2. The generated pulses are centered at $\sim 1600$ cm$^{-1}$ ($\sim 6$ $\mu$m), have a pulse energy of $\sim 60$ $\mu$J, a pulse duration of $\sim 55$ fs and a spectral bandwidth of $\sim 350$ cm$^{-1}$.

As in the previous chapter, we excite the amide vibrations with narrowband pump pulses that are obtained by spectrally filtering the broadband mid-infrared pulses with a Fabry-Pérot filter. The thus obtained pump pulses have a bandwidth of $\sim 50$ - $60$ cm$^{-1}$ and a pulse energy of $\sim 6$ $\mu$J.

The pump pulse excites either the amide I (AI) or amide II (AII) vibration of NMA, thereby promoting either vibration from its ground state $\nu = 0$ to the first excited state $\nu = 1$. This excitation results in ground-state depletion and stimulated emission $\nu = 1 \rightarrow 0$, thus leading to a decrease in absorption (bleaching) at frequencies corresponding to the $\nu=0\rightarrow1$ transition. Simultaneously, the population of the $\nu = 1$ state leads to an induced absorption at frequencies corresponding to the $\nu=1\rightarrow2$ transition. A detailed description of the pump-probe setup can be found in section 3.3.
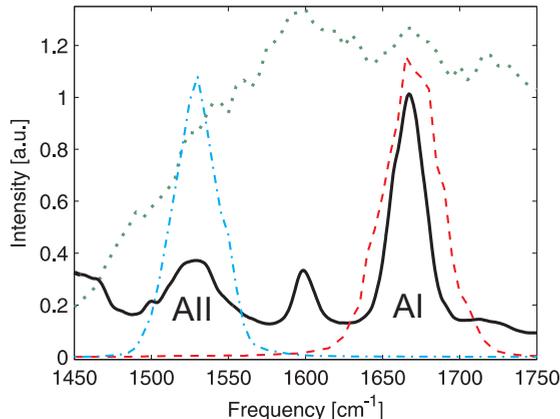
Figure 7.1. Experimental spectra of the probe pulse (dotted) and the two pump pulses used to excite either the amide I or amide II mode of the NMA molecule (dashed and dashed-dotted lines, respectively). The solid line represents the absorption spectrum of a 10 mM solution of NMA in CHBr$_3$.

The sample is a $\sim$10 mM solution (1:1000 molar ratio) of NMA in bromoform (CHBr$_3$). The advantage of using bromoform over carbontetrachloride is that there are no vibrational resonances overlapping with the amide modes. For highly diluted solutions as studied in this chapter, the weak vibrational mode of CCl$_4$ at $\sim$1530 cm$^{-1}$ overwhelms the AII absorption band . Bromoform possesses a weak absorption at $\sim$1600 cm$^{-1}$ in between the absorption bands of the AI and AII modes. Hence, these amide modes can be excited without exciting the solvent molecules. The sample is contained in an infrared sample cell consisting of two 2 mm thick CaF$_2$ windows and a 1.2 mm thick teflon spacer.

## 7.3　Results and discussion

### 7.3.1　Linear spectra

In figure 8.4 we show the linear absorption spectrum of a solution of 10 mM NMA in bromoform (CHBr$_3$). The two amide modes are centered at $\sim$1665 cm$^{-1}$ (AI) and $\sim$1535 cm$^{-1}$ (AII). The small absorption band centered at 1600 cm$^{-1}$ originates from the solvent. At this low concentration only NMA monomers will be present in solution. The AI absorption band is somewhat asymmetric with a shoulder on the lower frequency side. The AII band is weaker ($\sim$1/5) and somewhat broader than the AI band. The central frequency of the AI mode ($\sim$1665-1670 cm$^{-1}$) is redshifted with respect to the central frequency of the AI mode of NMA dissolved in carbon tetrachloride ($\sim$1690 cm$^{-1}$) at the same concentration. This difference likely results from the dipole-dipole interaction between the NMA molecule and the small ($\sim 3^{-30}$
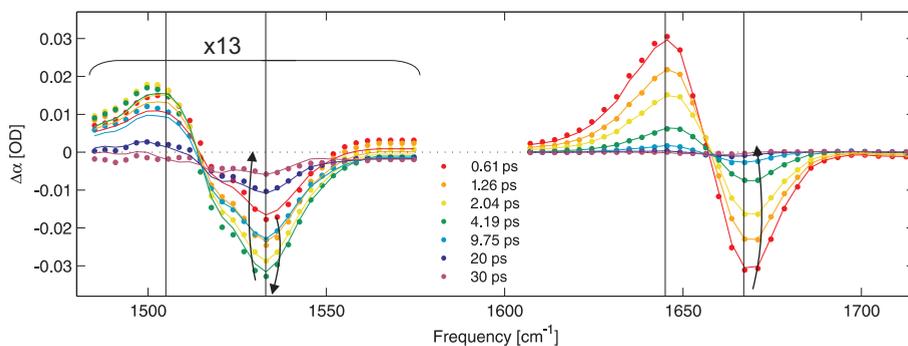
FIGURE 7.2. Transient spectra in the frequency range of the AI and AII modes at different delay times following excitation of the AI mode of a 10 mM solution of NMA in CHBr$_3$. The solid lines represent the results of a fit to the relaxation model described in the text. For clarity, the response of the AII mode has been multiplied by a factor of 13. The arrows indicate the evolution of the spectra in time.

[C·m]) dipole moments of the solvating bromoform molecules. The frequency splitting of the two amide modes is similar to that of hydrogen-bonded NMA clusters in CCl$_4$.

## 7.3.2   VIBRATIONAL ENERGY RELAXATION

EXCITING THE AMIDE I MODE

Figure 7.2 shows transient absorption spectra in the frequency ranges of the AI and AII modes at different delay times after excitation of the AI mode. The spectral response in the AII region has been multiplied by a factor of 13 for clarity. Both the transient spectra of the AI and AII mode are characterized by a negative (bleach) contribution at high frequencies (>1515 and >1660 cm$^{-1}$ respectively) representing the reduced absorption and stimulated emission of the $\nu = 0 \rightarrow 1$ transition, and a positive signal at lower frequencies (<1515 and <1660 cm$^{-1}$), representing the induced $\nu = 1 \rightarrow 2$ absorption. For the AI mode both the bleach and induced absorption decay in time. After ∼30 ps the transient spectrum is nearly zero and does not change anymore with delay time.

The spectral changes in the AII frequency region show very different dynamics from the AI frequency region. At early delay times, up to a delay time of ∼4 ps, the amplitude of the AII transient spectrum increases. For delays larger than ∼4 ps the signal slowly decays. After about 40 ps the transient spectrum does not change anymore. The induced absorption shows a much less pronounced ingrowth than the bleaching.

In figure 7.3 we show delay traces (circles and squares correspond to AI and AII modes, respectively) that are recorded at the frequencies corresponding to the maxima of the bleach and the induced absorption signals of both amide modes. These frequencies are marked with black vertical lines in figure 7.2. It is clear that the dynamics of both modes is very different and involves at least
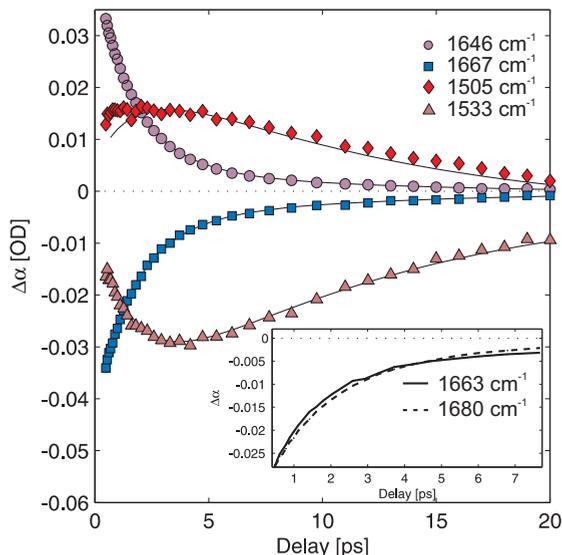
FIGURE 7.3. Time traces recorded at four different frequencies corresponding to the maxima of the bleach and the induced absorption signal of the AI and AII modes. The frequencies are marked with solid vertical lines in figure 7.2. The solid black lines represent the results of a fit to the relaxation model described in the text. In the inset we show time traces of the bleach signal of the AI mode at two different frequencies within the absorption band.

two distinct regimes. The response of the AI mode shows a fast decay at early delays (<4 ps) and a much slower decay at later delays. The response of the AII mode is characterized by two similar rates, however, in contrary to the AI dynamics, the first fast process leads to an ingrowth of the intensity of the AII signal. This process is followed by a decay with the slower rate.

Upon close inspection of the spectral dynamics of the AI mode we observe a frequency dependence of the decay (see inset in figure 7.3). For delays <5 ps the signal in the blue wing of the AI transient spectrum (dashed line) decays slower than the signal in the red wing of the spectrum (solid line). The high frequency side of the transient spectrum decays with a time constant of ∼2 ps, whereas the low frequency side decays faster with a time constant of ∼1 ps. This variation in the dynamics across the AI transient spectrum leads to a transient blue shift of the AI spectral response (the red wing decays faster than the blue wing). At later delays this difference vanishes - the transient signal decays uniformly across the spectrum on a much slower time scale. We did not observe any spectral dependence of the dynamics in the AII frequency region.

EXCITING THE AMIDE II MODE

In figure 7.4 we show transient spectra recorded in the frequency range of the AI and AII modes for a few delay times after excitation of the AII mode. Both
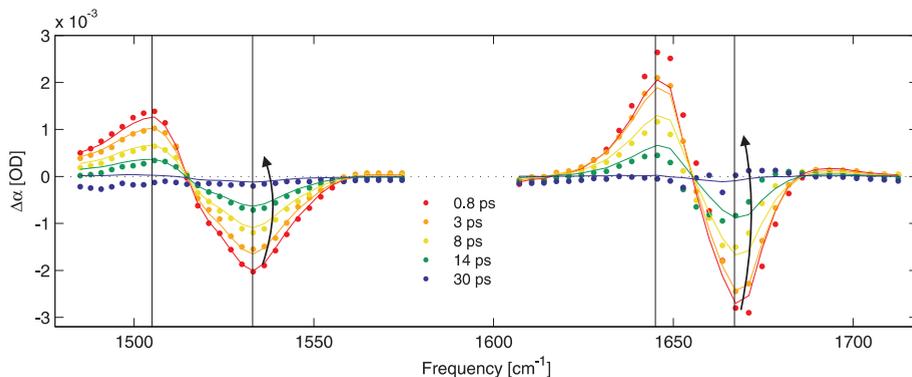
FIGURE 7.4. Transient spectra at different delay times following excitation of the AII mode of a 10 mM solution of NMA in CHBr₃. The solid lines represent the results of a fit to the relaxation model described in the text. The black arrows indicate the time evolution of the spectra.

the AI and AII responses consist of a negative absorption change on the high frequency side of the fundamental absorption band and a positive signal on the low frequency side, similar as was observed when the AI mode was excited. The AII and AI responses have their maximum intensity around 0 ps and both show a similar slow decay. After about 30 ps the transient spectrum does not change anymore, which implies that the system has reached thermal equilibrium.

Figure 7.5 shows time traces (circles and squares correspond to AI and AII mode respectively) at the four frequencies that are marked with solid black lines in figure 7.4. Clearly, the signals at the four different frequencies are very much alike, all showing a decay time constant of about 10 ps.

INTERPRETATION AND MODELING

The AI mode shows a fast decay that is faster in the red wing than in the blue wing of the absorption band. This observation indicates that the AI vibrational band contains different subbands with different vibrational relaxation rates. In previous experimental and theoretical work strong indications were found that the absorption band of the AI mode indeed contains two subbands [35, 137]. Therefore we will model the vibrational relaxation dynamics with two AI $\nu = 1$ states with different vibrational relaxation time constants.

The excitation of the AI mode leads to a direct response in the frequency region of the AII mode. This observation indicates that the AI and AII mode are anharmonically coupled. This response consists of a bleaching in the blue wing of the AII absorption spectrum and an induced absorption in the red wing, which means that the excitation of the AI mode induces an anharmonic redshift of the AII mode. The transient spectrum of the AII mode resulting from this redshift shows a smaller frequency difference between the maxima of the bleach and the induced absorption than in case the AII mode is excited. Following this direct anharmonic response of the AII mode, we observe a further ingrowth of
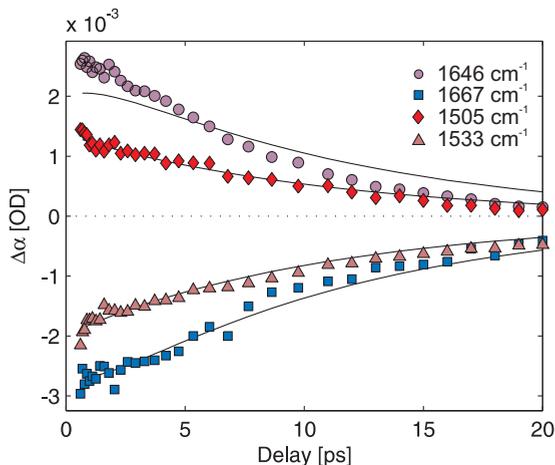
FIGURE 7.5. Time traces recorded at four different frequencies corresponding to the maxima of the bleach and the induced absorption signals of the AI and AII modes following excitation of the AII mode. The solid lines result from a fit to the relaxation model described in the text.

the bleach and the induced absorption on a time scale that is similar to the time scale of the decay of the two AI subbands. The complimentary character of these dynamics indicates that the $\nu = 1$ states of the two subbands of the AI mode transfer their energy at least in part to the $\nu = 1$ state of the AII mode. This state constitutes a third level in the relaxation model.

If there is a coupling leading to energy transfer from the $\nu = 1$ states of the two AI subbands to the $\nu = 1$ state of AII, the same coupling will also lead to transfer of energy in the other direction, i.e. from the $\nu = 1$ state of AII to the $\nu = 1$ states of the two AI subbands. Because of detailed balance, the two rates differ by a Boltzmann factor which for the energy exchange between the $\nu = 1$ states of AI and AII ($\Delta E = \sim140$ cm$^{-1}$) equals $\sim0.5$. The rate at which the energy is equilibrated between the two modes is the sum of the two rates, irrespective of which mode is excited in the first place. This means that the rapid decay observed for the two AI subbands cannot be due to energy transfer to AII because we do not observe a similar partial fast decay when the AII mode is excited. Figure 7.5 clearly shows that excitation of the $\nu = 1$ state of AII only leads to a slow relaxation on a time scale of $\sim10$ ps. Therefore, we conclude that that only a minor part of the excitation of the two AI subbands is transferred to AII. The dominant relaxation channel of the two AI subbands involves transfer of energy to combination tones of other lower-frequency (amide) vibrations. This final state is the fourth and final level of the relaxation and has a spectral response that is not very different from the response that is obtained after the energy of the excitation is fully equilibrated (thermalized).

The excitation of the AII mode is observed to lead to a direct transient spectral response in the frequency regime of the AI mode, which shows that
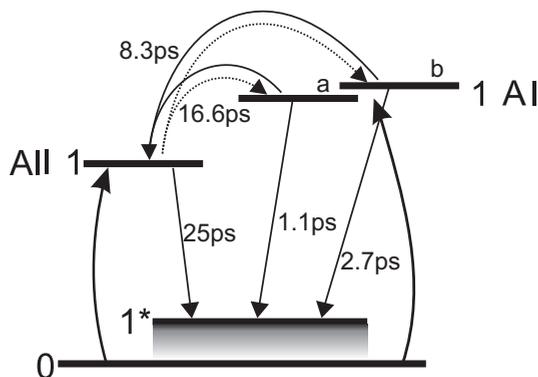
FIGURE 7.6. Schematic representation of the relaxation model used in describing the relaxation pathways of the AI and AII modes in single NMA molecules upon excitation of either of the two modes.

the AI and AII modes are anharmonically coupled, similar as was observed in the experiment in which the AI mode was excited. Both the responses in the frequency region of the AII and the AI mode decay on a timescale of about 10 ps. This decay is partly due to energy transfer to the $\nu = 1$ states of the two AI subbands and partly due to energy relaxation to combination tones of lower-frequency (amide) vibrations.

The complete relaxation model thus consists of four levels: two levels represent the $\nu = 1$ states of two AI subbands and account for the frequency dependence of the fast relaxation following excitation of the AI mode, the third level represents the $\nu = 1$ state of the AII mode and the fourth level represents the final thermal state. All levels have associated differential spectral responses (difference between the absorption spectrum starting from that level and the linear absorption spectrum) in the frequency regions of the AI and the AII modes. In modeling the data we assume that the spectral responses of the two AI excited states are the same in the frequency region of the AII band, and we also assume that the rate of energy transfer between the two AI subbands and the AII mode is the same for both AI subbands. The relaxation model is illustrated in figure 7.6. We fit all measurement results simultaneously to this relaxation model in a global fit. The results of this fit are represented in figures 7.2, 7.3, 7.4 and 7.5 by the solid lines.

From the fit we obtain the differential spectra associated with each of the levels, as shown in figure 7.7 and the relaxation time constants that connect the states of the relaxation model. The differential spectra associated with two AI excited states are represented by the blue and green spectra in figure 7.7. The spectra show a strong bleaching and induced absorption in the frequency region of the AI mode that are similar in shape for the two levels but shifted by $\sim 10$ cm$^{-1}$ with respect to each other. The response of the two excited AI levels in the frequency region of the AII mode is clearly upshifted with respect to $\Delta\alpha=0$ and differs from the usual antisymmetric differential spectral shape
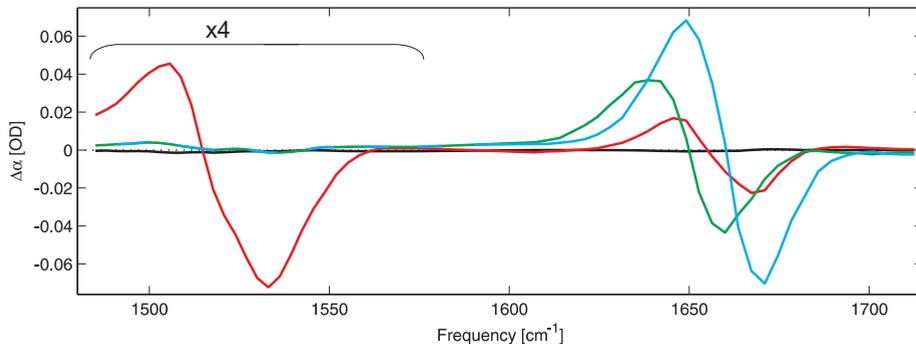
FIGURE 7.7. Extracted differential spectra corresponding to the excited states of the AI mode (blue and green), the excited state of the AII mode (red), and the thermally equilibrated state (black).

that results from an anharmonic frequency shift. The upshift probably results from the presence of a long low-frequency tail of the $\nu = 1 \rightarrow 2$ induced absorption of the excited AI subbands. The total transient spectral response in the frequency region of the AII mode is thus the sum of this low-frequency tail and an antisymmetric signal due to the anharmonic shift of the AII mode induced by the excitation of the AI subbands. Both contributions decay when the AI subbands relax. The level associated with the $\nu = 1$ state of the lower-frequency AI subband decays with a time constant $T_{1,AIa}$ of $1.1\pm0.1$ ps to the final (thermal) level, and the level associated with the higher-frequency AI subband decays with a time constant $T_{1,AIb}$ of $2.7\pm0.4$ ps. In addition to these relaxation channels, both AI subbands transfer energy to the AII level with a time constant of $8.3\pm1$ ps.

The differential spectrum associated with the $\nu = 1$ state of the AII state is represented by the red line. This differential spectrum consists of a strong $\nu = 0 \rightarrow 1$ bleaching and $\nu = 1 \rightarrow 2$ induced absorption in the AII frequency region, and a much weaker bleaching and induced absorption in the frequency region of the AI mode. The latter differential spectral response represents the anharmonic redshift of the two AI subbands due to the excitation of the AII mode. The $\nu = 0 \rightarrow 1$ bleaching and $\nu = 1 \rightarrow 2$ induced absorption of the AII mode have a much larger amplitude than the differential spectrum that results from the anharmonic shift induced by the excitation of the two AI subbands. Therefore, the energy transfer from the two AI subbands to AII leads to an ingrowth of the signal in the AII frequency region. The $\nu = 1$ state of the AII mode decays both as a result of energy transfer to the two AI subbands with a time constant of $16.6\pm2$ ps, and because of relaxation to the final (thermal) state with a time constant of $25\pm5$ ps. The two relaxation channels together explain the observed relaxation time scale of $\sim10$ ps.

The differential spectrum of the final thermalized state is represented by the black line. This differential spectrum has very little amplitude in both the frequency regions of AI and AII. Therefore the relaxation to the final thermal
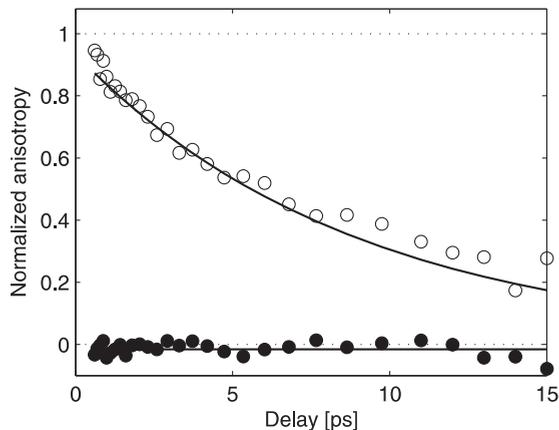
FIGURE 7.8. Anisotropy time traces of the AI mode (open circles) and the AII mode (solid circles) after excitation of the AI mode. The solid lines represent an exponential function fitted to the AI mode anisotropy and a constant value for the anisotropy of the AII mode.

state leads to a decay of the responses in both the AI and the AII frequency regions.

ANISOTROPY DYNAMICS

From the two recorded signals $\Delta\alpha_\parallel$ and $\Delta\alpha_\perp$ we constructed the anisotropy parameter $R(\mathrm{t})$. In figure 7.8 we show the anisotropy decay for the AI mode (open circles) and for the AII mode (black circles) following excitation of the AI mode. The anisotropy of the AI mode decays with a time constant $\tau_{\mathrm{or}}$ of $9\pm1$ ps, which reflects the time scale of the reorientation of this vibration. The initial value of the anisotropy of the AII mode reflects the relative orientation of the transition dipole moment of the AII mode with respect to that of the excited AI mode. Using equation 6.4 we find an angle of $\sim55°$, the same value as we found in the previous chapter for the relative orientation of the AI and AII transition dipole moments of hydrogen-bonded NMA clusters.

## 7.3.3   DISCUSSION

The relaxation dynamics observed for NMA monomers strongly differs from the relaxation behavior observed for the hydrogen-bonded NMA clusters we studied in the previous chapter. In the first place the relaxation of the AI mode and in particular of the AII mode is much faster for the clusters than for the monomers (0.85 and 0.6 ps versus $\sim1.5$ ps and $\sim10$ ps). It thus appears that the presence of hydrogen bonds between the NMA monomers leads to a strong acceleration of the vibrational relaxation. This acceleration can be due to the fact that the hydrogen bonds take up part of the vibrational energy, thereby compensating for the energy mismatch between the excited AI and AII vibrations and the energy accepting combination tones of lower frequency vibrations.

Another interesting difference between the relaxation behavior of the monomers and the clusters is that for the monomers we observe a partial relaxation of the excited $\nu = 1$ state of the two AI subbands to the $\nu = 1$ state of the AII mode. For the clusters this transfer was not observed, probably because the direct relaxation to combination tones of lower-frequency vibrations was much faster. The energy transfer from AI to AII leads to a rise of the response of the AII spectral response on a time scale that corresponds to the time scale of the decay of the AI vibrations. This time scale is in fact much shorter than the characteristic time scale of the energy transfer of $\sim$8 ps, because the vibrational relaxation of the two AI subbands is dominated by another much faster relaxation channel. The reason that the time scale of the latter process is observed in the ingrowth of the AII response is because the AI modes can no longer further populate the AII mode after they have relaxed through the fast relaxation channel. The observation of energy transfer between the excited AI and AII vibrations does not agree with the results of Zhang *et al.* [176] who found that for isolated NMA molecules the AII mode does not participate in vibrational relaxation of the AI mode. It should be noted that we find the fraction of NMA molecules for which the two AI subbands relax via the AII mode to be quite small. From the rate constants we derive that this fraction is $(0.12/(0.12+0.90)+0.12/(0.12+0.37))/2 = 0.18$. Hence, less than 20% of the NMA molecules relax via the AII mode. In a molecular dynamics study by Bloem *et al.* evidence was found for a direct transfer between AI and AII, but on a time scale that is $\sim$10 times shorter than we observed.

Another interesting observation is that we find the vibrational lifetime of the AI mode to be frequency dependent. NMA molecules absorbing on the high frequency side ($\sim$1680 cm$^{-1}$) relax slower than molecules absorbing in the red wing of the spectrum ($\sim$1660 cm$^{-1}$). One possible explanation for this observation is that the NMA spectrum is inhomogeneously broadened due to a variation in conformation. Previous molecular dynamics simulations showed that the trans-NMA molecule can exist in four conformations of planar symmetry with different orientations of the C- and N- methyl groups [29]. If this variation in conformation would be the origin of the frequency dependence of the vibrational lifetime one would expect the lifetime to vary continuously over the AI absorption band. If the variation in conformation would be the origin of the frequency dependent vibrational lifetime one would expect a similar effect for the AII mode of NMA. However, for the AII mode we do not observe such a frequency dependence of the vibrational lifetime. We also find that a relaxation model involving only two different rates is fully sufficient to describe the experimental data at all delay times. This finding suggests that the frequency dependence may be due to the presence of two different NMA species, thus leading to two subbands in the vibrational spectrum. This finding agrees with the results of a previous experimental study [137] and with the results of molecular dynamics simulations [35]. Rubtsov *et al.* investigated the coupling between different amide modes of small peptides dissolved in chloroform with two-dimensional infrared spectroscopy. They found strong indications for the presence of two subbands in the spectrum of the AI mode, both in the linear absorption spectrum and in the transient nonlinear vibrational response. They attributed the two subbands to

the splitting of the AI mode by a Fermi resonance of this mode with an overtone of a lower-frequency vibration. DeCamp *et al.* performed molecular dynamics simulations on solutions of NMA in $CDCl_3$, and they attributed the presence of two subbands to a difference in the number of hydrogen bonds formed between NMA and $CDCl_3$ solvent molecules. They found that singly hydrogen-bonded NMA molecules absorb at the high-frequency side of the absorption spectrum, and that doubly hydrogen-bonded NMA molecules absorb at the red side of the absorption band. Figure 8.4 shows that the linear absorption spectrum of the AI mode of NMA in $CHBr_3$ possesses a shoulder on the low-frequency side. Interestingly, this shoulder is not present in the linear absorption spectrum of the AI mode for a solution of 10 mM NMA in $CCl_4$ solution. This result suggests that the shoulder arises from NMA molecules interacting with $CHBr_3$ solvent molecules, in line with the explanation of DeCamp *et al.* for the presence of two subbands in the absorption spectrum of the AI mode of NMA dissolved in $CDCl_3$.

We observed that the transition dipole moments of the AI and AII modes of NMA monomers have the same relative angle of $\sim 55°$ as we observed in the previous chapter hydrogen-bonded clusters. This angle is consistent with the findings of previous experimental studies [36]. Apparently, the hydrogen-bond interactions between the NMA molecules have very little effect on the normal mode character and thus the direction of the transition dipole moment of the AI and AII vibrations. The reorientation time $\tau_{or.}=9\pm1$ ps and is comparable with the time constant found by DeCamp *et al.* for NMA dissolved in $D_2O$ and $CDCl_3$ and with the time constant by Hamm *et al.* for deuterated NMA dissolved in $D_2O$. The reorientation time constant of $\sim9$ ps is somewhat longer than the reorientation time constant of 6 ps that we observed for hydrogen-bonded NMA clusters in $CCl_4$. This result may seem surprising as one would expect that single NMA molecules reorient faster than NMA oligomers. One reason for this unexpected result may be the difference in viscosity of the solvent. The viscosity of bromoform is approximately twice as high ($\sim1.85$ mPa·s) than that of carbon tetrachloride ($\sim0.97$ mPa·s). According to hydrodynamic theory [12] the reorientation time constant is proportional to the viscosity of the solvent: $\tau_{or.}=V\eta/k_BT$, with $V$ the volume of the solute, $\eta$ the viscosity, $k_B$ Boltzmann's constant, and $T$ the temperature. Hence, the difference in reorientation time constant between NMA monomers in $CHBr_3$ and NMA oligomers in $CCl_4$ can be explained from the difference in viscosity of the solvent. Even so, it remains surprising that the effective larger volume of an NMA cluster in comparison to an NMA monomer does not lead to a strong increase of the reorientation time constant of the AI mode. This observation suggests that the reorientation involves the orientational motion of NMA within the hydrogen-bonded cluster.

## 7.4   Conclusions

We studied the vibrational energy relaxation mechanisms of the amide I and amide II vibrations of monomeric N-methylacetamide (NMA) molecules dissolved in bromoform using polarization-resolved femtosecond two-color pump-

probe spectroscopy. We excited both the amide I and the amide II vibration to the $\nu = 1$ excited state with a short, narrow-band mid-infrared pump pulse and we monitored the vibrational relaxation in the frequency regions of both modes with a short, broadband mid-infrared probe pulse.

We observe that the vibrational relaxation of the amide I mode depends on frequency. This frequency dependence can be well explained from the presence of two subbands with different vibrational lifetimes in the absorption spectrum of the amide I mode. The presence of two subbands agrees with the observation of a low-frequency shoulder in the linear absorption spectrum of the amide I mode. The two subbands are likely caused by a difference in the interaction strength of NMA with the bromoform solvent molecules.

We find that the excited amide I mode relaxes via two vibrational relaxation channels. In one channel the vibration relaxes to a final state with an absorption spectrum that corresponds to a full equilibration of the vibrational excitation energy. The time constants for this relaxation are found to be 1.1±0.1 ps for the subband at the red side of the amide I absorption band and 2.7±0.4 ps for the subband at the blue side of the amide I absorption band. In the other channel the two subbands transfer their energy to the $\nu = 1$ state of the amide II mode. This process has a much longer time constant of 8.3±1 ps, which implies that only for ∼20% of the NMA molecules the amide I mode relaxes via energy transfer to the amide II mode. The excited amide II mode relaxes via two similar relaxation channels, i.e. to a final thermalized state with a time constant of 25±5 ps, and via energy transfer to the amide I mode with a time constant of 16.6±2 ps.

# 8 DISTRIBUTION OF WATER MOLECULES IN LIPID MEMBRANES

We study the structure and dynamics of water molecules embedded in 1,2-dioleoyl-sn-glycero-3-phosphocholine (DOPC) model membranes using polarization resolved, ultrafast pump-probe spectroscopy. We investigate the effect of the local environment of the membrane on the vibrational relaxation properties of water at various hydration levels ($\sim$**2-12** water molecules per lipid). We find that the water molecules that are hydrogen-bonded to different sites of the membrane exhibit different vibrational lifetimes. With increasing hydration level we observe a relative increase of the longer-lived, bulk-like water with respect to the shorter-lived lipid-bonded water molecules. We investigate the anisotropy decays of water molecules for different isotopic composition ($D_2O/H_2O$) of the hydrating water. For $D_2O/H_2O$ ratios $\geqslant 0.1$ the anisotropy decay of the OD vibration is dominated by vibrational energy transfer (VRET). The rate of VRET gives information on the distribution of water molecules at the membrane surfaces. We find this distribution to be very inhomogeneous.

## 8.1 INTRODUCTION

The smallest building blocks of living organisms are called cells. These building blocks are defined by a membrane that separates their content from the "outside" world. Membranes, in spite of being composed of only two layers of molecules (what makes them very flexible), are very tough, capable of withstanding high tension and compression from internal (cytoskeleton) and external (extracellular matrix) forces acting on them. The rigidity of these bio-membranes helps to maintain the integrity of cells while their flexibility allows cells to change their shape. Membranes regulate transport in and out of the cell, cell adhesion and motion, and signalling to other cells. An important role in the structuring of the membrane and its (bio)activity is played by the adherent water layers [89]. It has been shown that the structure and dynamics of these water layers strongly differ from bulk liquid water [16, 17, 20, 52, 118, 148, 161, 163, 164, 174, 177]. It has also been suggested that these water layers play an important role in the transport properties of the membrane. Water confined by lipid membranes is

not only present in the intercellular space between two neighboring cells, but also in the endocellular space where tightly packed hydrated membranes form the thylakoid (involved in photosynthesis) and the Golgi apparatus (crucial in the generation and distribution of molecules within the cell). Tightly packed hydrated membranes can also be found in biological transient states during vesicle fusion, endo- and exocytosis [90].

Water-membrane interactions and the structure of hydrated membranes were studied extensively using NMR [16, 162, 168, 174], X-ray and neutron scattering, infrared spectroscopy [16, 17, 118, 161, 163, 164, 177], MD simulations [14, 15, 54, 99, 176], CARS [30], SFG [20, 52, 148, 174] and dielectric spectroscopy [77, 155]. Thanks to recent developments in nonlinear infrared spectroscopy the study of ultrafast water-membrane interactions has now become possible [161, 163, 164, 177].

A common conclusion from the past work is that water near a lipid membrane behaves differently from water in the bulk. Water molecules at membrane interfaces are much less mobile than in bulk, due to the strong hydrogen-bonds formed with the lipid headgroups. Very little is still known about the structure and dynamics of the water layers in close contact to biological membranes, mainly because of the large variation of membranes structure, composition and activity. Moreover, there are only very few experimental techniques that can specifically probe the water molecules near the membrane surface.

To study the interactions between biological water, the membrane and other biomolecules embedded in the membrane, researchers usually turn to membrane model systems like liposomes, micelles or lamellar membrane stacks. Liposomes allow the study of water-membrane interactions under water-rich conditions, whereas membrane stacks form a well defined model system for studying the properties of water confined in between two membranes at rather water-poor conditions (water-poor in biological sense).

We have studied the vibrational properties of biological water using polarization resolved ultrafast pump-probe spectroscopy. This technique allows us to probe water molecules directly via their vibrational resonances, and not via the response of a nearby chromophore. We investigated the vibrational dynamics and localization of water molecules embedded in a membrane model composed of a stack of 1,2-dioleoyl-sn-glycero-3-phosphocholine (DOPC) bilayers. We have varied the hydration level and isotopic composition of the hydrating water. We probe the OD vibrations and their mutual coupling by measuring the rate of the vibrational resonant energy transfer (VRET). As a result, we obtain highly specific information on the structure, distribution and dynamics of water molecules at the membrane interface.

## 8.2   EXPERIMENT

The infrared laser pulses needed for the experiments are generated via optical frequency conversion processes that are pumped by the output of a Ti:sapphire regeneratively amplified laser system (Spectra-Physics Hurricane). This system generates pulses at a wavelength of 800 nm with a pulse energy of $\sim$900 $\mu$J at

a repetition rate of 1 kHz. The 800 nm beam is split into two parts. The first part is used as a seed for a white-light based OPA (Spectra Physics). After the OPA the idler is frequency doubled in a second BBO crystal. The doubled idler (1000 nm) is used as a seed in a parametric amplification process in a potassium niobate crystal (KNB), pumped with the remaining part of the 800 nm pulses, analogously to the infrared light generation scheme described in secton 3.2. In the experiment we used pulses centered at a frequency of $\sim 2500$ cm$^{-1}$ ($\sim 4$ $\mu$m) and a pulse energy of $\sim 6$ $\mu$J. The IR pump-probe setup is described in detail in section 3.3.

### 8.2.1    SAMPLE PREPARATION

We obtained 1,2-dioleoyl-sn-glycero-3-phosphocholine (DOPC) from Avanti Polar Lipids and used it without further purification. DOPC is a zwitterionic lipid, with an overall electrically neutral headgroup, carrying positive and negative charges on different atoms. Heavy and normal water ($D_2O$ (99.9% D) and $H_2O$) are obtained from Sigma Aldrich. The dry lipids were dissolved in a methanol/chloroform mixture (1:3 volumetric ratio) at a concentration of 50 g/L. By adding methanol we achieved a more homogenous spreading of the solution on the $CaF_2$ substrate (due to its hydrophilic character). To prepare solid supported oriented lipid multibilayers we used a technique adapted from previous reports [4, 59, 65, 159, 160]. In this procedure we deposit a small amount of the solution (5 - 15 $\mu$L) on the $CaF_2$ window and wait for a few minutes until the solvent evaporates and the sample becomes solid like. We repeat this process until the desired thickness of the sample is achieved. The sample is then placed in a home-built sample holder. The holder consists of two connected metal cylinders, each holding one $CaF_2$ window. The sample holder is sealed from the environment in order to keep the sample at the desired hydration level. One of the cylinders is equipped with two gas ports (inlet/outlet) that allow us to purge the sample with air of the desired humidity. First we dry the sample by purging nitrogen gas through the sample holder. The time needed to dry the stack of multibilayers depends on the sample thickness and varies from 1h - 5h. To ensure the removal of all the solvent traces and water we equilibrate the samples overnight in the nitrogen buffer gas.

The sample is subsequently hydrated with the use of a home-built hydration system. The hydration system consists of a reservoir with water ($D_2O/H_2O$ mixture), two precise electronically controlled valves, a PID controller and an electronic hygrometer (range: 10-95% RH, precision: 3% RH). The input of the humidity controller is a constant flow of nitrogen gas. The flow is split into two branches and the flow in each branch is controlled with a valve. One of the two nitrogen parts flows through a water reservoir and creates air saturated with water vapor. The two flows are again united and a hygrometer measures the relative humidity of the outgoing mixed air. Based on the hygrometer readings the two valves are adjusted via an active feedback loop to obtain the desired relative humidity (RH). The hydration device allows for generating air with relative humidities in the range of 15-95% RH with a precision of 3% RH.

We recorded linear spectra to monitor the dehydration and hydration pro-
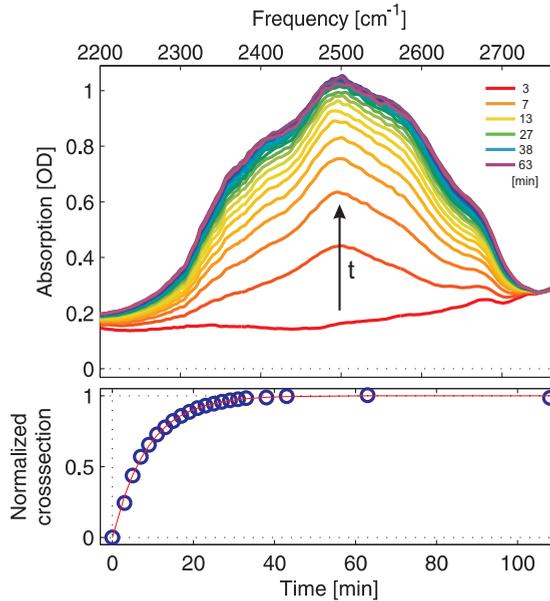
FIGURE 8.1. Top panel: Linear absorption spectra of the OD stretch vibration of water molecules embedded in the lipid multibilayers recorded during the hydration process with 25% RH and pure $D_2O$. The arrow indicates the evolution of the absorption spectrum in time. The bottom panel shows the integrated area of the OD absorption spectrum as a function of the hydration time. The solid line represents a monoexponential function and acts as a guide to the eye.

cesses. In figure 8.1 we show the absorption of the OD stretch vibration at different hydration times. In the bottom of figure 8.1 the integrated area of the OD stretch absorption band is shown as a function of the hydration time. The sample is fully equilibrated after about 60 min.

After the hydration process the sample is put in between two $CaF_2$ windows separated with a teflon spacer thereby sealing the sample from the environment. In order to obtain sufficient optical density of the OD stretch mode we varied the spacer thickness in a range from 10 to 150 $\mu$m, depending on the hydration level and the isotopic composition of the hydrating water.

A properly oriented sample consists of a stack of planar bilayers with their normal parallel to the normal of the $CaF_2$ substrate. A sample with such a geometry can be compared to an uniaxial crystal [130]. It was shown by X-ray diffraction experiments that such a sample consists of planar lipid bilayers separated by layers of water [65, 91, 92]. In order to perform polarization resolved experiments we have to ensure that the sample does not change the polarization of the transmitted light.

We produced aligned monodomain DOPC multibilayers by means of a thermal and mechanical sample treatment reported previously [4, 59, 130, 159, 160]. Once the sample is hydrated and sealed between the $CaF_2$, we move the two
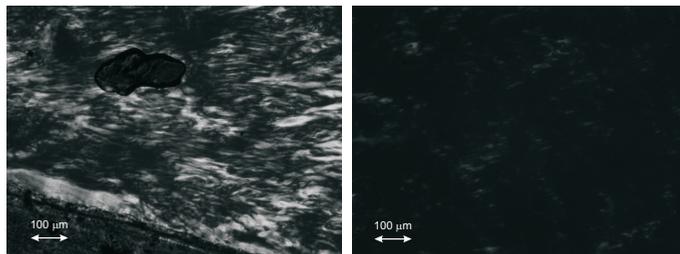
Figure 8.2. Solid supported DOPC multibilayers sample viewed in between two crossed polarizers under orthoscopic white light illumination. The sample was 50 $\mu$m thick and was hydrated to 50% RH ($\sim$3.5 water molecules per lipid). The images show the sample before (left) and after (right) mechanical/thermal treatment.

windows with respect to each other while gently applying pressure on the sample. The flow of the material resulting from the shear enables the sample to adapt to the energetically favorable planar form. Samples thicker than 50 $\mu$m could not be aligned with the mechanical treatment only. These samples were heated up to 40 °C - 100 °C (depending on the thickness and the hydration level), and are thus brought to a more fluid state. This implies that the viscosity of the sample decreases and the diffusivity increases causing, together with the applied shear stress, the multi-domain character to anneal away.

Following the hydration and alignment procedure described above we have placed every sample in between two orthogonally oriented polarizers and checked its transmission under orthoscopic white light illumination with a Nikon Eclipse Ti inverted microscope connected to a Photometrics Coolsnap HQ2 digital CCD camera.

Well aligned, monodomain lipid multilayers appear black when viewed between two crossed polarizers under an orthoscopic white light. In figure 8.2 we show the lipid multibilayer sample before (left) and after (right) the mechanical/thermal treatment. After the pump-probe measurements we re-examined each sample. We did not observe any changes in the linear absorption spectrum or the alignment of the samples.

The final hydration of the samples was checked by comparing their linear absorption spectrum with the absorption spectrum of a reference sample. The reference sample was a diluted, homogenous solution of DOPC in chloroform. We prepared 6 reference samples, each with addition of a precise amount of $D_2O$, such that we obtained a specific water/lipid molecular ratios (1:1, 1:2 ,1:4, 1:6, 1:8 and 1:10). We then measured linear absorption spectra of the reference samples and compared the relative magnitudes (by integrating the absorption band) of the absorption of the OD stretch band of water and the $CH_2$ stretch band of the lipid residing at $\sim$2857 cm$^{-1}$. Figure 8.3 shows that the calculated OD/$CH_2$ band ratio (blue circles) for the reference samples correlates very well with the linear increase of the amount of water molecules per lipid. For each sample used in the experiment we calculated the OD/$CH_2$ absorption band ratio and compared to the reference 'ruler' (red squares and blue circles in figure 8.3).
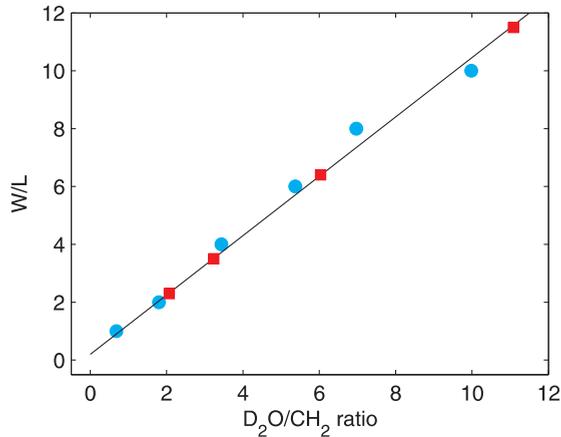
FIGURE 8.3. Blue circles represent a reference 'ruler', that is the lipid hydration (amount of water molecules per lipid) in function of the $OD/CH_2$ absorption band ratio. Red squares represent the $OD/CH_2$ ratio for the samples used in the nonlinear experiments.

The hydration numbers we obtained are in excellent agreement with a previous report [65] (see table I).

In our experiments we have studied lipid multibilayers at different hydration levels (25%, 50%, 75% and 100% RH - which correspond to $x = 2.3, 3.5, 6.4$ and 11.5 water molecules per lipid respectively). For each hydration level we varied the isotopic composition of water from 10%, through 25%, 50% to 100% $D_2O$ in $H_2O$. We further refer to the isotopic composition of water as the fraction of the OD oscillators in the system $f_D$ ($f_D$=0.1, 0.25, 0.5 and 1, respectively). Table I summarizes the hydration level - $x$ and the isotopic composition of water - $f_D$ of all the samples under study.

TABLE I. Number of the OD oscillators per lipid for all studied hydration levels and isotopic compositions of the hydrating water. *Hydration numbers for DOPC multi-bilayers from Hristova *et al.* [65].

| RH [%] | $x \left[ \dfrac{n_W}{L} \right]$ | $f_D$ | | | |
|--------|---------|-----|------|-----|-----|
| | | 0.1 | 0.25 | 0.5 | 1 |
| 25 | 2.3 (2.5)* | 0.5 | 1.1 | 2.3 | 4.6 |
| 50 | 3.5 (3.7)* | 0.7 | 1.7 | 3.5 | 7 |
| 75 | 6.4 (6.2)* | 1.3 | 3.2 | 6.4 | 12.8 |
| 95 | 11.5 (10.2)* | 2.3 | 4.6 | 11.5 | 23 |

## 8.3    RESULTS AND DISCUSSION

### 8.3.1    LINEAR SPECTRA
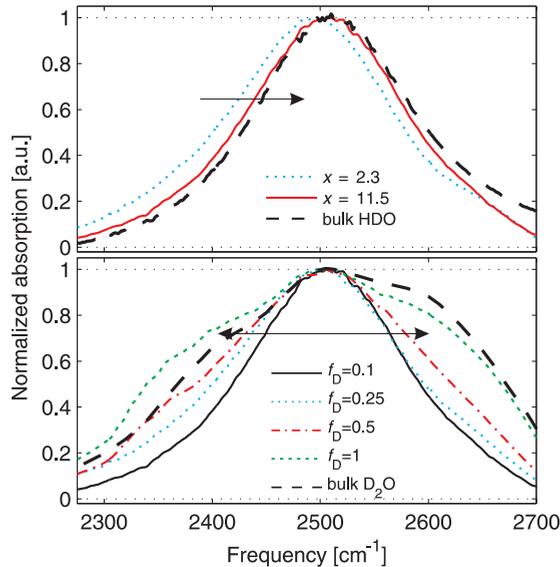


FIGURE 8.4. Linear absorption spectra of the OD stretch vibration of water molecules embedded in the lipid multibilayers. The top panel shows the absorption spectra for the two extreme hydration cases of $x = 2.3$ and $x = 11.5$ hydrated with the lowest $D_2O/H_2O$ isotope mixture ($f_D = 0.1$). The dashed line represents the bulk spectrum of 4% $D_2O$ in $H_2O$. The bottom panel shows the linear absorption spectra of the OD stretch mode of samples hydrated at $x = 11.5$ and different isotopic compositions of water. The dashed line represents a spectrum of pure $D_2O$.

In figure 8.4 we show linear absorption spectra of the OD-stretch vibration of water molecules embedded in the lipid multibilayers. The top panel shows that with increasing hydration level the spectrum shifts towards higher frequency. No significant changes in the spectral shape are observed, except for the vanishing of a weak shoulder at the high frequency side ($\sim$2650 cm$^{-1}$) with increasing hydration level. The bottom panel shows that upon increasing the $D_2O$ content the absorption spectrum broadens and becomes more asymmetric.

For all hydration levels and isotopic compositions, the OD stretch absorption spectrum is redshifted with respect to that of bulk water (indicated by the dashed line in figure 8.4). This observation agrees with previous experimental observations and indicates that at all hydration levels a significant part of the water molecules form stronger hydrogen bonds with the lipids than with other water molecules [16, 155, 177]. The blueshift of the OD stretch vibration with increasing hydration has been quantitatively reproduced by recent molecular dynamics simulations by Gruenbaum *et al.* [58]. These simulations also showed

that the hydrogen bond between a water molecule and a phosphate moiety is stronger than that between a water and a carbonyl group. The latter hydrogen bond may still be somewhat stronger than that between water molecules [14].

## 8.3.2   Vibrational energy relaxation

Figure 8.5 (left column) shows transient spectra (open symbols) at different delay times after the excitation of the OD stretch vibration for three different water isotope compositions. The most prominent changes are observed in the frequency range of the $\upsilon = 0{\rightarrow}1$ transition ($\sim$2500 cm$^{-1}$) representing the pump-induced depopulation of the OD stretch vibrational ground state. Below 2420 cm$^{-1}$ the signal changes sign and we observe the high-frequency wing of the induced $\upsilon = 1{\rightarrow}2$ absorption. For the samples hydrated with pure D$_2$O the $\upsilon = 1{\rightarrow}2$ transition frequency is shifted towards lower frequency, and thus only the 0$\rightarrow$1 bleaching signal is observed within the experimental spectral window.

With increasing delay time the transient signals decay and the residual bleach slightly shifts towards lower frequencies. Simultaneously, at high frequencies ($>$2570 cm$^{-1}$) an induced absorption arises. This spectral shape is a signature of an increase in sample temperature. An increase in sample temperature leads to a blueshift of the fundamental absorption spectrum. As a result we observe a negative signal at the red side of the spectrum ($<$2550 cm$^{-1}$) and a positive signal at the blue side of the spectrum ($>$2550 cm$^{-1}$). The increase in temperature is the result of the vibrational energy relaxation and the subsequent excitation of low frequency librational and translational modes. For the samples at higher hydrations and with higher D$_2$O content, the thermal difference signal becomes stronger and comparable with the magnitude of the bleaching signal. After $\sim$10 ps the spectra do not change anymore.

Figure 8.6 shows the delay dependent isotropic signal recorded at a single probe frequency of 2500 cm$^{-1}$. The top panel shows the delay traces for the two extreme hydration levels ($x = 2.3$ (squares) and $x = 11.5$ (circles)) and the lowest isotopic ratio of $f_D = 0.1$. At $\sim$4 ps we observe a clear deviation from mono-exponential behavior that is indicated with the dashed line. We also find that the relaxation rate is increasing significantly with increasing hydration level .

The data for $f_D$=0.25 (not shown) resembles the data for $f_D$=0.1. For $f_D = 0.5$ and $f_D = 1$ at $x = 2.3$ the transient signal decays in a similar non-exponential way (black squares), but the difference between the two rates is larger than for $f_D$=0.1. At early delays ($<$1 ps), the signal decays much faster for $f_D$=1 than for $f_D$=0.1, but at later delays it seems to decay slower than for the $f_D$=0.1 case. For higher hydrations (blue circles), due to very fast vibrational relaxation, the signal is, already at early delays, dominated by the thermal signal. Another interesting observation is that the heating signal for the samples hydrated with $f_D$=1 decays at late delays (after $\sim$10 ps), suggesting a two step thermalization process.

The experimental observations for the samples with a low isotope content of $f_D = 0.1$ and 0.25, and all hydrations are in very good agreement with the results of recent work by Zhao *et al.* [177]. Based on our experimental observations and
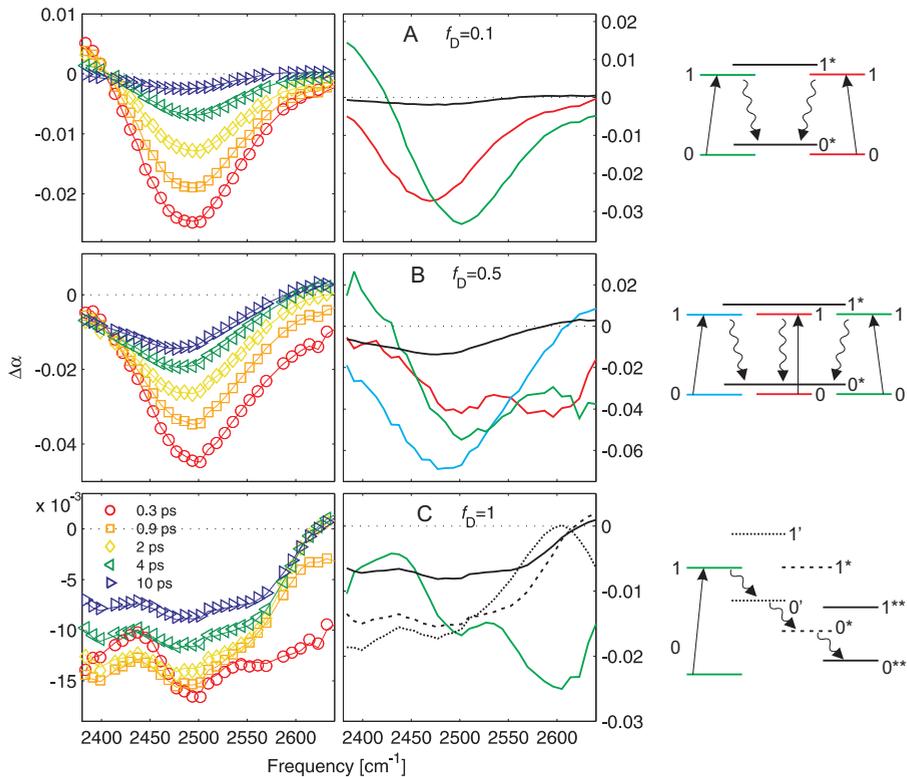
FIGURE 8.5. Transient spectra of the OD stretch vibration as a function of delay time between excitation and probe pulses for the samples hydrated at $x = 6.4$ with $f_D = 0.1$ (top), $f_D = 0.5$ (middle) and $f_D = 1$ (bottom). The solid lines in the left column result from a fit to the kinetic model . The middle column shows the spectra that are extracted from the fit to the kinetic model. The right column presents a schematic representation of the kinetic models used to describe the data hydrated with water of different isotopic composition. The straight and wavy arrows indicate excitation and relaxation pathway of different water species, respectively.

this previous report, we describe our data for $f_D$=0.1 and 0.25 with a model that involves two species of water molecules decaying independently with different rate constants (see the top schematic in figure 8.5).

The faster decaying component we attribute to water molecules being strongly hydrogen-bonded to the phosphate group of the lipids. The slower component we attribute to water molecules bonded to the carbonyl moieties and to other water molecules. The extracted relaxation rates from the fit are summarized in figure 8.7, panels A2 (open symbols). For both isotopic mixtures we find that the relaxation time constant $T_1$ decreases with increasing hydration. We find that the slower species (open circles) decays with $T_1 = \sim 6$ ps at $x = 2.3$. Its lifetime decreases to $T_1 = \sim 3$ ps at $x = 11.5$. The short lived species (open
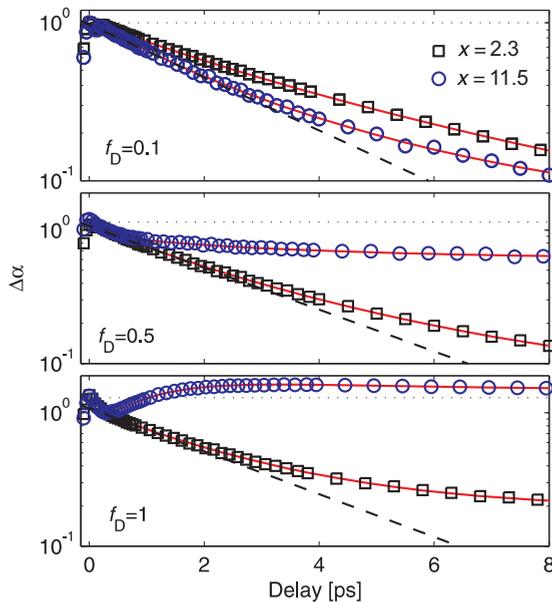
FIGURE 8.6. Isotropic signals recorded at 2500 cm$^{-1}$ as a function of the delay between the pump and probe pulses. Each panel shows the delay traces for two extreme hydration levels ($x$=2.3 and $x$=11.5). The solid (red) lines result from a fit to the kinetic model described in the text. The dashed lines result from a mono-exponential function and act as guides to the eye.

squares) relaxes with a $T_1 = \sim 2.1$ ps at $x = 2.3$ and $T_1 = \sim 1$ ps at $x = 11.5$. Our findings are in excellent agreement with recent sum-frequency generation experiments on the vibrational dynamics of water molecules at water-lipid interfaces, which show that lipid-bound water molecules relax approximately two times faster than those bound to other water molecules [20]. In figure 8.5 (middle column) we show the extracted spectra corresponding to the two species. The water molecules exhibiting the shorter lifetime absorb at lower frequencies ($\sim 2470$ cm$^{-1}$), whereas the longer lived species absorb at higher frequencies ($\sim 2500$ cm$^{-1}$)

For $f_D = 0.5$ the isotropic signal decays faster than for the samples with lower $f_D$. Especially at short delay times after excitation we observe a very fast (sub-picosecond) decaying component. We find that the data can not be satisfactorily described with the model involving just two water species. The presence of an additional component in the delay curves most likely arises from a different population distribution of the different isotopes of water with respect to the samples with $f_D$=0.1 and 0.25. For this isotopic mixture statistically 50% of water molecules are HDO, 25% are $D_2O$ and another 25% are $H_2O$. About 33% of the isotropic signal thus comes from the OD stretch vibration of $D_2O$ molecules, for which the vibrational lifetime is expected to be short, due to efficient intramolecular coupling. For bulk $D_2O$ we found a vibrational lifetime

$T_1$ of 400 fs (see chapter 4). We implement this contribution into the model as an additional third species decaying independently from the other two. We use this model to fit the data for $f_D = 0.5$ and the hydration levels of $x = 2.3, 3.5$ and 6.4.

For the fully hydrated sample ($x$=11.5) we observe a change in the magnitude of the isotropic signal at late delays (>10 ps). The spectral shape of the thermal signal remains the same, only the amplitude decreases. This indicates a two-step thermalization process. In order to account for this late-delay dynamics, we have adjusted the kinetic model by adding an additional heat state. This additional heated state reflects the fact that upon vibrational relaxation water molecules do not reach the thermal equilibrium immediately but first reach a local hot state that is followed by cooling and full thermalization of the sample.

The relaxation rates and populations of each of the three water species are shown in figure 8.7, panels B1 and B2. The band with an intermediate lifetime (open squares) shows a decreasing $T_1 = \sim 2$ ps for $x = 2.3$ to $T_1 = \sim 0.8$ ps for $x = 11.5$. Similarly the long-lived species (open circles) lifetimes decreases from $T_1 = \sim 4$ ps for $x = 2.3$ to $T_1 = \sim 2$ ps for $x = 11.5$. The lifetime of the most short lived species (open triangles) decreases from $T_1 = \sim 0.8$ ps for $x = 2.3$ to $T_1 = \sim 0.4$ ps for $x = 11.5$. Hence, at the highest hydration this lifetime is similar to the vibrational lifetime of the OD stretch vibration of $D_2O$ water molecules in the bulk. The cooling time for the sample with the highest hydration $x$=11.5 was found to be $\sim 8$ ps (not shown). The extracted spectra are shown in figure 8.5, panel B.

For samples hydrated with pure $D_2O$ ($f_D = 1$) the water molecules binding to different sites at the bilayer interface show the same relaxation rate. We did not find any spectral signatures or variation in the vibrational lifetime that could help in distinguishing $D_2O$ molecules forming hydrogen-bonds of different strengths (with different lipid moieties). We thus model the data with a consecutive model (a variation of that used previously for bulk water [128, 134, 135]). The excited state relaxes to an intermediate state. This step reflects the adaptation of the hydrogen bonds due to the sudden release of the vibrational energy and the excitation of lower frequency modes. This process is followed by a thermalization of the system. Similarly to the samples hydrated with $f_D$=0.5 we observe a further change of the thermal signal at later delays, after the vibrational relaxation from the OD stretch mode is complete. In this process, the energy is further redistributed out of the local, heated water cluster and the system cools down and equilibrates. We thus model our data with a 4 step consecutive relaxation model. This model describes the experimental data very well at all hydration levels. Panels A1 and A2 in figure 8.8 show the extracted populations and lifetimes of all the consecutive states.

DISCUSSION I

The largest variation in the vibrational lifetime with hydration ($x$) is observed for membranes hydrated with a low isotopic mixture of $D_2O$ in $H_2O$ ($f_D$=0.1). In such a dilute case the OD vibration of the HOD molecule is decoupled from other high frequency modes thus allowing the direct probing of the effect of the local binding site on its vibrational lifetime. We clearly observe two distinct

relaxation rates at all hydration levels. Figure 8.7, panel A2, shows the change of the two relaxation rates with hydration (open symbols). At the lowest hydration ($x$=2.3) the longer of the two lifetimes is more than 3 times longer, whereas the shorter one is about 2 times longer than the lifetime observed in bulk HDO:$H_2O$. Both lifetimes decrease when increasing hydration and reach a final value of $\sim$3 ps and $\sim$1.7 ps for hydrations $x$ >6.4. The extracted spectra are shown in figure 8.5, panel A. The blueshifted spectrum, absorbing at $\sim$2500 cm$^{-1}$ is associated with the longer vibrational lifetime, and the redshifted one with the shorter lifetime. We find that the positions of the two bands do not change with hydration. Only their relative amplitudes vary. The spectral position of the two bands confirms the notion that the strongly hydrogen bonded water molecules (presumably bonded to the phosphate group) have a shorter lifetime, most likely due to efficient coupling of the OD stretch vibration ($\sim$2500 cm$^{-1}$) with the stronger hydrogen bond and the vibrational modes of the phosphate group (1200 - 1300 cm$^{-1}$). The spectrally blueshifted spectrum reflects water molecules hydrogen bonded to carbonyl groups and/or other water molecules.

Assuming that the different water species have similar absorption cross sections, we directly obtain information about the dependence of the population of the two species on hydration level from the fit to the kinetic model. We find that with increasing hydration level the relative amount of redshifted, short-lived species decreases with respect to the long-lived species (see figure 8.7, panel A1). The phosphate group can be hydrated by at most 4 water molecules [55]. It is thus understandable that once the phosphate groups are saturated with water molecules, a further increase of the hydration will only add water molecules hydrogen-bonded to carbonyl groups or to other water molecules.

The the hydration dependent population dynamics of the two species are in excellent, quantitative agreement with the recent molecular dynamics simulations by Gruenbaum *et al.* [58]. The population dynamics extracted from their simulations are marked with asterisks in figure 8.7 (A1). Gruenbaum *et al.* also calculated the isotropic signal decay using vibrational lifetimes of each of the water species as fit parameters. Their best-fit vibrational lifetimes are in very good agreement with those observed in our experiments (see figure 8.7 A2, marked with asterisks). Qualitatively our findings agree well with those reported for hydrated DLPC multilayers by Zhao *et al.* [177].

The population dynamics of the three species present in the samples hydrated with $f_D$=0.5 are shown in figure 8.7, panel B1. As for the lower isotope ratios, the amount of strongly bonded water molecules (solid squares) decreases relatively to the whole excited population with increasing hydration. The population of the additional, very short lived species increases with hydration. This may arise due to two effects. First, at higher hydrations more HDO molecules will be hydrogen-bonded to $D_2O$ molecules. These HDO molecules may couple well to modes of the $D_2O$ molecule and thus show a very fast relaxation. Another reason may be that at low hydration the $D_2O$ molecules that are hydrogen-bonded to the lipids have a longer $T_1$ lifetime. With increasing hydration the relative amount of the lipid-bonded $D_2O$ molecules will decrease, thus increasing the population of $D_2O$ molecules that are hydrogen-bonded to water (HDO/$D_2O$/$H_2O$).
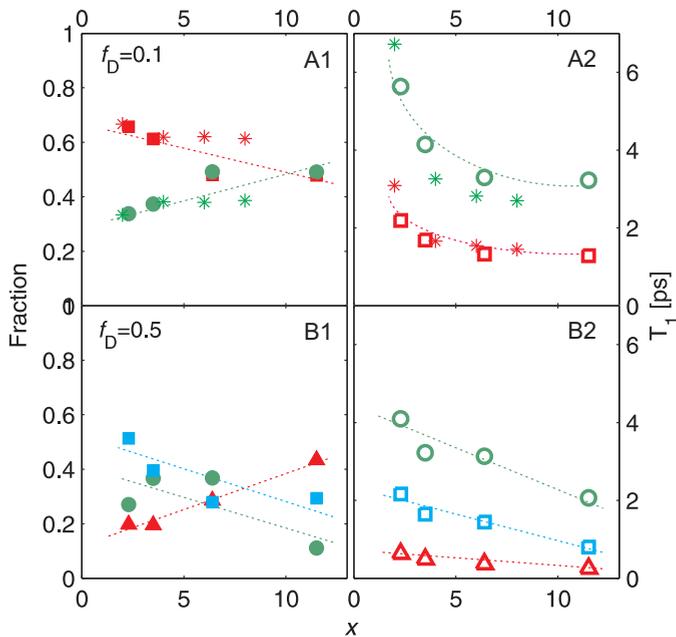
FIGURE 8.7. Summary of the extracted lifetimes and populations of different water species embedded in the DOPC multibilayers for different isotopic content of hydrating water (A-B). Left column (A1-B1) shows the extracted populations as a function of the hydration level. The populations of each species were normalized to the sum of all the populations at that specific hydration. Right column (A2-B2) shows the dependence of the vibrational lifetime on the hydration level. The dashed lines are guides to the eyes.

For the highest hydration level we have introduced an additional thermal equilibration state in the relaxation process to account for the spectral changes at late delays. From the fit we find that the thermal equilibration time amounts to ~8 ps (not shown) and involves an amplitude decrease of the thermal spectrum ( red to black spectrum in figure 8.5).

The isotropic data for the samples hydrated with pure $D_2O$ ($f_D$=1) is fitted with a four state consecutive relaxation model. We do not find any spectral or dynamical features that would allow us to disentangle water molecules forming hydrogen bonds with the phosphate groups, carbonyl groups or with other water molecules. In figure 8.8 we show the extracted lifetimes. The excited state lifetime amounts to $T_1 = {\sim}0.4$ p and does not change with hydration. No variation is also observed for the second state lifetime that represents the adaptation of the hydrogen bonds to the fast relaxation of the excited state. Interestingly, the cooling rate, decreases strongly with increasing hydration, from $T_* = {\sim}2.3$ ps for $x$=2.3 to $T_* = {\sim}6.3$ ps for $x = 11.5$. The thermal equilibration between water clusters and lipids takes place via lipid-bonded water molecules. At low hydra-
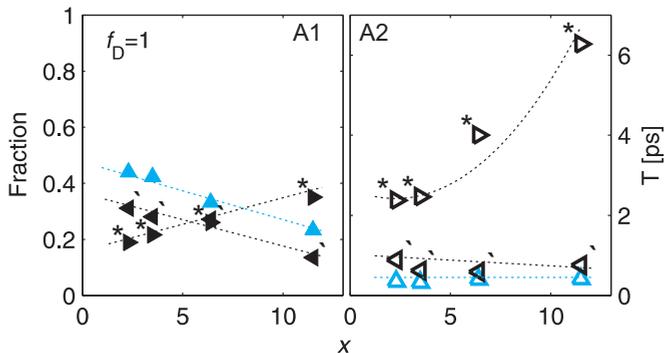
FIGURE 8.8. Summary of the extracted lifetimes and populations of the water species embedded in between the DOPC multibilayers for samples hydrated with pure $D_2O$ ($f_D=1$). The left panel shows the extracted populations as a function of the hydration. The populations of each state were normalized to the sum of all populations. The right panel shows the dependence of the vibrational lifetime on the hydration level. The dashed lines are guides to the eyes.

tion all the water molecules are bonded to the lipids, thus the (equilibration) redistribution of the vibrational energy between the low frequency modes of water and lipid molecules occurs relatively fast. At the highest hydration, however, the water forms nanopools, and these pools cool slower with increasing volume to surface ratio. The final, thermally equilibrated state is thus reached on a slower time scale than in the case of low hydration. The excited state spectral line shape (see figure 8.5) follows the strongly asymmetric shape of the linear absorption spectrum of $D_2O$ shown in figure 8.4 (bottom panel). In addition the excited state spectrum is somewhat deformed which results most likely from a partial excitation of the inhomogeneous absorption band. In the experiment we used infrared pulses with a bandwidth of about $\sim 150$ cm$^{-1}$ (FWHM) which is not sufficient to cover the whole OD stretch absorption spectrum of pure $D_2O$.

The two thermal states - local hot state and final thermally equilibrated state have similar spectral shapes since both result from a blueshift of the fundamental absorption spectrum. The final equilibrated state however has a smaller amplitude since the vibrational energy is redistributed over the whole system thus the blueshift of the absorption spectrum is smaller. A similar cooling process following vibrational relaxation has been observed for water confined in ionic micelles [37], for which the local thermalization among the water molecules is followed by the thermal equilibration between the water and the apolar solvent outside the micelle.

## 8.3.3    ANISOTROPIC DATA

In figure 8.9, we present the time dependent anisotropy parameter $R(t)$ for
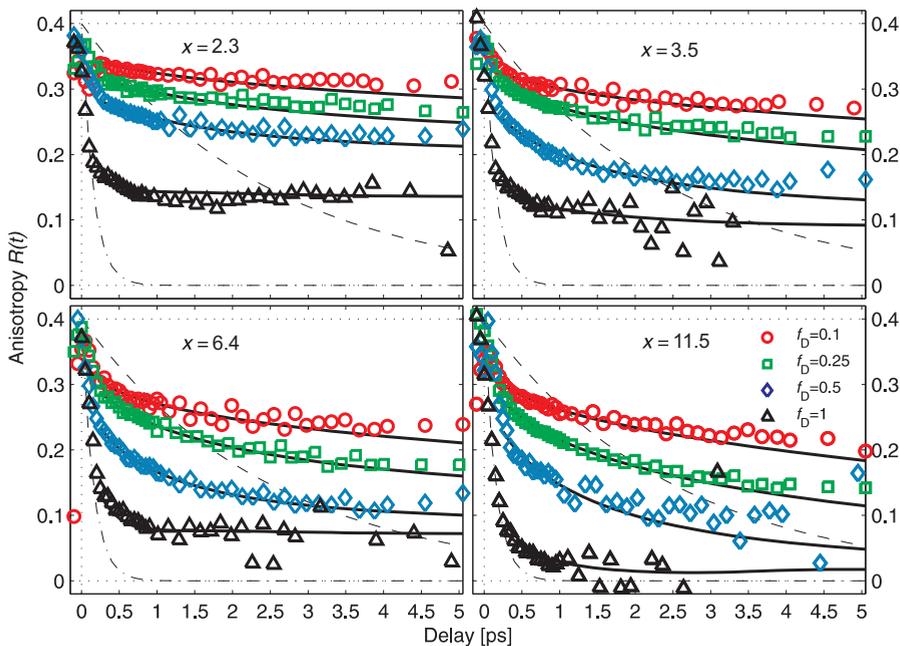
FIGURE 8.9. Anisotropy parameter $R(t)$ as a function of the delay time between the pump and probe pulses, for all the studied samples. Each panel shows anisotropy decays for different isotopic compositions of hydrating water ($f_D$) at one particular hydration level ($x$). For comparison the dashed and dash-dotted lines represent the anisotropy decays for diluted mixture of HDO in $H_2O$ ($\tau_r \sim 2.5$ ps) and for pure $D_2O$ ($\tau_r \sim 400$ fs) [128]. The solid black lines result from the fit to the model described in the text.

all studied samples. Each panel shows the anisotropy decay for samples at a specific hydration ($x$) and the four studied isotopic mixtures ($f_D$) of $H_2O$ and $D_2O$. The anisotropy time traces were constructed according to equation 2.33 with parallel ($\Delta\alpha_\parallel(t,\nu)$) and perpendicular ($\Delta\alpha_\perp(t,\nu)$) signals averaged over $\sim 30$ cm$^{-1}$ around the central frequency of 2500 cm$^{-1}$. Before constructing the anisotropy, the isotropic data were corrected for the heating effect, resulting from the dissipation of the vibrational energy. The correction involves subtraction of the heat signal from the isotropic data at all delay times. The time dynamics of the heat signal are assumed to follow the vibrational relaxation dynamics [134]. For the samples hydrated with $f_D = 0.5$ (highest hydration of $x = 11.5$) and pure $D_2O$ (all hydrations) we find that the intermediate local hot state is anisotropic. The presence of such an anisotropic heat state can be explained as follows. After the fast relaxation of the excited state of the OD stretch mode of $D_2O$ molecules (which is much faster than the relaxation of the OD stretch vibration of the HDO molecules, see figure 8.7 B2 and figure figure 8.8), the vibrational energy is redistributed over the lower frequency modes

among water molecules in the direct surroundings of the excited molecule. Due to the limited mount of water, this energy remains localized within the cluster for a longer time, forming a local, transient hot spot. Hence, the heating effect primarily influences the response of the originally excited OD vibrators, thus retaining the anisotropy of the transient spectrum. We correct for this effect by subtracting the anisotropy value taken at a delay where the vibrational relaxation of the OD stretch excited state is completed and all the population is in the intermediate hot state ($\sim$6 ps for $f_D$=0.5 and $x$=11.5; $\sim$4$\rightarrow$2.5 ps for $f_D$=1 and $x$=2.3$\rightarrow$11.5). We subtract this anisotropy value at all delays with a time evolution defined by the vibrational relaxation.

The anisotropy traces at all hydration levels are strongly non-exponential and are characterized by a fast initial decay (within the first $\sim$500 fs) followed by a much slower decay ($>$10 ps). After $\sim$5 ps, the anisotropy traces decay on such a slow timescale that in our experimental window we consider them reaching a constant end level. With increasing hydration we observe a moderate acceleration of the anisotropy decay for data hydrated with $f_D = 0.1$ (open red circles in each panel). The anisotropy decay changes from essentially non-decaying for $x = 2.3$ to slowly decaying on a $\sim$20 ps timescale for $x = 11.5$. We observe a similar trend for the anisotropy decays for the samples hydrated with $f_D = 0.25$ and 0.5. The anisotropy decays for the samples hydrated with pure $D_2O$ ($f_D$=1) show a very fast initial decay (within $\sim$1 ps) to an end level for all hydration levels.

The most significant changes in the anisotropy decay profile are observed when varying the isotopic composition of the hydrating water. Increasing the $D_2O$ content leads to a strong speed up of the decay within the first $\sim$2 ps. At later delays the decay rate is comparable for different $f_D$, except that the end level has decreased significantly with increasing $D_2O$ content.

The dashed lines in figure 8.9 represents the anisotropy for a dilute, bulk $D_2O$/$H_2O$ mixture [128]. It is clear that for all measured samples the anisotropy decays faster at early delays and slower at later delays than in the case of bulk water. The dash-dotted lines indicate the anisotropy decay for pure bulk $D_2O$ [128]. With increasing $D_2O$ content the anisotropy decays resemble more and more that of pure $D_2O$. Especially for $x = 11.5$ and $f_D = 1$ (black open triangles) the decay up to 500 fs resembles very much that of bulk $D_2O$. The discrepancy however occurs at later times at which the measured anisotropy does not decay to zero but reaches a non-zero end level.

The main part of the anisotropy decay may be caused by two effects (as discussed in sections 2.5.1 and 2.5.1): reorientation of the excited water molecules or vibrational resonant intermolecular energy transfer (VRET). For the samples hydrated at $x = 2.3$ with a dilute mixture of $D_2O$ in $H_2O$ ($f_D = 0.1$), one can assume that the intermolecular dipole-dipole coupling, due to its $1/r_0^6$ dependence, is very weak. Moreover, the lipids also act as a diluting medium, thus further increasing the distances between the OD oscillators. Thus the observed moderate acceleration of the anisotropy decay when increasing the hydration ($\sim$150 ps $\rightarrow$ $\sim$ 25 ps), most likely results from an increase in the (partial) mobility of the water molecules. We have tested this hypothesis by measuring the anisotropy decay for a sample hydrated at $x$=11.5 and a very dilute

mixture of 2% $D_2O$ in $H_2O$ ($f_D = 0.02$). It is clear that at these low isotope ratios the anisotropy decay is driven by the (limited) reorientation of water molecules rather than the vibrational resonant energy transfer. We observed that the anisotropy decay is identical to that of the sample hydrated at $x=11.5$ and $f_D=0.1$.

The fast component in the anisotropy decays observed at early delay times results most likely from a wobbling in a cone motion (hinging rotation) of the OD oscillators. Even strongly bonded and confined water molecules will maintain some freedom and fluctuate thermally giving rise to a spread of the direction of the OD oscillator within a cone. Such molecular motions has been observed for water molecules hinging between DMA molecules [156], water in reverse micelles [38, 109], and more recently for water embedded in DLPC stacked bilayers [177]. The amplitude of the fast component is approximately two times bigger (anisotropy amplitude drop of ∼20%) than for bulk water (∼10%), suggesting a larger angular cone spread. This may occur if the measured OD group of the water molecule is hydrogen-bonded to the lipid and the other OD group is free. The free OD may then rotate in propeller-like motion, "wobbling" the whole molecule around, thus increasing the angular spread of the hydrogen-bonded OD group. This picture is consistent with previous dielectric relaxation measurements on lipid multibilayers [155]. We observed, even at low hydration levels ($x < 4$), a presence of a fast (nearly bulk-like) rotational component in the THz spectra.

With increasing concentration of OD oscillators the mutual distances get smaller and the resonant dipole-dipole interactions become important. For higher $D_2O/H_2O$ ratios the decay of the anisotropy is mainly dictated by VRET, as observed for bulk water [128, 171]. VRET leads to a fast delocalization of the vibrational energy among randomly oriented water molecules. Thus VRET leads to a complete decay of the anisotropy to zero. The experimental data, however show that the anisotropy traces decay to a non-zero end level. This observation indicates that not all the water molecules participate in VRET which suggests that a fraction of the water molecules is located far enough from the other water molecules not to take part in the energy transfer. These isolated water molecules are likely hydrogen-bonded to the lipid and show very little or no reorientation just as the water molecules at $x=2.3$ and $f_D=0.1$.

In the case of pure $D_2O$ very fast intramolecular energy transfer will occur. Such intramolecular energy transfer leads (quasi-instantaneously) to a decay of the anisotropy to a value of ∼0.12 (energy transfer over an angle of 104°). This effect will contribute to the anisotropy decay for the samples hydrated with $f_D = 0.5$ and $f_D = 1$. Part of the initial decay observed for $f_D = 0.5$ (diamonds) and $f_D = 1$ (triangles) samples will thus result from this intramolecular energy transfer.

Based on the above observations we can construct a model to describe the experimental data. We consider all three contributions that may lead to the anisotropy decay:
- reorientation of the water molecules - $R_{reor.}(x;t)$,
- vibrational resonant energy tansfer between the water molecules - $R_{VRET}(x, f_D;t)$,

- intramolecular energy transfer for $D_2O$ molecules - $R_{IET}(f_D; t)$.

The time dependent anisotropy can be thus described with the following formula:

$$R(x, f_D; t) = \left[ R_{reor.}(x; t) \cdot R_{VRET}(x, f_D; t) \cdot A(x) + B(x) \right] \cdot R_{IET}(f_D; t), \quad (8.1)$$

where, $A(x)$ is the fraction of the water molecules participating in VRET and $B(x)$ is the fraction of the isolated water molecules that do not show VRET or (fast) reorientation. These molecules can only show intramolecular energy transfer if they are $D_2O$ molecules.

The intramolecular energy transfer term is given by:

$$R_{IET}(f_D; t) = \left( \frac{0.3 f_{D_2O}(f_D) \, e^{-k_{D_2O}t} + (1 - f_{D_2O}(f_D)) \, e^{-k_{HDO}t}}{f_{D_2O}(f_D) \, e^{-k_{D_2O}t} + (1 - f_{D_2O}(f_D)) \, e^{-k_{HDO}t}} \right) \quad (8.2)$$

where, $f_{D_2O}$ is the fraction of the $D_2O$ water molecules showing intramolecular energy transfer. The factor of 0.3 in the formula indicates a decay of the anisotropy from the initial value of $R(t) = 0.4$ to $R(t) = 0.12$ (30% of the initial value). The $D_2O$ and HDO water molecules have different vibrational lifetimes which determine their "visibility" in the anisotropy. It is therefore necessary to normalize each of these contributions to their lifetimes, thus the exponential terms characterized by $k_{D_2O}$ and $k_{HDO}$. In the global fit we use the vibrational lifetimes extracted from the fits to the isotropic data: the $D_2O$ lifetime $(1/k_{D_2O})$=0.4 ps, and the hydration dependent HDO lifetime, as depicted in figure 8.7.

Reorientation of the water molecules is described with a biexponential decay (as proposed in previous reports [14, 58, 176, 177]):

$$R_{reor.}(x; t) = c(x) \, e^{-k_{r1}t} + (1 - c(x)) \, e^{-k_{r2}t}, \quad (8.3)$$

where $c(x)$ and $(1-c(x))$ are the two fractions reorienting with $k_1$ and $k_2$ respectively.

Finally, the term describing the intermolecular energy transfer is given by:

$$R_{VRET}(x, f_D; t) = \exp\left(-F(x, f_D; t)\right), \quad (8.4)$$

where

$$\begin{aligned} F(x, f_D; t) = \frac{4}{3}\pi [2f_D C_W(x)]a^3 \exp\left(-\frac{k_1 r_0^6 t}{a^6}\right) \\ - \frac{4}{3}\pi^{3/2}[2f_D C_W(x)]\sqrt{k_1 r_0^6 t} \; \text{erf}\left(\sqrt{\frac{k_1 r_0^6 t}{a^6}}\right), \end{aligned} \quad (8.5)$$

where $[C_W(x)]$ is the concentration of water molecules involved in the VRET (expressed in $1/\text{Å}^3$), $k_1$ is the vibrational relaxation rate of the OD oscillator ($k_1 = 0.6$) and $r_0$ is the so-called Förster radius. Parameter $a$ is the minimal distance over which VRET can take place.

Here we modified the well known formula describing the resonant energy transfer in order to explicitly separate the two contributions: VRET and IET.

The derivation details can be found in appendix 8.5. In order to exclude the possibility for IET to contribute to the decay described by VRET term, we allow VRET to occur only between neighboring molecules and not between the two hydroxyl groups within the same molecule (see appendix 8.5). This is achieved by choosing the minimum value $a$ (over which energy transfer can take place) larger than the distance between the OD transition dipole moments within $D_2O$ molecule. This way we account for the two energy transfer contributions to the anisotropy decay separately.

Equation 8.5 differs from the well known, so-called Förster formula used previously to describe VRET in bulk water [128, 171].

$$R_{\text{VRET}}(x;t) = \exp\left(\frac{-4\pi^{3/2}}{3}[C_{\text{w}}(x)]\sqrt{k_1 r_0^6 t}\right), \tag{8.6}$$

This equation describes the anisotropy decay in bulk water very well, but it does not distinguish the contributions from VRET and IET.

In the fitting procedure we first separately fit the reorientation term $R_{\text{reor.}}$ to the data hydrated with $f_D = 0.1$ at all hydrations. We use the fitted values as constants in the global fit for all the data with increasing $f_D$. We find that our model is in excellent agreement with the experimental data. The result of the global fit is shown with solid, black lines in figure 8.9. The fit parameters are summarized in table II.

TABLE II. Parameters extracted from the global fit.

| $x$ | 2.3 | 3.5 | 6.4 | 11.5 |
|---|---|---|---|---|
| $A$ | 0.21 | 0.24 | 0.25 | 0.3 |
| $B$ | 0.11 | 0.07 | 0.05 | 0.01 |
| $c$ | 0.04 | 0.05 | 0.065 | 0.045 |
| $1/k_{\text{r1}}$ [ps] | 1 | 0.8 | 0.65 | 0.5 |
| $1/k_{\text{r2}}$ [ps] | 150 | 80 | 50 | 25 |
| $C_{\text{W}}\left[\frac{\text{n}}{\text{Å}^3}\right]$ | 0.018 | 0.0225 | 0.028 | 0.027 |
| $a$ [Å] | 1.7±0.2 | | | |
| $r_0$ [Å] | 2.4±0.2 | | | |

For each specific hydration level there will be a corresponding distribution profile of water molecules within the bilayer. Since the distribution does not change with the isotopic composition of the hydrating water, the distribution profile for each hydration level is determined by a single set of $A$, $B$ and $c$ fractions (see table II). To compensate for the uncertainty in the exact hydration level between the data sets hydrated with different $f_D$ we allowed the $A$, $B$ and $c$ fractions to vary within 10%. Thus the fractions are denoted as average values in table II. We have fitted the concentration of water molecules $C_{\text{W}}(x)$ that

participate in VRET provided that these molecules are all $D_2O$ ($f_D$=1). For samples hydrated with isotopic mixtures the amount of water molecules showing VRET is given by: $C_{OD} = 2f_D C_W$ ($f_D$=0.1, 0.25 or 0.5). The value of $C_W$ was allowed to differ by $\sim$15% from this value to account for the uncertainty in the exact hydration level.

### Discussion II

In figure 8.10 (top panel) we show the fractions A (water molecules involved in VRET) and B (isolated water molecules). We find that at very low hydrations, approximately 40% of the water molecules are involved in VRET. This is surprising taking into account the hydration level of only $\sim$2 water molecules per lipid. Due to the $r^{-6}$ dependence of the transfer rate these water molecules need to reside rather close to each other to exhibit the experimentally observed VRET. Our findings thus suggest that at low hydrations water molecules form clusters. With increasing hydration level the distribution of water molecules becomes more and more homogenous and at the hydration level of $\sim$12 water molecules per lipid (which is the maximal amount of water molecules a DOPC molecule can coordinate [72]) nearly all water molecules are involved in VRET. One can imagine that at this hydration level water forms a 2-dimensional layer separating the two bilayers, whereas at lower hydrations this 2D water sheet is torn at places. "Touching" bilayers will expel water molecules at some places, "forcing" them to aggregate elsewhere. At the hydration level of $x = 12$ DOPC bilayers start to swell, the interbilayer distance increases and water is comfortably accommodated between the bilayers forming a continuous layer [65].

The bottom panel in figure 8.10 shows the extracted fractions of $D_2O$ ($f_{D_2O}$) molecules exhibiting intramolecular energy transfer. The dashed line indicates the theoretical amount of $D_2O$ water molecules in the sample. As expected the fraction of intramolecular energy transfer increases with increasing $D_2O/H_2O$ isotope ratio. Interestingly we also observe that $f_D$=1 the amount of $D_2O$ molecules showing intramolecular energy transfer increases with the hydration level. The intramolecular energy transfer in bulk water is extremely efficient because of the strong spectral overlap of the OD stretch vibrations. At low hydration levels, all water molecules are hydrogen bonded to the lipids, with which they from stronger bonds than among each other ($HB_{phosphate} > HB_{carbonyl} > HB_{water}$). For many of these $D_2O$ molecules one of the hydroxyl groups will be hydrogen bonded to the lipid (phosphate or carbonyl group) and the other one will be bonded to other water molecules or will remain free. Due to this asymmetry, the two vibrations of the two hydroxyl groups will not be as strongly mixed as in bulk (red circles in figure 8.10, lower panel). For samples with higher hydration levels there are more and more molecules forming hydrogen bonds to other water molecules, thereby increasing the fraction of $D_2O$ molecules for which the OD vibrations are in resonance, and thus show rapid IET.

From the fit of the anisotropy decays to the model we can determine the hydration level dependent specific concentration of OD oscillators [$C_{OD}(x) = 2f_D C_W(x)$] involved in the resonant energy transfer. The extracted values are indicated in figure 8.11 with open circles. It is interesting to compare this con-
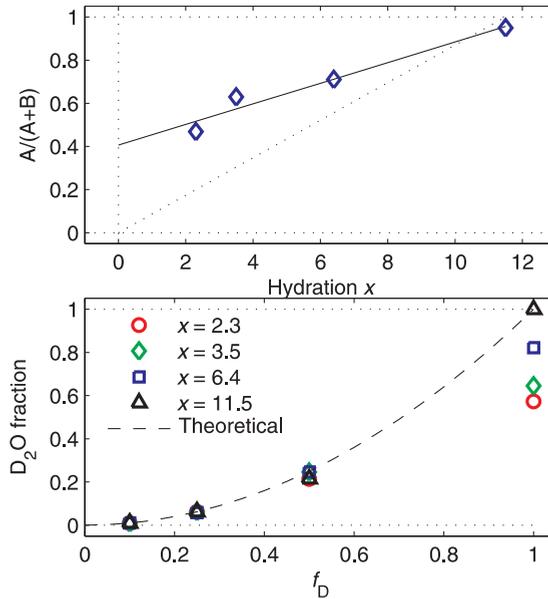
FIGURE 8.10. Top panel: Fractions A and B as a function of the hydration level. Bottom panel: The fraction of $D_2O$ molecules showing intramolecular energy transfer as a function of the isotopic composition at studied hydration levels. The dashed line indicates the fraction of $D_2O$ molecules present in the system and overlaps well with the extracted $D_2O$ fractions for $x=11.5$. The dotted lines represent quadratic fit at each hydration level ($D_2O$ fraction $= f_D^2$). For lower hydration levels the extracted $D_2O$ fractions for $f_D=1$ are smaller than the amount of $D_2O$ molecules in the system indicating that not all the $D_2O$ exhibit intramolecular energy transfer.

centration with the average concentration of OD oscillators, assuming a homogeneous distribution over the lipid layers. This concentration is given by:

$$N_{OD} = \frac{2f_D x}{V_L + V_W x},\tag{8.7}$$

where $x$ is the hydration number, $V_L$ is the volume of a DOPC molecule and $V_W$ is a volume of water molecule. The volume of the DOPC molecule in the lamellar liquid crystalline phase amounts to $\sim$1300 $\text{Å}^3$ [56, 169]. The volume of a water molecule is $\sim$30 $\text{Å}^3$. The concentration of OD oscillators based on this estimation is indicated with the dashed line in figure 8.11. Clearly at all hydrations, the concentration of the OD oscillators extracted from the fit to the observed VRET, is much higher than the concentration of water homogenously distributed within the bilayer. It is reasonable to assume that nearly all water molecules are located, as shown by numerous x-ray and neutron scattering experiments, in between the lipid bilayers and protrude the bilayers only up to the carbonyl moieties [65, 159]. By using the volume of a lipid headgroup (estimated to be $\sim$1/3 of a volume of the whole lipid), instead of the
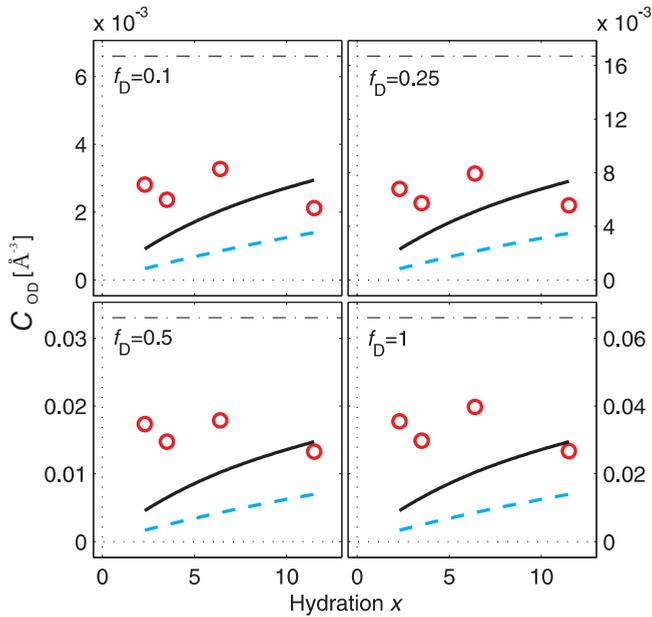
FIGURE 8.11. Concentration of OD groups $C_{OD}$ showing VRET as a function of the hydration level. The dashed line indicates the average OD concentration when the water molecules are homogeneously distributed over the complete volume of the lipid. The solid line indicates the average OD concentration when the water molecules are homogeneously distributed over the volume of the lipid headgroup. The dash-dotted lines indicate the OD concentration of bulk water for each isotope mixture.

volume of the whole lipid, we can thus calculate the average concentration of OD oscillators assuming the water molecules to be located only near the headgroup volume of the membrane. We indicate this concentration as a function of the hydration level with the solid lines in figure 8.11. We find that at low hydration levels this concentration is still lower than the concentration of OD oscillators extracted from the fit to the observed VRET. The two values become similar for maximum hydration of the membranes.

The concentration of OD oscillators showing VRET is quite independent of the hydration level. This means that the average distance between the OD groups does not decrease with increasing hydration level. The OD concentration only depends on the isotope composition. This suggests that the water molecules form small clusters. With increasing hydration level the number density of these clusters increases as expressed in the increase of the fraction A. The independence of $C_{OD}$ on the hydration level indicates that the composition and size of the clusters is very similar at all hydration levels.

The non-homogenous character of water distribution at the interface of lipid membranes is consistent with Monte Carlo simulations of the interactions between stacked lipid bilayers [54]. Gouliaev *et al.* demonstrated the presence of

strong local perturbations (ripples) in the membrane ordering, often leading to soft collisions between the bilayers. Especially at low hydrations these collisions will assist water molecules to cluster at places where there is space available between the bilayers and at the same time water will be "expelled" from places where the two bilayers touch.

The very slow reorientation time of water molecules at the membrane interface at low hydration and $f_D$=0.1 is most likely dictated by the residence time of water molecules at the binding site, which then essentially reflects the hydrogen bond lifetime. Using molecular dynamics simulations, Bhide *et al.* determined the residence time of water molecules at different regions in the membrane: Region I (phosphate and carbonyl associated water molecules) - $\sim$600 ps, region II (lipid headgroup) - $\sim$40 ps [14]. We can thus assume that within the time we determine the anisotropy parameter the measured water molecules remain hydrogen-bonded. In region III (second hydration shell around lipid headgroup) the reorientation time is $\sim$3 ps, however we do not reach hydration levels high enough for these water molecules to contribute significantly [14].

## 8.4    CONCLUSIONS

We used polarization-resolved, ultrafast pump-probe spectroscopy to study the vibrational energy relaxation and anisotropy decay of water molecules at a cell membrane model interface. The studied samples consisted of a stack of monodomain DOPC multibilayers. In the experiment we vary both the hydration level of the membrane and the isotopic composition of the hydrating water ($D_2O$/$H_2O$ ratio).

We find that water molecules at the membrane's interface experience very different local environments depending on which site of the lipid they are hydrogen-bonded to. Water molecules forming strong hydrogen-bonds with phosphate relax faster than water molecules that are hydrogen-bonded to carbonyl groups and other water molecules. For samples that are highly hydrated and/or contain a high fraction of $D_2O$ ($\geqslant$50%), the vibrational relaxation is observed to be followed by a thermalization and cooling process.

We also performed polarization-resolved experiments to measure the anisotropy dynamics of the OD oscillators. By varying the isotopic composition of the hydrating water we find that the anisotropy decays are dominated by two contributions: intermolecular resonant (Förster) energy transfer and intramolecular energy transfer within $D_2O$ molecules. There is also a fraction of water molecules for which there is no vibrational resonant energy transfer (VRET). These water molecules are apparently isolated. With increasing membrane hydration level the fraction of isolated water molecules decreases and at a hydration of approximately 12 water molecules per lipid, the water between the two bilayers forms a two-dimensional continuous sheet. Our findings demonstrate that in tightly packed membranes with a low hydration level the distribution of water molecules is highly inhomogeneous. Throughout the membrane interface there are regions poor in water and regions with nearly bulk-like water pools as schematically depicted in figure 8.12.
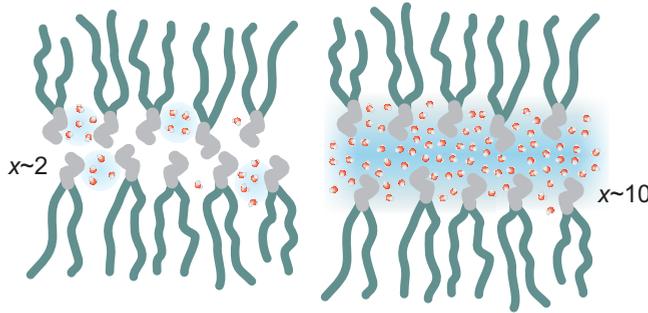
FIGURE 8.12. A cartoon showing the difference between the water distribution between the two lipid monolayers at low ($x \sim 2$) and high ($x \sim 10$) hydration levels.

## 8.5   APPENDIX: ANISOTROPY

In section 2.5.1 we showed how the Förster formula for resonant energy transfer is derived. We showed that the anisotropy decay due to this transfer is described by the excitation survival probability $\rho(t)$:

$$\rho(t) = \left\{ \frac{4\pi}{V} \int_0^R exp\left(\frac{-tr_0^6}{T_1 r^6}\right) r^2 dr \right\}^N, \tag{8.8}$$

This approach assumes a statistical distribution of molecules, thus includes all possible distances between them. Hence the integral is performed from $R=0$. In the case of water molecules it thus intrinsically takes into account an intramolecular energy transfer. To describe the anisotropy decays for water molecules at the lipid membranes interface we want to separate the contributions from vibrational resonant energy transfer (VRET) and intramolecular energy transfer (IET). We account for IET with equation 8.2. From the term describing solely VRET we need to exclude the possibility of energy transfer within the same molecule (over a distance of $\sim 1.55$ Å). This is achieved by performing the integration from a distance $R = a$, which should be on the order of an intermolecular distance ($\sim 2.2$ Å considering the intermolecular hydrogen-hydrogen distance).

The excitation survival probability $\rho(t)$ is thus given by:

$$\rho(t) = \left\{ \frac{4\pi}{V} \int_a^R \exp\left(\frac{-tr_0^6}{T_1 r^6}\right) r^2 dr \right\}^N, \tag{8.9}$$

Performing the integration, we obtain:

$$\begin{aligned} \rho(t) = & \left\{ \frac{4\pi}{V} \left[ \frac{1}{3} R^3 \exp\left(-f(t)\right) - \frac{1}{3} a^3 \exp\left(-g(t)\right) + \right. \right. \\ & \left. \left. + \frac{1}{3}\sqrt{\frac{\pi t r_0^6}{T_1}}\, \text{erf}\left(\sqrt{f(t)}\right) - \frac{1}{3}\sqrt{\frac{\pi t r_0^6}{T_1}}\, erf\left(\sqrt{g(t)}\right) \right] \right\}^N, \end{aligned} \tag{8.10}$$
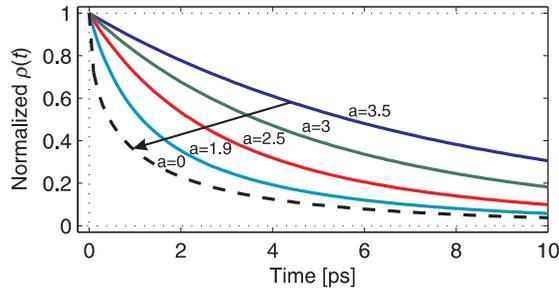
FIGURE 8.13. Excitation survival probability function for various minimal energy transfer distances $a$. VRET becomes slower for larger intramolecular distances $a$. For $a \to 0$ the decay profile is given by equation 8.6

where

$$f(t) = \frac{t r_0^6}{T_1 R^6} \quad \text{and} \quad g(t) = \frac{t r_0^6}{T_1 a^6}$$

Following the steps shown in section 2.5.1 we obtain:

$$\rho(t) = \exp\left(-\frac{4\pi C_{\mathrm{OD}} a^3}{3} \exp(-g(t)) - j(t)\,\mathrm{erf}\left(\sqrt{g(t)}\right)\right), \qquad (8.11)$$

where,

$$j(t) = \frac{4\pi^{3/2} C_{\mathrm{OD}} r_0^3 \sqrt{t}}{3\sqrt{T_1}}. \qquad (8.12)$$

Here $C_{\mathrm{OD}}$ is expressed as the number of OD groups per unit volume $(1/\text{Å}^3)$. This formula can be used to describe resonant energy transfer for any system with a non-zero minimal distance between the donors and acceptors.

From the above equation it follows that for $a \to 0$ the above formula converges to the well known form derived in section 2.5.1 (also see figure 8.5):

$$\rho(t) = \exp\left(\frac{4\pi^{3/2} C_{\mathrm{OD}} r_0^3 \sqrt{t}}{3\sqrt{T_1}}\right). \qquad (8.13)$$

# 9 INTERFACIAL WATER STRUCTURE

We study the structure of water at interfaces with ultrafast two-dimensional surface-specific vibrational spectroscopy. We find that the structure of heavy water at the water-air interface is highly heterogeneous and strongly differs from that at the water-lipid interface.

## 9.1 INTRODUCTION

Water differs markedly from liquids of similar molecular weight in properties such as specific heat, phase behavior, and dielectric constant. Many of these special properties can be traced back to the unique intermolecular interactions that occur through hydrogen bonds between the hydrogen atoms and oxygen atoms of different water molecules [11]. At the surface or interface of water, the water hydrogen-bonded network is abruptly interrupted, conferring yet different properties on interfacial water [143]. Despite its importance for disciplines such as electrochemistry, atmospheric chemistry, and membrane biophysics, the structure of interfacial water has remained highly debated [6, 26, 40, 41, 44, 51, 53, 111, 138, 143, 144, 147, 148, 150, 153].

The challenge of specifically probing molecules at the outermost surface layers of water has been met with sum-frequency generation (SFG) spectroscopy of the O-H stretch vibrations of the water molecules. In an SFG experiment, infrared and visible laser pulses are overlapped in space and time on a surface, and the sum-frequency of the two laser fields is generated, but in the top molecular layers only [142]. If the infrared light is resonant with the O-H stretch vibration of surface water, this process is resonantly enhanced. The shape and intensity of the SFG spectrum are determined by the frequency dependence of the second-order non-linear susceptibility $\chi^{(2)}$. Information about the interfacial water structure is then inferred through the correlation between the O-H stretch vibrational frequency of an O-H group in a water molecule and its local hydrogen-bonded environment.

Initial SFG studies revealed distinct peaks in the SFG spectra of interfacial water, as exemplified in the SFG spectra of the water-air and water-lipid interfaces shown in figure 9.1. The lipid is a standard cationic lipid, 1,2-dipalmitoyl-3- trimethylammonium-propane (DPTAP). The two peaks appearing at ~2350 and ~2500 cm$^{-1}$ have been assigned in different ways, to "ice-like" and "liquid-like" structures [40, 41, 138] and to the result of intra- and intermolecular
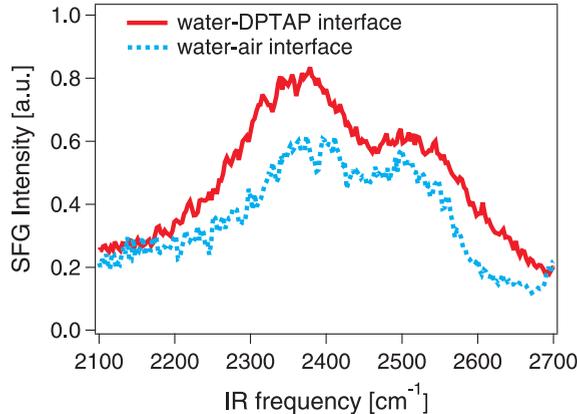
FIGURE 9.1. Normalized SFG spectra at the $D_2O$ water-air (dotted, blue) and water-lipid (solid, red) interfaces. The spectrum for the water-lipid interface has been offset by 0.2 for clarity.

couplings [117, 148]. There is surprising similarity between the two spectra, suggesting that the interfacial water structure is also very similar. The spectra reported in figure 9.1 are SFG intensity spectra, with $I_{SFG} \sim |\chi^{(2)}|^2$. Heterodyne detected SFG measurements, which allow one to disentangle the real and imaginary parts of the vibrational response ($\mathrm{Re}[\chi^{(2)}]$ and $\mathrm{Im}[\chi^{(2)}]$), have shed additional light on the origin of the SFG spectra [74, 116]. $\mathrm{Im}[\chi^{(2)}]$ reflects the dissipative part of the response function, and constitutes the surface equivalent of a bulk absorption spectrum. These experiments have shown that, while the water-DPTAP $I_{SFG}$ spectrum directly reflects $\mathrm{Im}[\chi^{(2)}]$, the situation is more subtle for the water-air interface, where $\mathrm{Im}[\chi^{(2)}]$ can differ significantly from the $I_{SFG}$ spectrum [74, 116].

In bulk water, the complex absorption spectrum has been unraveled and interpreted in terms of water structure and structural dynamics by measuring the ultrafast frequency fluctuations and correlations of the O-H stretch vibration, with spectral whole burning [7, 50] and two-dimensional infrared (2D-IR) spectroscopy [46, 136].

## 9.2   EXPERIMENT

Here, we analyze the origin of the interfacial water SFG spectrum in terms of the structure and dynamics of interfacial water using surface-specific two-dimensional infrared sum-frequency generation spectroscopy [23].

In the experiment, we used an IR-pump – SFG-probe scheme (see section 3.4), in which the pump spectrum was spectrally narrow and continuously tuned across the absorption band of water. The laser pulses used in the experiment were generated with the laser system and the frequency conversion processes described in sections 3.1 and 3.2. As a pump we used an intense infrared

pulse ($\sim 12$ $\mu$J) of $\sim$80-150 cm$^{-1}$ bandwidth (pulses duration of $\sim 150 - 180$ fs), tuned in steps of 75 cm$^{-1}$ across the entire water band to resonantly excite the vibrations of specific subsets of D$_2$O molecules. For the detection process, broadband mid-IR ($\sim 500$ cm$^{-1}$ bandwidth and energy of $\sim$6.5 $\mu$J and pulse duration of $\sim$60 fs) and narrowband visible (15 cm$^{-1}$ bandwidth and energy of $\sim$10 $\mu$J) upconversion pulses were mixed at the interface to generate a conventional SFG signal. The experimental time resolution, determined by the cross-correlation between the pump and the IR detection pulses is approximately 200 fs. Both the pump and the IR detection pulses were continuously monitored with a frequency-resolved IR detection set-up (see section 3.3) consisting of an ORIEL monochromator and a 2x32-pixel, mercury-cadmium-telluride (MCT) array detector. Different pump frequencies (2275, 2350, 2425, 2500, 2575, 2625, 2750 and 2825 cm$^{-1}$) were used to excite the hydrogen-bonded and the free O-D part of the interfacial O-D stretch absorption band. The spectra of these pulses are shown in figure 9.2. All experiments were performed at least twice to ensure their reproducibility.

2D-SFG spectra were composed from the transient spectra recorded at delay times of 0, 600/540 and 3000 fs following standard procedures [28]: vertical cuts at specific excitation frequencies were calculated using a weighted average of transient spectra at different pump frequencies, with the weights determined by the relative intensities of the pump spectra at that frequency, as inferred from the spectra in figure 9.2. The resulting 2D-SFG spectrum was Fourier-filtered to remove high-frequency noise resulting from the detection. Care was taken while removing the high-frequency noise not to affect the 15 cm$^{-1}$ experimental resolution (determined by the bandwidth of the VIS pulses), that is, to avoid smearing out experimental features in the recorded two-dimensional spectrum. Within the frequency window 2400-2800 cm$^{-1}$, the two-dimensional spectra could be determined with an accuracy better than 1% of the original SFG spectra; outside this window the low IR probe energy caused some noise. In the experiment, the pump frequency that determined the horizontal axis of the two-dimensional vibrational spectrum was scanned. The vertical axis is defined by the infrared frequency of the SFG probing process. The experiments were preformed in the S/S/P (SFG/VIS/$IR_{\text{probe}}$) polarization configuration with respective incident angles of 56°, 40° and 70° with respect to the surface normal. The polarization of the pump pulses was P. The third-order cross-correlation between the IR pump, IR probe and visible pulses generated from the heavy water surface was used to optimize the spatial overlap and to define the position of $\tau = 0$.

Heavy water - D$_2$O (Cambridge Isotope Laboratories. Inc., 99.96 atom %D; pH=$\sim$5.5) was used without further purification. 1,2-dipalmitoyl-3-trimethylammonium-propane - DPTAP was purchased from Avanti Lipids and used without further purification. The teflon sample trough was cleaned with piranha solution (3:1 volume ratio of sulfuric acid and 30% hydrogen peroxide solution). During the experiment the trough was rotated to avoid accumulated heating by the laser pulses. The vertical sample position was controlled by a feedback loop to compensate for water evaporation. The entire set-up was enclosed and flushed with N$_2$ gas to remove spectral distortions originating
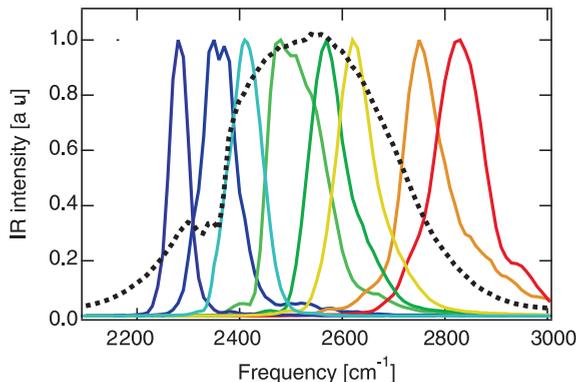
FIGURE 9.2. Pump spectra used in the experiment. Dotted line indicates infrared probe spectrum.

from $CO_2$ absorption in the air.

## 9.3 RESULTS AND DISCUSSION

The left column of figure 9.3 shows 2D-SFG spectra in the O-D stretch region of the heavy water ($D_2O$)-air interface. It shows the interfacial water response as a function of the excitation (horizontal axis) and detection (vertical axis) frequencies at different delay times between the excitation and detection pulses.

For the water-air interface, clearly only one feature is observed in the 2D-SFG spectrum, although the SFG spectrum contains two peaks. This can be traced back to the fact that the excitation axis of the 2D-SFG spectrum is determined by the IR absorption of the surface water molecules, rather than by their SFG intensity spectrum. This absorption spectrum contains only one broad peak in the hydrogen-bonded region, as is evident from both the IR absorption spectrum of bulk water and the frequency dependence of the $\text{Im}[\chi^{(2)}]$ spectrum [74, 116]. Along the detection axis we also observe only one broad peak, which most likely results from the specific incidence angles of IR probe and VIS pulses. It has been shown previously that the shape of the SFG spectrum depends on the incidence angle of the two beams [146].

For a completely inhomogeneous surface, the response in a 2D spectrum would lie along the diagonal (dashed line in figure 9.3; slope = 1), as only those water molecules are affected that have been resonantly excited. For a completely homogeneous surface, the response would give rise to a spherical lineshape: irrespective of the excitation frequency, the response would always be the same (see section 2.6.2). The observed 2D spectral response in the H-bonded region of the water-air interface clearly lies in between these two extremes (see figure 9.3). The solid lines in the spectra are linear fits to the signal maxima at different excitation frequencies, resulting in a line whose initial slope of $0.23 \pm 0.06$ decreases with waiting time. This is direct evidence for the heterogeneity of

interfacial water, although the heterogeneity is clearly limited (the slope is only 0.23). Hence, the 2D spectra show that a continuum of different hydrogen-bonded interfacial water structures exists within the broad H-bonded spectral feature, with no evidence for distinct ("ice-like" and "liquid-like") substructures.

The apparent decay of the slope of the diagonal feature in the 2D spectra is due to rapid spectral diffusion. Such spectral diffusion can be due to structural relaxation processes [3, 32, 79], but may also be indicative of intermolecular energy transfer: vibrational energy transfer can occur between differently hydrogen-bonded O-D groups with different frequencies [32, 79, 128, 171] due to dipole-dipole coupling between different O-D groups. Irrespective of the cause of the spectral diffusion, the initial slope of 0.23 sets a lower limit on the intrinsic heterogeneity of water at the water-air interface.

We can translate the slope of 0.23 into the homogeneous and inhomogeneous linewidths of the interfacial water vibration. Assuming that the vibrational response can be described by a Gaussian distribution of Lorentzian lines characterized each by a width (full width at half-maximum) of $\Delta_{\text{inh.}}$ and $\Gamma_{\text{hom.}}$, respectively, we can define an inhomogeneity parameter $\Upsilon = \Delta_{\text{inh.}}/(\Delta_{\text{inh.}}+\Gamma_{\text{hom.}})$. In the inhomogeneous limit, $\Upsilon = 1$ ; it equals zero in the homogeneous limit. The initial slope in the 2D spectrum of 0.23 corresponds to a value of the inhomogeneity parameter of $\Upsilon = 0.31$. The obtained inhomogeneous and homogeneous linewidths are $\Delta_{\text{inh.}}$=115 cm$^{-1}$ and $\Gamma_{\text{hom.}}$=240 cm$^{-1}$, which yield the overall linewidths of the O-D stretch absorption band of $\sim$310 cm$^{-1}$. A detailed description of the procedure of obtaining the inhomogeneity parameter $\Upsilon$ can be found in appendix 9.5.

Remarkably, the results obtained for water-lipid interface shown in the right column of figure 9.3, reveal a completely different picture of water at lipid interfaces. Distinct (weakly and strongly H-bonded) water molecules can be identified at the water-lipid interface (figure 9.3, right column), with strongly different vibrational dynamics. Strongly H-bonded water molecules on the red side of the peak show very fast vibrational dynamics (indicated by the circle in the center image): after 600 fs most of the bleach has vanished, while the peak at higher frequency (oval in center plots) has the same shape and displays the same dynamics as that observed for the water-air interface. Note that the two ovals drawn in the center panels are identical. The results obtained here are consistent with, and further refine our earlier time-resolved one-color study of water dynamics at lipid interfaces [20]. In this previous study, single-color lifetime measurements indicated the presence of two distinct water species, which is unambiguously proven here. The strongly H-bonded water molecules apparently do not exchange vibrational energy with the near-surface water molecules, and are therefore concluded to interact with the lipid head group, explaining their absence at the water-air interface. The presence of distinct peaks in the 2D-SFG spectrum has been predicted theoretically [115], and interpreted in terms of water species exhibiting different spectral diffusion dynamics. Nagata *et al.* concluded that the near-bulk water nonadjacent to lipids (residing at higher frequency) has faster spectral diffusion than the top-layer water directly hydrating the lipids (residing at lower frequency). The strongly H-bonded water molecules observed here are expected to play an important role in protein function and
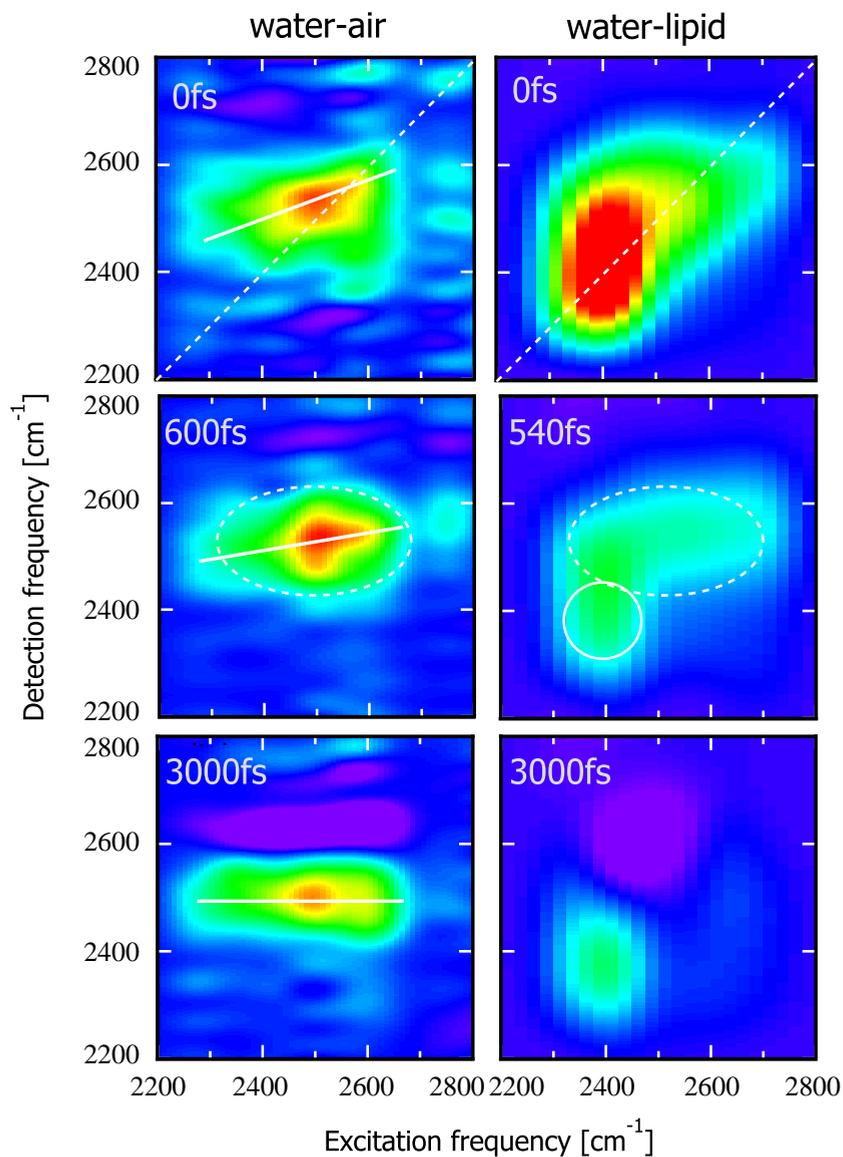
FIGURE 9.3. Two-dimensional SFG spectra of the $D_2O$ water-air (left column) and water-lipid (right column) interfaces at various pump-probe delay times indicated in the graphs. The dashed line in the upper panels denotes the diagonal. The solid lines in the left column represents the average slope of the diagonal peaks. The dotted ovals indicate the bulk-like water, whereas the solid circle denotes the lipid-associated water.
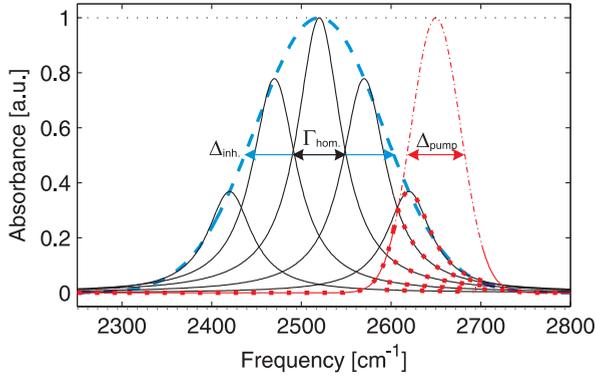
FIGURE 9.4. A set of homogenously broadened lineshapes (solid, black) and inhomogeneous broadening line shape (dashed, blue). The dash-dotted (red) line represents the pump spectrum with FWHM $\Delta_{\text{pump}}$. The dotted (red) lines indicate the overlap area between the pump spectrum and the homogenously broadened absorption lines.

proton transport along the membrane.

## 9.4    CONCLUSIONS

In summary, the similarity between the static SFG spectra of water at the water-air and water-lipid interfaces (figure 9.1) is shown to break down in the 2D-SFG measurements (figure 9.3), which reveal that the water structure is very different for these interfaces. 2D-SFG spectrum of water-air interface is characterized by a single spectral feature possessing a short-lived heterogeneity. For the water-lipid interface we find two distinct spectral features in the 2D-SFG spectrum, which indicates presence of two distinct water species. The technique of 2D-SFG is thus shown to provide a new way of investigating the structure and previously inaccessible structural dynamics of aqueous interfaces.

## 9.5    APPENDIX: INHOMOGENEITY PARAMETER

In order to quantify how homogeneous/inhomogeneous our interfacial water is, we define an inhomogeneity parameter:

$$\Upsilon = \frac{\Delta_{\text{inh.}}}{\Delta_{\text{inh.}} + \Gamma_{\text{hom.}}} , \tag{9.1}$$

which relates the inhomogeneous broadening linewidth $\Delta_{\text{inh.}}$ to the homogeneous linewidth $\Gamma_{\text{hom.}}$. In the homogeneous limit $\Delta_{\text{inh.}} \rightarrow 0$ so $\Upsilon = 0$. For an extremely inhomogeneous system $\Delta_{\text{inh.}} \gg \Gamma_{\text{hom.}}$ and $\Upsilon = 1$.

     The vibrational absorption band can be described by an inhomogeneous (Gaussian) distribution ($G(\nu_{\text{inh.}}, \nu_0)$) of homogenously broadened lineshapes
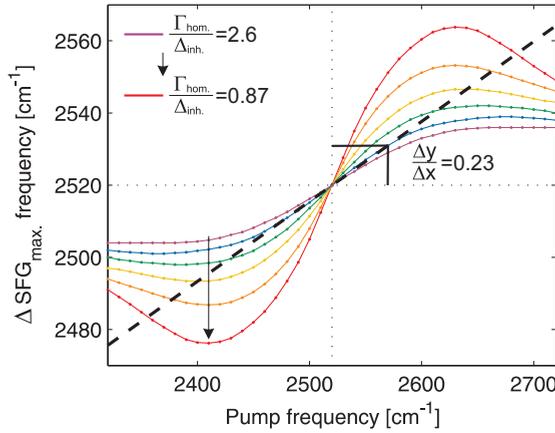
FIGURE 9.5. The effect of inhomogeneous broadening on the slope of the SFG response. The larger is the $\Delta_{\text{inh.}}/\Gamma_{\text{hom.}}$ ratio, the more inhomogeneous the systems is and $\Upsilon \rightarrow 1$.

(Lorentzians - $L(\nu, \nu_{\text{inh.}})$) characterized with widths (FWHM) $\Delta_{\text{inh.}}$ and $\Gamma_{\text{hom.}}$ respectively (see figure 9.4):

$$F(\nu, \nu_0, \nu_{\text{inh.}}) = G(\nu, \nu_0)L(\nu, \nu_{\text{inh.}}),  \tag{9.2}$$

where

$$G(\nu_{\text{inh.}}, \nu_0) = \exp\left(-\frac{2.7726(\nu_{\text{inh.}} - \nu_0)^2}{\Delta_{\text{inh.}}^2}\right),  \tag{9.3}$$

and

$$L(\nu, \nu_{\text{inh.}}) = \frac{\Gamma_{\text{hom.}}}{(\nu - \nu_{\text{inh.}})^2 + \Gamma_{\text{hom.}}^2}.  \tag{9.4}$$

$\nu_{\text{inh.}}$ is the central frequency of a homogenous lineshape and $\nu_0$ is a central frequency of the broadening gaussian function. It should be noted that this approach is a simplification, because we assume that the inhomogeneous broadening has a Gaussian shape, and because we do not distinguish the symmetric and asymmetric stretch vibration contributions to the overall absorption band. The overall lineshape of the absorption band is given by $\int F(\nu, \nu_0, \nu_{\text{inh.}}) \, d\nu_{\text{inh.}}$. We further calculate the probability of exciting each subset of water molecules $E_{\text{exc.}}$ with a pump spectrum described with a Gaussian shape with a width $\Delta_{\text{pump}}$ (figure 9.4, red line). The excitation probability for a given subset is given by the overlap of the homogenous lineshape with the pump spectrum (outlined with the dashed red line in figure 9.4):

$$E_{\text{exc.}}(\nu_{\text{inh.}}, \nu_0, \nu_{pump}) = \int L(\nu, \nu_{\text{inh.}})G(\nu_{\text{inh.}}, \nu_0)P(\nu, \nu_{\text{pump}}) \, d\nu,  \tag{9.5}$$

where $P(\nu, \nu_{\text{pump}})$ is the pump spectrum defined as:

$$P(\nu, \nu_{\text{pump}}) = \exp\left(-\frac{2.7726(\nu - \nu_{\text{pump}})^2}{\Delta_{\text{pump}}^2}\right).  \tag{9.6}$$

For a given pump spectrum and inhomogeneity, the pump-probe signal profile $S(\nu, \nu_0, \nu_{\text{pump}})$ is given by the sum of the excitation probabilities of all of the subsets multiplied by their homogeneous lineshapes:

$$S(\nu, \nu_0, \nu_{\text{pump}}) = \int E_{\text{exc.}}(\nu_{\text{inh.}}, \nu_0, \nu_{pump}) L(\nu, \nu_{\text{inh.}}) \, d\nu_{\text{inh.}} \tag{9.7}$$

In figure 9.5 we show the relation between the pump frequency ($\nu_{\text{pump}}$) and the maximum of the pump-probe signal ($\max(S(\nu, \nu_0, \nu_{\text{pump}}))$) for various ratios between the homogeneous ($\Delta_{\text{inh.}}$) and inhomogeneous ($\Gamma_{\text{hom.}}$) linewidths. From figure 9.5 we can thus find a combination of inhomogeneous and homogeneous linewidths $\Delta_{\text{inh.}}$ and $\Gamma_{\text{hom.}}$ such that the slope of the pump-probe (IR-pump SFG-probe) response corresponds to that in the experimental data. We obtain the absolute values for $\Gamma_{\text{hom.}}$ and $\Delta_{\text{inh.}}$ by fitting the $\int F(\nu, \nu_0, \nu_{\text{inh.}}) \, d\nu_{\text{inh.}}$ with a given $\Gamma_{\text{hom.}}/\Delta_{\text{inh.}}$ ratio to the $D_2O$ linear absorption band.

# 10 ULTRAFAST VIBRATIONAL ENERGY TRANSFER AT THE WATER–AIR INTERFACE

One of the unique properties of water is the very efficient transfer of vibrational energy between molecules, which arises as a result of strong dipole-dipole interactions between the O-H oscillators. Although we have a sound understanding of this energy transfer process in bulk water, we know less about how, and how quickly, energy transfer occurs at the water surface. Here, we use ultrafast two-dimensional surface-specific vibrational spectroscopy to probe the interfacial energy dynamics of heavy water ($D_2O$) at the water/air interface. The measurements reveal the presence of surprisingly rapid energy transfer, both between hydrogen-bonded interfacial water molecules (intermolecular), and between O-D groups sticking out from the water surface and those located on the same molecule and pointing towards the water bulk (intramolecular).

## 10.1 INTRODUCTION

The hydrogen bond structure of water surfaces strongly differs from that of bulk water. For instance, at planar hydrophobic surfaces, including the water/air interface, approximately one in every four interfacial water molecules has a free, non-hydrogen-bonded O-H group that protrudes into the hydrophobic phase [40, 41].

For a complete, molecular-scale understanding of the chemical processes that occur at the water interface one requires insights not only into its structure, but also into the rates and mechanisms of energy transfer and dissipation. In bulk water, energy flow mechanisms and dynamics have been quantified using femtosecond infrared laser techniques [32, 97, 171]. The O-H stretch vibrations of the water molecules were found to show rapid resonant (Förster) energy transfer on a timescale of <100 fs, largely as a result of the strong dipole-dipole interactions between the O-H oscillators.

As the rates and pathways of interfacial energy transfer processes are relevant for chemical transformations at aqueous interfaces, the question that presents itself is, how do the local structural changes affect the mechanism and timescale of energy flow at an aqueous interface? The challenge of characterizing the

structure of the outermost surface molecules has been met by sum frequency generation (SFG) spectroscopy of their O-H stretch vibrations [40, 41, 53, 117, 138, 143, 148, 153, 149]. In an SFG experiment, infrared and visible laser pulses are overlapped in space and time on the surface, and the sum-frequency of the two laser fields can be generated, but only in the surface region [142]. If the infrared light is resonant with the O-H stretch vibration of surface water, this process is resonantly enhanced. Initial SFG studies made use of the distinct correlation that exists between the local hydrogen bonding strength and the O-H stretch vibrational frequency of an OH group in a water molecule. These studies indicated that, in addition to the free O-H groups pointing away from the surface [40, 41], different types of hydrogen-bonded interfacial water also exist [40, 41, 138], and that the interfacial layer is limited to approximately one monolayer [149].

In bulk water, very rapid resonant (Förster) energy transfer between O-H vibrations of different water molecules was demonstrated by measuring the anisotropy dynamics [171] and the ultrafast spectral diffusion of the OH stretch vibrations [32]. The spectral diffusion was measured using two-dimensional infrared (2D-IR) spectroscopy [31, 76]. In this technique a vibration is excited with a femtosecond infrared laser pulse and the effect of this excitation on other, nearby vibrations is monitored with a second femtosecond infrared laser pulse. In this way, rapid hopping of the excitation over different vibrations was observed. For water at interfaces, a similar efficient vibrational energy transfer has been suggested to take place [104, 145]. This suggestion was based on time-resolved SFG experiments of the water-fused silica [104] and the water/air [145] interfaces, and specifically from the absence of any spectral dynamics of the excited O-H stretch vibrations.

We studied the interfacial energy flow dynamics using surface specific 2D-IR sum-frequency generation (2D-SFG) spectroscopy [23]. This technique combines the unique capabilities of 2D-IR spectroscopy with the surface specificity and (sub)monolayer sensitivity of SFG spectroscopy (see sections 2.6.1 and 2.6.2).

## 10.2   EXPERIMENT

In our SFG-2D-IR experiment, we used an IR-pump–SFG-probe scheme. The pump with a limited spectral width (typically set at 100 cm$^{-1}$) is continuously tuned across the absorption band of water (2100 - 3000 cm$^{-1}$). For the detection process, broadband mid-IR and narrowband visible upconversion pulses were mixed at the interface to generate a conventional SFG signal. The experimental details are the same as for the experiments presented in previous chapter (see section 9.2). In order to obtain sufficient time resolution for determining vibrational dynamics, the 2D-SFG spectra were composed from the transient spectra recorded at delay times of -1200, -600, -300, 0, 300, 600, 900, 1200, 2100, 3000 and 6000 fs following procedure described in section 9.2.

We studied heavy water (D$_2$O) rather than normal water, because the intermolecular energy transfer is expected to be slower due to the smaller transition dipole moments of the O-D stretch vibrations and the narrower homogeneous
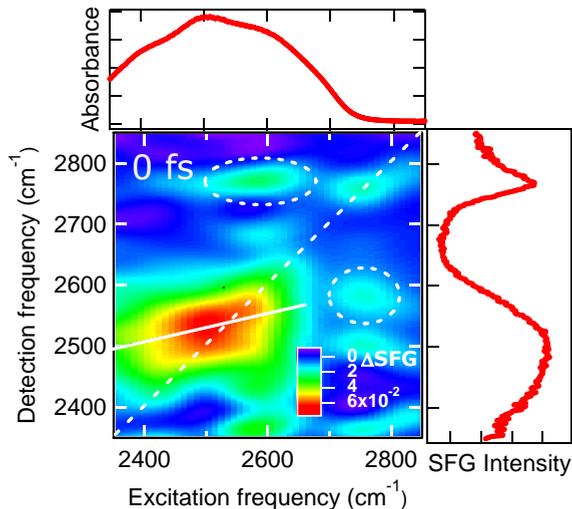
FIGURE 10.1. Two-dimensional spectrum recorded at zero delay time between excitation and detection pulses, together with the linear absorption (horizontal, top) and SFG (vertical, right) spectra of $D_2O$. The two-dimensional spectrum is reconstituted from difference spectra between excited and unexcited SFG spectra, at various excitation frequencies. Red (blue) indicate a decrease (increase) in the SFG signal, a shown by the scale bar. The dashed line indicates the diagonal, with the slope of 1; the solid line indicates the average slope (0.23) of the main, broad SFG response. As second diagonal peak appears at the free O-D frequency of 2750 cm$^{-1}$. Off-diagonal intensities - cross peaks, appear at 2580/2750 cm$^{-1}$ and 2750/2580 cm$^{-1}$ (dotted ovals).

linewidths compared to the O-H stretch vibrations [128].

## 10.3  RESULTS AND DISCUSSION

Figure 10.1 shows an example of a 2D-SFG spectrum in the O-D stretch region of the $D_2O$/air interface at 0 fs delay between the excitation and detection pulses. The 2D-SFG spectra were constructed following the procedure described in previous chapter (see section 9.2). Along the horizontal (excitation) axis, the linear absorption spectrum of bulk $D_2O$ is shown. The steady-state SFG spectrum along the vertical axis reveals the free O-D group, sticking out of the surface, with a vibrational frequency of 2750 cm$^{-1}$. Between 2100 and 2600 cm$^{-1}$, a broadband response of hydrogen-bonded water molecules is apparent.

The solid line is a linear fit to the signal maxima at different excitation frequencies, resulting in a line with a slope of $0.23 \pm 0.06$. The finite slope of the diagonal response at small delay is direct evidence for the heterogeneity of hydrogen-bonded water molecules at the water/air interface. The spectral heterogeneity reflecting the distribution of hydrogen bond strengths can be quantified by assuming that the vibrational response can be described by a Gaussian distribution of Lorentzian lines, the latter being characterized by a width $\Gamma_{\mathrm{hom}}$.

In the previous chapter we have introduced an inhomogeneity parameter $\Upsilon$ and determined that $\Upsilon = 0.31$. Our results revealed that the homogeneous linewidth $\Gamma_{\text{hom}} = {\sim}240$ cm$^{-1}$, with the overall linewidth of the absorption band amounting to 310 cm$^{-1}$. The large homogeneous linewidth explains the spectrally broad response directly after excitation with a relatively narrow-band excitation pulse.

In addition to the response along the diagonal, distinct (off-diagonal) cross-peaks are apparent in the two-dimensional spectrum, highlighted by the dotted lines in the two-dimensional spectrum of figure 10.1. The origin and implications of these cross-peaks for the interfacial heterogeneity will be discussed later in more detail. The spectral heterogeneity within the hydrogen-bonded region, reflecting structural inhomogeneity, is very short-lived. Figure 10.2 shows transient spectra at different delay times, following excitation using a pump pulse centered at a relatively high frequency of 2625 cm$^{-1}$. The maximum in the signal shifts from high to low frequencies; that is, the signal displays spectral diffusion on a ${\sim}600$ fs timescale. Exciting and detecting the differential SFG signal near the peak of the SFG spectrum, provides us with a relatively good way of determining the lifetime of the O-D stretch vibration, as the effect of spectral diffusion and slow ingrowth of the thermal signal are minimized (the derivative of the spectral response $d\Delta\text{SFG}(\nu)/d\nu$ is essentially zero). We find that the vibrational relaxation of the O-D stretch mode occurs with a time constant of $1 \pm 0.1$ ps. Figure 10.3 (A-E) shows that the two-dimensional spectra evolve on a similar timescale. For long delay times, the signal is dominated by thermal effects, which give rise to both positive and negative signals in the differential SFG response, due to a blueshift of the SFG response. The time constant for the thermal relaxation step was not directly quantified, but, as is evident from figure 10.3 E, the thermal signal around ${\sim}2630$ cm$^{-1}$ exhibits a delayed ingrowth [96], and at 2100 fs the thermal signal is still weak in comparison to the signal of the excited OD vibrations. In our analysis, we can therefore neglect contributions from the thermal signal to spectral diffusion for timescales up to ${\sim}3$ ps.

The spectral diffusion can be quantified from the time-dependent slope of the diagonal response of the two-dimensional spectra, as summarized in figure 10.3F. Such spectral diffusion may be due to structural relaxation at the water interface, so that by hydrogen bond rearrangement, strongly hydrogen-bonded water molecules can become weakly bonded and vice versa. However, spectral diffusion is also indicative of intermolecular energy transfer. For bulk $H_2O$, very efficient transfer of vibrational energy between different water molecules has been demonstrated [32, 79, 128, 171]. This energy transfer is expected to contribute significantly to the spectral diffusion within the O-D stretch vibrational band, as vibrational energy transfer can occur between differently hydrogen-bonded O-D groups, with different frequencies. Although we cannot exclude a contribution from structural relaxation to the dynamics, we first explore whether vibrational energy transfer, expected also to be very efficient at the interface, provides a sufficient explanation of the observed spectral dynamics.
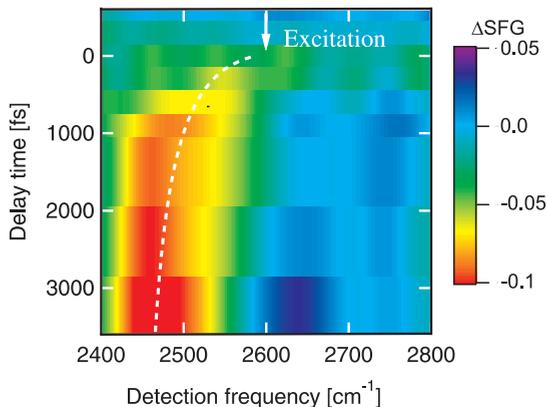
FIGURE 10.2. Direct observation of spectral diffusion at the water-air interface. Frequency-resolved transient SFG spectra at different delay times after excitation at $2625$ cm$^{-1}$ reveal a redshift of the maximum signal. The dashed line is a guide to the eye. The intensity increase above $2600$ cm$^{-1}$ observed at delays $\geqslant 3$ ps is due to the ingrowth of the thermal effects following vibrational relaxation.

## 10.4 INTERFACIAL INTERMOLECULAR ENERGY TRANSFER

We modeled the decay of the time-dependent slope $S(t)$, which is a measure of heterogeneity, using the model for resonant energy transfer in D$_2$O [128]. The decay of the slope is directly proportional to the decay of the frequency-frequency correlation function, as demonstrated previously for conventional 2D-IR [84]. The decay of this correlation function originates from energy transfer between O-D groups of different frequency. Assuming that energy transfer is the only mechanism scrambling the frequency, and that each transfer step leads to a complete randomization of the vibrational frequency, we can express the slope at time t for a concentration of O-D groups of $C_{OD}$ (in MÅ$^{-3}$) $= 2C_{D20}$ as (see section 2.5.1):

$$S(t) = S_0 \exp\left(-(4\pi^{3/2}/3)C_{OD}N_A\sqrt{r_0^6 t/T_1}\right) \qquad (10.1)$$

where $N_A$ is Avogadro's number, $r_0$ is the distance over which the energy transfer occurs with 50% efficiency, and $S_0$ is the initial slope value. The dipole-dipole coupling strength is represented by the term $\sqrt{r_0^6/T_1}$. This term is proportional to the transition dipole moments of donor and acceptor. The Förster radius $r_0$ is the distance between donor and acceptor for which energy transfer plays a role within the lifetime $T_1$. If $T_1$ increases, then $r_0$ also increases, not because there is a change in the dipole coupling, but because there is more time for the energy transfer to take place within the lifetime of the excitation. Following references [128, 171], the radius $r_0$ is referenced here to $T_1 = 1700$ fs, the intrinsic
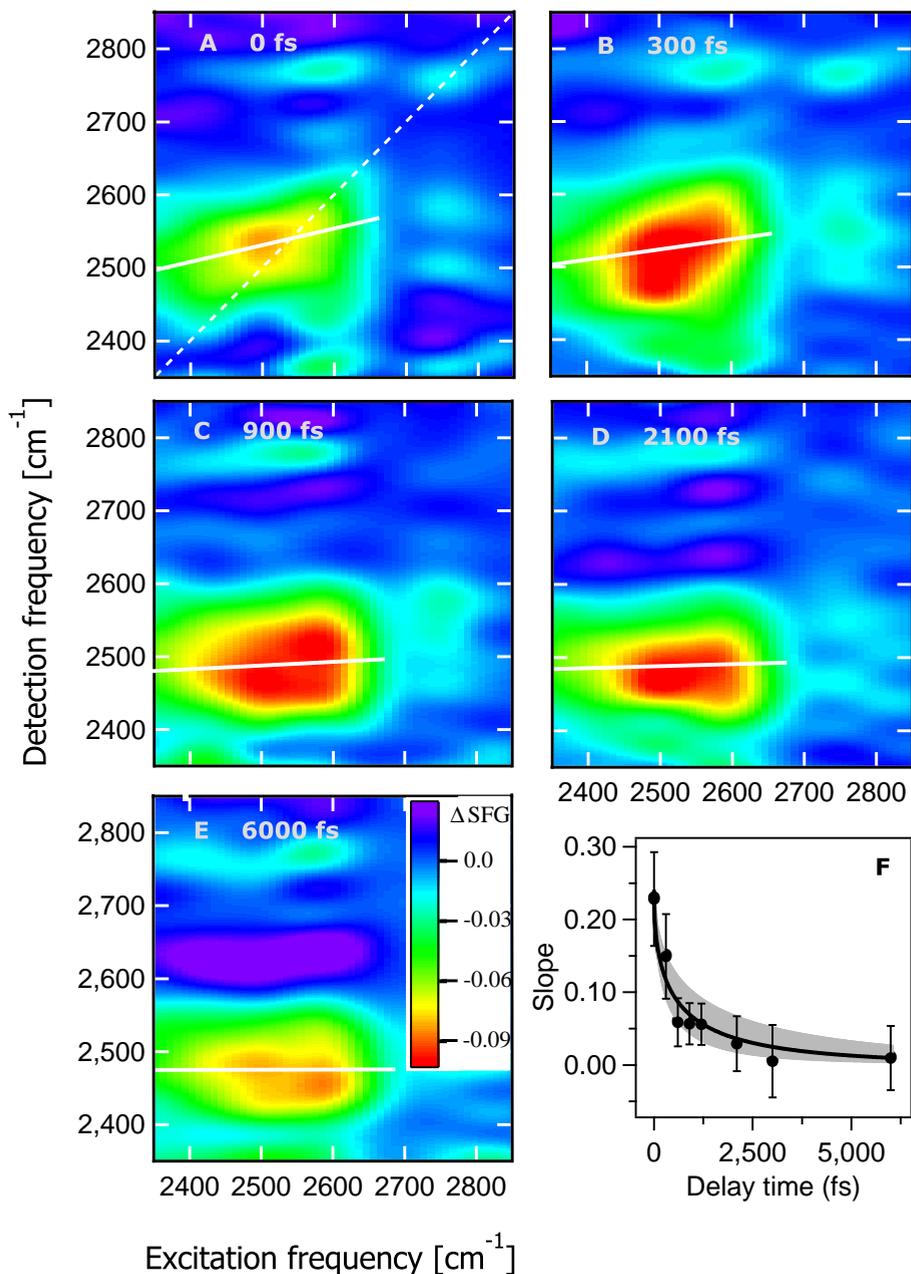
FIGURE 10.3. 2D-SFG spectra of the $D_2O$ water-air interface at various delay times after the excitation. Panels A-E: Solid lines represent the IR frequencies corresponding to the maximum SFG response as a function of the excitation frequency. Red (blue) indicates a decrease (increase) in the SFG signal, as shown by the scale bar in panel E. The slopes of the solid lines are plotted as a function of delay in panel F. The solid line in panel F is the result of a model calculation that accounts for the spectral diffusion by resonant Förster energy transfer (see main text) with $r_0 = 2.4 \pm 0.3$ Å (error indicated by gray shaded area).

vibrational lifetime of the O-D stretch vibration of HDO in bulk $H_2O$. We note that $T_1$ is much shorter than the radiative lifetime of the transition.

Using this equation we find a very good description of the dynamics with $r_0 = 1.9 \pm 0.2$ Å. This value is appreciably smaller than the value of $r_0 = 2.3 \pm 0.2$ Å found for bulk $D_2O$ [128]. This indicates that energy transfer between the O-D vibrations is slower at the $D_2O$ surface than in the bulk. This slower energy transfer can probably be attributed to the lower density of acceptors for $D_2O$ molecules near the interface. For the topmost layer of $D_2O$ molecules, the number density of available acceptors is expected to be only half the number density of $D_2O$ molecules in the bulk. In appendix 10.7 we derive a modified equation for the energy exchange between an O-D group at the surface and a bulk-like hemisphere below it:

$$S(t) = S_0 \exp\left(-(2\pi^{3/2}/3)C_{\mathrm{OD}}N_{\mathrm{A}}\sqrt{r_0^6 t/T_1}\right) \tag{10.2}$$

This equation differs from the previous equation in the two times smaller exponential factor. The result of fitting this model to the data is shown as the line in figure 10.3 F. Fitting this model we find $r_0 = 2.4 \pm 0.3$ Å, indistinguishable within the error from the 2.3 Å found for bulk $D_2O$ [128]. The success of equation 10.2 in describing the data implies that the 2D-IR SFG technique probes the $D_2O$/air interface over a penetration depth less than $r_0$. As $r_0$ is similar to the intermolecular separation in liquid $D_2O$, this finding demonstrates that the 2D-SFG technique only probes the outermost molecules of the $D_2O$ surface.

Although this energy transfer model provides a quantitative description of the observed spectral dynamics, this does not prove the model is correct. A rigorous test of the validity of the model is the measurement of the spectral diffusion rate in dependence on the isotope dilution [128, 171]. The result of a spectral diffusion measurements on a 1:1 mixture of $D_2O$ and $H_2O$ is shown in figure 10.4. The figure shows frequency-resolved transient SFG spectra at different delay times after excitation at 2625 cm$^{-1}$ for pure $D_2O$ (left), and at 2560 cm$^{-1}$ for a 1:1 $D_2O$/$H_2O$ mixture (right). The conventional SFG spectrum changes slightly upon isotopic dilution [147], and therefore somewhat different excitation frequencies were chosen to achieve the same excitation density. It is evident from these results that the spectral diffusion dynamics slows down upon isotopic dilution. The results are summarized in figure 10.5, which shows the frequency of the bleach maximum at different delay times. The solid lines in figure 10.5 are calculations following the intermolecular energy transfer model presented above, and are the same as the dashed lines in figure 10.4. These results are in quantitative agreement with the Förster energy transfer model, showing the expected slow-down of the spectral diffusion dynamics for the 2-fold diluted sample. Given that the structural, molecular dynamics remain unchanged upon isotopic dilution, this result proves that the spectral diffusion, and the time-dependent slopes of the 2D spectra, are the result of efficient intermolecular energy transfer, which justifies the use of the proposed model.

The observation that the energy transfer model provides a quantitative description of the observed spectral dynamics suggests that structural dynamics
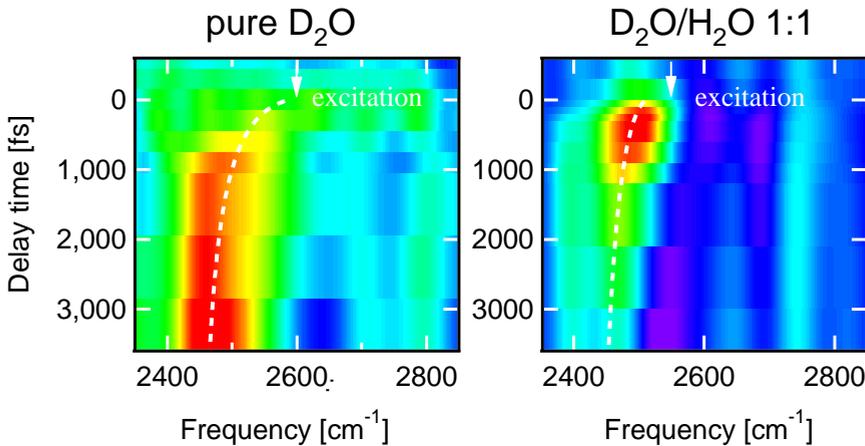
FIGURE 10.4. Isotopic dilution measurements show that spectral diffusion slows down with increasing isotopic dilution. Frequency-resolved transient SFG spectra at different delay times after excitation at 2625 cm$^{-1}$ for pure $D_2O$ (left) and 2560 cm$^{-1}$ for 1:1 $H_2O/D_2O$ mixture (right). Both experiments reveal a red shift of the maximum of the SFG signal. The dashed lines are calculations following the intermolecular energy transfer model described in the text. The experiments for 1:1 $H_2O/D_2O$ isotopically diluted sample reveal a slowdown of the spectral diffusion dynamics, precisely as expected for the energy transfer, due to the 2-fold lowering of the concentration of O-D groups $C_{OD}$.

do not contribute significantly to the spectral diffusion process. This observation is not very surprising, considering the very short timescale over which spectral diffusion due to Förster energy transfer occurs. 2D-IR studies of the structural dynamics of isotopically diluted water samples, for which there is no resonant energy transfer, have shown the presence of only a minor structural relaxation component on a 100 fs timescale [3, 98]. The dominant structural rearrangement of the hydrogen bond network of bulk water was observed to take place on longer timescales [3, 98]. The 2D-SFG spectra thus allow us to follow the dynamics of intermolecular energy transfer between interfacial water molecules in real time, revealing the predominance of dipole-dipole interactions in conjunction with the truncation of the water structure at the interface. The 2D-SFG spectroscopy results presented here allow for the quantification of the energy flow rate. The fact that simple geometric arguments (energy transfer into a half-sphere) completely account for the timescale on which resonant energy transfer occurs at the water/air interface, is consistent with the molecularly sharp density profile at the interface [113, 152].
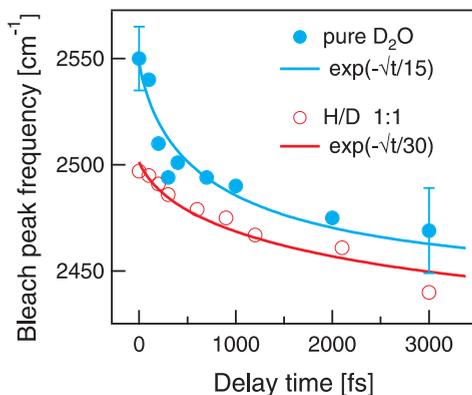
FIGURE 10.5. The frequency shift of the bleach maximum at different delay times. The lines correspond to those in the two panels in figure10.4, and quantitatively confirm the expected slow-down for the 2-fold diluted sample.

## 10.5   EFFICIENT   INTERFACIAL   INTRAMOLECULAR ENERGY  TRANSFER

We now turn to the off-diagonal cross-peaks observed in the two-dimensional spectra at (excitation, detection) frequencies of both (2580, 2750 cm$^{-1}$) and (2750, 2580 cm$^{-1}$), highlighted as dotted circles in figure 10.1. The presence of these cross-peaks implies the occurrence of energy transfer between the free O-D stretch and a vibration on the blue side of the hydrogen-bonded peak. Considering the large energy mismatch between these two frequencies, this coupling cannot be due to resonant dipole-dipole interactions between the two O-D groups. The interaction must therefore rely on an interaction between the donor and acceptor vibration in which the energy mismatch is taken away or supplied by a third, low-frequency degree of freedom. The coupling is therefore at least of third order in the vibrational coordinates (that is, the donor, acceptor and a low-frequency mode), which means that this coupling is anharmonic. The anharmonic coupling is most likely through-bond and therefore rather of intra- than of inter-molecular nature. This means that the resonance at 2580 cm$^{-1}$ on the blue side of the hydrogen-bonded peak belongs to the O-D group which is part of the same water molecule that has a free O-D group at 2750 cm$^{-1}$ sticking out of the surface. This assignment agrees with previous polarization-resolved [51] and isotope-dependent [149] static SFG experiments, which have indicated that the hydrogen-bonded O-D group attached to the free O-D has a vibrational frequency on the blue side of the broad hydrogen-bonded absorption band. The two-dimensional spectra presented here unambiguously reveal the strong coupling between these two O-D groups.

We investigate the dynamics of the (2750, 2750 cm$^{-1}$) and (2750, 2580 cm$^{-1}$) spectral features, as shown in figure 10.6. The dynamics of the cross-peak re-
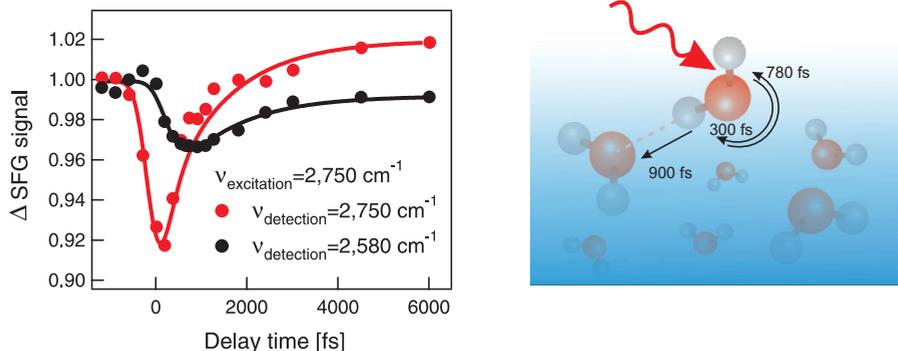
FIGURE 10.6. A: Dynamics of the free O-D vibration excited and detected at 2750 cm$^{-1}$ (red), and the cross-peak excited at 2750 cm$^{-1}$ and detected at 2580 cm$^{-1}$. The signal of the free O-D stretch at 2750 cm$^{-1}$ shows a rapid initial decay, and the cross-peak shows a delayed rise. These dynamics are due to an ultrafast energy transfer from the excited free O-D vibration sticking out of the surface to the O-D group that is located on the same water molecule and pointing into the bulk. After equilibration, the two modes relax together with the same effective rate. B: Schematic representation of the interfacial energy redistribution process with the time constants obtained from fit of the data to the model described in the main text.

veals that the mechanism of vibrational relaxation is rather intricate; the somewhat delayed in-growth of the cross-peak indicates rapid vibrational energy transfer from the free O-D to the hydrogen-bonded O-D within the same $D_2O$ molecule. The rapid equilibration of vibrational energy between the two modes is followed by a decay due to vibrational relaxation, presumably through the hydrogen-bonded O-D group. A model that includes in parallel both the energy equilibration and the vibrational relaxation provides a very good description of the data, as shown by the solid lines in figure 10.6. The model is described in the appendix 10.8. From the fit we obtain a time constant of $k_1 = (300 \pm 60 \text{ fs})^{-1}$ for the energy transfer from the free O-D to the hydrogen-bonded OD. The time constant for the reverse process fulfils detailed balance: $k_1/k_{-1} = \exp[(2750 - 2580)/k_B T]$ which implies that $k_{-1} = (780 \pm 150 \text{ fs})^{-1}$. Vibrational relaxation of the hydrogen-bonded O-D group occurs with a time constant of $900 \pm 50$ fs, in good agreement with the ~1 ps lifetime inferred from the diagonal response, when exciting and detecting the hydrogen-bonded O-D groups. The results are summarized in figure 10.6. The lifetime is similar to the previously reported ~1 ps lifetime of the free O-H of $H_2O$ [104]. For this free O-H the relaxation is expected to take a similar path as the free O-D at the $D_2O$ surface, namely a rapid equilibration of the vibrational energy over the two O-H groups of the $H_2O$ molecule, followed by the cooperative relaxation of the two groups. In the present 2D-SFG experiment we can resolve the first equilibration process thanks to the dynamics of the cross-peaks. In this way, we find that the free O-D groups serve as efficient antennas for vibrational energy, and rapidly transfer this energy to the hydrogen-bonded O-D group within the same molecule. The

vibrational energy then delocalizes further as a result of resonant dipole-dipole coupling of the hydrogen-bonded O-D group with other water molecules.

## 10.6 CONCLUSIONS

In summary, we demonstrate that 2D-IR SFG data reveal the occurrence of surprisingly fast intra- and intermolecular energy transfer processes at aqueous interfaces. The results show that energy transfer among O-D stretching modes of water on the surface is rapid and efficient and that O-D excitations rapidly exchange between surface and bulk. This information on interfacial energy flow patterns is essential for understanding chemistry at aqueous interfaces: the occurrence of endothermic and exothermic reactions at aqueous surfaces, be it on catalytic water interfaces, in atmospheric chemistry or at cell membrane surfaces, requires the efficient transport of vibrational energy to and from the surface.

## 10.7 APPENDIX: VIBRATIONAL ENERGY TRANSFER OVER A HALF-SPHERE

We use the same procedure as we used before in section 8.5 to derive the vibrational energy transfer between water molecules located at the surface. Briefly, combining the two probabilities: the probability that the molecule is excited at time t=$\tau$ (equation 2.37) and the probability of finding an accepting molecule for each of the $N$ oscillators in the system (equation 2.38) we arrive at:

$$\rho(t) = \left\{ \frac{2\pi}{V} \int_0^R exp\left(-\frac{tr_0^6}{T_1 r^6}\right) r^2 dr \right\}^N ,$$

(10.3)

where $V$ is now the volume of hemisphere $V = 2\pi R^3/3$, $R$ is a radius of the hemisphere and $N$ is the number of the O-D oscillators in the system. Performing the integration, we obtain:

$$\rho(t) = \left\{ exp\left(-\frac{tr_0^6}{T_1 r^6}\right) + \sqrt{\frac{\pi t r_0^6}{T_1 R}}\, \mathrm{Erf}\left(\sqrt{\frac{\pi t r_0^6}{T_1 R}}\right) \right\}^N ,$$

Using the expression for the concentration of the O-D oscillators (expressed in MÅ$^{-3}$):

$$C_{OD} = \frac{3 N_{OD}}{2\pi R^3 N_A} ,$$

(10.4)

we can eliminate the hemisphere radius $R$ from expression 10.4. Performing the power expansion in terms of $1/N$ and eliminating higher order terms (since for N$\to \infty$ they become negligible) we obtain the expression:

$$\rho(t) = exp\left(\frac{2\pi^{3/2} C_{OD} N_A \sqrt{t r_0^6}}{3\sqrt{T_1}}\right)$$

(10.5)
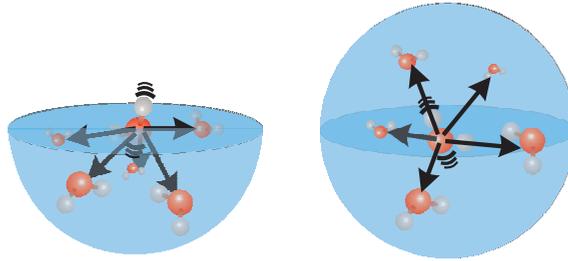
FIGURE 10.7. Schematic representation of the vibrational energy transfer at the water-air interface (left) and in the bulk (right).

The above expression describes resonant vibrational energy transfer for a molecule located at the surface, and assumes that the energy transfer step leads to a complete randomization of the vibrational frequency, i.e. that the energy step leads to a complete decay of the frequency-frequency correlation function. Note that the rate of energy transfer is smaller than the rate of energy transfer of a molecule located in the bulk (see section 2.41). This difference arises from the lower number of acceptors in a hemisphere, compared to that in a sphere.

Figure 10.7 shows a schematic representation of the resonant vibrational energy transfer for an interfacial water molecule (left) and a molecule located in the bulk (right).

## 10.8  APPENDIX: INTERFACIAL INTRAMOLECULAR ENERGY TRANSFER

In the following we present the model and the corresponding differential equations describing the intramolecular coupling process between the free O-D groups (denoted 'F') and the hydrogen-bonded O-D groups (denoted 'HB'). The subsequent relaxation involves the transition from the excited hydrogen-bonded O-D group to a state at a somewhat elevated temperature (denoted 'T'). Energy transfer from F to HB occurs with rate $k_1$; the reverse rate is given by $k_{-1}$. We assume that vibrational relaxation - with rate $k_2$ occurs only from the HB state into the T state.

If we denote the occupation of each of the states as $N_X$, where X = F, HB or T. Initially the excitation pulse, characterized by the time-independent intensity $I(t)$, gives rise to population of $N_F$. The time-dependent occupation of each state is given by:

$$\frac{\partial N_F}{\partial t} = \sigma_{01} I(t)[N_0 - N_F] - k_1 N_F + k_{-1} N_{HB}$$
$$\frac{\partial N_{HB}}{\partial t} = k_1 N_F - k_{-1} N_{HB} - k_2 N_{HB}$$
$$\frac{\partial N_T}{\partial t} = k_2 N_{HB}$$

$(10.6)$

The forward and backward rates $k_1$ and $k_{-1}$ are linked by the Boltzmann factor that accounts for the energy difference between the two levels:

$$\frac{k_1}{k_{-1}} = \exp\left(\frac{(2750 - 2580)}{k_B T}\right) \tag{10.7}$$

Owing to the fact that the differential signals are detected on the background of the steady state SFG signal, the differential SFG signals for the free and hydrogen-bonded O-D groups are simply proportional to $N_F$ and $N_{HB}$, both with a contribution (accounting for the long-time signal offset) from $N_T$.

# Bibliography

1. M. Akiyama and H. Torii. Cooperative effect in hydrogen bonding of N-methylacetamide in carbon tetrachloride solutions confirmed by NMR and IR spectroscopy. *Spec. Chim. Acta A. Mol. Bio.*, 56:137, 1999.

2. B. Alberts, A. Johnson, J. Lewis, M. Raff, K. Roberts, and P. Walter. *Molecular biology of the cell*. New York: Garland Science, 2002.

3. J. B. Asbury, T. Steinel, K. Kwak, S. A. Corcelli, C. P. Lawrence, J. L. Skinner, and M. D. Fayer. Dynamics of water probed with vibrational echo correlation spectroscopy. *J. Chem. Phys.*, 121:12431–12446, 2004.

4. S. A. Asher and P. S. Pershan. Alignment and defect structures in oriented phosphatidylcholine multilayers. *Biophys. J.*, 27:393–421, 1979.

5. S. Ashihara, N. Huse, A. Espagne, E. T. J. Nibbering, and T. Elsaesser. Vibrational couplings and ultrafast relaxation of the O-H bending mode in liquid $H_2O$. *Chem. Phys. Lett.*, 424:66, 2006.

6. B. M. Auer and J. L. Skinner. Vibrational sum-frequency spectroscopy of the liquid/vapor interface for dilute HOD in $D_2O$. *J. Chem. Phys.*, 129:214705, 2008.

7. H. Bakker, H.-K. Nienhuys, G. Gallot, N. Lascoux, G. Gale, J.-C. Leicknam, and S. Bratos. Transient absorption of vibrationally excited water. *J. Chem. Phys.*, 116:2592–2598, 2002.

8. H. J. Bakker. Structural dynamics of aqueous salt solutions. *Chem. Rev.*, 108:1456–1473, 2008.

9. H. J. Bakker, Y. L. A. Rezus, and R. L. A. Timmer. Molecular reorientation of liquid water studied with femtosecond midinfrared spectroscopy. *J. Phys. Chem. A*, 112:11523–11534, 2008.

10. H. J. Bakker and J. L. Skinner. Vibrational spectroscopy as a probe of structure and dynamics in liquid water. *Chem. Rev.*, 110:1498–1514, 2010.

11. P. Ball. Water: an enduring mystery. *Nature*, 452:291–292, 2008.

12. D. R. Bauer, J. I. Brauman, and R. Pecora. Molecular reorientation in liquids. experimental test of hydrodynamic models. *J. Am. Chem. Soc.*, 96:22, 1974.

13. R. Bennet, R. P. Schwenker, and R. Kellog. Radiationless intermolecular energy transfer. 2. Triplet to singlet transfer. *J. Chem. Phys.*, 41:3040, 1964.

14. S. Y. Bhide and M. L. Berkowitz. Structure and dynamics of water at the interface with phospholipid bilayers. *J. Chem. Phys.*, 123:224702, 2005.

15. S. Y. Bhide and M. L. Berkowitz. The behavior of reorientational correlation functions of water at the water-lipid bilayer interface. *J. Chem. Phys.*, 125:094713, 2006.

16. H. Binder. Water near lipid membranes as seen by infrared spectroscopy. *Eur. Biophys. J.*, 36:265–279, 2007.

17. H. Binder and W. Pohle. Structural aspects of lyotropic solvation-induced transitions in phosphatidylcholine and phosphatidylethanolamine assemblies revealed by infrared spectroscopy. *J. Phys. Chem. B*, 104:12039–12048, 2000.

18. R. Bloem, A. G. Dijkstra, T. L. C. Jansen, and J. Knoester. Simulation of vibrational energy transfer in two dimensional infrared spectroscopy of amide I and amide II modes in solution. *J. Chem. Phys.*, 129:055101, 2008.

19. P. Bodis, O. F. A. Larsen, and S. Woutersen. Vibrational relaxation of the bending mode of HDO in liquid $D_2O$. *J. Phys. Chem. A*, 109:5303–5306, 2005.

20. M. Bonn, H. J. Bakker, A. Ghosh, S. Yamamoto, M. Sovago, and R. K. Campen. Structural inhomogeneity of interfacial water at lipid monolayers revealed by surface-specific vibrational pump-probe spectroscopy. *J. Am. Chem. Soc.*, 132:14971–14978, 2010.

21. R. W. Boyd. *Nonlinear optics*. Elsevier, 2003.

22. B. H. Bransden and C. J. Joachain. *Introduction to quantum mechanics.* Addison Wesley Longman Limited, 1989.

23. J. Bredenbeck, A. Ghosh, H.-K. Nienhuys, and M. Bonn. Interface-specific ultrafast two-dimensional vibrational spectroscopy. *Acc. Chem. Res.*, 42:1332–1342, 2009.

24. J. Bredenbeck, A. Ghosh, M. Smits, and M. Bonn. Ultrafast two dimensional-infrared spectroscopy of a molecular monolayer. *J. Am. Chem. Soc.*, 130:2152–2153, 2008.

25. G. Brink and M. Falk. Infrared spectrum of HDO in aqueous solutions of perchlorates and tetrafluoroborates. *Can. J. Chem.*, 48:3019–3025, 1970.

26. E. C. Brown, M. Mucha, P. Jungwirth, and D. J. Tobias. Structure and vibrational spectroscopy of salt water/air interfaces: predictions from classical molecular dynamics simulations. *J. Phys. Chem. B*, 109:7934–7940, 2005.

27. M. P. J. Brugmans, H. J. Bakker, and A. Lagendijk. Direct vibrational energy transfer in zeolites. *J. Chem. Phys.*, 104:64, 1996.

28. V. Cervetto, J. Helbing, J. Bredenbeck, and P. Hamm. Double-resonance versus pulsed Fourier transform two-dimensional infrared spectroscopy: an experimental and theoretical comparison. *J. Chem. Phys.*, 121:5935–5942, 2004.

29. X. Chen, R. Schweitzer-Stenner, S. Asher, N. Mirkin, and S. Krimm. Vibrational assignments of trans-n-methylacetamide and some of its deuterated isotopomers from band decomposition of IR, visible and resonance Raman spectra. *J. Phys. Chem.*, 99:3074–3083, 1995.

30. J.-X. Cheng, S. Pautot, D. A. Weitz, and X. S. Xie. Ordering of water molecules between phospholipid bilayers visualized by coherent anti-stokes raman scattering microscopy. *PNAS*, 100:9826–9830, 2003.

31. M. Cho. Coherent two-dimensional optical spectroscopy. *Chem. Rev.*, 108:1331–1418, 2008.

32. M. L. Cowan, B. D. Bruner, N. Huse, J. R. Dwyer, B. Chugh, E. T. J. Nibbering, T. Elsaesser, and R. J. D. Miller. Ultrafast memory loss and energy redistribution in the hydrogen bond network of liquid $H_2O$. *Nature*, 434:199, 2005.

33. D. Cringus, S. Yeremenko, M. S. Pshenichnikov, and D. A. Wiersma. Hydrogen bonding and vibrational energy relaxation in water-acetonitrile mixtures. *J. Phys. Chem. B*, 108:10376–10387, 2004.

34. T. Dahinten, J. Baier, and A. Seilmeier. Vibrational energy transfer processes in dye molecules after ultrafast excitation of skeletal modes. *Chem. Phys.*, 232:239–245, 1998.

35. M. F. DeCamp, L. DeFlores, J. M. McCracken, A. Tokmakoff, K. Kwac, and M. Cho. Amide i vibrational dynamics of N-methylacetamide in polar solvents: the role of electrostatic interactions. *J. Phys. Chem. B*, 109:11016–11026, 2005.

36. L. P. DeFlores, Z. Ganim, S. F. Ackley, H. S. Chung, and A. Tokmakoff. The anharmonic vibrational potential and relaxation pathways of the amide I and II modes of NMA. *J. Phys. Chem. B*, 110:18973–18980, 2006.

37. A. M. Dokter, S. Woutersen, and H. J. Bakker. Anomalous slowing down of the vibrational relaxation of liquid water upon nanoscale confinement. *Phys. Rev. Lett.*, 94:178301, 2005.

38. A. M. Dokter, S. Woutersen, and H. J. Bakker. Ultrafast dynamics of water in cationic micelles. *J. Chem. Phys.*, 126:124507, 2007.

39. J. M. Drake, J. Klafter, and P. Levitz. Chemical and biological microstructures as probed by dynamic processes. *Science*, 251:1574–1579, 1991.

40. Q. Du, E. Freysz, and Y. R. Shen. Surface vibrational spectroscopic studies of hydrogen bonding and hydrophobicity. *Science*, 264:826–828, 1994.

41. Q. Du, R. Superfine, E. Freysz, and Y. R. Shen. Vibrational spectroscopy of water at the vapor/water interface. *Phys. Rev. Lett.*, 70:23132316, 1993.

42. K. B. Eisenthal. Liquid interfaces probed by second-harmonic and sum-frequency spectroscopy. *Chem. Rev.*, 96:1343–1360, 1996.

43. M. Falk. Frequencies of H-O-H, H-O-D and D-O-D bending fundamentals in liquid water. *J. Raman Spectrosc.*, 21:563–567, 1990.

44. Y. Fan, X. Chen, L. Yang, P. S. Cremer, and Y. Q. Gao. On the structure of water at the aqueous/air interface. *J. Phys. Chem. B*, 113:11672–11679, 2009.

45. C. Fang, A. Senes, L. Cristian, W. F. DeGrado, and R. M. Hochstrasser. Amide vibrations are delocalized across the hydrophobic interface of a transmembrane helix dimer. *PNAS*, 103:16740, 2006.

46. M. D. Fayer, D. E. Moilanen, D. Wong, D. E. Rosenfeld, E. E. Fenn, and S. Park. Water dynamics in salt solutions studied with ultrafast two-dimensional infrared (2D IR) vibrational echo spectroscopy. *Acc. Chem. Res.*, 42:1210–1219, 2009.

47. C. J. Fecko, J. D. Eaves, J. J. Loparo, A. Tokmakoff, and P. L. Geissler. Ultrafast hydrogen-bond dynamics in the infrared spectroscopy of water. *Science*, 301:1698–1701, 2003.

48. T. Forster. Experimentelle und theoretische untersuchung des zwischen-molekularen uberangs von elektronenanregungsenergie. *Z.Naturforschg.*, 4:821–827, 1940.

49. K. J. Gaffney, P. H. Davis, I. R. Piletic, N. E. Levinger, and M. A. Fayer. Hydrogen bond dissociation and reformation in methanol oligomers following hydroxyl stretch relaxation. *J. Phys. Chem. A*, 106:12012–12023, 2002.

50. G. M. Gale, G. Gallot, F. Hache, N. Lascoux, S. Bratos, and J.-C. Leicknam. Femtosecond dynamics of hydrogen bonds in liquid water: A real time study. *Phys. Rev. Lett.*, 82:1068–1071, 1999.

51. W. Gan, D. Wu, Z. Zhang, R. Feng, and H. Wang. Polarization and experimental configuration analyses of sum frequency generation vibrational spectra, structure, and orientational motion of the air/water interface. *J. Chem. Phys.*, 124:114705, 2006.

52. A. Ghosh, R. K. Campen, M. Sovago, and M. Bonn. Structure and dynamics of interfacial water in model lung surfactants. *Faraday Discuss.*, 141:145–59, 2009.

53. S. Gopalakrishnan, D. Liu, H. C. Allen, M. Kuo, and M. J. Shultz. Vibrational spectroscopic studies of aqueous interfaces: salts, acids, bases, and nanodrops. *Chem. Rev.*, 106:1155–1175, 2006.

54. N. Gouliaev and J. F. Nagle. Simulations of interacting membranes in the soft confinement regime. *Phys. Rev. Lett.*, 81:2610–2613, 1998.

55. J. Grdadolnik, J. Kidric, and D. Hadzi. Hydration of phosphatidylcholine reverse micelles and multilayers an infrared spectroscopic study. *Chem. Phys. Lipids*, 59:57–68, 1991.

56. A. I. Greenwood, S. Tristram-Nagle, and J. F. Nagle. Partial molecular volumes of lipids and cholesterol. *Chem. Phys. Lipids*, 143:1–10, 2006.

57. S. Gregurick, G. Chaban, and R. Gerber. Ab initio and improved empirical potentials for the calculations of the anharmonic vibrational states and intramolecular mode coupling of n-methylacetamide. *J. Phys. Chem. A*, 106:8696–8707, 2002.

58. S. M. Gruenbaum and J. L. Skinner. Vibrational spectroscopy of water in hydrated lipid multi-bilayers. I. infrared spectra and ultrafast pump-probe observables. *J. Chem. Phys.*, 135:075101, 2011.

59. K. J. Hallock, K. H. Wildman, D. K. Lee, and A. Ramamoorthy. An innovative procedure using a sublimable solid to align lipid bilayers for solid-state NMR studies. *Biophys. J.*, 82:2499–2503, 2002.

60. P. Hamm, M. Lim, and R. M. Hochstrasser. Structure of the amide I band of peptides measured by femtosecond nonlinear-infrared spectroscopy. *J. Phys. Chem. B*, 102:6123–6138, 1998.

61. K. A. Hartman. The structure of water and the stability of the secondary structure in biological molecules. An infrared and proton magnetic resonance study. *J. Phys. Chem.*, 70:270–276, 1966.

62. T. Hermann and D. J. Patel. Stitching together rna tertiary architectures. *J. Mo.l Biol.*, 294:829–849, 1999.

63. W. A. Herrebout, K. Clou, and H. O. Desseyn. Vibrational spectroscopy of N-methylacetamide revisited. *J. Phys. Chem. A*, 105:4865, 2001.

64. J. M. Heuft and E. J. Meijer. Density functional theory based molecular-dynamics study of aqueous iodide solvation. *J. Chem. Phys.*, 123:94506, 2005.

65. K. Hristova and S. H. White. Determination of the hydrocarbon core structure of fluid dioleoylphosphocholine (DOPC) bilayers by x-ray diffraction using specific bromination of the double-bonds: effect of hydration. *Biophys. J.*, 74:2419–2433, 1998.

66. C.-S. Hsieh, R. K. Campen, A. C. V. Verde, P. Bolhuis, H.-K. Nienhuys, and M. Bonn. Ultrafast reorientation of dangling oh groups at the air-water interface using femtosecond vibrational spectroscopy. *Phys. Rev. Lett.*, 107:116102, 2011.

67. H. Huang, S. Malkov, M. Coleman, and P. Painter. 2-D correlation infrared spectroscopic study of NMA as a function of temperature. *J. Phys. Chem. A*, 107:7697–7703, 2003.

68. N. Huse, S. Ashihara, E. T. J. Nibbering, and T. Elsaesser. Ultrafast vibrational relaxation of O-H bending and librational excitations in liquid $H_2O$. *Chem. Phys. Lett.*, 404:389, 2005.

69. N. Huse, K. Heyne, J. Dreyer, E. T. J. Nibbering, and T. Elsaesser. Vibrational mulitlevel quantum coherence due to anharmonic couplings in intermolecular hydrogen bonds. *Phys. Rev. Lett.*, 91:197401, 2003.

70. F. Ingrosso, R. Rey, T. Elsaesser, and J. Hynes. Ultrafast energy transfer from the intramolecular bending vibration to librations in liquid water. *J. Phys. Chem. A*, 113:6657–6665, 2009.

71. D. W. James and R. F. Armishaw. Effect of perchlorate salts on the hydrogen bonded strucure of water. *Inorg. Nucl. Chem. Lett.*, 12:425–434, 1976.

72. G. L. Jendrasiak and R. L. Smith. The interaction of water with the phospholipid head group and its relationship to the lipid electrical conductivity. *Chem. Phys. Lipids*, 131:183–195, 2004.

73. M. Jeremic, A. Antic-Jovanovic, M. Lalic, and V. Bojovic. Raman spectral study of ionic hydration in aqueous perchlorate solutions. *Spectroscopy Lett.*, 25:55–61, 1992.

74. N. Ji, V. Ostroverkhov, C. S. Tian, and Y. R. Shen. Characterization of vibrational resonances of water-vapor interfaces by phase-sensitive sum-frequency spectroscopy. *Phys. Rev. Lett.*, 100:096102, 2008.

75. X. N. Jiang and C. S. Wang. Rapid prediction of the hydrogen bond cooperativity in NMA chains. *Chem. Phys. Chem.*, 10:3330–3336, 2009.

76. M. Khalil, N. Demirdoven, and A. Tokmakoff. Coherent 2D IR spectroscopy: molecular structure and dynamics in solution. *J. Phys. Chem. A*, 107:5258–5279, 2003.

77. B. Klsgen, C. Reichle, S. Kohlsmann, and K. D. Kramer. Dielectric spectroscopy as a sensor of membrane headgroup mobility and hydration. *Biophys. J.*, 71:3251–3260, 1996.

78. T. Köddermann and R. Ludwig. NMA-water clusters in a hydrophobic solvent. *Phys. Chem. Chem. Phys.*, 6:1867–1873, 2004.

79. D. Kraemer, M. L. Cowan, A. Paarmann, N. Huse, E. T. J. Nibbering, T. Elsaesser, and R. J. D. Miller. Temperature dependence of the two-dimensional infrared spectrum of liquid $H_2O$. *PNAS*, 105:437–442, 2008.

80. M. F. Kropman and H. J. Bakker. Dynamics of water molecules in aqueous solvation shells. *Science*, 291:2118, 2001.

81. M. F. Kropman and H. J. Bakker. Effect of ions on the vibrational relaxation of liquid water. *J. Am. Chem. Soc.*, 126:9135–9141, 2004.

82. M. F. Kropman, H.-K. Nienhuys, and H. J. Bakker. Real-time measurement of the orientational dynamics of aqueous solvation shells in bulk liquid water. *Phys. Rev. Lett.*, 88:077601, 2002.

83. K. Kwac and M. Cho. Hydrogen bonding dynamics and two-dimensional vibrational spectroscopy: N-methylacetamide in liquid methanol. 36:326, 2005.

84. K. Kwak, S. Park, I. J. Finkelstein, and M. D. Fayer. Frequency-frequency correlation functions and apodization in two-dimensional infrared vibrational echo spectroscopy: a new approach. *J. Chem. Phys.*, 127:124503, 2007.

85. A. D. Laage and J. T. Hynes. Do more strongly hydrogen-bonded water molecules reorient more slowly? *Chem. Phys. Lett.*, 433:80–85, 2006.

86. R. Laenen, C. Rauscher, and A. Lauberau. Dynamics of local substructures in water observed by ultrafast infrared hole burning. *Phys. Rev. Lett.*, 80:2622–2625, 1998.

87. O. F. A. Larsen and S. Woutersen. Vibrational relaxation of the $H_2O$ bending mode in liquid water. *J. Chem. Phys.*, 121:12143, 2004.

88. C. P. Lawrence and J. L. Skinner. Vibrational spectroscopy of HOD in liquid $D_2O$. VII. Temperature and frequency dependence of the OH stretch lifetime. *J. Chem. Phys.*, 119:3840–3848, 2003.

89. A. G. Lee. How lipids affect the activities of integral membrane proteins. *Biochim. Biophys. Acta*, 1666:62–87, 2004.

90. A. L. Lehninger, D. L. Nelson, and M. M. Cox. *Principles of biochemistry*. Worth publishers, 1992.

91. Y. K. Levine, A. I. Bailey, and M. H. Wilkins. Multilayers of phospholipid bimolecular leaflets. *Nature*, 220:577–578, 1968.

92. Y. K. Levine and M. H. Wilkins. Structure of oriented lipid bilayers. *Nat. New Biol.*, 230:69–72, 1971.

93. Y. Levy and J. N. Onuchic. Water and proteins: a love-hate relationship. *PNAS*, 101:3325–3326, 2004.

94. J. Lindner, P. Vohringer, M. S. Pshenichnikov, D. Cringus, D. A. Wiersma, and M. Mostovoy. Vibrational relaxation of pure liquid water. *Chem. Phys. Lett.*, 421:329–333, 2006.

95. Y. Liu, M. A. Czarnecki, and Y. Ozaki. Fourier transform near-infrared spectra of n-methylacetamide: dissociation and thermodynamic properties in pure liquid form and $CCl_4$ solutions. *Appl. Spec.*, 48:1095, 1994.

96. A. J. Lock and H. J. Bakker. Temperature dependence of vibrational relaxation in liquid H2O. *J. Chem. Phys.*, 117:1708–1713, 2002.

97. A. J. Lock, S. Woutersen, and H. J. Bakker. Ultrafast energy equilibration in hydrogen-bonded liquids. *J. Phys. Chem. A*, 105:1238, 2001.

98. J. J. Loparo, S. T. Roberts, and A. Tokmakoff. Multidimensional infrared spectroscopy of water. II. hydrogen bond switching dynamics. *J. Chem. Phys.*, 125:194522, 2006.

99. C. F. Lopez, S. O. Nielsen, M. L. Klein, and P. B. Moore. Hydrogen bonding structure and dynamics of water at the dimyristoyl-phosphatidylholine lipid bilayer surface from a molecular dynamics simulation. *J. Phys. Chem. B*, 108:6603–6610, 2004.

100. R. Ludwig, O. Reis, R. Winter, F. Weinhold, and T. C. Farrar. Quantum cluster equilibrium theory of liquids: temperature dependence of hydrogen bonding in NMA. *J. Phys. Chem. B*, 102:9312–9318, 1998.

101. Y. Marcus. Effect of ions on the structure of water: Structure making and breaking. *Chem. Rev.*, 109:1346–1370, 2009.

102. Y. Marechal. Infrared spectra of water. I. Effect of temperature and of H/D isotopic dilution. *J. Chem. Phys.*, 95:5565–5573, 1991.

103. K. J. McConnell and D. L. Beveridge. DNA structure: what's in charge? *J. Mol. Biol.*, 304:803–820, 2000.

104. J. A. McGuire and Y. R. Shen. Ultrafast vibrational dynamics at water interfaces. *Science*, 313:1945–1948, 2006.

105. A. Millo, Y. Raichlin, and A. Katzir. Mid-infrared fiber-optic attenuated total reflection spectroscopy of the solid-liquid phase transition of water. *Appl. Spec.*, 59:460–466, 2005.

106. T. Miyazawa, T. Shimanouchi, and S. I. Mizushima. Normal vibrations of N-methylacetamide. *J. Chem. Phys.*, 29:611, 1958.

107. S. I. Mizushima, T. Simanouti, S. Nagakura, K. Kuratani, M. Tsuboi, H. Baba, and O. Fujioka. The molecular structure of N-methylacetamide. *J. Am. Chem. Soc.*, 72 (8):3490–3494, 1950.

108. D. E. Moilanen, E. E. Fenn, Y. Lin, J. L. Skinner, B. Bagchi, and M. D. Fayer. Water inertial reorientation: Hydrogen bond strength and the angular potential. *PNAS*, 105:5295, 2008.

109. D. E. Moilanen, I. R. Piletic, and M. D. Fayer. Water dynamics in nafion fuel cell membranes: the effects of confinement and structural changes on the hydrogen bond network. *J. Phys. Chem. C*, 111:8884–8891, 2007.

110. D. E. Moilanen, D. Wong, D. E. Rosenfeld, E. E. Fenn, and M. D. Fayer. Ion-water hydrogen-bond switching observed with 2D IR vibrational echo chemical exchange spectroscopy. *PNAS*, 106:375–380, 2009.

111. J. A. Mondal, S. Nihonyanagi, S. Yamaguchi, and T. Tahara. Structure and orientation of water at charged lipid monolayer/water interfaces probed by heterodyne-detected vibrational sum frequency generation spectroscopy. *J. Am. Chem. Soc.*, 132:1065610657, 2010.

112. M. Morin, P. Jakob, N. J. Levinos, Y. J. Chabal, and A. L. Harris. Vibrational energy transfer on hydrogen-terminated vicinal Si(111) surfaces: Interadsorbate energy flow. *J. Chem. Phys.*, 96:6203–6212, 1992.

113. M. Mucha, T. Frigato, L. M. Levering, H. C. Allen, D. J. Tobias, L. X. Dang, and P. Jungwirth. Unified molecular picture of the surfaces of aqueous acid, base, and salt solutions. *J. Phys. Chem. B*, 109:7617–7623, 2005.

114. N. S. Myshakina, Z. Ahmed, and S. A. Asher. Dependence of amide vibrations on hydrogen bonding. *J. Phys. Chem. B Lett.*, 112:11873–11877, 2008.

115. Y. Nagata and S. Mukamel. Spectral diffusion at the water/lipid interface revealed by two-dimensional fourth-order optical spectroscopy: a classical simulation study. *J. Am. Chem. Soc.*, 133:3276–3279, 2011.

116. S. Nihonyanagi, S. Yamaguchi, and T. Tahara. Direct evidence for orientational flip-flop of water molecules at charged interfaces: a heterodyne-detected vibrational sum frequency generation study. *J. Chem. Phys.*, 130:204704, 2009.

117. S. Nihonyanagi, S. Yamaguchi, and T. Tahara. Water hydrogen bond structure near highly charged interfaces is not like ice. *J. Am. Chem. Soc.*, 132:6867–6869, 2010.

118. A. Nilsson, A. Holmgren, and G. Lindblom. Fourier-transform infrared spectroscopy study of dioleoylphosphatidylcholine and monooleoylglycerol in lamellar and cubic liquid crystals. *Biochemistry*, 30:2126–2133, 1991.

119. I. Noda, Y. L. Y., and Ozaki. 2D correlation spectroscopy study of temperature-dependent spectral variations of NMA in the pure liquid state. *J. Phys. Chem.*, 100:8665–8673, 1996.

120. M. M. Omar. Dielectric properties of pure liquid N-methylacetamide. *J. Chem. Soc. Faraday Trans.*, 76:711–716, 1980.

121. A. Paarmann, T. Hayashi, S. Mukamel, and R. J. D. Miller. Probing intermolecular couplings in liquid water with two-dimensional infrared photon echo spectroscopy. *J. Chem. Phys.*, 128:191103, 2008.

122. A. Pakoulev, Z. Wang, Y. Pang, and D. D. Dlott. Vibrational energy relaxation pathways of water. *Chem. Phys. Lett.*, 380:404–410, 2003.

123. S. K. Pal, J. Peon, B. Baghi, and A. H. Zewail. Biological water: Femtosecond dynamics of macromolecular hydration. *J. Phys. Chem. B*, 106:12376–12395, 2002.

124. S. K. Pal, J. Peon, and A. H. Zewail. Biological water at the protein surface: Dynamical solvation probed directly with femtosecond resolution. *PNAS*, 99:1763–1768, 2002.

125. S. K. Pal and A. H. Zewail. Dynamics of water in biological recognition. *Chem. Rev.*, 104:2099–2123, 2004.

126. S. Park and M. D. Fayer. Hydrogen bond dynamics in aqueous NaBr solutions. *PNAS*, 104:16731–16738, 2007.

127. S. Park, M. Odelius, and K. J. Gaffney. Ultrafast dynamics of hydrogen bond exchange in aqueous ionic solutions. *J. Phys. Chem. B*, 113:7825–7835, 2009.

128. L. Piatkowski, K. B. Eisenthal, and H. J. Bakker. Ultrafast intermolecular energy transfer in heavy water. *Phys. Chem. Chem. Phys.*, 11:9033–9038, 2009.

129. G. C. Pimental and A. L. Maclellan. *The Hydrogen Bond*. Freeman, 1960.

130. L. Powers and N. A. Clark. Preparation of large monodomain phospholipid bilayer smectic liquid crystals. *PNAS*, 72:840–843, 1975.

131. K. Pralat, J. Jadzyn, and S. Balanicka. Dielectric properties and molecular structure of amide solutions. 1. N-methylacetamide in carbon tetrachloride. *J. Phys. Chem.*, 87:1385, 1983.

132. D. Rehm and K. B. Eisenthal. Intermolecular energy transfer studied with picosecond light pulses. *Chem. Phys. Lett.*, 9:387–389, 1971.

133. R. Rey, F. Ingrosso, T. Elsaesser, and J. T. Hynes. Pathways for $H_2O$ bend vibrational relaxation in liquid water. *J. Phys. Chem. A*, 113:8949–8962, 2009.

134. Y. L. A. Rezus and H. J. Bakker. On the orientational relaxation of HDO in liquid water. *J. Chem. Phys.*, 123:114502, 2005.

135. Y. L. A. Rezus and H. J. Bakker. Orientational dynamics of isotopically diluted $H_2O$ and $D_2O$. *J. Chem. Phys.*, 125:144512, 2006.

136. S. T. Roberts, K. Ramasesha, and A. Tokmakoff. Structural rearrangements in water viewed through two-dimensional infrared spectroscopy. *Acc. Chem. Res.*, 42:1239–1249, 2009.

137. I. V. Rubtsov, J. P. Wang, and R. M. Hochstrasser. Vibrational coupling between Amide-I and Amide-A modes revealed by femtosecond two color infrared spectroscopy. *J. Phys. Chem. A*, 107:3384–3396, 2003.

138. L. F. Scatena, M. G. Brown, and G. L. Richmond. Water at hydrophobic surfaces: Weak hydrogen bonding and strong orientation effects. *Science*, 292:908–912, 2001.

139. G. Seifert, T. Patzlaff, and H. Graener. Pure intermolecular vibrational relaxation of the OH bending mode of water molecules. *J. Chem. Phys.*, 120:8866–8867, 2004.

140. D. Selkoe. Folding proteins in fatal ways. *Nature*, 426:900–904, 2003.

141. Y. R. Shen. *The principles of nonlinear optics.* John Wiley & Sons, Inc., 1984.

142. Y. R. Shen. Surface properties probed by second-harmonic and sum-frequency generation. *Nature*, 337:519–525, 1989.

143. Y. R. Shen and V. Ostroverkhov. Sum-frequency vibrational spectroscopy on water interfaces: polar orientation of water molecules at interfaces. *Chem. Rev.*, 106:1140–1154, 2006.

144. M. J. Shultz, S. Baldelli, C. Schnitzer, and D. Simonelli. Aqueous solution/air interfaces probed with sum frequency generation spectroscopy. *J. Phys. Chem.*, 106:53135324, 2002.

145. M. Smits, A. Ghosh, M. Sterrer, M. Muller, and M. Bonn. Ultrafast vibrational energy transfer between surface and bulk water at the airwater interface. *Phys. Rev. Lett.*, 98:098302, 2007.

146. M. Sovago, R. K. Campen, H. J. Bakker, and M. Bonn. Hydrogen bonding strength of interfacial water determined with surface sum-frequency generation. *Chem. Phys. Lett.*, 470:7–12, 2009.

147. M. Sovago, R. K. Campen, G. W. H. Wurpel, M. Mller, H. J. Bakker, and M. Bonn. Vibrational response of hydrogen-bonded interfacial water is dominated by intramolecular coupling. *Phys. Rev. Lett.*, 100:173901, 2008.

148. M. Sovago, E. Vartiainen, and M. Bonn. Observation of buried water molecules in phospholipid membranes by surface sum-frequency generation spectroscopy. *J. Chem. Phys.*, 131:161107, 2009.

149. I. V. Stiopkin, C. Weeraman, P. A. Pieniazek, F. Y. Shalhout, J. L. Skinner, and A. V. Benderskii. Hydrogen bonding at the water surface revealed by isotopic dilution spectroscopy. *Nature*, 474:192–195, 2011.

150. G. Stirnemann, P. J. Rossky, J. T. Hynes, and D. Laage. Water reorientation, hydrogen-bond dynamics and 2D-IR spectroscopy next to an extended hydrophobic surface. *Faraday Discuss.*, 146:263–81, 2010.

151. J. R. Tame, S. H. Sleigh, A. J. Wilkinson, and J. E. Ladbury. The role of water in sequence-independent ligand binding by an oligopeptide transporter protein. *Nat. Struct. Biol.*, 3:998–1001, 1996.

152. R. S. Taylor, L. X. Dang, and B. C. Garrett. Molecular dynamics simulations of the liquid/vapor interface of SPC/E water. *J. Phys. Chem.*, 100:11720–11725, 1996.

153. C. S. Tian and Y. R. Shen. Sum-frequency vibrational spectroscopic studies of water/vapor interfaces. *Chem. Phys. Lett.*, 470:1–6, 2009.

154. K. J. Tielrooij, N. Garcia-Araez, M. Bonn, and H. J. Bakker. Cooperativity in ion hydration. *Science*, 328:1006–1009, 2010.

155. K. J. Tielrooij, D. Paparo, L. Piatkowski, H. J. Bakker, and M. Bonn. Dielectric relaxation dynamics of water in model membranes probed by terahertz spectroscopy. *Biophys. J.*, 97:2484–2492, 2009.

156. R. L. A. Timmer and H. J. Bakker. Water as a molecular hinge in amidelike structures. *J. Chem. Phys.*, 126:154507, 2007.

157. H. Torii. Effects of intermolecular vibrational coupling and liquid dynamics on the polarized raman and two-dimensional infrared spectral profiles of liquid N,N-dimethylformamide analyzed with a time-domain computational method. *J. Phys. Chem. A*, 110:4822–4832, 2006.

158. H. Torii, T. Tatsumi, T. Kanazawa, and M. Tasumi. Effects of intermolecular H-bonding interactions on the AI mode of NMA. Matrix isolation IR studies. *J. Phys. Chem. B*, 102:309–314, 1997.

159. S. Tristram-Nagle and J. F. Nagle. Lipid bilayers: thermodynamics, structure, fluctuations, and interactions. *Chem. Phys. Lipids*, 127:3–14, 2004.

160. S. A. Tristram-Nagle. Preparation of oriented, fully hydrated lipid samples for structure determination using x-ray scattering. *Methods Mol. Biol.*, 400:63–75, 2007.

161. V. V. Victor, D. J. Palmer, and R. Righini. Distinct water species confined at the interface of a phospholipid membrane. *Phys. Rev. Lett.*, 99:078302, 2007.

162. F. Volke, S. Eisenblatter, J. Galle, and G. Klose. Dynamic properties of water at phosphatidylcholine lipid-bilayer surfaces as seen by deuterium and pulsed field gradient proton NMR. *Chem. Phys. Lipids*, 70:121–131, 1994.

163. V. V. Volkov, F. Nuti, Y. Takaoka, R. Chelli, A. M. Papini, and R. Righini. Hydration and hydrogen bonding of carbonyls in dimyristoylphosphatidylholine bilayer. *J. Am. Chem. Soc.*, 128:969–982, 2006.

164. V. V. Volkov, D. J. Palmer, and R. Righini. Heterogeneity of water at the phospholipid membrane interface. *J. Phys. Chem. B*, 111:1377, 2007.

165. G. E. Walrafen. New spectroscopic method for aqueous solutions: Raman $\xi$- function dispersion for $NaClO_4$ in water. *J. Chem. Phys.*, 122:094510, 2005.

166. G. E. Walrafen and L. Blatz. Weak raman bands from water. *J. Chem. Phys.*, 59:2646–2650, 1973.

167. G. E. Walrafen, M. Hokmabadi, and W. H.Yang. Raman invesitagation of the temperature dependence of the bending mode and combination bands from liquid water. *J. Phys. Chem.*, 92:2433–2438, 1988.

168. S. R. Wassall. Pulsed field gradient-spin echo NMR studies of water diffusion in a phospholipid model membrane. *Biophys. J.*, 71:2724–2732, 1996.

169. S. H. White, R. E. Jacobs, and G. I. King. Partial specific volumes of lipid and water in mixtures of egg lecithin and water. *Biophys. J.*, 52:663–665, 1987.

170. T. W. Whitfield, G. J. Martyna, S. Allison, S. P. Bates, H. Vass, and J. Crain. Structure and hydrogen bonding in neat n-methylacetamide: classical molecular dynamics and raman spectroscopy studies of a liquid of peptidic fragments. *J. Phys. Chem. B*, 110:3624–3637, 2006.

171. S. Woutersen and H. J. Bakker. Resonant intermolecular transfer of vibrational energy in liquid water. *Nature*, 402:507–509, 1999.

172. S. Woutersen, U. Emmerichs, and H. J. Bakker. A femtosecond mid-infrared pump-probe study of hydrogen-bonding in ethanol. *J. Chem. Phys.*, 107:1483–1490, 1997.

173. S. Woutersen, Y. Mu, G. Stock, and P. Hamm. Hydrogen-bond lifetime measured by time-resolved 2D-IR spectroscopy-nma in methanol. *Chem. Phys.*, 266:137, 2001.

174. G. W. H. Wurpel, M. Sovago, and M. Bonn. Sensitive probing of dna binding to a cationic lipid monolayer. *J. Am. Chem. Soc.*, 129:8420–8421, 2007.

175. M. Yang, F. Li, and J. Skinner. Vibrational energy transfer and anisotropy decay in liquid water: Is the Förster model valid. *J. Chem. Phys.*, 135:164505, 2011.

176. Y. Zhang, H. Fujisaki, and J. E. Straub. Mode-specific vibrational energy relaxation of AI and AII modes in NMA/water clusters. *J. Phys. Chem. A*, 113:3051–3060, 2009.

177. W. Zhao, D. E. Moilanen, E. E. Fenn, and M. Fayer. Water at the surfaces of aligned phospholipid multibilayer model membranes probed with ultrafast vibrational spectroscopy. *J. Am. Chem. Soc.*, 130:13927–13937, 2008.

# Summary

In this thesis I present a series of experiments which elucidate the structure and dynamics of molecules involved in various biologically relevant systems. The understanding of these molecular-scale properties is crucial for understanding the behavior of biological systems as a whole. Most of our work is dedicated to water, which plays a crucial role in mediating and actively participating in biochemical reactions.

Many biochemical processes occur on very short timescales - sometimes even on a millionth of a millionth of a second (picosecond). In order to capture molecules as they take part in a molecular process (in analogy to taking a picture of a fast moving object in a macroscopic world), we use ultrashort (femtosecond) laser pulses as 'flashes' for our experimental 'camera'. The molecules are 'seen' via their molecular vibrations, which, due to the sensitivity of the vibrational frequency to the structure, conformation and direct environment of the molecule, form an excellent probe to study a large range of biomolecular systems.

In many of these experiments we use two laser pulses. The first of the two pulses excites a molecule (in this thesis water or N-methylacetamide) to the first excited vibrational state. With the second, weaker pulse we monitor the dynamics of the excited molecule. These dynamics comprise the orientational motion, the hydrogen-bond dynamics, the resonant energy transfer to other molecules, and the relaxation of the excitation by which the molecule returns to the vibrational ground state. Hence, this experiment provide useful information about the molecular motions and the interactions of the molecule with its surroundings.

For some of the experiments we have expanded the experimental setup to a two-dimensional pump-probe scheme, where the two dimensions are the frequencies of the pump and probe pulses. The excitation of one of the vibrational resonance, while probing the other provides information on the coupling between the different vibrational modes, and thereby on the relative orientation and position of the molecular groups on which these modes are located.

The molecules of interest are not always forming a bulk medium. In many cases water molecules are located at various interfaces like a cellular water-membrane interface. In order to obtain information about those molecules we used time-resolved two-dimensional sum frequency generation (SFG) spectroscopy. This technique allows us to probe vibrational properties of only the molecules located at the interface. It thus provides highly surface-specific information on interfacial energy flow patterns which is essential for the understanding of chemical processes at aqueous interfaces.

Resonant energy transfer in bulk water

In chapter 4 I report on the study of the vibrational energy relaxation and resonant vibrational (Förster) energy transfer of the OD stretch vibrations of pure $D_2O$ and mixtures of $D_2O$ and $H_2O$. We monitored the occurrence of vibrational resonant energy transfer (VRET) of the OD vibrations by measuring the dynamics of the anisotropy of the vibrational excitation of the OD vibration for different concentrations of HDO in $H_2O$. With increasing HDO concentration, the distances between the OD oscillators decrease and the anisotropy decay becomes faster, showing the increased contribution of resonant energy transfer between the OD oscillators. For pure $D_2O$ the anisotropy decays with a time constant of $\sim$150 fs, showing that the transfer of vibrational energy between different $D_2O$ molecules is extremely efficient. We find the ratio of Förster resonant energy transfer rates of the OH vibrations of $H_2O$ and the OD vibrations of $D_2O$ to be $\sim$2.3. This ratio can be well explained from the difference in cross-section and spectral distribution of the OD and the OH stretch vibrations in water and heavy water.

Water interacting with ions

In chapter 5, I report results of our studies on the vibrational relaxation dynamics of the bending mode of the $H_2O$ water molecules in the presence of different salts (LiCl, LiBr, LiI, NaI, CsI, $NaClO_4$ and $NaBF_4$). We find that the bending mode of water molecules that are hydrogen-bonded to an anion exhibit much slower relaxation rates ($T_1 \sim$1 ps) than water molecules that are hydrogen-bonded to other water molecules ($T_1$=400 fs). The effect of the anion on the absorption spectrum and relaxation time constant of the water bending mode is not only determined by the strength of the hydrogen-bond interaction but also by the shape of the anion. For $ClO_4^-$ and $BF_4^-$ the water forms its hydrogen bond towards the narrow O–O and F–F ridges of the ions, and we find that this special geometry affects the linear and nonlinear spectral response of the bending mode of the water molecule.

Vibrational relaxation in NMA molecules

In chapters 6 and 7 I report the results of 2-dimensional polarization-resolved pump-probe experiments on a model system for small peptide model molecules - N-methylacetamide (NMA). We studied the pathways of vibrational energy relaxation of the amide I and amide II vibrational modes of hydrogen-bonded NMA aggregates and single NMA molecules.

The results for the hydrogen-bonded NMA aggregates show that there is no energy transfer between the amide I and amide II modes. Instead we find that irrespectively of which mode is excited, the vibration relaxes via rapid energy transfer to a non-thermal intermediate state. This relaxation is followed by a second process that leads to full thermal equilibration of the excitation energy. The spectral dynamics associated with the latter relaxation step shows that the thermalization involves the dissociation of larger NMA aggregates like trimers and higher order structures, into dimers and monomers.

In chapter 7 I report on our study of the vibrational energy relaxation mechanisms of the amide I and amide II modes of NMA monomers. In contrary to

the results for the hydrogen-bonded NMA clusters, we find that for part of the NMA molecules ($\sim$20%) the excited amide I vibration transfers its excitation energy to the amide II vibration with a time constant of 8.3$\pm$1 ps (with a back transfer time constant of 16.6$\pm$2 ps). In addition to this energy exchange process, we observe that the excited amide I and amide II vibrations both relax to a final thermal state. For the amide I mode this latter process has a time constant of $\sim$1.5 ps, which dominates the vibrational relaxation of this mode.

Using polarization-resolved measurements, we find that the average reorientation time of the amide I vibration within the NMA aggregates is $\sim$6 ps, whereas for a single NMA molecules this reorientation time is longer and amounts to $\sim$9 ps. This difference in reorientation time can be well explained from the difference in viscosity of the solvents used in the experiments. The relative angle between the transition dipole moments of the amide I and amide II modes is $\theta(\text{AI,AII}) = 56° \pm 3°$, and is unaffected by the presence of inter-NMA hydrogen bonds.

### Distribution of water molecules in lipid membranes

In chapter 8 we study water molecules embedded in 1,2-dioleoyl-sn-glycero-3-phosphocholine (DOPC) model membranes. We investigate the effect of the local environment of the membrane on the vibrational relaxation properties of water, at various hydration levels ($\sim$2-12 water molecules per lipid). We find that water molecules at the membrane's interface experience very different local environments, depending on which site of the lipid they are hydrogen-bonded to. Water molecules forming strong hydrogen-bonds with phosphate and carbonyl groups relax faster than water molecules that are hydrogen-bonded to other water molecules. We investigate the anisotropy decays of water molecules for different isotopic compositions ($D_2O/H_2O$) of the hydrating water. We find that for isotope ratios $D_2O/H_2O > 0.1$ the main contribution to the anisotropy decay comes from vibrational resonant energy transfer (VRET). The rate of VRET gives information on the distribution of water molecules at the membrane surface. Our findings demonstrate that the distribution of water molecules is highly inhomogeneous in tightly packed membranes. Throughout the membrane interface there are regions poor in water and regions with nearly bulk-like water nanopools.

### Dynamics and structure of interfacial water molecules

The last two chapters of the thesis are dedicated to studies of the structure and dynamics of water molecules at water-air and water-lipid interfaces using two-dimensional surface sum-frequency generation (2D-SFG) spectroscopy. In chapter 9 I report on the investigation of the structure of heavy water at the two interfaces. We found that the similarity between the static SFG spectra of water at the water-air and water-lipid interfaces breaks down in the 2-dimensional sum frequency generation measurements. This shows that the structure of the water-air interface strongly differs from that at the water-lipid interface. The technique of 2D-SFG is thus shown to provide a new way of investigating the structure of aqueous interfaces.

In chapter 10 I report on the study of the energy transfer dynamics of wa-

ter molecules at water-air interface using 2D-SFG spectroscopy. Our measurements reveal the presence of surprisingly rapid energy transfer, both between hydrogen-bonded interfacial water molecules (intermolecular), and between the OD group sticking out from the water surface (free OD) and the OD located on the same water molecule and pointing towards the water bulk (intramolecular). The results show that the energy transfer between the stretching vibrations of surface water and bulk water is extremely rapid and efficient, which is an important property for chemical reactions taking place at the water surface.

# SAMENVATTING

In dit proefschrift bestudeer ik de structuur en dynamica van moleculen en moleculaire groepen die een belangrijke rol spelen in biologisch relevante systemen. De verkregen informatie is van groot belang om het werkingsmechanisme van biologische systemen beter te kunnen begrijpen. Het grootste deel van het werk gaat over water, wat een essentiële rol speelt bij veel biochemische reacties.

Veel biochemische processen vinden plaats op een hele korte tijdschaal – sommige deelprocessesn vinden zelfs plaats op een tijdschaal korter dan een miljoenste van een miljoenste van een seconde (picoseconde). Om dit soort moleculaire processen scherp in beeld te krijgen (zoals we in onze macroscopische wereld een foto zouden willen nemen van een snel bewegend voorwerp) gebruiken we ultrakorte (femtoseconde) laserpulsen als 'flitslicht' voor onze experimentele 'camera'. We 'zien' de moleculen door te kijken naar hun moleculaire vibraties. Deze vibraties zijn zeer gevoelig voor de structuur, conformatie en locale omgeving van het molecuul, en lenen zich zodoende uitstekend voor het bestuderen van een groot aantal biomoleculaire systemen.

In veel van deze experimenten gebruiken we twee laserpulsen. De eerste puls slaat het molecuul (in dit proefschrift is dat water of N-methylacetamide) aan naar de eerste aangeslagen toestand. Met de tweede, zwakkere puls meten we vervolgens de dynamica van het aangeslagen molecuul. Onder deze dynamica verstaan we een aantal zaken: de oriëntationele bewegingen en de waterstofbrug-dynamica van het molecuul, resonante energieoverdracht naar andere moleculen en de relaxatie van de excitatie waardoor het molecuul terugkeert naar de vibrationele grondtoestand. De experimenten leveren dus informatie over de moleculaire bewegingen en over de wisselwerking van het molecuul met zijn omgeving.

Bij sommige experimenten maken we gebruik van een twee-dimensionale aanpak. De twee dimensies betreffen de frequenties van de pomp en de probe puls. Door selectief één van twee vibraties in een molecuul aan te slaan en de andere vibratie te observeren, wordt de onderlinge koppeling van de twee vibraties gemeten, wat informatie geeft over de onderlinge afstand en oriëntatie van de chemische groepen die deelnemen aan de vibraties.

De moleculen waarin we geïnteresseerd zijn vormen niet altijd een bulk systeem (een groot volume). Vaak bevinden watermoleculen zich op een scheidingsvlak, zoals bijvoorbeeld bij een celmembraan. Om meer te weten te komen over deze moleculen hebben we tijdsopgeloste som-frequentie generatie spectroscopie gebruikt. Met deze techniek is het mogelijk om zeer selectief de moleculaire vibraties te onderzoeken die zich aan het oppervlak bevinden. De techniek levert ook informatie over de energiestromen aan het oppervlak, wat essentieel is om chemische processen die zich aan waterige oppervlakken afspelen beter te

begrijpen.

### Resonante energieoverdracht in bulk water

In hoofdstuk 4 beschrijf ik een studie naar de resonante vibrationele energieover-dracht (Försteroverdracht) tussen de OD strekvibraties in puur $D_2O$ en in mengsels van $D_2O$ en $H_2O$. We hebben voor verschillende oplossingen van HDO in $H_2O$ de snelheid van de Försteroverdracht bepaald door de anisotropie van de vibratie-excitatie te meten. Het idee hierachter is dat met een stijgende HDO concentratie de gemiddelde afstand tussen de OD oscillatoren afneemt waardoor de Försteroverdracht toeneemt. Voor puur $D_2O$ vervalt de anisotropie met een tijdsconstante van $\sim$150 fs, wat aantoont dat de Försteroverdracht tussen ver-schillende $D_2O$ moleculen zeer efficiënt is. We vinden dat de Försteroverdracht ongeveer 2.3 maal zo langzaam plaatsvindt voor OD vibraties in $D_2O$ als voor OH vibraties in $H_2O$. Deze verhouding kunnen we goed verklaren uit het verschil in extinctiecoëfficiënt tussen de OD- en de OH-strekvibraties in respectievelijk zwaar en gewoon water.

### Water in wisselwerking met ionen

In hoofdstuk 5 beschrijf ik de resultaten van ons onderzoek naar de vibratiere-laxatie van de buigvibratie van watermoleculen ($H_2O$) in de nabijheid van ver-schillende zouten (LiCl, LiBr, LiI, NaI, CsI, $NaClO_4$ en $NaBF_4$). We hebben ontdekt dat voor watermoleculen die een waterstofbrug vormen met een anion, de buigvibratie veel trager relaxeert ($T_1 \sim$1 ps) dan voor watermoleculen die een waterstofbrug vormen met andere watermoleculen ($T_1$=400 fs). We ontdekten dat het effect van het anion op de relaxatiesnelheid en op het absorptiespec-trum van de buigvibratie niet alleen afhangt van de sterkte van de waterstof-brug, maar ook van de vorm van het anion. In het geval van $ClO_4^-$ en $BF_4^-$ vormen de watermoleculen waterstofbruggen met de smalle O–O en F–F ran-den van de ionen. We vinden dat deze bijzondere geometrie zowel de lineaire als de niet-lineaire respons van de buigvibratie van het watermolecuul beïnvloedt.

### Vibratierelaxatie in NMA moleculen

In hoofdstukken 6 en 7 beschrijf ik de resultaten van een aantal polar-isatieopgeloste twee-dimensionale pomp-probe experimenten aan een molecuul dat dient als modelsysteem voor korte peptiden: N-methylacetamide (NMA). We hebben het relaxatiemechanisme van de amide I en de amide II vibratie bestudeerd voor zowel monomere NMA moleculen als voor NMA clusters die door waterstofbruggen verbonden zijn.

Voor de gewaterstofbrugde clusters zien we dat er geen energieoverdracht plaatsvindt tussen de amide I en de amide II modes. In plaats daarvan vinden we dat, onafhankelijk van de mode die wordt aangeslagen, de vibratie via snelle energieoverdracht relaxeert naar een niet-thermische tussentoestand. Deze re-laxatie wordt gevolgd door een tweede proces dat leidt tot volledige thermalisatie van de excitatie-energie. Uit de spectrale dynamica die optreedt bij deze laat-ste relaxatiestap leiden we af dat het thermalisatieproces gepaard gaat met het uiteenvallen van grotere NMA clusters, zoals trimeren en hogere-ordestructuren, in NMA dimeren en monomeren.

In hoofdstuk 7 beschrijf ik ons onderzoek naar het relaxatiemechanisme van

de amide I en II modes van NMA monomeren. In tegenstelling tot de gewater-
stofbrugde clusters vinden we dat voor een deel van de NMA moleculen (∼20%)
de aangeslagen amide I vibratie nu wel haar energie overdraagt op de amide II
vibratie. Dit proces vindt plaats met een tijdsconstante van $8.3 \pm 1$ ps (de snel-
heidsconstante voor het proces in omgekeerde richting bedraagt $16.6 \pm 2$ ps).
Naast dit energie-uitwisselingsproces zien we dat de aangeslagen amide I en
amide II vibraties beide naar een thermische eindtoestand relaxeren. Voor de
amide I vibratie vindt dit laatste proces dat de relaxatie domineert, plaats met
een tijdsconstante van ∼1.5 ps.

Uit polarisatieopgeloste metingen leiden we af dat de gemiddelde re-
oriëntatietijd van de amide I vibratie in de NMA clusters ∼6 ps bedraagt,
terwijl voor een NMA monomeer deze reoriëntatietijd langer is (∼9 ps). Dit
verschil in reoriëntatietijd kan worden verklaard uit het verschil in viscositeit
van de oplosmiddelen die in de experimenten gebruikt zijn. De hoek tussen
de overgangsdipoolmomenten van de amide I en amide II modes bedraagt
$\theta(AI,AII) = 56° \pm 3°$ en verandert niet als de NMA moleculen aan elkaar
vastzitten met waterstofbruggen.

RUIMTELIJKE VERDELING VAN WATERMOLECULEN IN LIPIDE MEMBRANEN
In hoofdstuk 8 bestuderen we watermoleculen die ingebed zijn in 1,2-dioleoyl-sn-
glycero-3-phosphocholine (DOPC) modelmembranen. We hebben het effect van
de locale membraanomgeving op de vibratierelaxatie van water onderzocht voor
verschillende graden van hydratatie van de membranen (∼2–12 watermoleculen
per lipide). We ontdekten dat de watermoleculen aan het membraanoppervlak
zich heel verschillend gedragen, afhankelijk van de lipide groep waarmee ze
een waterstofbrug vormen. Watermoleculen die een sterke waterstofbrug vor-
men met de fosfaat- of carbonylgroepen laten een snellere relaxatie zien dan
de watermoleculen die aan andere watermoleculen gebonden zijn. We hebben
het anisotropieverval onderzocht van de watermoleculen voor verschillende iso-
toopsamenstellingen van het hydraterende water. Voor isotoopverhoudingen
$D_2O/H_2O$ >0.1 wordt het anisotropieverval voornamelijk veroorzaakt door
Försteroverdracht. De snelheid van de Försteroverdracht levert informatie over
de ruimtelijke verdeling van watermoleculen aan het membraanoppervlak. Onze
resultaten laten zien dat de verdeling van watermoleculen zeer inhomogeen is:
de membranen bevatten zowel zeer waterarme gebieden als gebieden met bijna
bulkachtig water.

DYNAMICA EN STRUCTUUR OF VAN WATERMOLECULEN AAN EEN OPPERVLAK
De laatste twee hoofdstukken van dit proefschrift gaan over studies naar de
structuur en dynamica van watermoleculen aan het lucht-wateroppervlak en aan
het lipide-wateroppervlak met behulp van oppervlakte som-frequentie generatie
(2D-SFG) spectroscopie. In hoofdstuk 9 beschrijf ik een studie naar de structuur
van zwaar water aan de twee oppervlakken. De twee-dimensionale SFG spectra
van water aan het lucht-wateroppervlak en aan het lipide-wateroppervlak bli-
jken, in tegenstelling tot de statische SFG spectra, erg van elkaar te verschillen.
Hieruit volgt dat ook de structuur van het lucht-wateroppervlak sterk verschilt
van de structuur van het lipide-wateroppervlak. 2D-SFG vormt dus een nieuwe

methode om de structuur van waterige oppervlakken te bestuderen.

In hoofdstuk 10 doe ik verslag van een studie naar de energieoverdrachts-dynamica van watermoleculen aan het lucht-wateroppervlak met behulp van 2D-SFG spectroscopie. We hebben een opmerkelijk snelle energieoverdracht waargenomen, zowel *tussen* de watermoleculen aan het oppervlak die door waterstofbruggen aan elkaar gebonden zijn (intermoleculair), als *binnen* het watermolecuul, waarbij de overdracht plaatsvindt tussen de OD groep die uit het wateroppervlak steekt (vrije OD) en de OD groep die het bulk water inwijst (intramoleculair). Deze resultaten laten zien dat de energieoverdracht tussen de strekvibraties van oppervlakte en bulk water extreem snel en efficiënt is. Dit is van belang voor chemische reacties die zich aan het wateroppervlak afspelen.

# ACKNOWLEDGEMENTS

A little over five years ago I have joined AMOLF and already within the first few months it felt right. It felt right scientifically and it felt right on a personal level. I'm grateful that after these years this feeling didn't change and I certainly leave AMOLF with a certain sadness. Many people have contributed to this joyful and successful time, in particular my promotor - Huib. I am very grateful that you made a brave step and hired your first foreign PhD student. Your genuine joy in solving physical problems, transforming the data into an elegant physical picture is truly motivating and inspiring. I have learned a lot from you in many aspects. Thank you for your supervision and both numerous scientific and personal advices. I hope that in the future aside the physical resemblance people will start to point out also scientific one.

Mischa - I truly enjoyed working with you. Thank you for the successful cooperation and that your door was always open to those seeking scientific and personal advice. I hope that one day, which hopefully will arrive soon, we will sit down and laugh at those emails from the 'editors' together ;)

Yves and Rutger - my first, different as fire and water, roommates - thank you for taking me under your wings. Rutger, you have provided me with an excellent lab training. I'll never forget the day when we rebuilt the YLF laser from scratch. You helped me to take my first steps in programming, which turned to be an important factor in finishing this thesis. Yves, you have always been willing to discuss (enthusiastically) science and to pass your knowledge in various ways. I have always enjoyed our lively discussions, even though for the people around us they appeared to be a bit loud. Thank you for all you did for me. An unintentional training in practical jokes provided by you guys is highly appreciated. Also thanks for the great time outside AMOLF - Niagra Falls road trip, playing squash, climbing and many more...

Christian Petersen - the quiet viking from the Danish lowlands - thanks for keeping a joyful/whistly atmosphere in our office and these gossiping sessions at Wong-Koen.

My recent office mates Sietse and Liyuan - thank you so much for making our office a happy place. Sietse, my 'guess what that song is' buddy - keep up with the good work! Thanks for the joyful road trip in US. Liyuan - it's really nice to watch how you're becoming an excellent experimentalist! Thanks for keeping my spirits up with all the treats from your secret drawer.

All the other group members: Jocelyn (for the great Halloween party), Adriaan (for all the chit-chats), Klaas (for being my first and only snowboard instructor), Ellen (for the Sinterklaas parties and the excellent erwtensoep), Johannes, Nuria, Janneke, Pavol, Matthijs, Christian Weststrate. The newest members of our group - Marcin, Wouter, Simona, Niklas - good luck with your research!

# EPILOGUE

The images shown on the front and the back cover are actual photographs representing a bursting balloon filled with water. These photos were taken with a standard digital camera with a single femtosecond laser pulse acting as a flash light. The laser flash was triggered manualy and the pneumatic actuator (used to puncture the balloon) was synchronized to the laser flash.

The femtosecond visible photography setup is schematically depicted below.
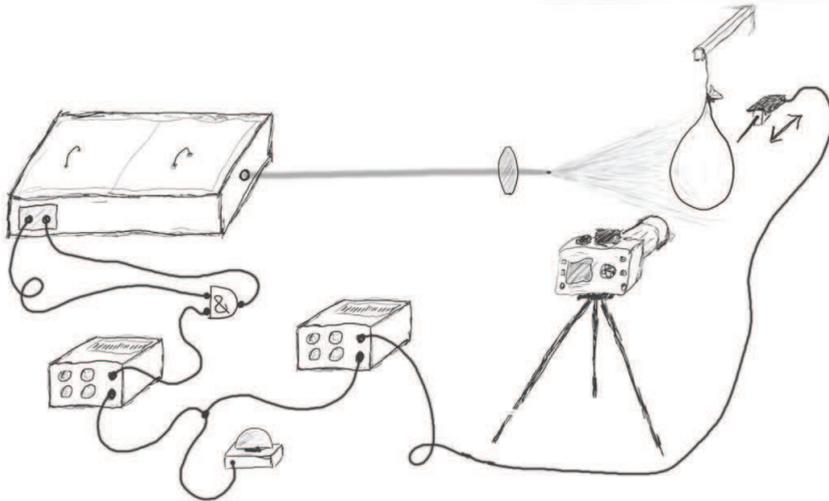
To the knowledge of the authors these photographs were taken with the shortest exposure ever!